Surface Modification and Metal Printing Using Atmospheric Pressure Plasma

M. Emre Sener

Department of Chemistry
UCL

This dissertation is submitted for the degree of
Doctor of Philosophy

September 2021

Declaration

'I, Mustafa Emre Sener confirm that the work presented in this thesis is my own. Where information has been derived from other sources, I confirm that this has been indicated in the thesis.'

M. Emre Sener
September 2021

Abstract

Non-thermal atmospheric plasma sources are at the centre of a growing new field of research that promises significant benefits in areas ranging from catalysis to medicine. The main value of atmospheric pressure sources lie in their ability to generate highly energetic and reactive species under near-ambient conditions. This characteristic makes atmospheric plasma an appealing alternative to well-established vacuum plasma processes.

In this study, radio frequency atmospheric pressure plasma sources are used for modification of metal oxide surfaces and direct metal deposition. In atmospheric pressure plasma afterglow, plasma electrons are shown to be capable of reducing Cu_2O films, this is proven by applying an external electric field to collect or to retard plasma electrons and observing the evolution of the oxide film. Using a micro-plasma jet, Cu_2O and SnO_2 are demonstrated to be completely reduced to their parent metals when exposed to helium plasma. A reducing plasma is required to induce partial reduction in TiO_2, WO_3 and ZnO, generating oxygen deficiencies. Oxygen deficient TiO_2, also known as *black titania* is a well-known defective metal oxide photocatalyst. In this work, a facile method for producing black titania is developed using reducing plasma jets. This method improves photocatalyic efficiencies of nano-porous anatase up to sixfold while dispensing the need for vacuum or high pressure equipment.

Deposition of conductive metals is a topic of ongoing research, with an aim to develop techniques and precursors that can enable printing of electrical circuits onto unconventional substrates. In this work, a novel technique for metal printing using plasma jets is developed. The method developed in this work enables single-step deposition of conductors from low-cost metal salt based precursors. Using aerosolized $CuSO_4$ in the plasma jet stream, it is shown that metallic traces can be deposited on a large variety surfaces with fine spatial control.

Impact Statement

A large portion of modern technological manufacturing processes rely on plasmas to perform *dry* chemistry; plasmas are used in an estimated third of all steps in modern semiconductor fabrication. Industrial vacuum plasmas come with significant equipment and energy costs, making them unsuitable for many manufacturing processes.

The work done in this thesis is geared towards exploitation of low-cost and accessible atmospheric pressure plasma sources to drive chemical processes that are normally achieved through wet-chemical methods or in some cases, under extreme temperature and pressure. The findings in this thesis will support the development of a variety of technologies ranging from non-destructive surface restoration in the heritage sector to improved catalysts for solar energy conversion.

Building on top of fundamental findings, a novel printing technology for single step, waste-free printing of circuit traces is also described in this work. This method can be used for production of electronic sensors and circuit boards on non-conventional substrates. It is likely that development of atmospheric printing plasma technology disclosed here will also have an impact on nanoparticle synthesis and coatings sector as a low-cost, high throughput alternative to vacuum plasma methods. Technology based on this work has been licensed and is being developed commercially in the aeronautical and electronics sectors at the time of writing.

List of Relevant Publications:

- Sener, M. E. & Caruana, D. J. Modulation of copper (I) oxide reduction/oxidation in atmospheric pressure plasma jet. *Electrochem. Commun.* **95**, 38-42 (2018)
- Sener, M. E., Sathasivam, S., Palgrave R., Quesada-Cabrera, R. & Caruana, D. J. Patterning of metal oxide thin films using a H_2/He atmospheric pressure plasma jet. *Green Chem.* **22**, 1406-1413 (2020)
- Sener, M. E. & Caruana, D. J. Plasma Jet Deposition Process. *WIPO* WO2021047761 (2021)

Acknowledgements

I would like to acknowledge Prof. Daren J. Caruana, my primary project supervisor, for his immense support and contributions to all the work presented here, from inception to completion. Additionally, I thank and acknowledge Prof. Paul McMillan and all the help he has provided during this project.

I would also like to sincerely thank Dr. Raul Quesada-Cabrera, for his intellectual contributions and insight to the work done on TiO_2 catalysts. I'd like to acknowledge Dr. Steve Firth for providing training and help with electron microscopy alongside Professor Robert Palgrave for his contributions in providing training and mentorship in photoelectron spectroscopy. I would like to extend my gratitude to Dr. Michael Parkes for his help with Schlieren photography and optics.

I'd like to extend my gratitude to Dr. Ram-Prasad Gandhiraman and NASA Ames Research Centre for providing guidance and technology development opportunities in the field of plasma deposition.

Finally, I'd like to acknowledge EPSRC for providing me with this research opportunity (EP/N509577/1), and a chance to continue this work after the completion of this project (EP/N509577/1).

Table of contents

List of figures

List of tables

Chapter 1

Introduction

1.1 Plasmas

The word plasma derives itself from the Greek word plássō meaning, to mould. Irving Langmuir was the first to use the term plasma, hinting at the fluid properties of this form of matter in which electrons and ions are transported freely just as the way blood plasma "carries red and white corpuscles and germs" [1]

The modern commonly cited definition of plasma is given by Chen [2] as a quasi-neutral gas comprised of charged and neutral particles, exhibiting collective behaviour. This enormously broad definition of plasma shows parallels with the ubiquity of this phase of matter, making up an estimated 99% of the visible universe [2, 3].

Besides its place in space and glowing displays of auroras, plasmas serve important technological roles in industry and research. Plasmas are used in fields as diverse as nuclear fusion, semiconductor fabrication, medicine, and illumination. This versatility of plasmas is strongly linked to the incredibly wide array conditions and chemistries that they afford. Hot plasmas, such as flames, and electric arcs can sustain extremely high temperatures routinely above 3,000 K [4] and are therefore used in metallurgy and high energy research. Unlike most forms of matter commonly encountered, plasmas can exist outside of thermodynamic equilibrium whilst still containing free and energetic, charged particles. Charged particles such as electrons interact strongly with electric and magnetic fields, allowing control over the composition and energies of the particles comprising this ionised gas. Having control over the energies of electrons, ions and, excited species creates a unique chemical environment that is beyond the reach of wet or solid-state equilibrium chemistry. For example, in the semiconductor industry, finely tuned plasmas are used to generate highly reactive and energetic species is for etching, doping and deposition processes at near ambient temperatures

[5].

In this work, non-equilibrium plasmas generated via electrical discharges at atmospheric pressure are studied for their use in modification of surfaces and deposition of materials. This chapter will aim to first provide a general background to electrical gas breakdown processes and important parameters that are used to characterise such a discharge. Later, a brief look at different types of atmospheric pressure plasma sources will be laid out, alongside a discussion on the experimental and computational methods commonly used in the study of these plasma sources. This work is mainly concerned with the applications on atmospheric pressure, low-temperature discharges known as *atmospheric pressure plasma jets* (APPJs), therefore the latter sections in this chapter will provide an outlook onto the existing application areas of atmospheric pressure plasmas and more specifically APPJs in material deposition and surface modification.

1.2 Gas Breakdown Process

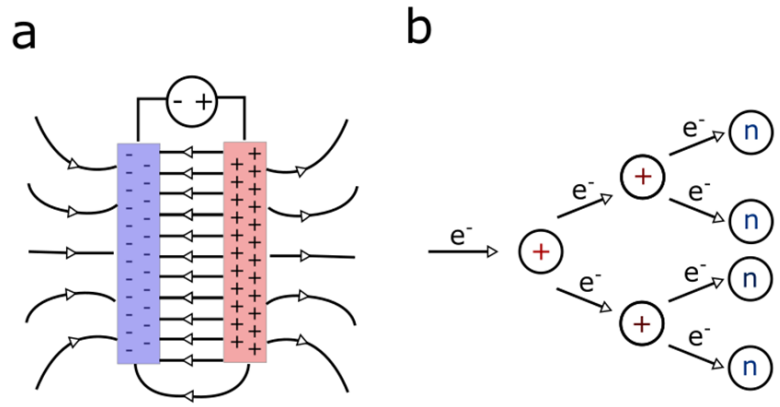

Fig. 1.1 Drawing of an electric field generated between parallel plates of opposing polarity (a). Chain ionisation events where electrons (e-) are accelerated and inelastically collide with neutrals (n), producing ions (+) and secondary electrons (b).

While multiple sources of energy can be used to generate plasma including intense ionising radiation, thermal excitation or oscillating magnetic fields, this work is primarily concerned with electrical discharges that are sustained through applied electric fields. Electrical discharge plasma is requires the transition of an insulating gas with a negligible electron density (n_e) to a conductive fluid containing a significant number of ions and electrons. This process is called plasma ignition. Plasma ignition in electrical discharges was initially studied

and mechanistically described by Townsend [6] and later on Loeb, Meek [7], and Raether [8].

In broad terms, ignition and sustainment of plasma requires the acceleration of a few seed electrons, the most mobile charged species in the gas, in an applied electric or magnetic field (Figure 1.1a). These electrons, if sufficiently energetic, then collide with the background gas particles to cause ionisation reactions where further free electrons are generated. This repeated acceleration – collision cascade, as depicted in Figure 1.1b rapidly increases the number of electrons in the gas, producing plasma. Depending on the discharge geometry, mode of excitation and the plasma gas, the breakdown can then continue in various discharge modes ranging from corona, streamers, glow discharges to electric arcs.

1.2.1 Collisions in Plasmas, a Microscopic View

Following ignition, charged species density in a plasma will rapidly grow. Electrons accelerated in the electric field will undergo multiple collisions with the surrounding gas as discussed previously. These collisions can either be elastic or inelastic depending on whether the collision conserves the total kinetic energy of the colliding pairs. Frequency of collisions determines the distance travelled by an electron between two collision events. This mean distance is called the electron mean free path (λ_e). Electron mean free path depends strongly on the number density (n_g) and the effective collision cross-section $\left(\sigma_{eff}\right)$ of surrounding gas species, an estimate mean of electron mean free path is given by $\lambda_e = \frac{1}{\sigma_{eff}\, n_g}$.

Plasmas used in this work are considered *weakly ionised* with the ionisation ratios $n_e/n_g << 1$. Consequently, the dominant collisions in weakly ionised plasmas are between electron and neutral species. Under such conditions, σ_{eff} is almost entirely determined by the elastic collision cross section of the parent neutral gas. In helium plasmas at atmospheric pressure, the elastic collision cross-section is on the order of $10^{-19}\ m^2$[9], and the number density of helium is $10^{25}\ m^{-3}$, giving a mean free path of $\lambda_e \approx 1\ \mu m$. To aid comparison, the mean free path of helium atoms in helium gas is an order of magnitude smaller, $\lambda_{He} \approx 100\ nm$, highlighting the asymmetry between the behaviour of heavy species and electrons in a plasma.

While the mean free path of electrons is determined by *elastic* collisions, the ionisation and excitation events that sustain the plasma are governed by *inelastic* collision cross sections which are highly dependent on electron energy. Due to the high energies typically involved, these values are commonly expressed as electron temperature (T_e), defined as $T_e = 2/3\varepsilon_e$ where ε_e is the mean electron energy in the plasma. For convenience, electron temperature is commonly expressed in units of electron-volts (eV) by dividing the thermodynamic

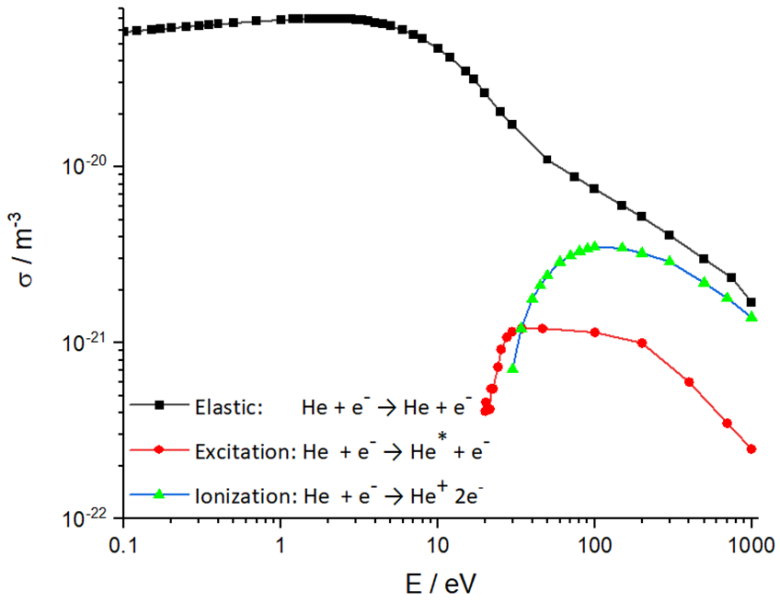

Fig. 1.2 Collision cross sections as a function of electron energy for three types of electron helium collision in helium plasma. Data obtained from SIGLO database[11].

temperature of the electrons in Kelvin (K) by the Boltzmann constant ($1\ eV \approx 11600\ K$).

Figure 1.2 shows the electron energy dependent cross sections of helium, where only the ground state, excited and singly ionised helium species are considered. Unlike elastic collisions, ionisation and excitation pathways require a minimum electron energy equal to the energy-loss during excitation. This implicitly suggests a minimum electric potential difference that is needed to sustain a plasma, highlighted by the well-known Paschen curve [10].

Plasma-Wall Collisions

Laboratory plasmas are generally contained using physical barriers, generating plasma/solid interfaces. For example, in this work, plasmas are generated within insulating glass tubes, creating a plasma/insulator interface. As plasma extends towards walls or a non-gaseous phase, the difference in electron and ion mobilities causes an imbalance in the number species that are collected onto the walls containing the plasma. Close to a solid surface, electrons within a small distance are lost to the surface at a faster rate than ions (Figure 1.3). A surface charge builds up on the wall to the point where retardation of the negatively charged electrons and acceleration of positively charged ions due to the wall potential leads to an equilibrium between flux of both positive and negative charges to the wall. At equilibrium, the plasma

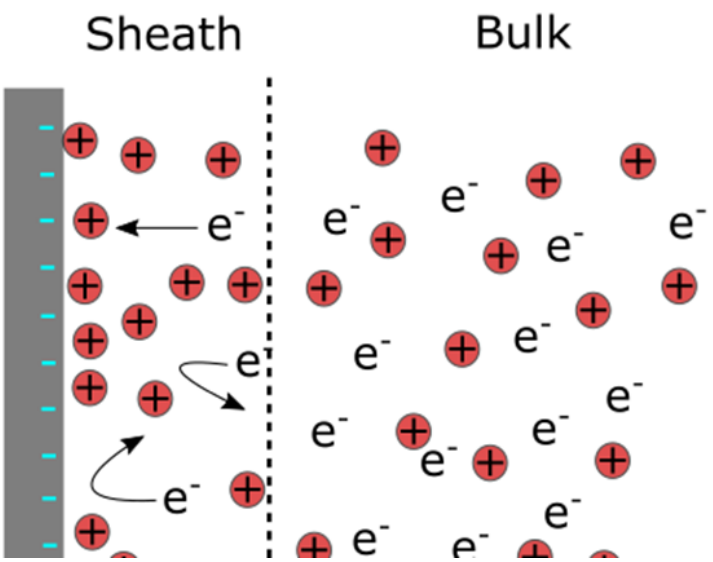

Fig. 1.3 Drawing of plasma in contact with a wall, forming a sheath.

wall interface consists of a positive space charge layer adjacent to the wall with more ions than electrons, called the Debye sheath. The thickness of this sheath is inversely proportional to the pressure as increasing collision frequency at higher pressures disrupts self-organisation of the sheath. At atmospheric pressure, sheath thicknesses are small, on the order of 10^{-4} m [12].

1.2.2 Thermodynamics in Plasmas, a Macroscopic View

The previous section highlighted the energy threshold required for electron collisions to sustain a plasma discharge. This also implies that a plasma can always be produced from any substance simply by raising its temperature until it transitions into the plasma state. These plasmas would exist at thermodynamic equilibrium, described by a single, thermodynamic temperature.

By increasing or decreasing the temperature of this thermal plasma, the electron density and the energy of the electrons can be changed. This relationship is given by the Saha equation [1]. While equilibrium (thermal) plasmas predominate in nature, most plasma sources in laboratories, and indeed in this work, are created under non-equilibrium conditions by the application of external electric fields to an ioniseable gas.

Energy exchange within and out of a system is controlled by intensive quantities, for example *temperature* is an intensive parameter that determines heat exchange. Under local thermodynamic equilibrium (LTE) conditions, these intensive parameters are assumed to

vary slowly compared to the rate of mass and energy exchange in the system. LTE systems such as thermal plasmas can be well described with intensive parameters, and if every particle in an LTE ensemble were to be measured, their kinetic energies would be found to lie along a Boltzmann distribution, with a well-defined temperature.

Unlike most other chemical systems, electrical discharges may be generated both in and outside of thermodynamic equilibrium. Plasmas that cannot be well-described by a single temperature parameter are called *non-thermal*, or more precisely, non-LTE plasmas [13]. In a non-LTE plasma, energy distributions of particles (electrons, ions, and neutrals) can diverge significantly from a thermally predicted distribution. As temperature is only *strictly* defined under equilibrium conditions, this leads to a breakdown of the very definition of temperature when investigating non-LTE plasmas [13].

Terminology such as electron (T_e), ion (T_i), excitation (T_{exc}), vibrational (T_{vib}), rotational (T_{rot}) and gas (T_{gas}) temperature is commonly used to distinguish between the distribution of energies for a chosen type of particle, or degree of freedom in a non-LTE plasma. This re-definition of temperature requires the assumption that observed energy distributions are in equilibrium within themselves but not in equilibrium with plasma as a whole. For the type of atmospheric pressure non-LTE plasmas in this work, divergence from equilibrium is exemplified by the following set of typical temperature inequalities.

$$T_e \approx 10^5 K > T_{exc} \approx T_{vib} \approx 10^3 K > T_{gas} \approx T_{rot} \approx 10^2 K$$

In plasmas, this inequality fundamentally stems from the inefficiency of momentum transfer between electrons and neutral particles owing to the large mismatch between electron and heavy particle masses. As a consequence, thousands of inelastic collision events are needed between electrons and heavy particles for a plasma to reach LTE, in a process called *thermalisation*. The specific time scale for electrons reaching thermal equilibrium in atmospheric pressure plasmas approaches 10^{-7} s [14]. This value is significantly large in comparison to the timescales for reaching vibrational $(10^{-8}$ $s)$ or rotational $(10^{-10}$ $s)$ equilibrium that may require hundreds or as low as tens of collision events. With exceptions, it can be said that the temperature of any given degree of freedom in an electric discharge is proportional to the time required for its thermalisation in a non-LTE plasma.

If, in this thermalisation timescale, significant mass or energy flux takes place, plasmas can be sustained in a non-LTE regime, whether they rely on mass (blown arcs [15]), or energy flux (pulsed, radio-frequency and microwave discharges). This fact alone drives the design of many atmospheric pressure plasma sources discussed in the next section.

1.3 Atmospheric Pressure Plasma Sources

It is important to note that non-thermal does not strictly imply cold plasma. While thermal plasmas must necessarily be *hot* due to the high amount of energy needed to vaporise and ionise most substances, the definition of non-thermal plasmas does not exclude hot plasmas. Indeed, some plasma sources such as inductively coupled plasmas (ICP) at atmospheric pressure can routinely reach kinetic temperatures of $2,000\ K$ [16], while satisfying the $T_e > T_g$ inequality previously discussed.

In a vast majority of applications, *cold* atmospheric pressure plasmas are used in fields where they need to be brought in contact with surfaces, and where conventional vacuum processes may be undesirable or impractical. For many applications, such as surface treatment of materials, maintaining a plasma discharge under cold and non-LTE conditions is critical as thermal plasma temperatures can be difficult to contain, and damaging to most materials. Multiple strategies for generating suitable non-LTE discharges have been explored by researchers, resulting in a wide array of atmospheric pressure plasma source designs The following sections will aim to provide a brief an overview of commonly used atmospheric plasma sources and the underlying phenomena behind their modes of operation. A recent review by Bruggeman and co-workers provides a comprehensive discussion of atmospheric pressure plasma discharges and plasma source designs [14].

In electrically driven discharges, energy from an externally applied field is coupled to plasma electrons in the form of kinetic energy. Through repeated collisions, electron kinetic energy cascades into other available degrees of freedom in the surrounding gas, seeking thermal equilibrium. To minimise thermalisation and therefore maintain non-LTE conditions, atomic gasses such as helium and argon are commonly chosen as the working gas for atmospheric pressure plasma discharges. Atomic gases lack vibrational and rotational modes that can absorb energy via electron impact, making it easier to sustain a non-LTE discharge.

In an atomic gas discharge, sustained by an applied electric field, the kinetic temperature of the gas can be estimated by balancing the energy input from the free electrons being accelerated in the electric field with the losses due to elastic collisions with the background gas, this energy balance equation [14] is given below.

$$T_g = T_e\left(1 - \frac{m_g}{4m_e}\frac{(\lambda_e eE)^2}{E_c^2}\right) \tag{1.1}$$

Where:

m_g is mass of the background gas,

m_e is the mass of an electron,

λ_e is the electron mean free path,

e is the electron charge,

$\mathscr{E}_c$ is the electron energy.

As λ_e, is inversely proportional to pressure, it is seen that $\frac{T_e}{T_g} \propto p^{-2}$. This implies that at increasing pressures, it becomes harder and harder to sustain plasmas in a non-LTE regime. In fact, atmospheric pressure plasma sources are plagued with instabilities, leading to rapid thermalisation. A common example is transitions of un-stabilised diffuse atmospheric pressure plasmas into contracted sparks or arcs that are accompanied with a rapid increase in gas temperature [17]. These types of instabilities are sometimes circumvented by rapidly cycling the driving potential off before the instability can develop. Upon removal of the electric field, the plasma electrons and ions rapidly recombine, quenching the plasma. This approach underlies the plasma source designs that operate in a pulsed regime where applied electrical impulses that can be as short as nanoseconds [18].

A second strategy is to limit the available power by interposing a high impedance path between the power source and the plasma body. A high impedance path effectively limits the peak current, and therefore, power that is available for dissipation in the plasma. This approach forms the foundation of ballasted direct current (*DC*) discharges [19] and dielectric barrier discharges (DBD) where a resistor or a capacitor equivalent is used to limit plasma current, respectively. Most atmospheric pressure plasma sources used in research utilise either one of these two approaches to achieve cold and non-LTE discharge.

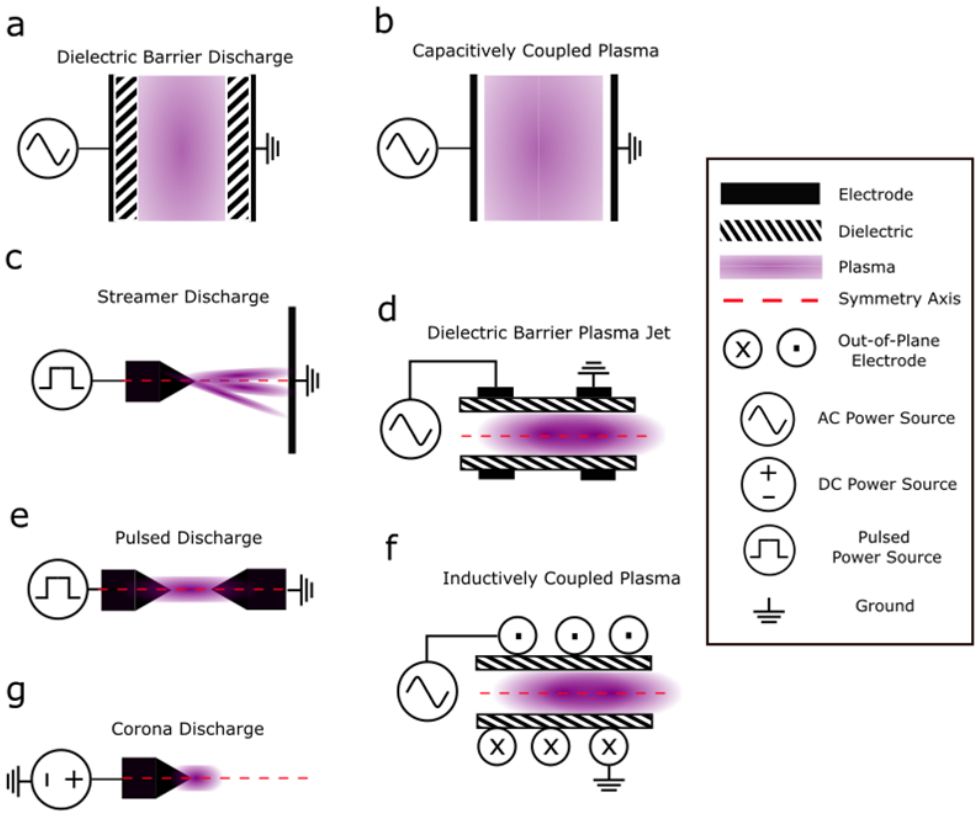

Fig. 1.4 Schematic description of multiple atmospheric pressure plasma sources. Adapted from [14]

Dielectric barrier discharges (Figure 1.4a) are a common source of atmospheric plasma that can generate diffuse discharges that occupy an appreciable volume. In this work, DBD type plasma is used, where one or both the electrodes are covered by a dielectric layer. In DBDs, an insulating dielectric layer is placed between the plasma and the driven electrodes. In most cases, dielectric barrier discharges are also capacitively coupled discharges (Figure 1.4b).

Under steady state conditions if electrodes are driven under DC power, flux of charged species to the dielectric surface generates a surface charge density on the dielectric. If charge loss from the surface is small enough, this surface charge acts to shield the plasma bulk from the applied potential, eventually extinguishing the discharge. In cases where the dielectric allows sufficient current flow, DC discharges can still be sustained, albeit with low energy density. Therefore, to enable efficient operation behind a dielectric barrier, these discharges

are often operated with high frequency (HF) or pulsed power sources instead of DC, leading to capacitive coupling of the plasma to the driving circuit.

To generate DBD, a rapidly changing electric field is applied through the background gas while one or both current carrying electrodes are separated from the plasma via a layer of dielectric material. The dielectric acts as a series capacitor, limiting the current flow from the electrodes to the plasma, stabilising the discharge as either multiple streamers (contracted columns of plasma) [20] or as in some cases, for example high frequency ($> 1\ MHz$) excitation, a diffuse volume glow between the electrodes [21]. Multiple geometric arrangements of the electrode and dielectric layer are possible, a common arrangement that is also used in this work is that of the coaxial plasma jet (Figure 1.4d). In a coaxial plasma jet, gas flow between the coaxially placed ring electrodes transfers plasma species to the outside of the discharge manifold. This generates a volume of decaying plasma afterglow where part of the discharge is spatially separated from the inter-electrode region.

An alternative method of coupling energy into the plasma relies on the use of magnetic rather than electric fields. This results in inductively coupled plasmas (ICP) shown in Figure1.4f where a coil carrying high frequency current generates a strong oscillating magnetic field along the axis of the coil. Plasma gas is flown through the centre of this inductor, leading to the coupling of the magnetic field to the charged particles in the plasma bulk, sustaining the discharge. Inductively coupled plasmas are routinely used in analytical chemistry equipment for mass spectrometry [22] and optical spectroscopy [23], serving a convenient source of ionised and excited species in the plasma bulk.

Other forms of plasma generators are also possible using pulsed energy sources. In a pulsed (Figure1.4e) or multiple streamer discharge (Figure1.4c), fast cycling of the plasma driving electrodes causes ionisation followed by rapid recombination of gas surrounding the electrodes as discussed previously. Depending on the discharge geometry, pulse rate, and duration, these discharges occur either as single filaments or multiple streamers.

Corona discharges (Figure1.4g) occur when a high electric field is present but no low-impedance path to ground exists for current flow, these types of discharges are commonly seen on electrodes with high curvature and high electric potential ($> 1\ kV$) where the local electric field is strong enough to cause ionisation of the surrounding gasses [24].

A large variety of plasma sources are employed in scientific research, used both for fundamental inquiry into high pressure plasmas and also a large range of technological applications. In recent years, there have been attempts in developing standardized plasma sources to re-focus the existing research effort and help establish *reference* plasma discharges. Two such sources are the kINPen [25] developed in INP Griefswald for primarily medical

applications and the COST Plasma Jet [26, 27] developed by Schulz-von der Gathen and collaborators.

1.3.1 Atmospheric Pressure Plasma Diagnostics

As a wide range of atmospheric pressure plasmas are used in research and industry, comparison and characterisation of different plasma sources across laboratories and studies is a significant challenge. Plasma diagnostic methods are commonly employed to extract fundamental information related to the physical and chemical quantities within the plasma such as energy distributions and species densities. Diagnostics are essential for understanding the foundational processes occurring in a gas discharge, for obtaining predictive insights that can help guide experiments and to inform potential applications of atmospheric pressure plasmas. Considering the extremely large variety of possible plasma source arrangements and gases, as discussed in the previous section, effective characterisation of these plasma sources becomes crucial.

For these aforementioned reasons, plasma diagnostic techniques are featured in the two most recent "plasma roadmaps" [28, 29], aimed to provide a review of the state-of-the-art and future directions in plasma research. These reviews suggest that the advancement of plasma diagnostics methods is key for both better understanding of fundamental plasma processes and control of applied plasmas [28].

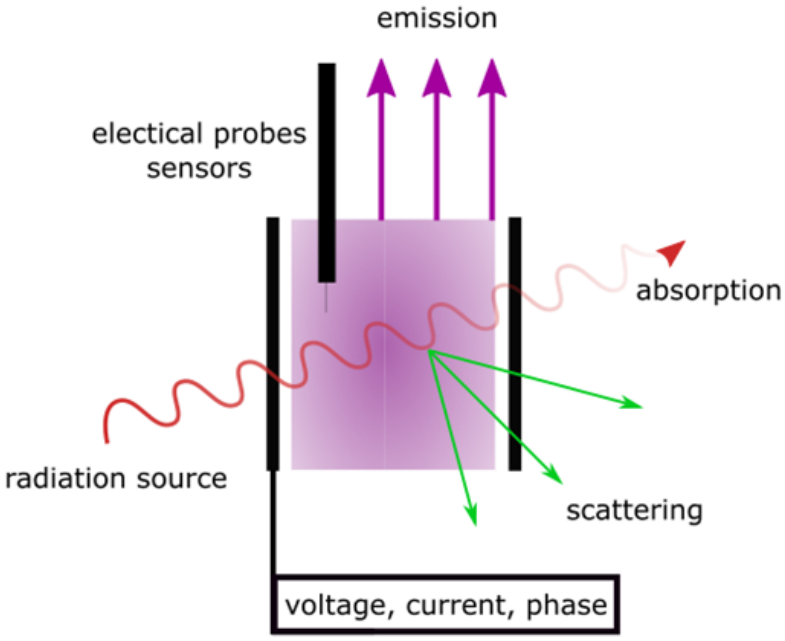

Fig. 1.5 Schematic showing the major diagnostic routes applicable to atmospheric pressure plasma research. Adapted from [29].

Many diagnostic methods of varying complexity are available for plasma research. These methods can be broadly divided into three main categories: optical methods, electrical measurements, and electrostatic probes. It is not uncommon to use multiple techniques to extract complementary information related to the plasma discharge. The following section will provide an overview of existing diagnostic methods found in literature.

Optical Diagnostics

Due to the large number of highly excited species present in plasmas, electrical discharges are characterised by light emission, perhaps best exemplified by the common fluorescent light bulbs. Emission spectroscopy (OES) is one non-invasive optical diagnostic technique that utilises the light given off by the plasma bulk without perturbing the plasma under consideration, it is used to: identify species present [30], estimate the energy distribution of the light emitting excited species [31], and extract plasma parameters [32].

Unfortunately, optical emission from plasmas only contain information related to the excited states in the plasma body as they rely on the light given off during relaxation of these excited species. In order to probe species at ground state, scattering methods such as laser induced fluorescence [33], Thomson [34] and Raman [35] scattering are also commonly used.

Electrostatic Probes

Electrostatic probes, also commonly called Langmuir probes (LPs) after their inventor Irving Langmur [36], are conductive probes inserted into the plasma to obtain plasma parameters such as electron energy distributions and charged particle densities. This process requires applying a bias to the conductive, plasma exposed probe while simultaneously measuring probe potential and currents.

While LPs are routinely used in vacuum plasmas [37], their application in atmospheric pressure plasmas is more limited. Unlike optical techniques, electrostatic probes are inherently invasive. At atmospheric pressure, mean free path of electrons and ions are smaller than any practicable probe size, causing a large gradient of plasma density near an inserted probe. Therefore, the existing LP theories defined for vacuum plasmas are not universally applicable at elevated pressures.

Despite inherent shortcomings, Langmuir probes are easy to construct and operate. With increasing interest in atmospheric pressure plasmas, there have been reports of successful LP measurements in atmospheric pressure plasmas [38, 39]. Xu and Doyle [40] have recently compiled existing LP models that may be adapted for atmospheric pressure use.

Electrical Measurements

A fundamental and indirect method of characterising a gas discharge is by considering it as a part of an electrical circuit and extracting salient parameters such as power dissipation, breakdown voltage and current/voltage characteristics. These parameters are widely studied with an aim to generate electrical circuit model descriptions which can be correlated to physical plasma parameters such as plasma density and electron temperature. To this end, various models have been proposed, ranging from simple [41] to complex [42]. Furthermore, electrical measurements provide straightforward way to extract fundamental quantities related to the plasma source such as power dissipation [43] and discharge mode [44].

1.3.2 Numerical Modelling of Atmospheric Pressure Plasmas

Despite significant advances in non-invasive plasma diagnostics, extracting plasma parameters from experimental sources still requires significant effort and analysis. Prediction of reactive species generation and specific reaction rates that are relevant to plasma application areas are on the whole not feasible through analytical models.

One common method used in fundamental plasma research to address these issues is numerical modelling. Computational methods can allow prediction of species concentrations and reaction rates in plasmas as well as extraction of local plasma parameters with fine

spatio-temporal resolution. Numerical models are used routinely in a large range of fields ranging from astrophysics [45] to semiconductor technology [46].

Fundamentals of plasma simulation lie in kinetic models of plasmas. For a given electric field, gas composition and associated reaction cross-section data, solution of the Boltzmann equation provides a distribution function for all particles in the position and velocity domain. Appendix A discusses this process in more detail. This approach is routinely employed for zero dimensional ($0D$) studies to calculate source and transport coefficients, and generation of pre-calculated parameters for further modelling. In the field of atmospheric pressure plasmas, work by Gaens and Bogaerts [47] is a good example of kinetics modelling where a 0D model was used to describe an argon plasma jet in air. Their considerably detailed model involved 84 different species and a total of 1880 reactions between plasma species, allowing identification and quantification of relevant long-living species in the plasma jet effluent such as O_3 and N_2O.

Monte Carlo or particle-in-cell methods are some of the common approaches plasma modelling where individual particles or statistically equivalent ensembles of particles are tracked in a given volume as a function of time. Much like kinetic models, the computational costs associated are significant, especially at atmospheric pressures where number density of relevant species is high. Some examples of particle based modelling at atmospheric pressure include work by Sang et al. [48]. In their work, computational resource requirements were minimized by employing a one dimensional model of a dielectric barrier discharge, the resulting model was able to simulate the evolution of atmospheric pressure discharges in the nanosecond regime. Zhang et al. [49], using a super-particle approach where multiple plasma particles can be simulated as a single entity, have employed particle modelling in a two-dimensional domain. They have demonstrated the ability of a Monte-Carlo approach in capturing complex plasma behaviour such as streamer formation in a geometrically elaborate, packed DBD reactor at a nanosecond timescale.

The approach used in this work is based on the fluid model of plasma where plasma particle and energy densities are considered to exist in a continuum, as opposed to distinct particle entities. In fluid descriptions of plasma, flux of energy and mass in a system is calculated based on aggregate parameters such as mobilities and diffusion coefficients of plasma species without resorting to solutions of the Boltzmann equation. This approach removes the need for a physical treatment of forces on particles, greatly decreasing the associated computational cost compared to particle-in-cell methods. Fluid models pose a trade-off between computational cost and accurate physical representation. Due to the continuum approximation, both large gradients in time and space, and sparse plasmas are

not well represented. Furthermore, the form of electron energy distribution functions in fluid models are often pre-determined as an input parameter. This avoids the computational cost of tackling the Boltzmann equation but results in a notable divergence from a physically consistent energy distribution function, potentially leading to errors in reaction rate estimates.

Despite their shortcomings, fluid models have been used widely for investigating plasma discharges at atmospheric pressure. For example, Wang et al. [50] have used fluid modelling for helium plasma jets in contact with dielectric surfaces, investigating the propagation of the discharge from the electrode to the surface in the form of dense plasma packets, also known as *plasma bullets*. Hemke et al. [51] have used a similar approach to probe the species concentrations in a helium plasma jet effluent, showing that long lived reactive oxygen species are present in the plasma plume, away from the discharge zone even in the absence of electrons an ions. Norberg et al. [52] have probed the effect of dielectric barriers with different dielectric constants on the plasma discharge characteristics, predicting an increase in plasma electron density above surfaces with higher dielectric constants.

Fluid modelling of plasmas is an incredibly valuable a companion to experimental approaches as the latter allows for verification of the computational models while the former provides *insight* into fundamental plasma discharge processes. Zhu et al. [53] have used fluid models to understand the development of electron and metastable species densities in a DBD. Model results were compared to results obtained via high speed imaging of the discharge, showing remarkable agreement between experimental and computational approaches. Jansky et al. [54] have used a similar approach in their investigation of discharge propagation velocities in confined pulsed plasmas, validating the model results via comparison to experimentally determined velocities.

In this work, a highly simplified (4 species, 9 reactions) fluid discharge model is used to qualitatively describe plasma behaviour in a dielectric discharge. The results are then extended to a case where an external electric field is applied within the plasma afterglow to gain insight into the potential response of charged species and their flux to the electrode surface. In Chapters 4 and 5, the results of computational models are used to help explain the observed effects of plasma exposure on metal oxide thin films.

1.4 Atmospheric Pressure Plasma Jets

Atmospheric pressure plasma jets (APPJs) are well-known plasma sources used for surface treatment and medicine [55] where ionised gas is generated in a manifold and the discharge is ejected into open air or towards the surface to be exposed. This plasma plume effluent

is abundant in highly excited and charged species while simultaneously having kinetic gas temperatures close to ambient. The working gas for an APPJ is typically a noble gas that can be mixed with other molecular gases to control plasma chemistry. APPJs offer distinct advantages over vacuum plasmas and other atmospheric pressure plasma sources by allowing the plasma to be carried to the surface of interest. This makes it possible to selectively treat surfaces that might be too large for conventional plasma chambers or incompatible with vacuum, such as human skin. A micro-plasma jet impinging on skin is depicted in Figure 1.6a. This ability to generate a conductive and highly reactive medium at low temperatures has made APPJs an excellent tool for surface modification and deposition applications.

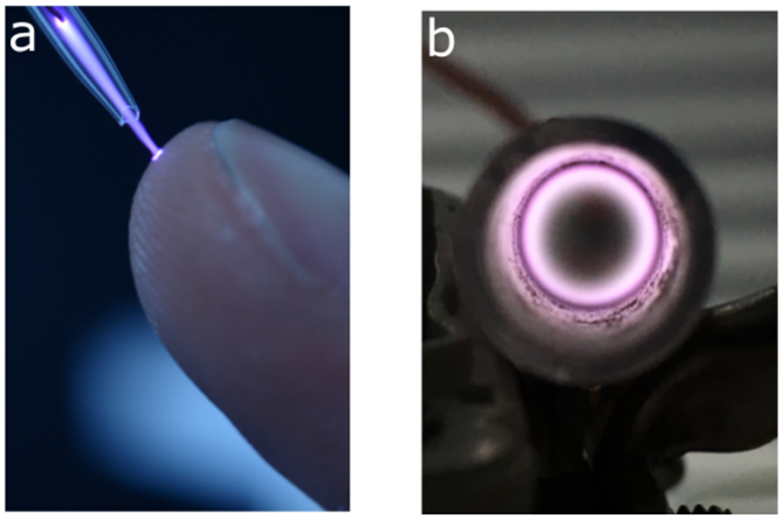

Fig. 1.6 A cold micro-plasma jet in contact with a fingertip (a), annular helium plasma generated in a coaxial plasma jet (b).

First reports of APPJs were published in the early 1960s using arc or radio frequency discharges that were generated with noble gases and blown outwards at high velocity [56–58] These type of plasma jets, while *non-LTE*, were nevertheless produced at high temperatures. Later on, spurred by the proliferation of solid-state power electronics and microwave magnetrons, cold plasma jets that could operate under near-ambient conditions were investigated using microwave [59, 60] and radio frequency excitation. Following further developments in the 1990s and 2000s [55, 61, 62], plasma jets were in one sense re-discovered, and applied to research in a wide range of fields, most notably in medicine. A rapid increase in the volume of publications utilising plasma jets followed, chiefly driven by biomedical applications. The still growing appetite for applied and fundamental plasma jet research is highlighted in Figure 1.7. Multiple, comprehensive reviews on atmospheric pressure plasma jets and

their applications have been published in the last decades [55, 63–65], mirroring the overall interest in these versatile technical plasma sources .

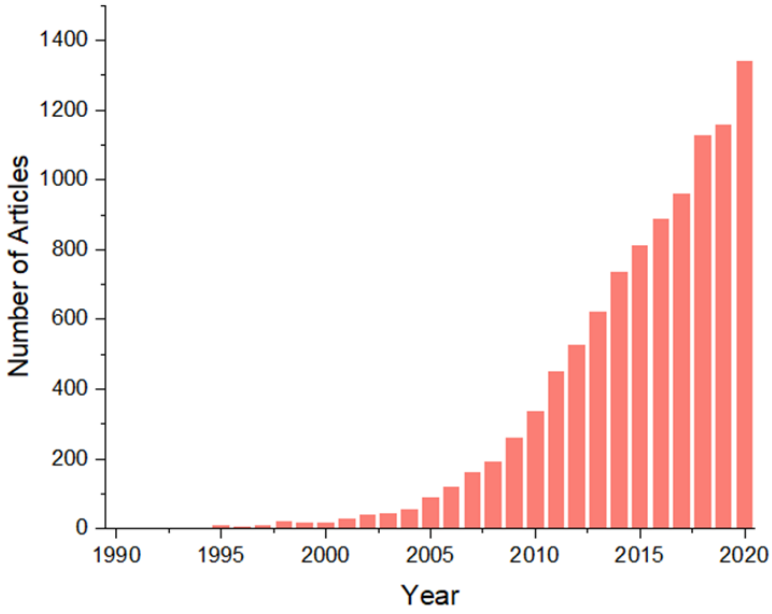

Fig. 1.7 Number of articles appearing on Google Scholar that contain the phrases "atmospheric pressure plasma jet" and/or "APPJ" between the years 1990-2020.

1.5 Applications of APPJs

Atmospheric pressure plasma jets show great promise in controlling surface chemistry of organic and inorganic materials. Significant amount of research focuses primarily in the optimisation of plasma jet chemistry to suit particular surface treatment applications, and describing the effects of atmospheric pressure plasmas on various surfaces. These new application areas utilise the ability of plasma jets to deliver highly reactive species to target surfaces at near ambient temperatures.

One of the most active areas of plasma jet research is in the field of biomedicine, where plasma jets have been proposed for sterilisation [66], wound healing [67], treatment of skin diseases [68] and as an anticancer therapy [69]. A number of recent reviews highlight the potential use cases for APPJs in medicine [70–72].

Another area of intense research utilising plasma jets is materials science and nanotechnology where plasma jets are used as *tools* for synthesis of materials or modification of surface properties. Tunable chemistry, low-temperature and dry nature of plasma jets show promise

in research avenues ranging from heritage and conservation to optics manufacturing. Large collaborative projects such as the PANNA initiative in Europe [73] has recently produced reports demonstrating the use of plasma jets in surface cleaning and coating applications in the field of conservation studies. Of specific relevance to this work, Schalm et al. [74] have focused on the ability of plasma jets in reducing oxidized silver and copper surfaces without loss of material, suggesting potential uses in the heritage sector for restoration.

Perhaps the best established technical uses of plasma jets are in the fields of surface modification and deposition of coatings on polymer surfaces. Specifically, plasma jets are widely used in commercial and research settings for adhesion promotion and surface activation [75, 76] where the surface properties such as surface energy and wettability of polymers can be tuned via exposure to atmospheric pressure plasma. Potential mechanisms behind observed surface energy increase is still the subject of active research with plasma generated reactive oxygen species [77] cited as the likely active agent. Deposition of materials via plasma jets has also been a promising avenue of research, with numerous recent articles demonstrating the deposition of a number of coatings that range from aerosolized carbon nanotubes on paper [78] to silica deposited on polypropylene via decomposition of hexamethyldisiloxane (HDMSO) in an air plasma jet [79].

Building on existing literature, this work focuses on two related areas where plasma jets can be applied. In the field of surface modification, Chapters 4-5 discuss the use of plasma jets for reduction of metal oxides at near-ambient conditions, the reduction process is shown to depend on overall exposure time and proceeds differently depending on the oxide surface. For all oxides, a reducing plasma is shown to lead to introduction of oxygen deficiencies. Later on, Chapter 7 extends this previous work by demonstrating direct deposition of zero-valent metals from metal salt solutions using an RF driven plasma jet.

1.5.1 Atmospheric Pressure Plasma as a Reducing Agent

The previous section detailed the use of plasma jets in a variety of surface treatment applications. Majority of the research in this area has relied on the generation of strongly oxidizing reactive oxygen and nitrogen species (RONS) such as atomic oxygen [80] and ozone [81] as discussed previously. Identification of RONS generation and transport mechanisms in atmospheric pressure plasmas is still subject of active research, drawing on fundamental plasma research avenues such as optical diagnostics [82, 83] and numerical modelling [84, 47].

Beyond the generation of oxidizing species, atmospheric pressure plasmas can also be used as reducing agents. The following chapters in this work specifically deal with the use of

inert or chemically reducing plasmas in surface modification and deposition. The main routes to achieving reducing activity in plasmas is the addition of a reducing gas such as hydrogen into the plasma gas. A poorly understood second mechanism for plasma induced reduction also involves the use of free electrons present in plasmas for driving electrochemical change, as will be discussed in Chapter 3.

Major work regarding plasma reduction has been undertaken by Mohan Sankaran and co-workers, focusing on the liquid/plasma interface. In the last decade they have explored "soft electrochemical reduction" of metal ion solutions exposed to atmospheric pressure plasmas [85, 86]. They have shown that even in the absence of added gases, inert gas non-thermal plasmas can achieve electrochemical reduction. For these studies, free plasma electrons were suggested as a potential reducing agent. By using plasma jets impinging on aqueous metal ion containing solutions, Richmonds and Sankaran [87] have demonstrated a novel synthetic route to metal nanoparticles (NPs), directly reduced at the plasma-liquid interface. Again implicating plasma electrons as the electrochemically active reagent in reduction reactions. Following this work, the use of plasmas columns as gaseous electrodes in electrochemical cells has also been explored [88] where the polarity of plasma with respect to the solution could be used to modulate oxidation or reduction reactions in the liquid phase. More recently, [89] Hawtof and co-workers were able to demonstrate the formation of ammonia in water, applying solvated plasma electrons to synthesis.

In the field of plasma reduction in the solid phase, vacuum plasma studies have historically demonstrated an impressive array of chemical control, for example, by [90] et al. and [91] et al. who demonstrated the complete reduction of Sn^{4+} to Sn^{0} in a hydrogen- or water-doped argon plasma. Yan et al. [92] and Wang et al. [93] have described the reduction of titania (TiO_2) to produce so called black TiO_2 in a plasma chamber for photocatalytic applications. Plasma reduction of copper oxide layers to metallic copper in a low pressure H_2/He plasma has been also described by [94] et al. Sabat et al. [95] have more recently published an overview on the reduction of metal oxides via plasma routes implicating plasma produced hydrogen radicals in the reduction process.

1.5.2 Plasma Jet Deposition of Metals

Due to their ability to carry out gas phase reactions at near ambient temperatures, APPJs have been promising candidates for spatially selective, mask-less deposition of a range of materials. Therefore, plasma jets are at the centre of a growing body of research focused on implementing atmospheric pressure plasma techniques in additive manufacturing. A recent

review by Sui and co-workers highlights the state of the art [96].

Existing examples of materials deposited with plasma jets cover a wide range of metal oxides such as ZnO [97, 98], SiO_x [99], TiO_2 [100, 101], AlO_x [102] and a wide number of polymeric surface coatings [103–105] such as conformal surface coatings for the electronics industry [106].

Majority of these deposition processes use plasmas as a strongly oxidizing environment where precursors are decomposed through ion and electron impact processes and/or oxidized by addition of O_2 into the plasma gas, forming reactive oxygen species. While this approach is well established for metal oxide film synthesis, the body of literature on depositing zero-valent metallic species is comparatively sparse. Despite this, metal deposition remains an especially promising application of plasma jets due to its potential applications in electronics, sensors and antimicrobial coatings. With increasing volume of additively manufactured printed electronics in industrial settings, the need for single-step deposition of certain highly conductive metals such as copper is increasing. Applications of plasma metal deposition in additive manufacturing are further discussed in Chapter 6.

Existing approaches capable of metal deposition either rely on high temperature processes such as atmospheric pressure sputtering, or plasma assisted densification of pre-prepared nanoparticulate inks. Both these solutions have so far failed short of achieving the main goal of highly adherent, conductive prints at low substrate temperatures that can enable atmospheric pressure plasma based additive manufacturing methods. Table1.1 provides a non-exhaustive list of recent research articles focused on deposition of metals using atmospheric pressure plasma methods.

Table 1.1 Previous literature on plasma metal deposition.

Year	Ref.	Precursor	Deposit Type	Deposition Method	Plasma Type	Gas
2013	[107]	Ag Solution	Ag/SiO_2	Aerosol Assisted	Pulsed	Air
2013	[108]	Cu Target	Cu	Evaporation	13.56 MHz	H_2/Ar
2014	[109]	Ag Nanowires	Ag Nanowires	Aerosol Assisted	Pulsed	Ar/He
2015	[110]	Cu Target	Cu NPs	Evaporation	13.56 MHz	Ar
2016	[111]	Cu Target	CuO	Evaporation	DC	Air
2019	[112]	Cu NPs	Cu/CuO	Aerosol Assisted	Pulsed	Ar/He
2019	[113]	Au Solution	Au NPs	Aerosol Assisted	10 kHz	He
2020	[114]	Au Target	Au	Evaporation	DC	Ar

The largest body of work concerning plasma jet deposition of metal containing conductive films is based on atmospheric pressure sputtering of a metallic target. This approach, first described by Nakahiro et al. [115] for copper, employs a wire placed in a high temperature plasma to sputter Cu and carry it beyond the jet orifice. Whether the process relies on

sputtering or thermal evaporation is unclear. Authors demonstrate that deposition rates of up to $40 nm/min$ can be reached with such an approach. More recently in two publications, Zhao et al. [108, 116] have demonstrated a similar plasma source capable of depositing copper films under H_2/Ar and N_2 gas feed using a solid metal source. They have characterized the optical emission spectra obtained from the plasma, proving the existence of ionized Cu species in the plasma column.

Alongside the slow rate of deposition via sputtering, a major drawback of direct deposition from solid Cu targets is the very high temperatures ($> 800\ K$) and input power ($> 300\ W$) required for deposition at atmospheric pressure. Reports on the resulting coatings suggest resistivities higher than that of bulk copper by two orders of magnitude, implicating oxidation or porosity as the cause of high resistivity [115].

Evaporation or sputtering of metals are inherently high-energy processes that are difficult to reconcile with the need for deposition onto heat sensitive substrates. A promising, low temperature, alternative to evaporation and condensation of solid metal is the use of aerosolised precursors. Generating micron to nano scale particles via aerosolisation provides a large precursor surface area to mass ratio, increasing the rate of plasma induced chemistry on the surfaces of particles. This method has been pioneered by Connor et al. [117], demonstrating the deposition of gold nanoparticles onto a silicon substrate from colloidal gold solutions. Following the development of this method, Gandhiraman et al. have improved upon the technique, depositing silver [109] and copper [112] nanoparticles using plasma jets with H_2 admixture, from nanoparticulate suspension precursors. These methods have shown improved adhesion due to plasma activation of target surfaces and the effect of reducing plasmas in preventing oxidation of the pre-synthesized suspensions.

1.6 Aims and Contributions of This Work

This project aims to study atmospheric pressure plasma / surface interactions with a goal to establish new application areas for atmospheric pressure plasmas in surface modification of metal oxides. This thesis is comprised of seven further chapters, detailing the experimental methods, results and conclusions of research work done on atmospheric pressure plasmas.

In Chapter 2, an overview of the plasma sources designed and used for following experiments is provided. In addition, the tools and techniques used for both plasmas and surface characterisation are presented. In Chapter 3, a helium DBD plasma source is described alongside the effects of flow rate and gas admixture on the electrical properties of the plasma. A computational model of the plasma source and the plasma afterglow is then presented and

compared to the results obtained via Langmuir probes.

Chapter 4 contains the results of experiments on the effect of plasma exposure on cuprous oxide. He DBD afterglow, characterised in Chapter 3, is found to act as a reducing environment, converting cuprous oxide into metallic copper. It is shown for the first time that the oxidation state of copper placed in the atmospheric pressure discharge can be modulated by the application of an external bias, independent of plasma gas composition, implicating plasma electrons in causing reduction of oxide to metallic copper.

Chapter 5 is concerned with further application of reducing plasmas, generated via admixture of H_2, in generating defective metal oxide films containing sub-oxides and, in some cases the parent metal. Results of atmospheric pressure plasma reduction on metal oxides are described for Cu_2O, SnO_2, TiO_2, ZnO and WO_3. In all cases, effect of plasma exposure to the surface composition is reported using spectroscopic techniques, demonstrating rapid, low-temperature reduction.

A specific potential application of plasma jet reduction is studied in detail in Chapter 6. A recently discovered, defective photocatalyst material known as *black titania* is produced for the first time via an atmospheric pressure plasma route. The chapter details this synthetic route that removes existing barriers to black titania production such as high pressure H_2 or vacuum requirements. Atmospheric pressure plasma treated catalysts are shown to have significantly improved photocurrent efficiencies, comparable to literature reports. The resulting composition of the titana films are reported, showing a significant amount of oxygen deficiency generated through H_2 doped plasma.

Chapter 7 builds on previous observations by demonstrating a novel material deposition technique that utilises a plasma jet for printing conductive metal traces under near-ambient conditions from aqueous copper salt solutions. This route is a distinct improvement over existing plasma methods as it establishes a single step deposition technique that does not require pre-prepared inks or post-processing. The mode of mass transport via aerosol impaction is studied via fluid dynamics models and experimentation. Furthermore, the time dependent evolution of the deposited metal films are discussed, considering both the morphology and the composition of the plasma jet printed traces.

Finally, Chapter 8 provides a conclusion to the thesis, discussing the overarching themes and results in the previous chapters. Remaining open questions are discussed, with suggestions for continuing research and an overview of further work planned for the future.

Chapter 2

Methods and Experimental Set-Up

2.1 Experimental Set-up

The aim of this work was to investigate the potential of atmospheric pressure plasma jets for driving redox reactions for modification and deposition of thin films. To this end, two atmospheric pressure plasma jets were designed, built, and characterised. Experimental characterisation of the plasma jets was done via optical emission spectroscopy, Langmuir probes, Schileren photography, electrical and thermal measurements. In addition to experimental techniques, computational fluid models for both plasma and gas flow were employed.

In characterisation of plasma treated surfaces and deposits, X-ray photoelectron, UV-Vis absorption and Raman spectroscopy was used. The following sections will detail the major experimental equipment and set-up used for the work described in following chapters.

2.2 Plasma Jet Construction

Two different plasma jet configurations were built and used in this work. A dielectric barrier discharge (DBD) tube was used to generate atmospheric pressure glow plasma in experiments as detailed in Chapter 3 and 4. For the remaining experimental work, a *plasma needle* type plasma micro-jet was used to expose well defined surfaces to the plasma jet. The plasma micro-jet was modified further for the deposition experiments, the details of which are provided in Chapter 6.

2.2.1 Dielectric Barrier Discharge Jet

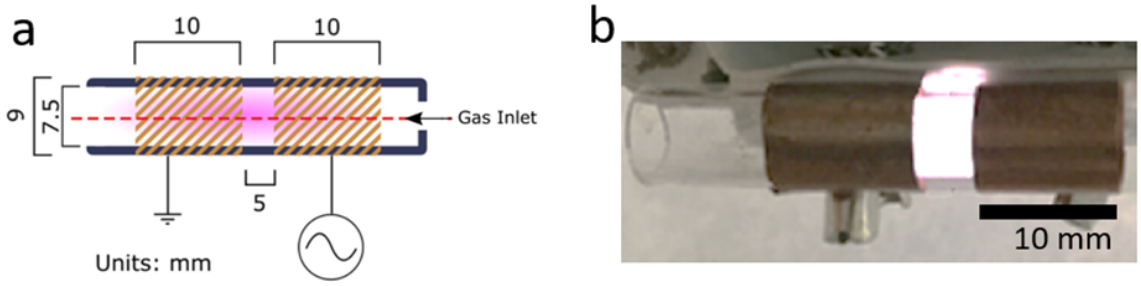

Fig. 2.1 Diagram of the plasma jet construction, highlighting the electrodes sustaining the DBD discharge and the discharge zone (a). Photograph of the plasma jet, bright plasma discharge visible in the centre of the quartz tube (b).

A dielectric discharge tube for generating glow discharge, shown in Figure 2.1 was built using a quartz tube of 7.5 *mm* ID and 9.0 *mm* OD. Two tubular electrodes made from 0.15 *mm* thick bent copper sheet were tightly wrapped around the outside of the quartz tube and fixed in place, leaving a 5 *mm* inter electrode distance. Electrode facing the open end of the tube was grounded and the remaining electrode was connected to a 13.56 MHz RF power supply (Coaxial Power, UK) via a modified manual matching network (Coaxial Power, UK). The matching network comprised of two variable air gap capacitors and one fixed inductor. Helium (CP Grade, BOC Gases, UK) and dopant gases O_2, H_2 and CH_4 (BOC Gases, UK) were fed through mass flow controllers (Brooks Instruments, UK) through the quartz tube as the plasma working gas.

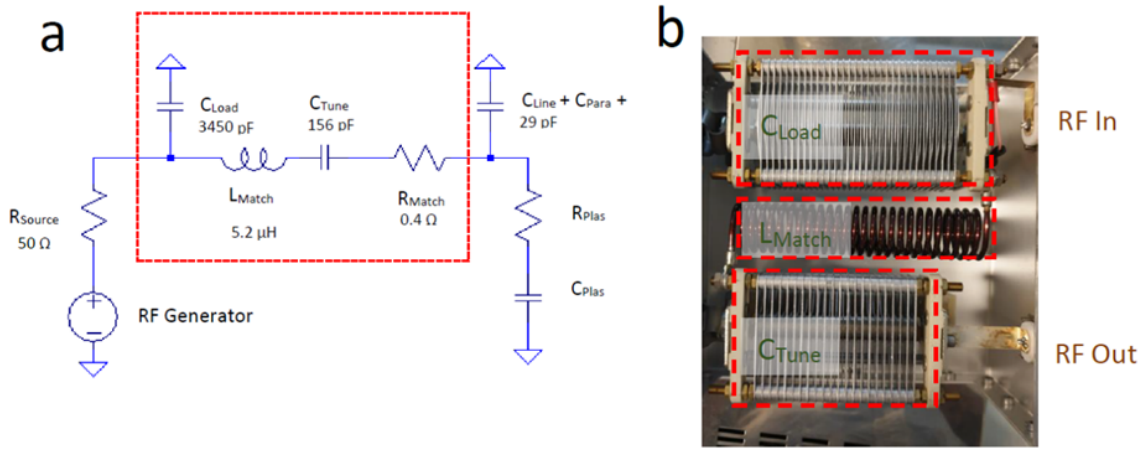

Fig. 2.2 Circuit schematic description of the dielectric barrier plasma set-up, showing the match network (red outline) and approximate measured lumped element values in the match network during operation (a). Photograph of the match network, highlighting the two variable capacitors and the fixed inductor used for impedance matching (b).

A mismatch of electrical impedance between the load and the generator output leads to significant amounts of power being reflected back to the generator, making it impossible to achieve steady discharge. To avoid damaging the generator, the plasma assembly was connected through an impedance matching circuit to the generator RF output. Prior to experiments, and before introduction of plasma gas, the assembly was tuned for minimum reflected power. Values of the matching circuit in the tuned position are given in Figure 2.2. Purely capacitive impedance of the plasma jet assembly comprising of the electrodes, connectors (C_{Line}) and parasitic capacitances (C_{Para}) were matched to the 50 Ω output impedance of the generator. Matching was done by alternatively sweeping the load (C_{load}) and tune capacitors (C_{tune}) in turn while simultaneously monitoring the forward and reflected power. Variable capacitors were deemed to be in tune at a position where the reflected power was minimum. In order to achieve plasma ignition, the working gas was flown through the quartz tube. At 50 W forward power (measured at the generator) plasma was found to self-ignite and stabilise into an annular diffuse glow as discussed in the next chapter.

During operation and tuning, voltage and current waveforms at the powered electrode were recorded with a wideband high voltage probe P6015 (Tektronix, US) and current probe TCP0020 (Tektronix, US). Digital storage oscilloscope DPO7054 (Tektronix, US) was used to sample and record the measured waveforms. Probes were always left electrically connected to the plasma set-up during operation in order to minimise the variability between experiments due to de-tuning observed when parallel probe loading $(\approx\ 1.7\ pF)$ was removed.

2.2.2 Micro-plasma jet

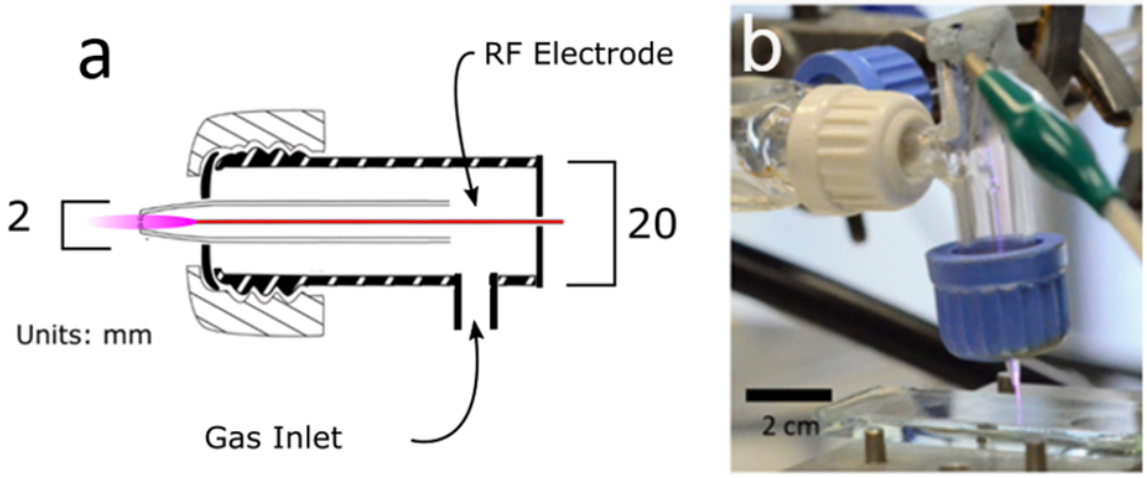

Fig. 2.3 Schematic of the plasma jet head, showing the placement of the powered electrode inside the capillary tube and the dimensions of the assembly (a). Photograph of the plasma jet impinging on the surface of a glass substrate, the jet formed is visible at the tip of the capillary exit (b).

The apparatus used for deposition and surface treatment described in Chapters 5 and 6 was designed and built using commercially available parts and custom elements. The experimental set-up consisted of a plasma jet head shown in Figure 2.3, power electronics and gas flow control.

The plasma jet head is the section of the deposition apparatus where the plasma is ignited and ejected to the surface below through a pulled capillary nozzle. The jet head consisted of a glass tube of 20 *mm* OD with a 0.5 *mm* diameter tungsten wire inserted (Goodfellow, UK) centrally down the axis of the tube. The nozzle orifice was made of a pulled (PE-22, Narishige, Japan), ground, and flame polished borosilicate glass capillary with a 1.9 *mm* outside diameter. The capillary nozzle was inserted through a rubber septum into the glass tube. A tungsten wire, 0.25 *mm* diameter electrode was then inserted coaxially through this assembly, resting 0.1 *mm* behind the jet orifice.

For treatment or deposition over large areas, a computer controlled two axis motion stage (Physik Insturmente, Germany) was positioned below the plasma jet. The motion platform was grounded via a grounding strap to the RF generator. During the experiments, the substrates to be treated or deposited on were placed between the grounded platform and the plasma jet tip as shown schematically in Figure 2.4a.

RF power delivery to the plasma jet was done in an identical way to the DBD Jet

discussed above, in addition, the micro-plasma jet was operated in a pulsed mode by pulsing the RF generator output via a pulse width modulated (PWM) signal generated by an arbitrary function generator (Tabor Electronics, Israel). The resulting discharge consisted of repeated pulses lasting roughly 20 μs each, as shown in Figure2.4b. The frequency of the modulating wave (f_{pulse}) and the duty cycle of the PWM signal (α) were kept at 20 kHz and 20% for all experiments.

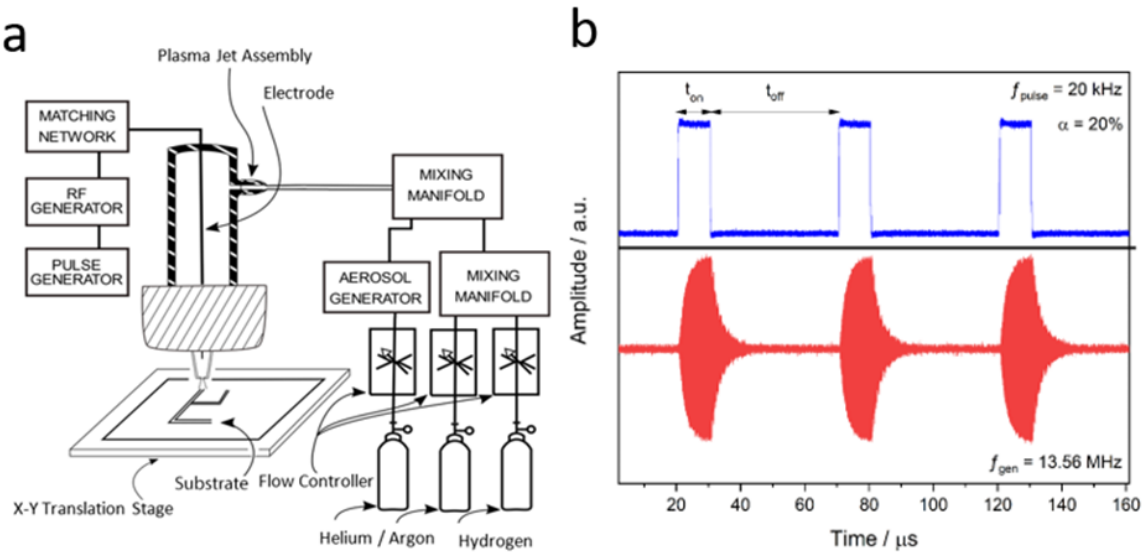

Fig. 2.4 Schematic description of the plasma jet apparatus (a). The PWM waveform (top) and the resulting RF pulses (bottom) during the operation of the pulsed RF plasma jet (b).

2.3 Plasma Diagnostics

Two main methods were employed for characterising the plasma sources described above. For all experiments, optical emission spectroscopy was used to identify the species present in the plasma plume and determine the relevant temperatures in the plasma. A self-built double Langmuir probe was used in Chapter 3 to aid the measurement of electron temperature and number density in the plasma afterglow for verification of numerical simulation results. Additionally, the temperature of the discharges were measured via a K-Type thermocouple where practicable.

2.3.1 Optical Emission Spectroscopy

Optical emission spectra were collected from the plasma sources with a fibre fed Czerny-Turner spectrometer (HR4000, Ocean Optics, US), capable of operation in $200 - 1100\ nm$ range equipped with a $5\ \mu m$ slit, affording approximately $0.7\ nm$ wavelength resolution. A reference light source (LS-1, Ocean Optics, USA) with known emission profile was used for calibration of the spectral sensitivity of the CCD array. No absolute intensity calibration was performed for the reported measurements. Light collection was via optical fibre (Thorlabs, US) with $300\ \mu m$ core diameter and a numerical aperture of 0.22, the arrangement of the fibre and the plasma sources are given in Figure 2.5.

For all experiments, the fibre was placed perpendicularly to the axis of the discharge body. Distance of the fiber to the plasma source was limited due arcing in air at close proximity, and geometry constraints. Fibre aperture was placed as close as practicable to the sources, experimental arrangements for both plasma sources are given in Figure 2.5. Due to the inefficient light coupling and the small slit size, the spectra were collected by integrating over $1.2\ s$ and averaging 100 collections.

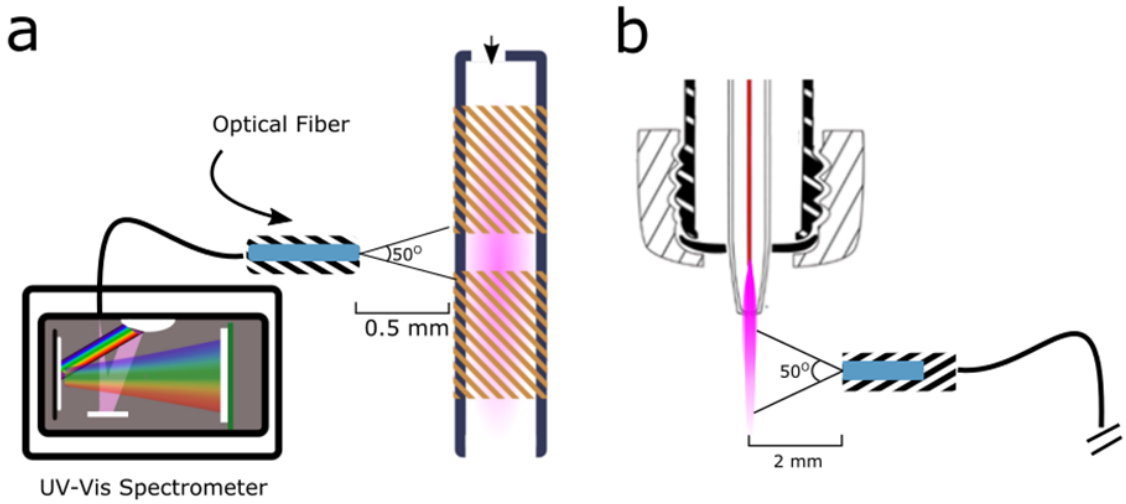

Fig. 2.5 Diagrammatic view of light collection from the dielectric barrier (a) and the micro-jet (b).

2.3.2 Double Langmuir Probe (DLP)

An electrically symmetrical double Langmuir probe (DLP) was used for experiments in Chapter 3 to determine electron density (n_e) and temperature (T_e) in the plasma afterglow.

A DLP consists of two electrically connected Langmuir probes placed in close proximity to each other within the plasma. This arrangement does not draw net DC current from the plasma itself and therefore removes the need for a well-behaved ground electrode.

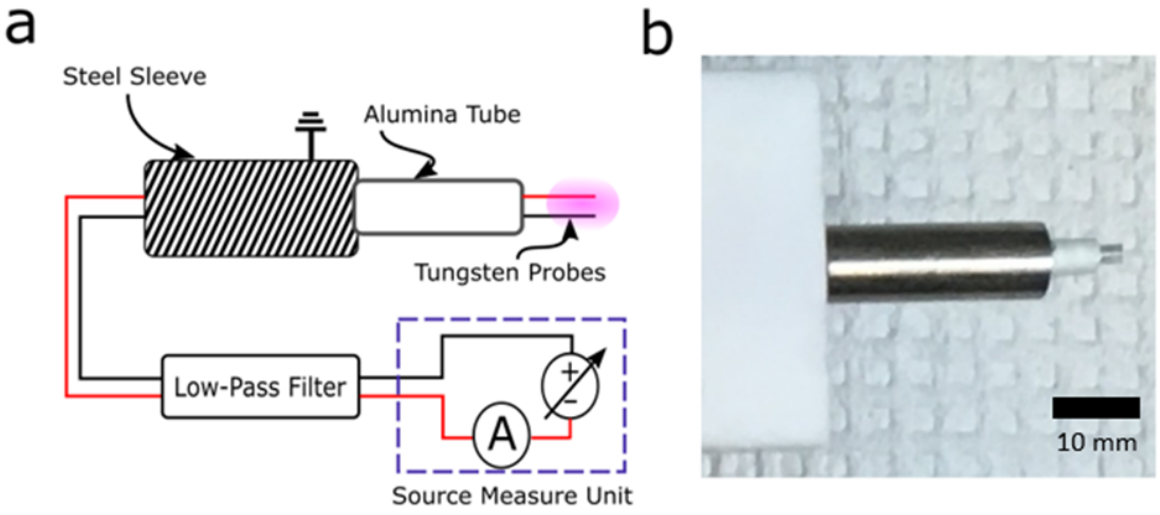

Fig. 2.6 Schematic of the DLP, the tungsten rod probes are inserted into the plasma while a source-measure unit provides simultaneous probe bias and current measurement (a). Photograph of the constructed probe, the two tungsten probes are visible on the right (b).

Figure 2.6 shows the DLP that was designed and built for plasma afterglow characterisation experiments. The assembly consisted of two tungsten rods of 0.5 *mm* diameter and 2 *mm* plasma exposed length, affixed in a double bore alumina tube with ceramic adhesive which was then inserted in a stainless-steel tube, 4 *cm* in length. Two low pass filters (Thorlabs, US) were used to eliminate RF currents in the current meter. The probes were connected to a source-measure unit (2450, Keithley, US) through a shielded twin-axial cable (Belden, US). The SMU provided potential bias to the tungsten probes while simultaneously measuring the probe current. The probe was used with the DBD plasma jet by placing it along the axis of the tube aided by a 2-axis micro positioner (Physik Instrumente, Germany) to probe at different points within the plasma discharge afterglow.

Bias range between the electrodes was set at $\pm$ 32V and the traces were swept back and forth 6 times in total to get an error estimate in current measurements. Spatial range of measurements were limited to the plasma afterglow due to arcing that occurred when the probe tips reached beyond the edge of the plasma ground electrode.

DLP Theory

To extract electron density and temperature measurements from probe voltage current characteristics, an analytical description of double probes in highly collisional plasma is required. Estimation of electron temperature and plasma density from DLP characteristics requires identification of the plasma operating regime and associated parameters. Based on the work by Xu and Doyle [40], DBD plasma was determined to be stationary, indicating that the bulk flow of gas does not influence the charge transport around the electrodes. The plasma is also highly collisional due operation at atmospheric pressure.

Based on these two factors, collisional DLP theory developed by Saito et al. [118] was used as the basis for DLP analysis. The main assumptions behind the theory are:

- Electron density and ion density are equal $(n_e = n_i)$. No doubly ionized species, negatively charged ions or significant space charge is present in the plasma afterglow.
- Electrons sampled from the plasma obey a Maxwell-Boltzmann energy distribution.
- No secondary electrons are emitted from the probes surface.
- Ion saturation current (I_d) is not bias dependent.

Under the above conditions, the expression for electron temperature (T_e) is given by Equation 2.1:

$$T_e = \frac{e}{\kappa}\frac{I_{is}}{6.16} \Big/ \left(\frac{dI_p}{dV_p}\right)_{I_p=0} \tag{2.1}$$

where, e is the electron charge in Coulombs, κ is Boltzmann's constant, I_{is} is the measured ion saturation current and I_p and V_p are probe current and potential, respectively.

While this approach allows for an estimate of the mean electron energy, it does not provide information on the electron density. Despite the assumption that ion current is independent of V_p, experimental data shows strong potential dependence as discussed in Chapter 3. To determine the value of bias-independent I_{is}, the *knee-point* where probe current transitions into an ion current limited regime was determined and taken as I_{is}. This was done by linear extrapolation of the ion saturation and the transition regime around $V_p = 0$. Figure 2.7 demonstrates this correction method graphically.

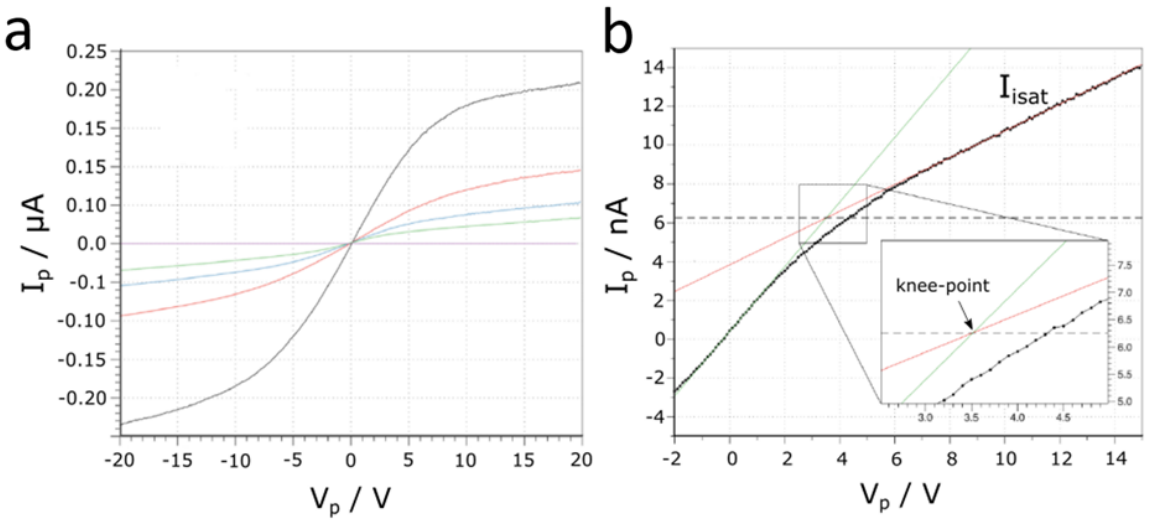

Fig. 2.7 Characteristic current / voltage traces of a double Langmuir probe in atmospheric pressure plasma, showing significant dependence of ion saturation current above 10 V of applied potential difference.

Electron density determination was done after extracting T_e values. Ion saturation current for cylindrical probes at high pressures as a function of ion density is given by Equation 2.2:

$$I_{is} = A_p e n_i \left(\frac{\pi}{8}\right)^{1/2} \left(\frac{\kappa T_e}{m_i}\right) \left(\frac{T_e}{T_i}\right)^{1/2} \frac{l_+}{R_p} \tag{2.2}$$

Where: $A_p = 0.6mm^2$ is the surface area of a single probe, $R_p = 0.25mm$ is the probe radius, $l_+ = 74nm$ is the ion mean free path, and T_i is the ion temperature.

An effective ion mean free path can not be easily determined as the precise composition of ionic species in the plasma is not known. For dominant helium ions (He^+, He^{2+}, $He_2{}^+$) in their parent gas under ambient conditions, an approximate value was used, based on the isotropic scattering cross section of He^+ in He at 330 K [119]. Ion temperature (T_i) was assumed to be equal to the kinetic gas temperature as measured with a thermocouple.

2.4 Surface Characterisation

For all the experiments, various surface characterisation methods were used to probe the chemical composition and physical features of the plasma processed surfaces. The experimental details for these methods are provided below.

2.4.1 Raman Spectroscopy

An inVia confocal Raman microscope (Renishaw, UK) with an unpolarized 532 *nm* argon ion laser excitation source was used for the characterization of substrates and deposits treated with the plasma jet. Raman spectra were obtained from an area of approximately $10\mu m$ diameter with a $50\times$ objective. The spectra were recorded in the 140 cm^{-1} to 1000 cm^{-1} Raman shift range at ambient temperature.

2.4.2 X-Ray Photoelectron (XPS) and Auger Electron Spectroscopy (AES)

A Thermo K-Alpha photoelectron spectroscopy system (Thermofischer, US) equipped with a monochromatic $Al-K\alpha$ (1486.6 eV) X-ray source was used for X-ray photoelectron and Auger electron spectra acquisition. Unless noted otherwise, spectra were collected from a spot of $50\mu m$ diameter on the sample surface, at a pass energy of 50 eV. Photoelectron energy offsets were minimized by using an electron flood gun source during XP spectra acquisition. Adventitious carbon C $1s$ peak at 284.8 eV [120] was used as an internal energy calibration as needed. Deconvolution and quantification of X-ray photoelectron peaks was done using the CasaXPS software suite [121] using Voigt line shapes and Shirley background functions, unless noted otherwise.

2.4.3 Scanning Electron Microscopy (SEM)

To obtain high resolution micrographs of sample surfaces, scanning electron microscopy was used. Micrographs were obtained with a JSM 6701F field emission SEM (JEOL, Japan) at an accelerating voltage of 10 kV. For non-conducting samples, the sample surface was sputter coated with gold to aid charge dissipation during imaging, intrinsically conductive samples such as copper were not coated prior to image acquisition and were instead grounded to the microscope body.

2.4.4 Diffuse Reflectance Spectroscopy

Optical reflectance spectra in the $200-1100$ *nm* wavelength range were collected from sample surfaces at a 45° angle with respect to surface normal. A fibre reflection probe bundle was used (RP20, Thorlabs, US) with a fibre fed spectrometer (HR4000, Ocean Optics, US) and a deuterium / halogen source for spectrum collection. A PTFE diffuse reflectance standard (Ocean Insight, US) was used to calibrate the experimental absorption spectra.

2.4.5 Stylus Profilometry

For deposition experiments described in Chapter 6, surface profiles of samples were measured with a Dektak-XT (Bruker, US) surface profiler, equipped with a 5 μm radius stylus tip. Linear background slope due to uneven substrate thickness was removed from all measurements prior to analysis and presentation.

2.5 Numerical Modelling

Spectroscopic and electrostatic probe measurements used in this work are well-established techniques that are suitable for estimating bulk plasma parameters. Unfortunately, these methods fail to provide spatio-temporally resolved insight into the processes that take place within the plasma and on the plasma-surface interface.

Computational fluid models of the DBD plasma source were used to understand plasma behaviour in the experiments. Details of the models used, and relevant background information is provided in Appendix A.

Further computational methods were used in Chapter 7, for simulating gas flow characteristics in the plasma nozzle and across the substrate surfaces. Particle tracking methods were also used for providing insight into the aerosol deposition process during plasma printing. Details of the model used are provided in Appendix B. All computational models were solved on a personal computer with 8 GB random access memory and a Ryzen 4800H processor.

Chapter 3

Characterisation and Modelling of Atmospheric Pressure DBD Jet

3.1 Introduction

Dielectric barriers can be used to mitigate plasma instabilities, preventing atmospheric pressure plasmas from constricting into filamentary discharge channels [122] and thereby generating stable *glow* discharges at atmospheric pressure [123, 122]. These glow plasmas are convenient to use in research due to their large uniform volume and predictable operation, analogous to their vacuum equivalents. In this work, a helium glow plasma source is built, characterised and numerically investigated.

Depending on factors such as discharge geometry, excitation frequency, gas flow and even proximity to electrically grounded surfaces, RF discharges can exhibit a large array of discharge characteristics. It is critical to understand these discharge parameters in order to draw meaningful conclusions regarding atmospheric pressure plasma interaction with solid surfaces. Following sections are concerned with the effect of fundamental experimental variables such as flow rate and electrical power on plasma characteristics of the self-built plasma source. This chapter thus serves as a preamble to Chapter 4, where the same source is used to modify a cuprous oxide electrode surface under ambient conditions.

First, salient features of the plasma discharge such as current-voltage characteristics, dissipated power and gas temperature are discussed, showing that the plasma source is capable at operating at near room temperature, with $\approx 1W$ of dissipated power. This is followed by optical emission and Langmuir probe diagnostics, determining experimentally relevant parameters such as electron density, excitation, and electron temperatures. These results are then compared to the results obtained from a simplified computational model of

the plasma discharge sharing the same geometry.

3.2 Experimental and Methods

The DBD discharge source, as described in section 2.2.1, was used for all experiments. Electrical measurements, optical emission spectroscopy and a double Langmuir probe were used in characterisation of the plasma discharge and plasma afterglow. A fluid model of the plasma discharge as described in Appendix A was solved to better understand the plasma discharge and compare the computational and experimental results.

3.3 Results

3.3.1 Electrical Characterisation of DBD in Pure Helium

The current voltage characteristics of the discharge during operation were measured to understand the effect of gas flow rate on the dissipated power. Furthermore, the effect of the resonant matching network assembly on the discharge itself was clarified, showing a strong interdependence between the quality (Q) factor and the plasma impedance.

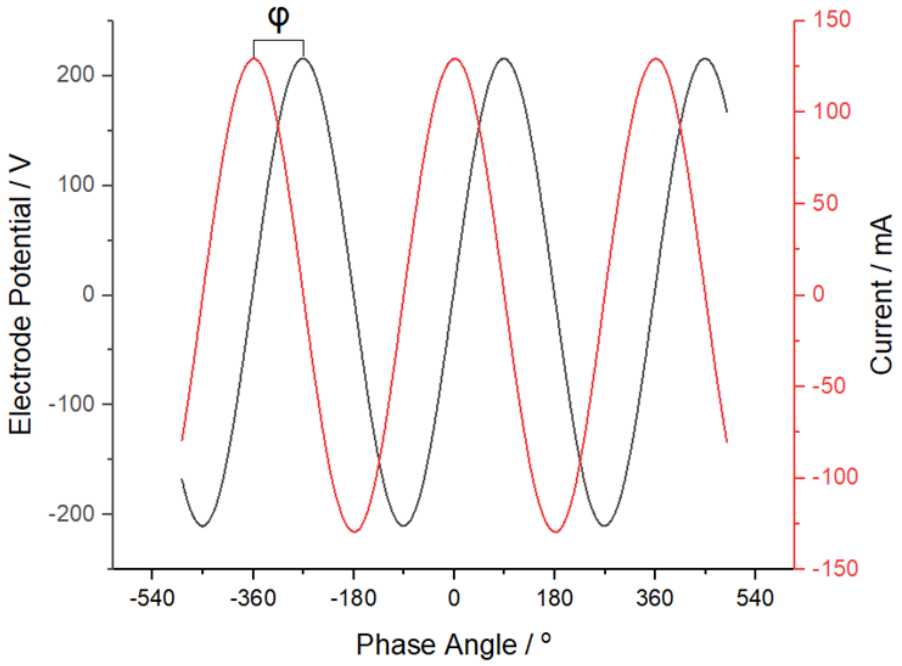

Fig. 3.1 Example of the measured DBD current and voltage waveforms, indicating the angle between the current and voltage traces. The waveform consists mainly of displacement currents, as evidenced by the phase angle magnitude (ψ) close to 90^o.

As the dielectric barrier set-up is primarily capacitive, the measured phase angle ϕ between the current and voltage waveforms before plasma ignition was close to -90^o, as would be expected of a purely capacitive circuit element (Figure 3.1). To electrically characterise the plasma discharge under different operating conditions, the peak-to-peak voltage, current as well as the phase angle between these waveforms were measured. After plasma ignition at a helium flow rate of 33 $mL\ s^{-1}$, the magnitude of ϕ decreased from purely capacitive -90^o to -87^o, this decrease in phase angle is indicative of resistive loading imposed by the plasma in parallel with the stray capacitance inherent in the system. Simultaneously, the peak-to-peak voltage (V_{p-p}) and current (I_{p-p}) was found to decrease.

The electrical parameters of the discharge are given in Figure 3.2. Prior to plasma ignition, the DBD setup is electrically described by a lumped element series capacitance (Z_s) that is due to stray capacitance through the electrodes and cabling. The resonant match circuit is adjusted under these conditions to minimise reflected power as described in Section 2.2.1 . On ignition, the plasma plume poses a secondary impedance (Z_p) in parallel with the stray capacitance in the system. At first glance, the measured decrease in current flow through the electrodes appears to conflict with the decreased impedance due to the second parallel load

imposed by the plasma. In the absence of the matching circuit, the total impedance would be expected to drop, and peak current to rise as $Z_s < Z_s Z_p / (Z_s + Z_p)$.

In the case of RF currents, as it is here, the decreased impedance causes increased loading of the resonant match network. As a result, the Q factor of the resonant circuit drops upon plasma ignition. Greater the plasma loading due to resistive losses, the lower the Q factor. This effect is also termed *frequency pulling*, and is well known in the field of vacuum plasma [124] and has been modelled electrically by Law and Anghel [125] at atmospheric pressure.

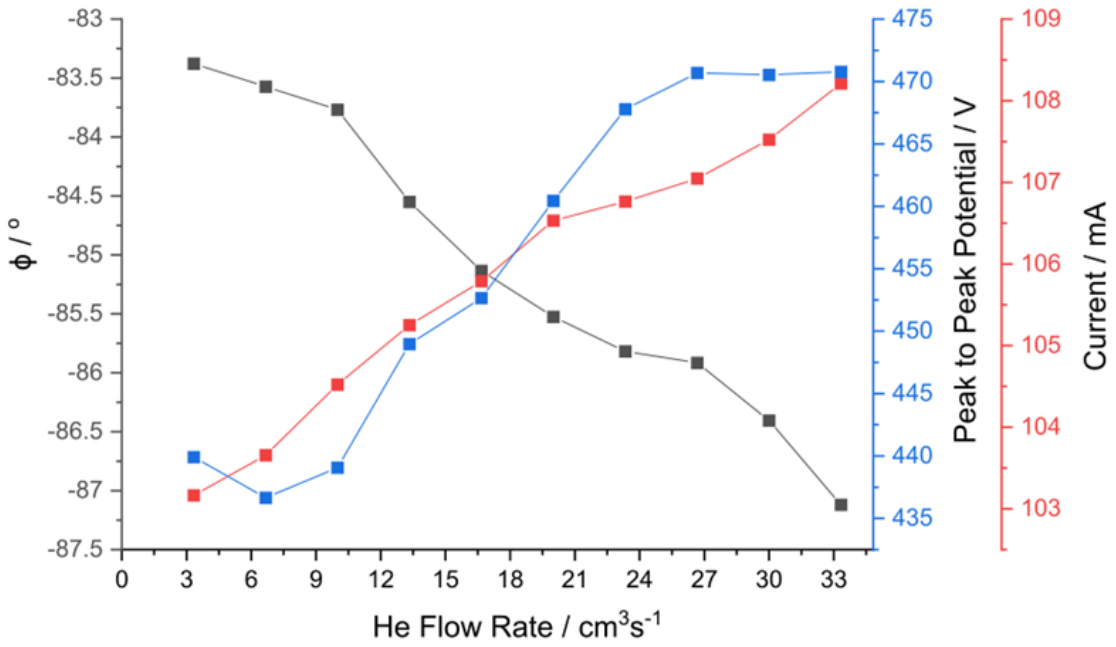

Fig. 3.2 Current-voltage phase angle (black), peak-to-peak electrode potential (blue) and peak-to-peak current (red) in the DBD set-up as it varies with helium flow rate.

Comparing the current-voltage characteristics of the DBD source under different flow rates provides further information on the electrical behaviour of the plasma source. By keeping the generator power stable at 50 W, plasma dissipated power can be modulated by changing the flow rate of helium. Under very low flow rates ($\approx 3\ mL\ s^{-1}$), the phase angle magnitude is smallest at around -83^o. For pure sinusoidal signals, real, or active dissipated power, is given by $P_a = V_{RMS} \times I_{RMS} \times cos(\phi)$ where V_{RMS} and I_{RMS} are the root-mean-square voltage and current, respectively. As the magnitude of ϕ decreases due to plasma impedance, power dissipation is also increased.

By increasing the flow rate, the phase angle magnitude increases alongside the electrode current and voltage. Despite the higher driving potential, the real power coupled to the plasma

is lower at high flow rates. This shows that the impedance of the glow plasma increases as helium flow rate is increased. Gas flow decreases the charged species density in the discharge tube by removing excited and ionised species from the inter-electrode region, increasing the total impedance of the system and bringing the phase angle closer to -90^o.

Alongside electrical power dissipation, the effluent temperature measured at the DBD exit can be used to estimate plasma dissipated power. Under adiabatic conditions, and assuming no loss due to light emission, the electrical and thermal power dissipation should be identical. An upper bound for the final effluent temperature can be estimated from electrical measurements by disregarding conductive heat losses. The relationship between temperature rise (dT) and heat input is given by $dQ = mc_p dT$ where m is the mass and c_p is the molar specific heat capacity of helium (5.19 $kJ\ kg^{-1}\ K^{-1}$ [126]). By expressing this equality in terms of $kJ/s = W$ for electrical power and kg/s for mass flow, the upper bound for temperature increase in flowing plasma gas was calculated.

In addition to an upper bound, a lower bound can also be estimated by assuming the quartz tube to be embedded in an ideal heat sink at ambient temperature, in this case the heat loss (Q) is given by $Q = 2\pi L(\Delta T)/[ln(r_o/r_i)/k]$ [127] where L is the length of the quartz discharge tube, ΔT is the temperature difference between the plasma gas and the outside (290 K), r_o and r_i are outside and inside diameters of the discharge tube and k is the thermal conductivity of quartz (1.4 $W\ m^{-1}\ K^{-1}$[128]).

Figure 3.3 shows the electrically measured power dissipation and temperature, the grey ribbon indicates the estimated effluent temperature under adiabatic conditions where plasma loses no heat to the outside (top) and the heat sunk (bottom) scenario. It is found that the measured and calculated temperatures are in good agreement, and the measured values lie strictly within the upper and lower bounds. This confirms the accuracy of electrical measurements and reaffirms that emissive losses in the plasma plume are negligible compared to total thermal losses. As the flow rate in the discharge channel is increased, the effluent temperature drops due to both increased mass flow and also decreased total power dissipation. With the DBD set-up, plasma can be generated under near-ambient temperatures in a glow-like regime, by keeping the flow rate above 10 $mL\ s^{-1}$.

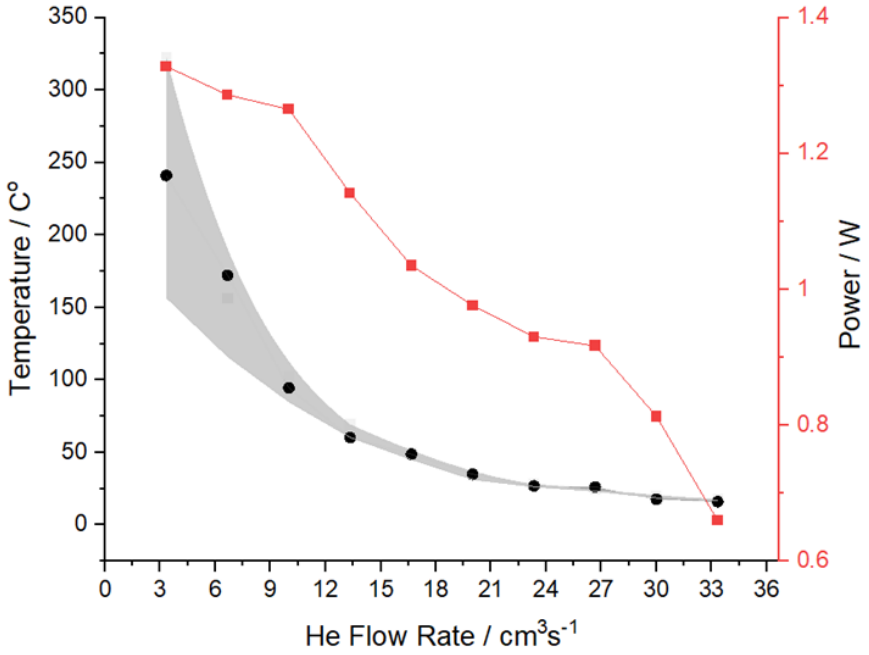

Fig. 3.3 Temperature and dissipated power as a function of gas flow rate in the DBD set-up. The grey ribbon shows the boundaries of predicted gas temperature under adiabatic (top) and lossy (bottom) conditions.

Knowing the plasma dissipated power and power generated at the RF source, it is possible to calculate the electrical plasma efficiency. The overall efficiency of the system is low, with a source power of 50 W, maximum obtainable efficiency obtained is 2.5% at near zero helium flow rate. Bulk of the losses are through the matching network and connectors, with a calculated power loss through the match network on the order of -5 dBW $\approx 70\%$, and additional loss of -1 dBW $\approx 25\%$ in the apparatus due to impedance mismatch.

3.3.2 Effect of Molecular Gas Admixture

To investigate the effect of gas admixture into the DBD discharge, the same set of experiments were repeated with admixtures of CH_4, H_2 and O_2 in the helium working gas, keeping the overall volumetric flow rate steady at 25 $mL\ s^{-1}$.

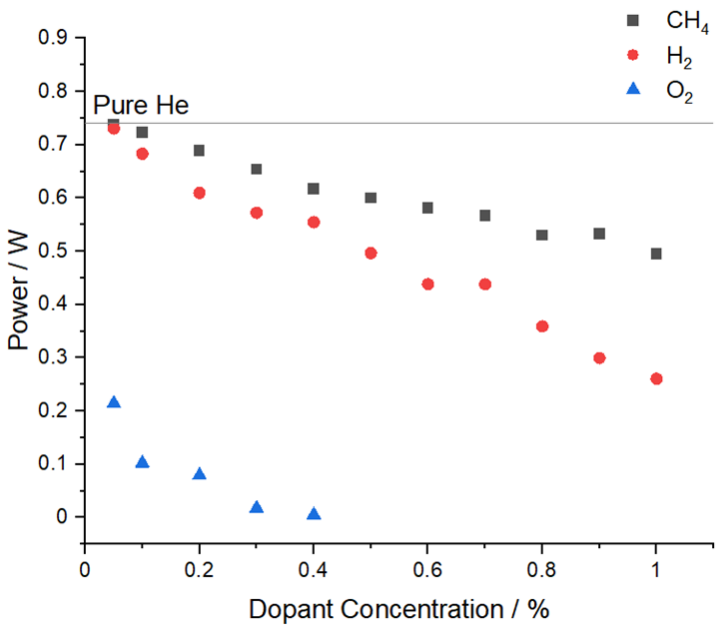

Fig. 3.4 Dissipated power in the plasma jet as a function of dopant gas concentration.

Admixture of any quantity of molecular gases decreases the dissipated power in the plasma by increasing the real impedance, as shown in Figure 3.4. In the case of oxygen, even 500 ppm of admixture leads to a precipitous, threefold decrease in plasma power. Without a kinetic model of the gas mixture, it is difficult to ascertain the reasons behind this drop. First of all, addition of CH_4 or H_2 might lead to Penning ionisation [129] routes where an excited helium atom can ionise another gas species ($He^* + M \rightarrow M^+ + e^- + He$), if this process was dominant, an increase in plasma density and a concurrent decrease in plasma impedance would be expected, contrary to what is observed.

Mixture of H_2 or CH_4 can also open inelastic collision pathways for the electrons in the plasma, leading to an overall drop in period averaged electron temperature. This might lead to a sharp decrease in the number of higher energy electrons that can ionise the plasma gas. For example, the threshold energy required for the electron impact reaction $e + He \rightarrow 2e + He^+$ is 25.14 eV with a cross section of $8.3x10^{-23}$ m^2 [11]. This can be compared to the inelastic excitation cross-sections between electrons and hydrogen molecules that are two orders of magnitude larger and have threshold energies that are as low as 0.05 eV (rotational) to 0.516 eV for vibrational transitions ($v = 0$ -> $v = 1$) [130].

For oxygen, the results of admixture are even more drastic, this is due to the additional possibility of electron attachment reactions ($e.g.\ e + O^2 \rightarrow {O_2}^-$) taking place in the presence of oxygen. In an RF discharge at high pressure, the negative ions generated cannot be

accelerated within the RF period due to their large mass leading to a decrease in power coupling efficiency. This is found to cause a steep decrease in electron density and energy, leading to a significantly increased electrical impedance in the plasma bulk. Power dissipation in the plasma discharge is decreased by at least an order of magnitude at 0.5% admixture. At this level, plasma glow is faint and barely visible, and electrical diagnostics are not possible due to the miniscule amount of power coupled to the discharge.

3.3.3 Optical Emission Spectroscopy

Optical emission spectra of the plasma bulk (Figure 3.5) is complex, containing major atomic lines of helium present in the spectra alongside intense emissions from molecular bands arising from impurities from the helium source and potential leaks due to the DBD being open to air. Major contaminant gases in the "pure" helium discharge are nitrogen [131] and air containing humidity, as can be deduced from the OH [132] molecular bands present. The intensity of emission from some molecular species is significantly greater than the atomic lines, owing to not strictly to abundance but rather the short lifetimes of the vibrationally excited states and low transition energies, compared to excited states of helium. In the plasma plume, the presence of reactive molecular gases results in strong emission bands from OH and NO [133] formed in-situ, alongside the ro-vibrational systems of N_2 [131].

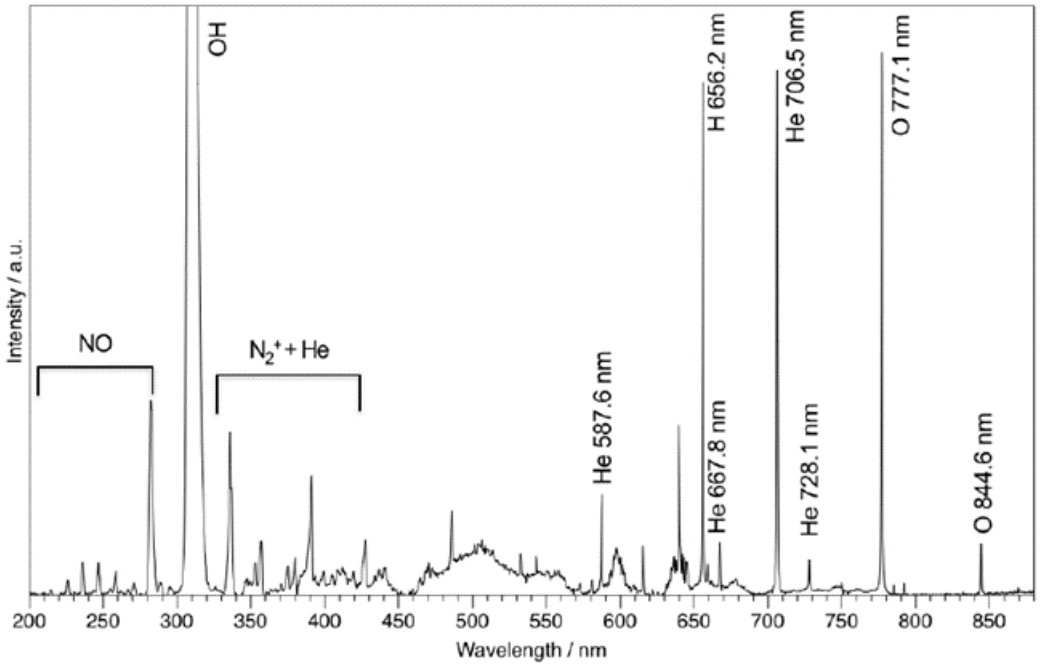

Fig. 3.5 Optical emission spectrum obtained from the DBD dischage at 50 W generator power and 33 $mL\ s^{-1}$ flow rate. The OH emission line at 310 nm is clipped in order to make other emission lines visible.

On addition of dopant gases the optical emission properties of the plasma are drastically changed as shown in Figure 3.6, the helium atomic lines are suppressed significantly upon addition of O_2 and CH_4. The overall emission intensity is also decreased, in line with the decrease dissipated power discussed above. Interestingly, addition of H_2 is seen to significantly decrease the emission lines attributed to atomic oxygen, likely due to the formation of OH in the discharge.

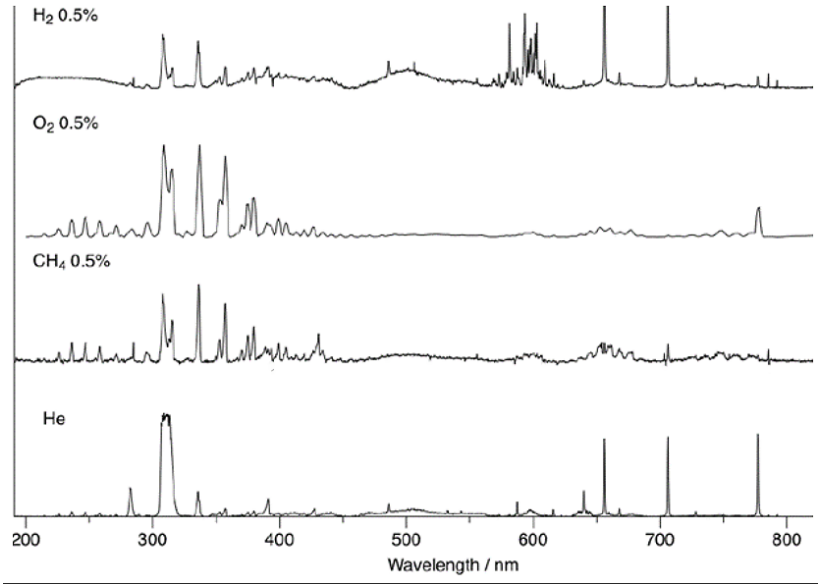

Fig. 3.6 Stacked and normalized optical emission spectra obtained from helium DBD with added gases.

Using the atomic emission lines of helium given in Table 3.1, it is possible to calculate the excitation temperature $T(_{exc})$ of helium in the plasma bulk. This requires the assumption that the excited states of helium are in partial LTE, obeying a Boltzmann distribution. This method is commonly called a Boltzmann plot [30]. In a Boltzmann plot, $\ln(I_{kl}\lambda_{kl}/g_k A_{kl})$ vs $-E_k$ should ideally give a straight line with a slope of $1/T_{exc}$, where I_{kl} is the intensity of atomic line for transition $k \rightarrow l$, k_{kl} is the wavelength, g_k is the degeneracy of level k, A_{kl} is the Einstein A coefficient giving the spontaneous transition probability for the transition, and E_k is the energy of level k. For this experiment, 4 atomic emission lines of helium that were clearly distinguishable in all spectra were used, as shown in Table 3.1 with associated coefficients taken from the NIST database [134].

Table 3.1 Spectral lines and associated coefficients of helium used for analysis.

λ_{kl}/nm	A_{kl}/s^{-1}	g_k	E_k/eV
728.14	1.81×10^7	1	22.9
706.52	6.38×10^7	3	22.7
667.82	6.38×10^7	5	23.1
587.56	2.94×10^7	5	23.1

The resulting Boltzmann plots for pure He and admixtures of CH_4 and H_2 are given in Figure 3.7. It is seen that the excitation temperature $\approx 1000\ K$ of helium is significantly

higher than the gas temperature $\approx 300\ K$ measured via thermocouple in the plasma effluent. This confirms that the discharge is under non-LTE conditions, as expected. Interestingly, the excitation temperature is found to not vary significantly due to gas admixture despite decreased power dissipation. In fact, most of the difference between different gas mixtures lies within the uncertainty in lines of best fit.

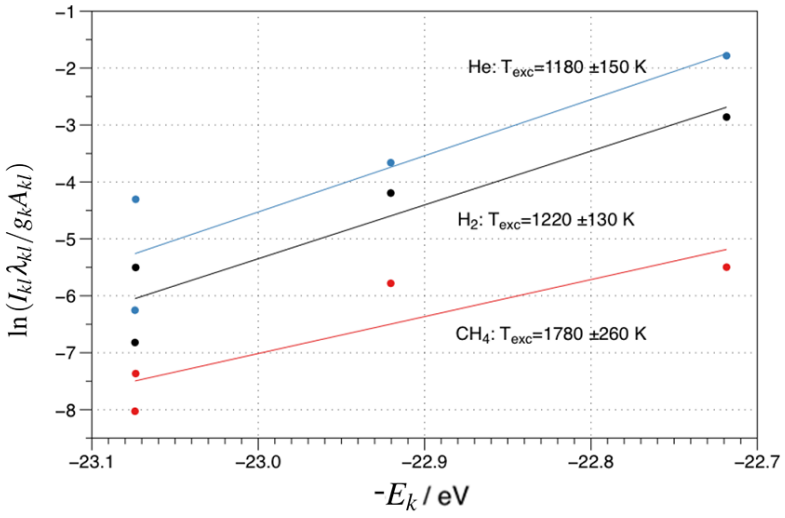

Fig. 3.7 Boltzmann plots generated using optical emission spectroscopy with the DBD jet at 50 W forward power and 33 $mL\ s^{-1}$ total gas flow rate. T_{exc} values and associated error estimates are given for pure helium and dopant gases.

3.3.4 Fluid Model of Helium DBD

A highly simplified computational fluid model of the helium plasma discharge (Appendix A) was solved to provide insight into the discharge characteristics. The model, as presented, was limited to three helium species (He, He^* and He^+) and did not include any impurity gases, dimers and excimers that are known to play a significant role in atmospheric pressure discharges [135, 136]. Experimental details such as discharge voltage, flow rate and plasma source geometry were replicated in the computational model as closely as practicable.

Converged results of the computational model are presented in the following sections, discussing the spatial variability of the important plasma parameters such as electron density (n_e) and electron temperature (T_e) within the discharge tube.

Electron Density

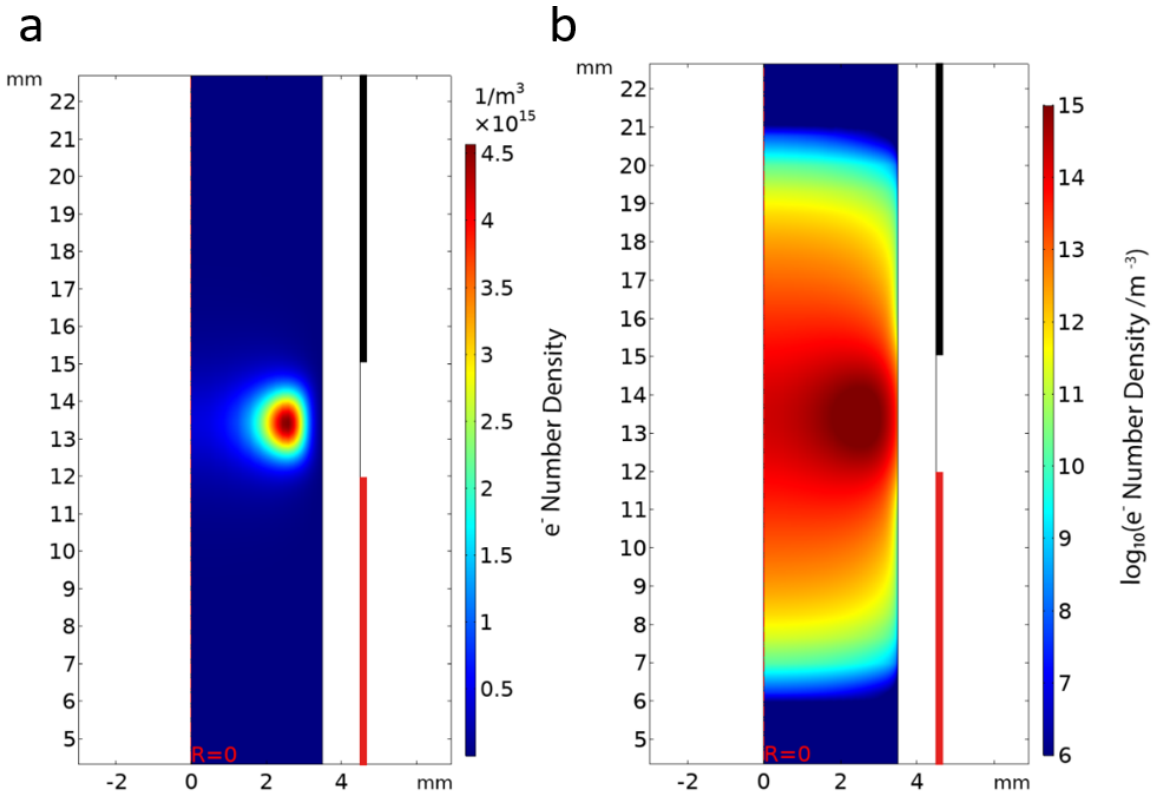

Fig. 3.8 Density plots of electron number in the discharge tube in linear (a) and logarithmic (b) colour scale. Plots are based on an axisymmetric model of the experimental setup described previously. Red and black lines indicate the positions of the powered and grounded electrodes outside the dielectric respectively.

The electron density averaged across one RF cycle is presented in Figure 3.8 as a two dimensional slice across the axisymmetric discharge tube. Electron distribution is concentrated in the region between the two electrodes, forming an annular discharge region, separated by 1.5 *mm* from the inner surface of the tube. Time averaged peak plasma density density is $5 \times 10^{15}\ m^{-3}$, corresponding to a level of ionisation that is on the order of 200 ppt. This level of ionisation is weak compared to small volume discharges [137], yet consistent with reports of atmospheric pressure *glow mode* discharges in literature (APGDs) [138] where the plasma densities can range from 10^{15} to $10^{13}\ m^{-3}$.

Electron density decreases from the centre of the discharge towards the ends of the dielectric tube in the afterglow region. This decay is clearly visible in the logarithmic plot of electron density (Figure 3.8 b). During afterglow decay, plasma density away from the

inter-electrode region drops by 5 orders of magnitude while extending axially down the discharge tube.

In the afterglow region, the period averaged reduced electric field magnitude decays rapidly from a maximum of 5 Td to ≈ 0 Td (Figure 3.9). Under low field conditions, electron temperatures drop rapidly due to elastic collisions, effectively halting further ionisation events sustaining the discharge. Therefore, in the afterglow region, rapid loss of low energy electrons to tube walls and ion-electron recombination in the bulk dominate, leading to decreased electron density. Beyond 4 *mm* from the grounded electrode edge, within the afterglow region, the electron density is negligible.

Electric Field and Electron Temperature

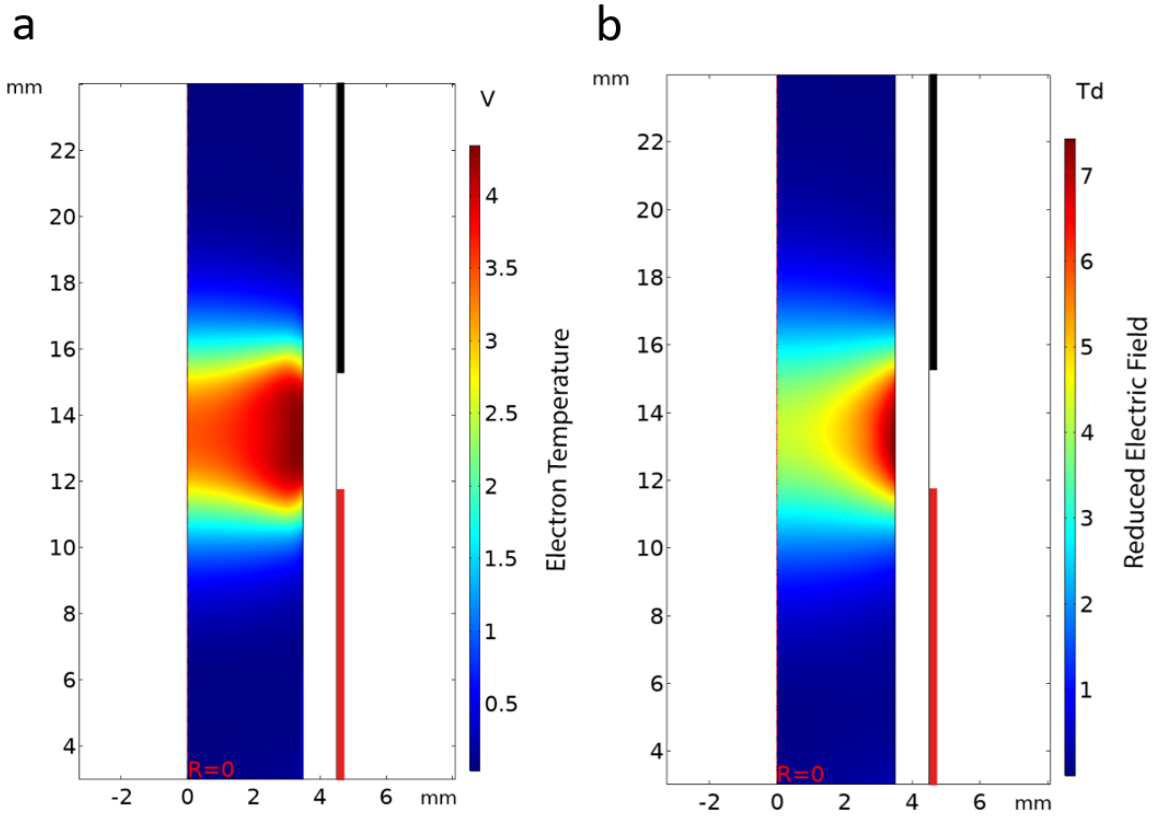

Fig. 3.9 Density plots of time averaged electron temperature (a) and reduced electric field magnitude (b)

Electron temperatures, obtained by assuming a Druyveystein distribution, reaches a maximum of 4.4 eV in an annular region between the electrodes, as shown in Figure 3.9a. Shape of

the electron temperature distribution follows the reduced electric field intensity, with higher energy $(T_e > 4)$ electrons present in a 1 mm slice of plasma adjacent to the tube walls.

The electric field magnitude is highest at the points where the two electrodes are closest, as expected. The field rapidly decays towards the axis of the tube due to both electric field propagation in free space, and shielding by the conductive plasma. Insulating walls of the discharge tube is seen to build a net negative surface charge, and the reduced electric field magnitude is found to reach a maximum of 7.4 Td adjacent to the accumulated surface charge.

Negative charge accumulation arises due to electron impact onto the walls, in return this charge is partially shielded by a space-charge region near the walls due to increased He^+ density in the sheath region. Due to significantly higher mobility of electrons compared to ions, overall charge collected by the walls from plasma bulk is negative. Distribution of charge density along the wall is given in Figure 3.10 with a peak value of $-22\ nC\ m^{-2}$. Charge density is highest at the edges the ring electrodes facing each other. This is due to the high electric field present at the edges of the electrodes, causing increased electron flux from the plasma. It is also seen that the surface charge is not symmetrically distributed despite the geometric symmetry of the electrodes. This asymmetry arises from the distributed capacitance boundary condition imposed on all external surfaces, meaning that the outside surface of the discharge tube is always referred to ground potential via weak capacitive coupling, leading to electrical asymmetry.

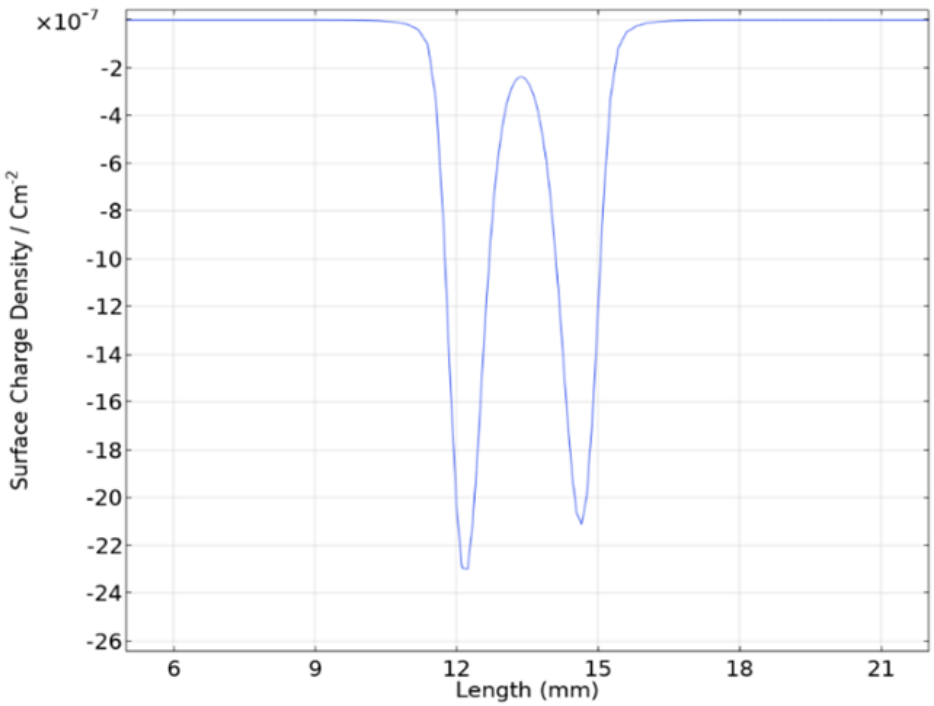

Fig. 3.10 Calculated surface charge density along the quartz wall, the negative peaks correspond to the edges of the electrode contact points where the electric field is strongest.

In the sheath region in contact with the charged wall, an increased number of ions are present, screening the surface charge. Figure 3.11 shows the distribution of plasma species and the resulting space charge layer next to the dielectric wall. Excess ion density generates a positive space charge sheath that reaches its maximum of 300 $\mu C\ m^{-3}$ at a distance of 0.5 *mm* away from the wall. Beyond this, space charge decays rapidly, and the sign of charge density in the centre of the tube is actually negative, reflecting a surplus of electrons in the plasma bulk.

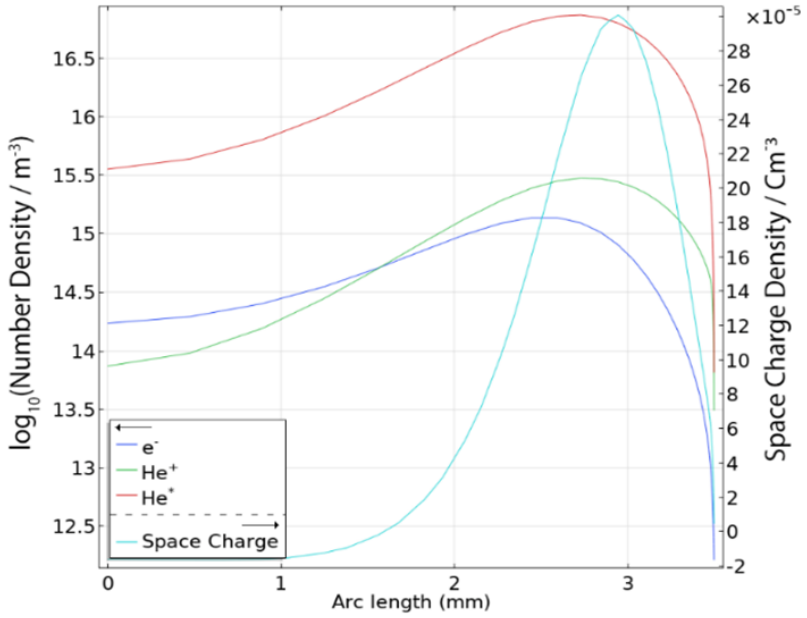

Fig. 3.11 Species and space charge density between in the inter-electrode gap, calculated along a line extending from the axis of symmetry at 0 mm to the dielectric wall.

Despite having high electron energy density, the number density of electrons in this sheath region is orders of magnitude lower compared to bulk. This leads to a drop in the rate of inelastic collisions and a sharp decrease in the generation of excited and ionised species through inelastic collisions within the sheath. In addition, screening of the applied electric field by the conductive plasma causes the electron energy density to drop near the central axis of the tube (Figure 3.9) as well. The combination of both these effects leads to a situation where the plasma density is lowest both immediately against the dielectric wall and also along the axis of the discharge tube. The highest plasma density is then confined in a toroidal region bounded between the sheath, the discharge axis and the two ring electrodes.

The ring shaped hollow discharge is illustrated in Figure 3.12, where photographs of the annular discharge is compared to the volume integrated excited helium state concentration obtained from simulations. Assuming that the light emission from the discharge is solely due to excited helium states (He^*), the two spatial emission profiles are found to closely match, indicating qualitative agreement between the experimental and computational results.

3.4 Langmuir Probe Measurements

It is not possible to experimentally probe the plasma bulk between the electrodes due to the significant perturbation of applied electric fields and arcing that would occur if a

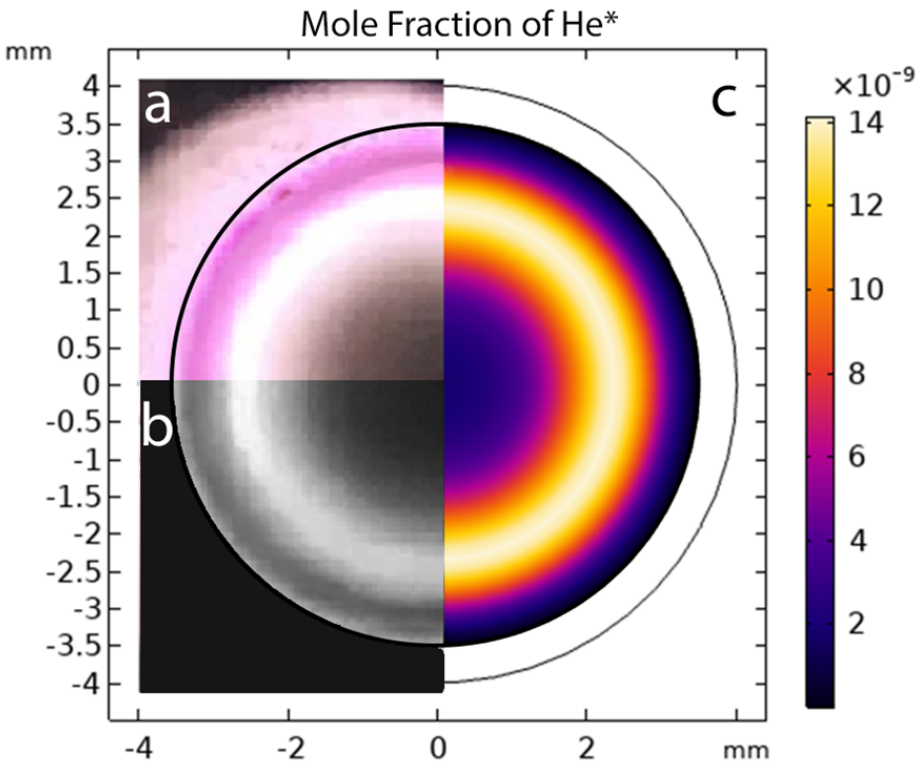

Fig. 3.12 Split figure showing a photograph of the discharge taken axially down the tube enterance (a). Monochrome photograph (contrast adjusted) is shown in (b). radial distribution of excited helium states obtained from simulation results is provided for comparison (c).

conductive probe were inserted between the electrodes. Instead, Langmuir probes were used in the afterglow region, away from the powered electrode, to extract experimental T_e and n_e parameters. By comparison of plasma parameters extracted from probe experiments to the results obtained from the fluid model, it is also possible to tentatively validate the two approaches against each other.

Figure 3.13a shows measured ion density in the plasma afterglow, along the axis of the tube, at increasing distance to the inter-electrode region. Under the assumption that ion and electron densities are equal, therefore the plasma is quasi-neutral, ion density can be considered to be equal to the electron density. It must be noted here that in the plasma afterglow region where the number densities of charged species is extremely low, the validity of this assumption may break down, leading to hard to predict errors in the provided electron density estimates.

Both the model and probe results agree in plasma density estimation at an order of magnitude level. The electron density estimates for both approaches provide values on the order of 10^{12} m^{-3} in the afterglow region, with rapid decay further away, as also predicted by

the computational model. Compared to Langmuir probe data, numerical results overestimate the electron density close to the plasma bulk edge, and the electron density is underestimated further away.

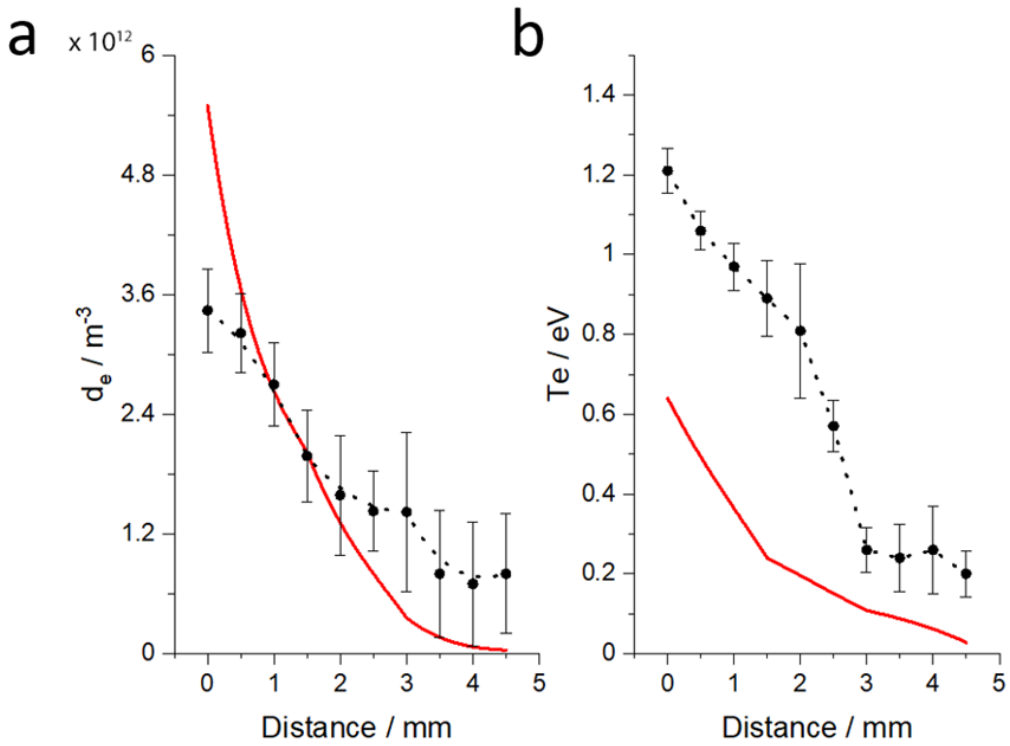

Fig. 3.13 Electron density (a) and electron temperature (b) at points extending away from the grounded electrode. Double Langmuir probe results (black) and computational model results (red) are both presented for comparison.

For the electron temperature measurements (Figure 3.13b), the double probe approach gives electron temperatures that are twice as large as given by the computational model. This is likely due to two effects, one stemming from the lack of important, longer lived plasma species and contaminant gases in the fluid model and one stemming from the perturbation of the plasma due to the insertion of the conductive probe.

The overestimation of T_e with the probe model, in turn, leads to overestimation of electron density, as the density model depends on determination of T_e (Section 2.3.2). Relative error associated with the probe measurements are also large, on the order of 80% for electron density due to inherent noise in current measurements at a level of femtoamperes, alongside the large uncertainties present in ion saturation current determination.

3.5 Conclusions

Helium coaxial dielectric barrier radio frequency discharge can be sustained under atmospheric pressure conditions in the glow disharge mode, producing an annular shaped volume discharge. Experimentally, discharge was found to be non-LTE, showing a significant divergence between measured gas, excitation and, electron temperatures.

Approximation of plasma dissipated power was done via electrical and temperature probe measurements. It was found that at low power dissipation ($< 1\ W$), effluent temperature could be used for approximating power dissipation without accounting for heat losses to the environment. At increasing power density and lower flow rates, power approximation via gas temperature was found produce relative errors up to 20 %.

With the existing set-up, dissipated power in the plasma was measured to be a small fraction of the power measured at the generator. Both the presence of molecular gases and the flow rate of the working gas was found to have a significant effect on the power coupling to the plasma, with efficiencies ranging from 2.5 % at low flow rates to $\approx 1\%$. The effect of plasma discharge on the Q factor of the impedance matching circuit was demonstrated, showing a strong dependence of the resonant match network characteristics on operational parameters such as flow rate and plasma gas composition.

It was found that a fluid plasma model using a highly simplified helium chemistry is able to replicate overall geometry and sheath thickness observed in the experimental discharge. Plasma density was low, both along the axis of the tube and adjacent to the dielectric barrier. A large space charge sheath was present in the numerical models, associated with significant surface charge accumulation on the dielectric.

Validation of the model with double Langmuir probe measurements showed that both methods agreed at an order of magnitude level, suffering from large inherent uncertainties for both methods. A more comprehensive kinetic model with increased number of plasma species and reactions (such as Penning ionisation processes) could help improve the accuracy of model results.

Chapter 4

Modulation of Cu(I)O Oxidation in DBD Afterglow Plasma

4.1 Introduction

Free electrons in the gas phase can provide significant reactivity as observed in plasmas. Previous research has shown that in the liquid phase, plasma electrons can be used for driving electrochemical reactions. Electron bombardment experiments in vacuum, using low energy electrons [139, 140] have also been shown to lead to oxygen desorption from otherwise stable surfaces and reduction of metal oxides. Atmospheric pressure plasmas have been previously used for reduction processes (Section 1.5.1), with scant understanding of the plasma species responsible.

In this chapter, electrons originating from an atmospheric pressure glow discharge are shown to be responsible for reduction of copper(I) oxide immersed in plasma afterglow. Control of redox properties of a Cu_2O thin film is demonstrated via the application of an external DC bias. Reduction of Cu_2O is shown to be repeatable under applied positive DC bias, owing to increased electron collection onto the oxide surface, under an electron retarding negative DC bias, the reduction process is halted. The extent Cu_2O reduction in the presence of hydrogen, methane, and oxygen as additive plasma gases is also explored. Using ex-situ Raman spectroscopy, it is demonstrated that the oxidation state of copper is dependent more on the polarity of the bias voltage applied rather than on the additive gas.

4.2 Experimental

Atmospheric pressure, dielectric barrier discharge (DBD), shown in Figure 4.1 was generated in the configuration as described in Chapter 2. For all experiments, the discharge was ignited with the helium gas flowing at a total volume of 17 $mL\ s^{-1}$. Prior to introduction of samples in the plasma afterglow, the DBD apparatus was run continuously for 30 minutes to ensure a thermal stability. After this point, the Cu_2O film samples described in the next section were introduced into the plasma afterglow region, enclosed within the quartz tube where the plasma is blown outwards from the inter-electrode region toward the open end of the discharge tube. The characteristics of the discharge were discussed previously in Chapter 3.

Fluxes of plasma species to the oxide surface were estimated using a simplified fluid model of the DBD, called DBD-EL as detailed in Appendix A. Experimental conditions were replicated in this model to probe the behaviour of plasma afterglow near the oxide coated electrode.

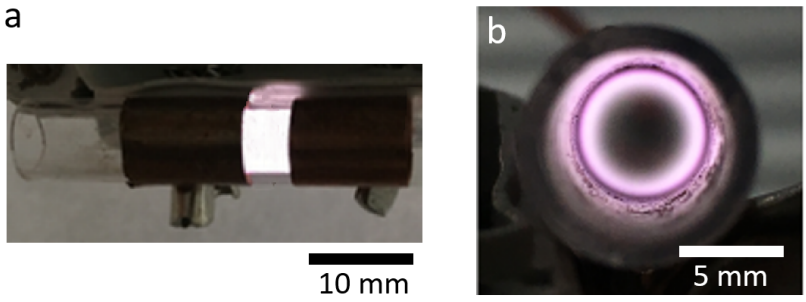

Fig. 4.1 Side (a) and end view (b) of the DBD plasma source used in the experiments.

4.2.1 Copper (I) Oxide Introduction

A coaxial electrode assembly (Figure 4.2b) with a 0.5 *mm* diameter platinum (Advent Materials, UK) disc and an outer copper ring was built and used to introduce a thin Cu_2O film into the plasma. Coated electrode assembly was placed into the plasma jet, 2 *mm* behind the plasma facing edge of the grounded RF electrode, centred within the discharge tube.

Figure 4.2a shows a schematic view of the experimental setup, the outer copper electrode was grounded, and the coated Pt electrode was biased to $\pm 60\ V$ (Model 2450, Keithley, UK) during plasma exposure. The experiments were run under positive bias, negative bias, and floating potential conditions. In all experiments, the Cu_2O coated electrode was exposed to the plasma for 60 *s* and analysed using ex-situ Raman spectroscopy immediately after. A photograph of the electrode assembly placed into the DBD afterglow is shown in Figure 4.2c.

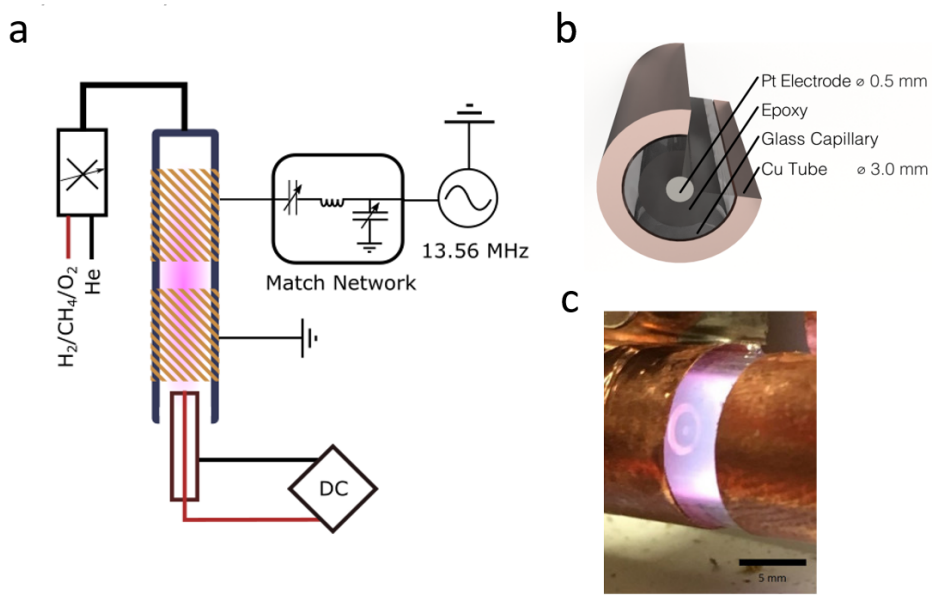

Fig. 4.2 Experimental schematic showing the coaxial electrode inserted within the discharge tube (a). Graphical rendering of the coaxial electrode assembly (b). Photograph of the experimental setup, showing the electrode inserted within the DBD apparatus(c).

4.2.2 Sample Preparation

The Pt electrode was coated with a thin film of Cu_2O, electrochemically deposited onto the polished surface, as described by Liu et al. [141]. The electrodeposition solution comprised of 0.4 M $CuSO_4 \cdot H_2O$ and 3 M lactic acid (Sigma-Aldrich, UK). pH of the plating solution was brought up to pH 12 by drop-wise addition of 5 M $NaOH$. Cu_2O layer was grown under potentiostatic control (PGSTAT100, Windsor Scientific, UK) at -0.5 V vs. $Ag/AgCl$ reference electrode using a large copper mesh counter electrode. Total charge transfer was -135 μC over 300 seconds at 40 $^{\circ}C$. Assuming 100% Faradaic efficiency and, uniform film density, estimated thickness of the deposited film was 170 nm.

4.2.3 Surface Characterisation

Raman spectra were taken with a Raman microscope (InVia, Renishaw, UK), using a 514.2 nm Argon ion laser as the excitation source. Care was taken to work with low power to avoid re-oxidation of the Cu surfaces during measurements. After spectra collection, the surface of the electrodes were wetted with deionised water (Millipore, UK) and the focused Argon laser was used to locally heat the surface and re-oxidize the reduced copper thin film.

4.3 Results and Discussion

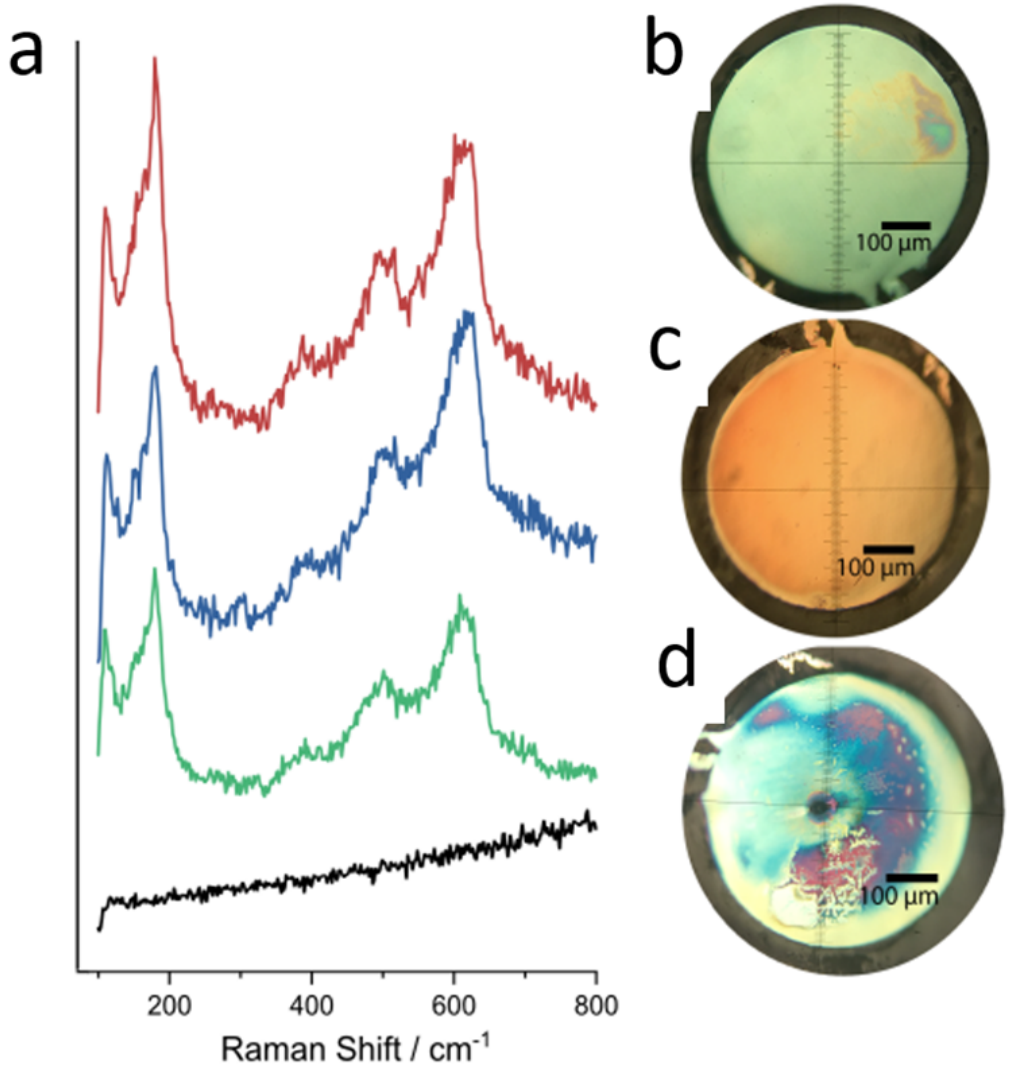

Fig. 4.3 Raman spectra of the coating (a) before exposure to pure helium plasma (red), after thermal re-oxidation (blue), after exposure under negative (green) and positive DC bias (black line). Micrographs of the pristine (b), reduced (c) and re-oxidized (d) thin films.

The Raman spectra of the copper coating before exposure to the plasma, given by the red line in Figure 4.3a, shows a typical spectrum [142] for Cu_2O. After exposure to helium plasma afterglow, under negative DC bias, the Raman signal for the copper oxide remains unchanged. However, when the bias polarity is reversed, colouration of the thin film due to the oxide layer (Figure 4.3c) and signal from the copper oxide almost entirely disappears after 60 *s*.

This can be attributed to either the removal of the cuprous film via ablation in plasma or reduction of the oxide to elemental copper.

Micrographs of the surface before and after plasma exposure Figure 4.3b-c) shows that the oxide film has been replaced with copper. Material loss and ablation is minimal as the surface can be re-oxidised via localised heating with a focused 512 *nm* laser illumination under DI water. Re-oxidation was shown to restore the pale blue copper oxide thin film and the Cu_2O peaks in the Raman spectra (Figure 4.3a) proving conclusively that the result of plasma exposure under positive bias is reduction of the Cu_2O layer into metallic copper.

4.3.1 Reduction of Cu_2O in the Presence of Molecular Gases

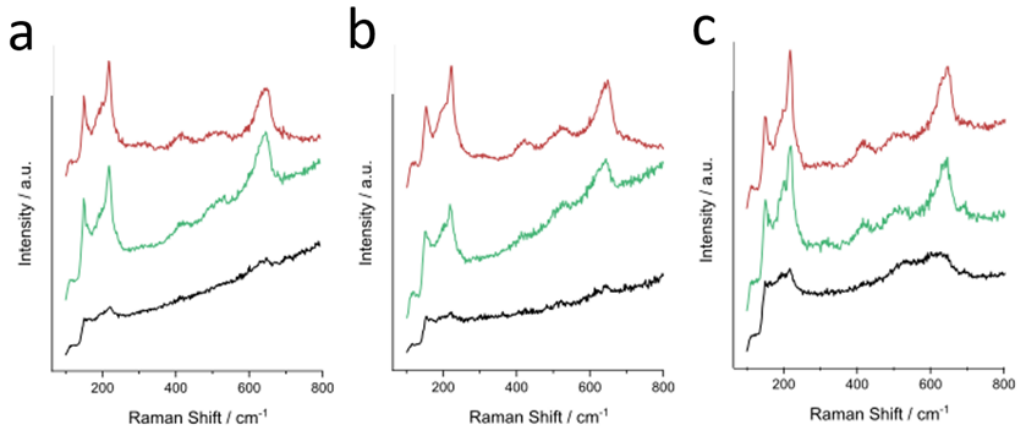

Fig. 4.4 Raman spectra taken from pristine (red line), negatively biased (green line), positively biased (black line) electrode surfaces after exposure to plasma containing 0.5 *v.%* H_2 (a), CH_4 (b) and O_2 (c).

The reduction process is found to be mostly independent of the reactive gases within the plasma, a similar effect of controlled reduction is seen when the plasma gas doped with reducing (Figure 4.4a-b) or oxidizing (Figure 4.4c) gases. The final redox state of the coating is dependent on the polarity of the bias voltage, not on the nature of the dopant gas. Perhaps surprisingly, despite the presence of chemically reducing gases such as hydrogen and methane in the plasma, virtually no change was observed in the Raman spectra when the electrode was polarised to $-60\,V$. These results suggest that the presence of a reducing atmosphere is neither necessary nor sufficient for reduction of the copper oxide in plasma afterglow.

It is noteworthy that Cu_2O Raman band intensity after plasma exposure is higher for all plasma gas mixtures, compared to pure He plasma. This qualitative change can be

ascribed to the decrease in plasma density in the discharge volume. A significant decrease in power coupled to plasma was previously demonstrated in section 3.3.2 upon addition of any molecular gas to the discharge stream. This is especially prevalent when oxygen is used as the additive gas, as formation of stable negatively charged oxygen ions can act as an effective electron sink, decreasing the plasma density in the afterglow region.

While Cu_2O could be reduced under positive bias with all gas mixtures, under negative bias the reduction was found to be completely halted. This might suggest that reduction in this case is caused by electrons that are collected from the plasma bulk rather than any chemical species present.

4.3.2 Fluid Model of Plasma

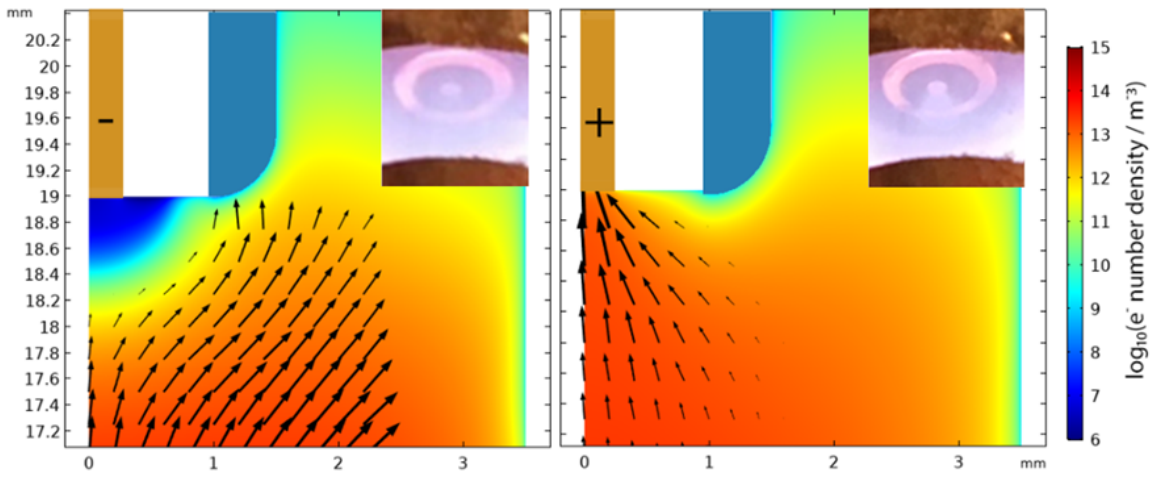

Fig. 4.5 Period averaged electron density (color) and flux (arrows) in the vicinity of the Cu_2O coated electrode under negative (left) and positive (right) bias. Inset: photographs of the biased electrodes during the experiments for comparison.

Modelling results, as depicted in Figure 4.5 show the effect of applied bias on the electron flux and plasma density distribution within the afterglow. As expected, the spatial electron density distribution is considerably distorted upon application of a potential bias to the electrode tip. Under negative bias, RF period averaged electron density drops by 7 orders of magnitude (compared to the non-biased reference case) around the electrode tip. Electrons are nearly completely deflected away from the electrode, resulting in a hemispherical depletion zone in front of the electrode face with a radius of 0.5 mm. Adjacent to the electrode face, calculated electron density is as low as 10 cm^{-3}. In this case the electron flux is drift dominated and points away from the electrode.

Conversely, under positive bias, the electron density is greatly enhanced near the central electrode, this is due to two main effects. First, electron drift under applied potential causes increased flux of electrons towards the positively biased surface. Secondly, acceleration of electrons in the applied field leads to increased electron energy. Coupled with greater electron density, this results in increased rate of ionisation reactions, leading to further enhancement of electron density in an avalanche process. This effect can be seen in the photographs of the discharge as a cone shaped glow above the positively biased central electrode (Figure 4.5). At 100 μm above the surface, the total rate of ionisation reactions under positive bias is on the order of 10^{-9} $mol/(m^3 s)$ whereas under negative bias, ionisation rate is negligible, 10^{-30} $mol/(m^3 s)$.

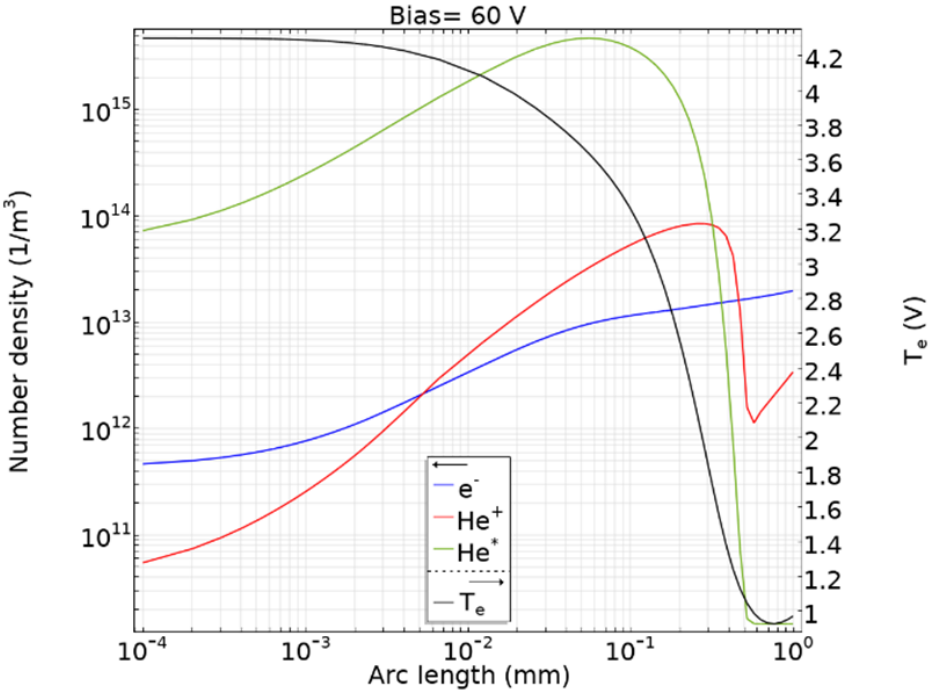

Fig. 4.6 Charged and metastable species densities and electron temperatures along a line extending from the centre of the coaxial electrode under positive bias (a), distance is given in logarithmic scale to aid presentation. 0 mm point is situated at the center of the Cu_2O electrode.

Examination of the density and energy profiles of plasma species in front of the electrodes (Figure 4.6) provides strong evidence towards the role of electrons in observed plasma reduction. Under positive bias, the number density of electrons in contact with the wall is an order of magnitude higher than ion number density. Similarly, the acceleration due to the auxiliary field imposed is seen to increase the electron temperature to 4.2 eV at the surface

compared to approximately 1 eV at a 1 mm distance from the electrode.

Number density of excited helium species (He^*) is also found to be significantly enhanced above the surface, but unlike electrons, the excited helium atom transport occurs only via diffusion, leading to a minute total flux of $\approx 10^5\ s^{-1}$ to the surface, providing further evidence towards an electron mediated rather than an excited or ionic species mediated reduction pathway.

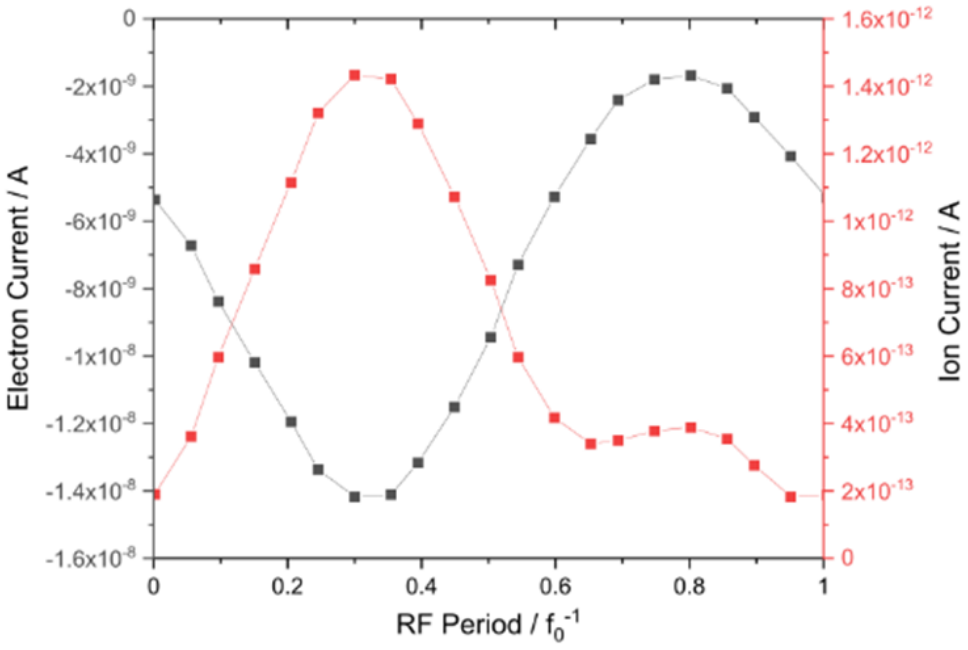

Fig. 4.7 Time dependent ion (red) and electron currents drawn to the auxillary electrode under positive bias. The RF period is given for the sinusoidal driving waveform.

Calculated ion and electron currents to the surface (Figure 4.7) agree with the observation that electron flux to the surface is significant under positive bias. Peak electron and ion currents to the surface on the order of $-20\ nA$ and $1\ fA$ respectively. It must also be noted that the values obtained from the model are in line with the range of $10-50\ nA$ net DC current $(I_{net} = I_i - I_e)$ measured during experiments through the electrode biasing circuit. Under positive bias, the current drawn to the electrode is seen to oscillate with the driving RF field. This is due to the periodic shift of the plasma potential in the bulk as the driven electrode switches polarity at 13.56 MHz. For example, as the RF electrode is driven to a positive value, the electron current is found to decrease as the effective electric field magnitude between the electrode tip and the plasma bulk is decreased.

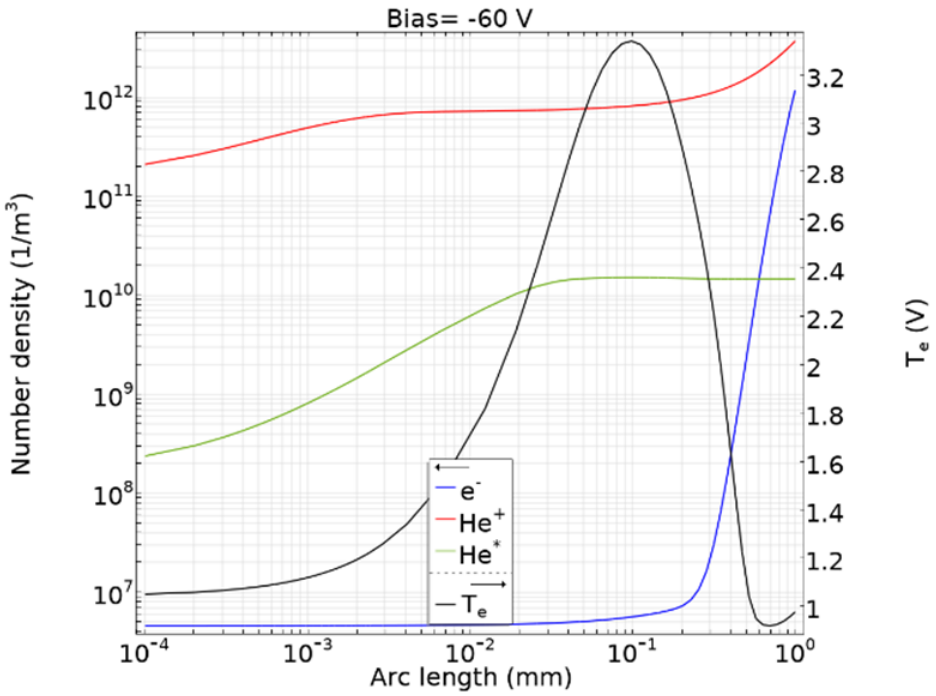

Fig. 4.8 Charged and metastable species densities and electron temperatures along a line extending from the centre of the coaxial electrode under negative bias (a), distance is given in logarithmic scale to aid presentation. 0 mm point is situated at the center of the electrode.

In the case of applied negative bias, an electron retarding region is established, extending 100 μm from the electrode surface towards the bulk (Figure 4.8). The significant decrease in electron density is also causes decreased production of ionic and excited species. Conversely, the ion density near the surface is increased two-fold compared to the positive bias scenario. Increase of ion density is meagre compared to the extent of electron depletion in this region, as the effect of drift on the ions is small compared to electrons considering relative mobilities [143].

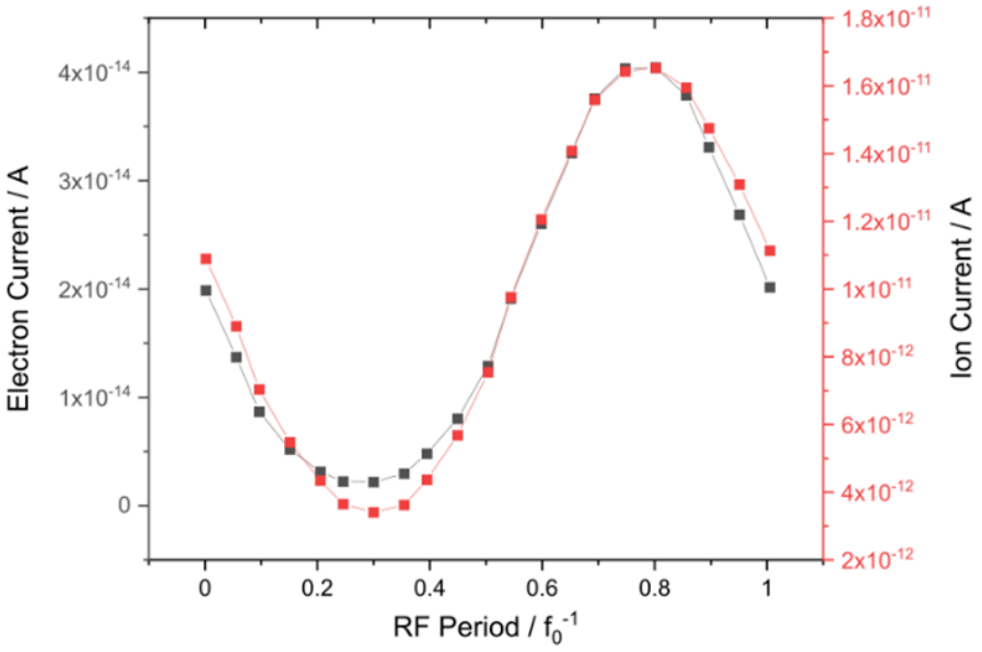

Fig. 4.9 Time dependent ion (red) and electron currents drawn to the auxillary electrode under negative bias. The RF period is given for a sinusoidal driving waveform.

Looking at the electron and ion currents collected to the electrode surface, under negative bias (Figure 4.9) both electron and ion currents are low ($< 100\ fA$) and oscillate significantly during the RF period. Under this condition, negligible current is drawn to the Cu_2O surface. Compared to the positively biased case, the total flux of ions to the surface under negative bias is increased by a factor of 10, whereas the electron current magnitude is decreased by a factor of 10^4.

4.4 Mechanism of Plasma Afterglow Reduction

As the samples are introduced into a high energy, non-equilibrium environment, many routes are available that can lead to the observed results. Seven potential pathways have been identified that may cause the reduction of Cu_2O observed in the plasma afterglow. These are:

- annealing in the hot, inert gas stream,
- UV induced oxygen desorption,
- reduction via chemical species,
- ion impact,

- metastable impact,
- and electron impact mechanisms.

Previous studies dealing with vacuum annealing of $Cu(I)O$ [144, 145] have shown that thin films of Cu_2O are stable up to temperatures of 200 $^{\circ}C$ in high vacuum, gradually desorbing oxygen at increasing temperatures. In-situ measurements of the gas temperature at the DBD exit (Section 3.3) suggest that this mode of reduction is not likely, considering the relatively *cold* plasma effluent temperatures (50 $^{\circ}C$).

Joule heating of the surface due to plasma drawn currents is another possible route that can lead to thermal desorption of oxygen from the surface. This is a significant possibility as current draw to the surface depends strongly on electrode polarity (Figures 4.9 - 4.7). Due to the differences in the sizes of the central coated electrode and the outer *(*ground), the ion current drawn to the surface under negative bias is significantly lower. This stems from the lower mobility of the positive ions in the plasma compared to electrons.

A worst-case estimate of power dissipated in the Cu_2O layer under positive bias is given by $P = I^2 \times R$ where electrode current $I = 100\ nA$, $R \approx 1\ G\Omega$. Accordingly, in 60 seconds of plasma exposure, an estimated 0.6 mJ of energy is dissipated as heat in the copper oxide layer. Under an approximation where no heat is transferred to the underlying platinum support, this should lead to a temperature increase of 75 K or a final temperature of 125 $^{\circ}C$, based on a film thickness of 170 nm and Cu_2O heat capacity of 67.6 $J\ mol^{-1}\ K^{-1}$[126]. Even under exceedingly conservative approximations, it is unlikely that Joule heating plays a significant role in the observed reduction of Cu_2O films.

Similarly, photo-induced reduction of Cu_2O is a known phenomenon [146] that might take place in the DBD, as the plasma discharge is known to emit short-wavelength UV light (Section 3.3). This is an unlikely route as there should be minimal change to the total UV light flux to the surface due to applied bias. To confirm this, the experiment was repeated with the coaxial assembly placed $\approx 5\ mm$ further away from the inter-electrode zone, where incident UV intensity should be comparable to the previous experiments, but the measured plasma density is significantly lower. The results indicated no change to the Cu_2O layer under any bias condition, suggesting that UV exposure was not responsible for reduction.

Plasma generated atomic hydrogen is known to be a strong reducing agent [95]. Therefore chemical reduction route, possibly arising from contaminant gases in the helium supply were also considered by intentional admixture of reducing gases into the plasma stream. Surprisingly addition of hydrogen or methane were both found to hinder, rather than speed up the reduction process under positive bias as discussed.

Instead, the two major differences between the two bias conditions are fluxes of charged and excited species to the surface. Computer models suggest that diffusion dominated flux of uncharged species and drift of ions to the electrode are insignificant. On the other hand, electron flux, and the energy of the electrons on impact with the surface are strongly affected due to the auxiliary electric field generated by the coaxial electrode assembly. By ruling out alternative mechanisms discussed above, the most likely mechanism behind the observed reduction process is due to inelastic collisions of plasma electrons with the surface.

A small change in electron temperature can lead to a large increase in the number of highly energetic electrons. It is possible to visualise the electron energy distribution functions for the electrons impacting the surface by assuming a Druyveystein [147] energy distribution function (EEDF) and using the computationally obtained electron temperatures on impact with the surface under bias. The numerically obtained T_e values are 5.0 eV and 1.1 eV for positive and negatively biased cases respectively.

The calculated EEDF is plotted in Figure 4.10, clearly showing a significant increase in the number of electrons with energies > 10 eV under positive bias. To confirm that the analytical distribution is not greatly skewed compared to the true Boltzmann distribution, a calculated EEDF is also provided for the 0-dimensional case under identical conditions.

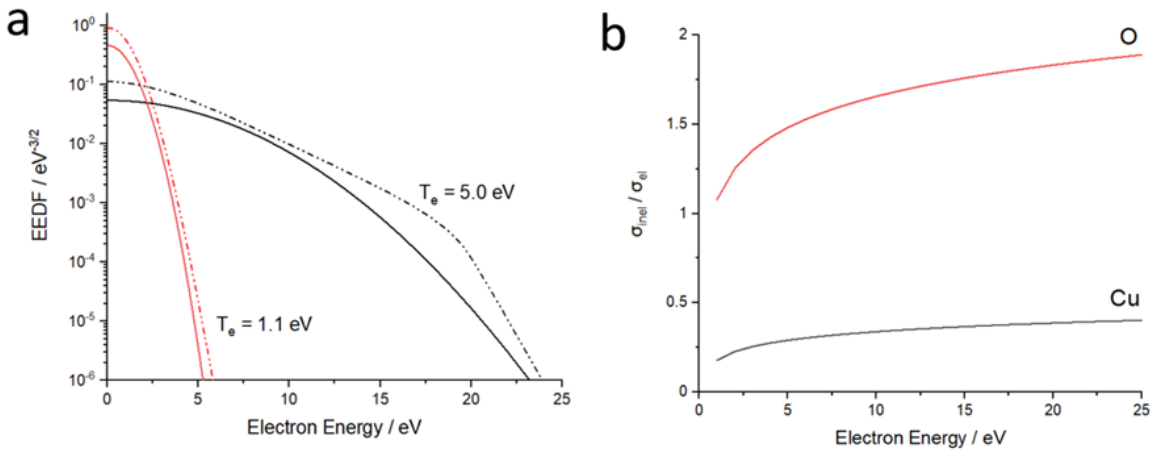

Fig. 4.10 EEDFs obtained through a Druyveystein distribution (solid lines) and via the Boltzmann equation in a 0-dimensional model (dashed lines) (a). Ratio of inelastic to elastic collision cross-sections as a function of electron energy for Cu and O (b).

Calculated EEDFs show virtually no electrons present with energies above 20 eV. Lack of high energy electrons under both bias conditions suggests that *knock-on displacement* of oxygen atoms from the Cu_2O lattice is impossible as the electron impact energies are orders of magnitude smaller than the threshold energies for knock-on damage [139]. Instead, it

is likely reduction in atmospheric pressure glow discharge follows an electron stimulated desorption pathway.

One electron stimulated desorption mechanism is the Knotek-Feibelman (KF) mechanism [148]. KF mechanism for Cu_2O involves ionisation of a Cu core level followed by Auger transitions from oxygen valence levels, with the excess energy resulting in desorption of O^+. Under experimental conditions, expected electron energies are too low for ionisation of Cu core levels that lie below $-100\ eV$ [149]. Furthermore, $Cu(I)O$ is not of maximal valency which is required by the KF model.

The ratio of inelastic to elastic collision cross sections for both oxygen and copper provide further clues as to the underlying reduction mechanism. Reduction of the metal oxide layer inevitably requires preferential desorption of oxygen from the surface. Equation 4.1 [150] gives the approximate ratio of inelastic (σ_{ine}) to elastic (σ_{el}) scattering cross-sections for atomic number (Z) as a function of electron energy (E).

$$\sigma_{ine}/\sigma_{\mathrm{el}} = \frac{2}{Z}\ln\left\{\frac{1194}{Z^{4/3}}E(1+E/1022)\right\} \tag{4.1}$$

As plotted in Figure 4.10b, in the low electron energy regime, the calculated likelihood of inelastic collisions of electrons with oxygen atoms in the oxide lattice is significantly higher compared to copper. Based on these observations, a second, more likely mechanism is the Menzel-Gomer-Redhead (MGR) model [151]. In MGR type desorption, initial electron impact results in the formation of an ionised excited state in copper oxide, followed by relaxation of this state through desorption of oxygen, with or without final re-neutralisation of O^+. Based on available results, it is most likely that MGR type desorption takes place at atmospheric pressure plasma, this proposed route is summarised below:

$$[M-O] + e^- \rightarrow [M-O^+]^* + 2e^- \rightarrow M + O^{+/\,0}$$

4.5 Conclusions

In this study, the reduction of copper (I) oxide to metallic copper in atmospheric pressure DBD is described. It is shown for the first time that the rate of the reduction of copper(I) oxide can be controlled via application of an external bias, suggesting that plasma electrons play a significant role in the modification of the oxide surface. Neutral components of the plasma effluent show little reduction or oxidation activity, ruling out a mechanism governed by chemical reactions on the surface and hinting towards an electron stimulated desorption type of pathway.

Electron stimulated non-thermal reduction is a well known phenomenon under vacuum conditions [152] but has not been previously explored at atmospheric pressures. The ability to electrically modulate surface oxidation states under atmospheric pressure plasma opens up new technological opportunities for post-deposition modification of coatings and removal of oxide contaminants from surfaces without wet chemistry at atmospheric pressures.

Further research is required to understand the exact mechanism behind these process, and also to clarify the range of oxides and metal compounds that can be selectively modified in this manner.

Chapter 5

Atmospheric Pressure Plasma Jet Patterned Metal Oxide Films

5.1 Introduction

Metal oxide surfaces can support rich chemistry; in fact, many metal oxides such as the ones used in this study have been harnessed as catalytic materials primarily due to their surface reactivity. Modifying or tailoring catalyst surface chemistry often involves chemical modification of both the surface and the bulk, typically using techniques such as doping during synthesis [153], vacuum annealing [154] or high energy beams [155]. These techniques are often power-hungry and/or expensive to access, e.g. using vacuum systems. So accessible techniques utilizing materials that are sustainable and benign are a priority.

The previous chapter has introduced the possibility of metal oxide reduction using atmospheric pressure plasmas, using a DBD configuration. DBD plasma sources are convenient from an experimental perspective due to their confined geometry. For the same reasons, they are not convenient for large-scale processing of substrates that might be desirable for technical uses. This chapter discusses the use of a pulsed, RF driven, micro-plasma jet (APPJ) for selective surface modification of metal oxide thin films, investigating the effects of atmospheric pressure plasma exposure on films of Cu_2O, TiO_2, SnO_2, WO_3 and ZnO. Unlike the physical reduction routes explored in the preceeding chapter, this work involves using hydrogen doped plasma for rapid chemical reduction of metal oxide surfaces. It is shown that a plasma jet operated at low power density can be used to selectively reduce metal oxide thin films, generating non-stoichiometric, oxygen deficient structures. This method offers an accessible and green route to mask-less, dry surface modification.

In this investigation, the treatment of metal oxides using an APPJ is shown to rapidly

reduce films of metal oxides. Highly stable oxides such as TiO_2 are rapidly reduced with non-thermal plasma under mild conditions. Using an in-house designed and built helium plasma jet doped with hydrogen, it is shown that coatings of TiO_2, WO_3 and ZnO results in mixed valence materials after exposure to plasma, and SnO_2 and Cu_2O may be completely reduced to the parent metal via plasma exposure, even in the absence of hydrogen.

5.2 Experimental

5.2.1 Plasma Jet Treatment

Experiments described in this chapter were performed on pre-deposited thin film coatings, produced using electrochemical and aerosol assisted chemical vapor deposition (AACVD) methods. The pulsed RF micro plasma jet described in Section 2.2.2 was used during the experiments, with helium and admixture of 5 *v.%* H_2 gas (BOC, UK). The working gas was maintained at a total flow rate of 3.3 $mL\ s^{-1}$ for all experiments. The metal oxide film coated samples were placed on a 2-axis motorized positioning stage beneath the plasma jet, 0.5 *mm* below the nozzle. The plasma treatment took place in open air, where the ejected plasma plume contacted the sample films kept outside the discharge region. Samples were moved back and forth 5 *mm* under the plasma jet during the treatment period. The travel speed of the stage was was 1 $mm\ s^{-1}$, creating *tracks* of plasma treated regions on the film surface.

The number of passes of the plasma jet over the surface was varied to probe the effect of plasma exposure time on the composition of metal oxide films. The surface temperature of the substrates was measured using an infrared thermometer (Fluke, USA) during experiments.

5.2.2 Sample Preparation

Cu_2O films were deposited electrochemically on ITO glass substrates (Osilla, UK). Deposition conditions were identical to as described in Section 4.2.2. Total deposition time was 30 minutes at 55 $^{\circ}C$. All other films were deposited on SiO_2 ($\approx 50\ nm$) barrier coated float glass (NSG, UK) by AACVD. Deposition was performed using a horizontal bed reactor. Precursor solutions were atomised using an ultrasonic nebulizer (Johnson Matthey, UK) and passed over the substrate using a carrier gas at a flow rate of 1 $L\ min^{-1}$. A stainless-steel plate was positioned 8 *mm* above the glass substrate to promote laminar flow of gases. During deposition, substrates were placed on a heated graphite block, a temperature controller (Eurotherm, UK) was used to keep the substrates at the set deposition temperature. All precursors and solvents were procured from Aldrich, UK and used as received.

Glass substrates were cleaned with detergent solution followed by 2-propanol and dried in an oven at 80 $^{\circ}C$. For TiO_2 deposition, precursor solution containing titanium ethoxide $(0.2\ g)$ in toluene $(20\ mL)$ was aerosolized and transferred to the deposition chamber using nitrogen (BOC, UK) carrier gas. For SnO_2, the precursor solution contained butyltin trichloride $(0.2\ g)$ in methanol with compressed air (BOC, UK) as carrier gas. For ZnO, the precursor solution contained zinc acetate hydrate $(0.2\ g)$ in methanol with nitrogen carrier gas. For WO_3 deposition, the precursor solution consisted of tungsten hexacarbonyl $(0.05\ g)$ in a mixture of acetone $(20\ mL)$ and methanol $(5\ mL)$ under nitrogen carrier gas. For all the coatings, substrate temperature was 500 $^{\circ}C$, except for WO_3 deposition which was carried out at 375 $^{\circ}C$. As deposited tungsten oxide films were then annealed under air flow at 500 $^{\circ}C$ to ensure complete oxidation.

5.3 Results and Discussion

For this study, five metal oxide thin films were tested. A change in oxidation state was observed for all treated films, showing different extents of reduction. For each of the five metal oxide materials exposed to the plasma jet, a detailed analysis of the XPS, Auger and Raman spectra are presented for the pristine films and the films exposed to the plasma jet for increasing lengths of time. In some cases, the morphology change upon exposure to the plasma was also characterised using SEM imaging.

5.3.1 Cu_2O

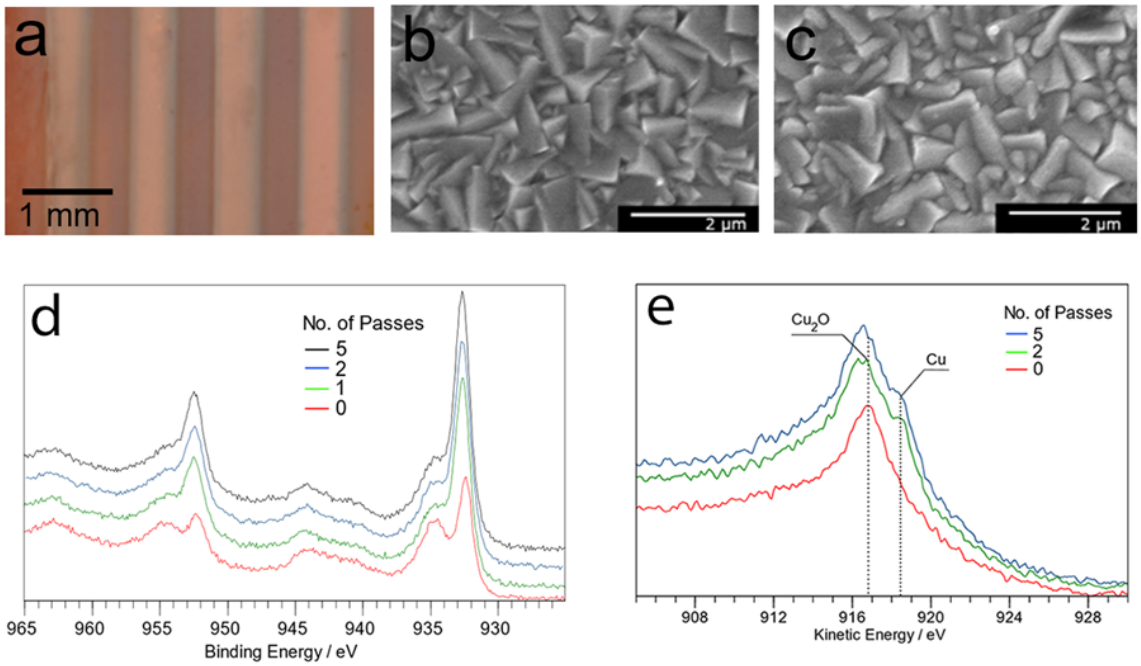

Fig. 5.1 Photograph of the plasma treated Cu_2O surface, showing the tracks of metallic copper produced by the plasma jet over the oxide surface (a). Scanning electron micrograph of the pristine Cu_2O surface showing large cubic crystals present (b). Scanning electron micrograph of the plasma treated region of the film, showing minimal change in morphology (c). Cu 2p high resolution XP spectrum of the surface at different plasma treatment times (d). Cu *LMM* Auger electron spectra of the pristine Cu_2O and the plasma treated regions (e).

Electrodeposited copper oxide films showed clear evidence of reduction to Cu^0 from Cu^+ even after a single pass of the plasma jet, this is in line with the observations made in Chapter 3, where it was shown that plasma exposure can lead to rapid reduction of the surface. It is also worth noting that the results in the absence of H_2 addition were nearly identical to results obtained with H_2 doped plasma gas.

Figure 5.1a, shows the metallic copper tracks on the red Cu_2O surface produced via plasma treatment after one, two, three and five passes of the plasma jet. SEM images of the surface before, Figure 5.1b, and after, Figure 5.1c, show that there is no significant change to the cubic Cu_2O crystal structure following plasma treatment. Substrate temperature, measured with a non-contact thermometer, did not rise beyond 5 $^\circ C$ above ambient during plasma exposure, highlighting the gentle nature of the plasma jet treatment process.

XP spectra of the surface after plasma treatment is given in Figure 5.1d. The main peaks of the spectra are located around 932 and 952 eV, due to photoelectron emission from Cu

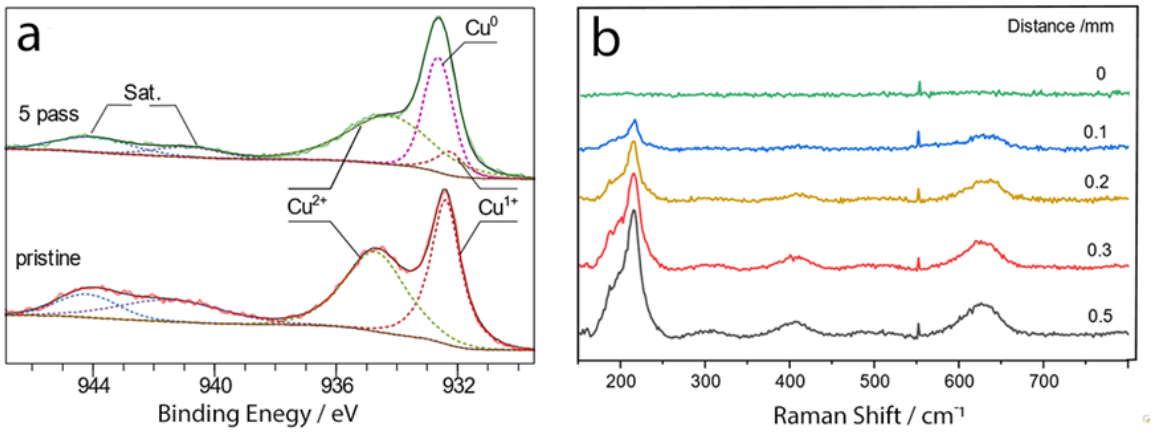

Fig. 5.2 Deconvoluted high resolution Cu$2p$ XP spectrum with spectral components labelled(a). Raman spectra taken from the surface of the Cu_2O film at increasing distances from the centre of the treated region after 5 passes of the plasma jet (b).

$2p_{3/2}$ and $2p_{1/2}$ levels, respectively. The Cu $2p_{3/2}$ spectrum taken from the pristine surface can be modelled with two main components centred at 932.3 and 934.7 eV with full width half maximum (FWHM) values of 1.2 and 2.8 eV (Figure 5.2 a). The peak at 932.3 eV is assigned to Cu_2O whilst the higher binding energy peak is attributed to $Cu(OH)_2$ and CuO based on literature values [149]. Shake-up satelite features arising from $Cu(II)$ species are labeled *Sat.* in Figure 5.2.

The Cu $2p$ XP spectrum taken from the plasma treated surface at five passes shows significant changes comapred with the pristine surface: the normalised spectral intensity of the low binding energy feature around 932.7 eV is increased comapred with the higher binding energy feature around 934.7eV, suggesting reduction of the surface by the plasma into elemental copper.

To confirm the presence of metallic copper, Cu *LMM* Auger electron spectra from the samples were also acquired, given in Figure 5.1e. The pristine surface showed a single Auger peak at 916.9 eV Auger electron energy. This peak was composed of unresolved contributions from both $Cu(OH)_2$ and Cu_2O. The plasma treated surfaces, in contrast, show a second peak at presence 918.5 eV characteristic of metallic copper.

Deconvolution of Cu $2p$ XP region at high resolution for the as-deposited Cu_2O surface and after plasma treatment are shown in Figure 5.2a. This region was modeled with three Cu $2p_{3/2}$ components in addition to two components due to shake-up processes. Peaks located at 932.3, 932.6 and 934.7 eV are assigned to the species Cu_2O, Cu, and $Cu(II)$ respectively, based on reference binding energies[149]. Metallic copper peak at 932.6 eV is present only in the plasma exposed areas, confirming that plasma treatment results in reduction of Cu_2O into

metallic Cu. Residual $Cu(I)$ and $Cu(II)$ species on the plasma treated traces can be attributed to the thin native oxide layer formed on the copper surface upon exposure to ambient air during handling, this is confirmed via Raman spectroscopy as discussed below. Beyond 5 passes of the plasma jet over the substrate, the surface composition of the plasma treated Cu_2O film is stabilized at 54% $Cu(OH)_2$, 30% Cu, 16% Cu_2O.

Raman spectra of the pristine film given in Figure 5.2 show characteristic bands of Cu_2O at 220 and 630 cm^{-1} [156]. Raman spectra collected from various points extending from the centre of the reduced copper tracks show no copper oxide signals at the centre of the plasma exposed area. Spectra collected further away from this point show a gradual increase in the intensity of Cu_2O bands, and the background spectrum is recovered at 0.55 mm away from the jet centre. This suggests that Cu^{2+} species observed in the XP spectra are due to a thin ($< 1\ \mu m$) layer of native oxide formed upon exposure to air after plasma treatment rather than bulk oxide presence.

5.3.2 TiO_2

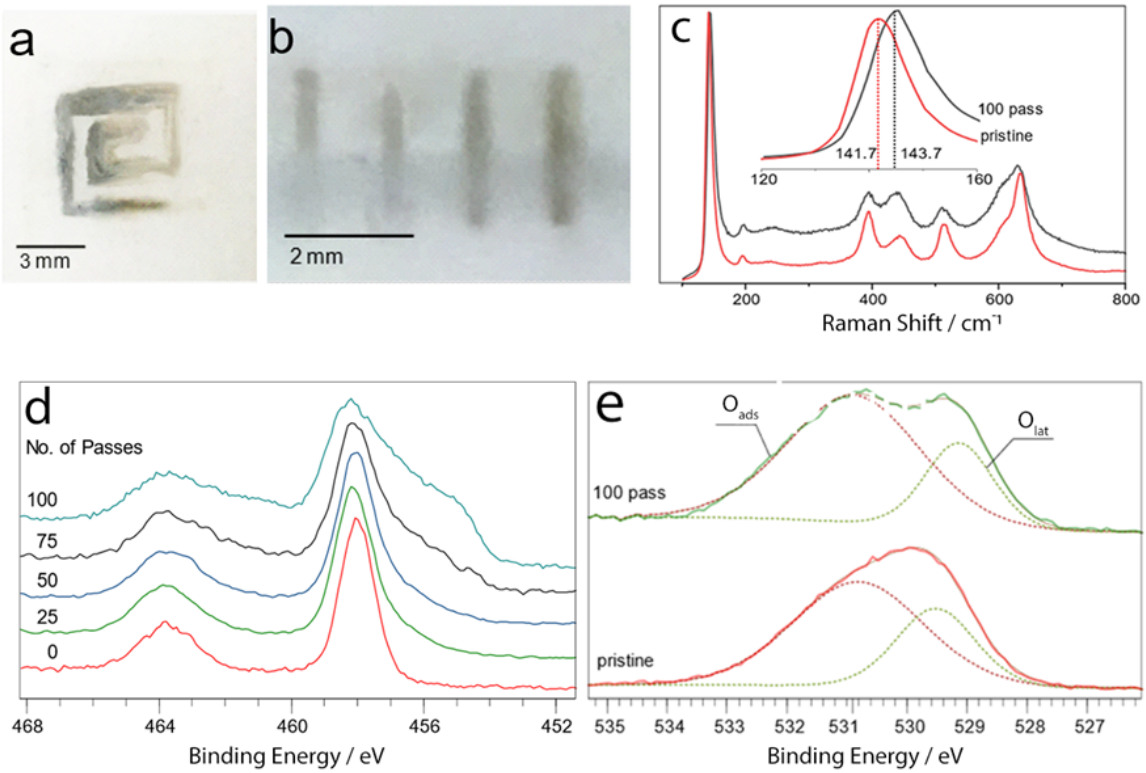

Fig. 5.3 Photographs of a selectively reduced, spiral shaped oxygen deficient black titania pattern drawn on the TiO_2 surface with the plasma jet (a) and linear tracks of reduced TiO_2 (b). Raman spectra of the plasma treated and pristine TiO_2 films (c) with inset highlighting a peak position shift following plasma exposure. Ti $2p$ high resolution X-ray photoelectron spectra taken from the film surface after increasing number of plasma jet passes over the surface (d). High resolution O $1s$ X-ray photoelectron spectra before and after plasma exposure (e).

Plasma treated regions on the TiO_2 are found to turn a dark grey colour, further exposure results in a blue colouration across the treated surface. Figures 5.3a-b depict the plasma patterned TiO_2 surfaces, the darker areas are attributed to the presence oxygen deficient reduced TiO_2. The reduced surface and the resulting colouration is air stable for at least 4 months at room temperature.

The reduction only takes place in H_2 doped plasma, with no measurable change in surface composition observed under pure helium plasma exposure. Pristine Ti $2p$ XP spectra in Figure 5.3d show two major peaks with spin-orbit splitting of 5.7 eV and intensity ratio of $2:1$. The Ti $2p_{3/2}$ peak for the pristine surface is centred at 458.7 eV with a FWHM of 1.16 eV, in agreement with reference values [157]. Plasma treated surfaces display a major

shift of the Ti 2*p* main peak from 458.8 to 458.1 *eV* beyond 50 passes of the plasma jet over the surface.

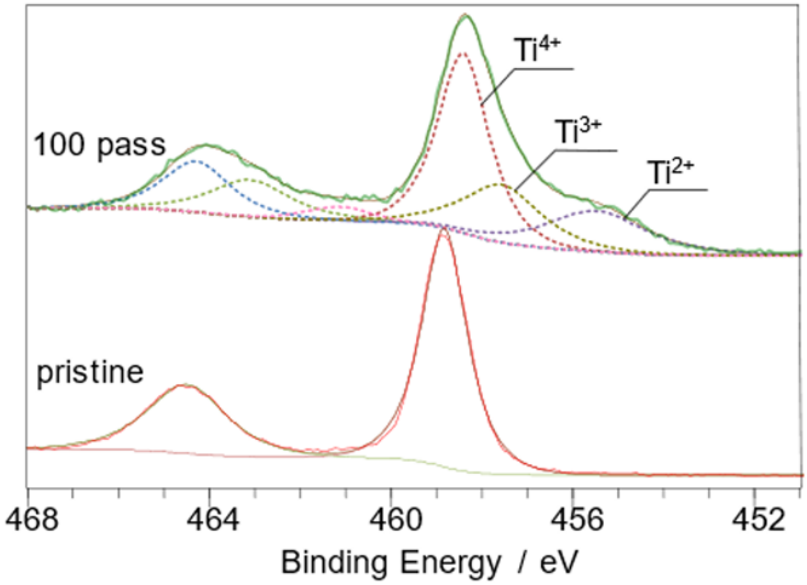

Fig. 5.4 High resolution Ti XP spectra for the pristine and treated films showing new spectral components emerging after plasma exposure.

Furthermore, a prominent feature at 455.5 *eV* appears and grows with longer plasma treatment durations, labelled Ti_{2+} in Figure 5.4 . The origin of this peak is ambiguous and can be attributed to either TiO sub-oxide species in a formal $+2$ oxidation state [158], or X-ray photoemission induced final state effects arising from the defective Ti^{3+} species [159]. This is discussed further in the context of black titania production, in Chapter 6.

High resolution O 1*s* spectra of the samples show two distinct peaks (Figure 5.3e). The high binding energy peak (O_{ads}) at 530.8 *eV* was assigned to surface OH groups, and $C-O$ contaminants. The lower binding energy peak (O_{lat}) at 529.5 *eV* was assigned to TiO_2 lattice oxygen. The values for these two components are in line with reference values reported for TiO_2 [157]. O_{lat} is found to shift to lower binding energies with increasing plasma treatment time. Following reduction and increasing concentration of Ti^{3+} defects, the resulting increased electron density on the oxygen sites are expected to result in a small decrease in the binding energy of oxygen core levels, as seen here.

Raman spectrum of the surface shows the characteristic peak structure arising from anatase/rutile phase mixture (Figure 5.3c). Interestingly, Raman bands of reduced TiO_2 exhibit distinct broadening and a 2 cm^{-1} blueshift of anatase E_g band from 141.7 cm^{-1} to 143.7 cm^{-1}. This has previously been reported in literature as an indicator of oxygen

vacancies in the anatase structure [160] in line with the observation of Ti^{3+} defect states seen in XP spectra. Annealing the surface in air heals the TiO_2 surface with complete reversal of the coloration and recovery of the original XPS and Raman spectra.

5.3.3 SnO_2

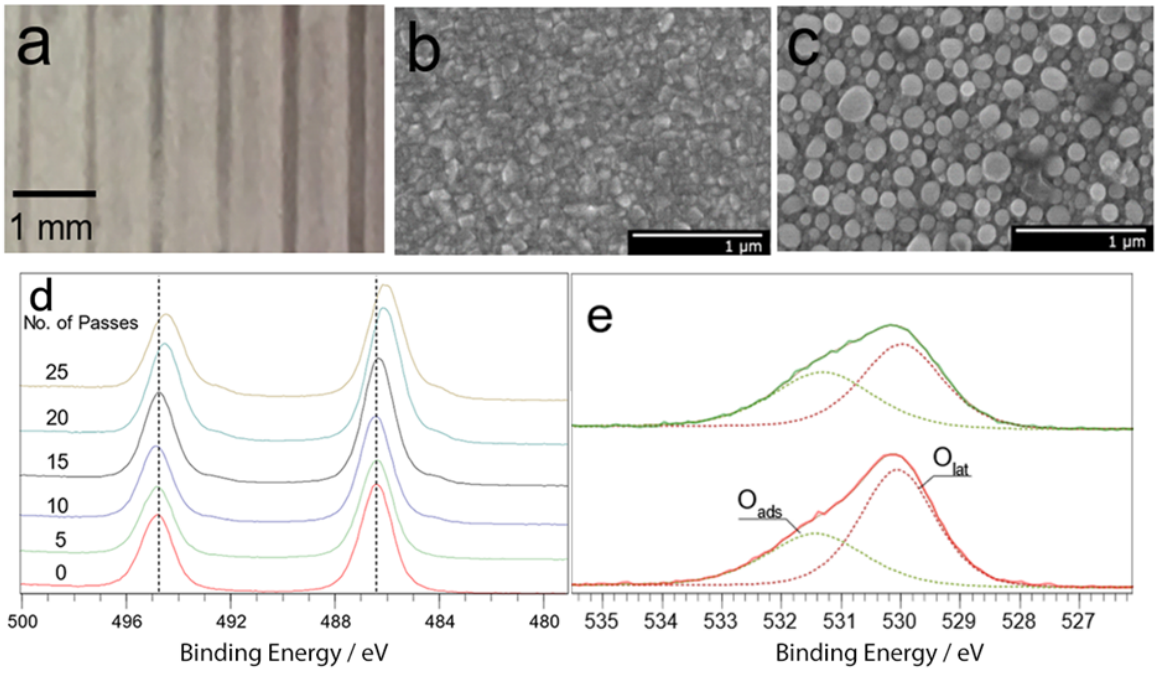

Fig. 5.5 Photograph showing the darkened *Sn* rich traces created by the plasma jet on the SnO_2 surface (a). Scanning electron micrographs of the pristine SnO_2 surface (b) and the same surface after 25 passes of the plasma jet (c). High resolution X-ray photoelectron spectra of the *Sn* 3*d* region acquired after different plasma treatment durations (d). High resolution XP spectra of the O 1*s* region for the pristine film and after 25 passes of the plasma jet(e).

Plasma treated SnO_2 films showed a distinct change in appearance, turning opaque and brown in colour (Figure 5.5a). This change in appearance depends on the overall plasma treatment time, with increasing opacity observed with increasing number of passes over the substrate. Electron micrographs of the surface, Figure 5.5b-c, suggest that the likely reason behind this change in optical properties is the evolution of *Sn beads* on the surface. Formation of these beads were later reproduced following publication of these results [161] by Sasaki et al. [162]. The reduction of the SnO_2 surface took place in a similar manner with and without hydrogen admixture in the plasma gas, results here are shown for the H_2 added case only.

The $Sn\ 3d_{3/2}$ and $Sn\ 3d_{5/2}$ peaks show significant changes in both position and FWHM, as shown in Figure 5.5d as the number of plasma passes increases. This peak position shift and broadening was attributed to the presence of sub-oxides and Sn metal on the surface. The O $1s$ spectrum (5.5e) is composed of two peaks positioned around 530 and 531.5 eV, assigned to SnO_x lattice oxygen (O_{lat}) and surface adsorbed oxygen (O_{ads}) respectively. O_{ads} is composed of contributions arising from surface contaminants in the form of $O-C$ containing contaminants and surface bound OH groups. Lattice oxygen peak for the pristine surface is at 530.1 eV with a FWHM of 1.5 eV. Plasma treatment was found to cause a decrease in the binding energy of O_{lat} by approximately 0.3 eV and cause a 0.2 eV increase in peak FWHM after 25 passes of the plasma jet over the surface. The shift in O_{lat} is indicative of the presence of sub oxides of SnO_2 and is caused by increased electron density on the oxygen sites due to reduction, as previously described for the TiO_2 case.

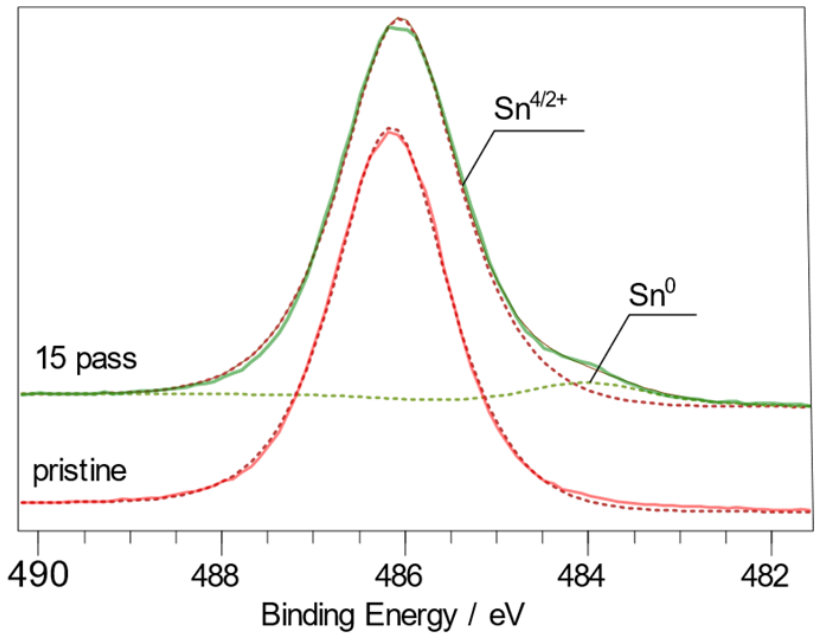

Fig. 5.6 High resolution Sn 3d X-ray photoelectron spectra for the pristine and plasma treated samples, showing the emergence of a new spectral component assigned to Sn0.

The deconvolved Sn $3d_{5/2}$ spectra in Figure 5.6 show that the plasma treatment results in the appearance of two major photoelectron peaks at 486.1 and 484.2 eV. These peak positions are consistent with literature values [163] and can be assigned to SnO_2 and Sn species, respectively [90]. The evolution of Sn on the surface confirms that Sn^{4+} was reduced to Sn upon plasma exposure. It is important to note that presence of any tin sub-oxide such as SnO and could not be confirmed via XPS. As SEM images 5.5e indicate Sn in the form of

nano-beads, it is possible that reduction follows a pathway such as:

$$2SnO_2 \xrightarrow[\text{reduction}]{} 2SnO + O_2 \xrightarrow[\text{disproportionation}]{} Sn^0 + SnO_2 + O_2$$

This process would explain the appearance of the spherical morphology, as Giefers and co-workers have shown [164], the disproportionation of SnO is not homogenous but rather follows a nucleation and growth mechanism which could lead to the unusual morphology observed.

5.3.4 WO_3

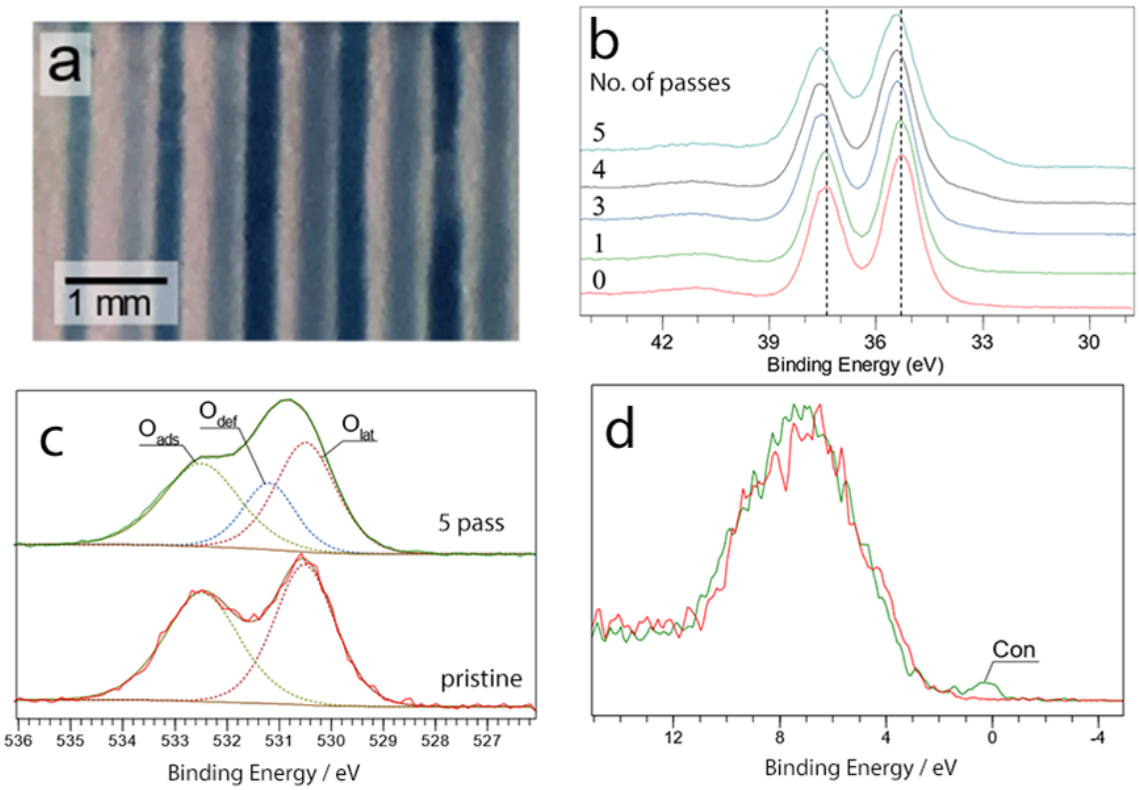

Fig. 5.7 Photograph of the blue, reduced WO_3 traces on transparent WO_3 created via plasma jet reduction (a). High resolution XP spectra in the W $4f$ region at increasing number of plasma jet passes (b). High resolution XP spectra in the O $1s$ region for the pristine and treated WO_3 film indicating the assigned spectral components (c). Valence band spectrum of pristine (red) and treated (green) WO_3 film with a band at Fermi level, labelled *Con.*(d).

Transparent tungsten trioxide thin films showed a deep blue colouration indicating reduction of the WO_3 surface upon treatment with hydrogen doped plasma, shown in Figure 5.7a. This

blue colouration is due to reduction of the W^{6+} into lower oxidation states [165]. Reduction takes place under hydrogen doped plasma only, and no evidence of reduction was observed under pure He. The high resolution $W\ 4f$ XP spectrum (Figure 5.7b) of the treated and untreated spots display two main features attributed to $W\ 4f_{7/2}$ and $W\ 4f_{5/2}$ spin orbit coupled states located at 35.5 and 37.8 eV for the pristine films [166, 167]. Low FWHM value of the $4f_{7/2}$ peak for the pristine film $(0.99 - 1.02\ eV)$ can be seen as an indicator of high crystallinity of the films [167]. As the plasma jet is repeatedly scanned across the surface, XPS peaks are broadened and a second set of peaks appear beyond 4 passes over the surface, shown in Figure 5.8.

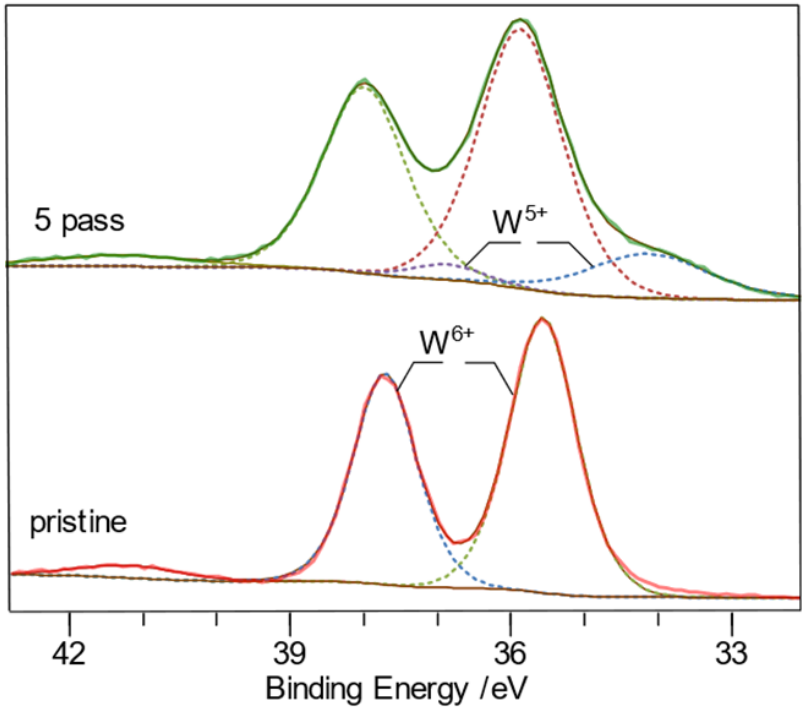

Fig. 5.8 High resolution XP spectra collected from the $W\ 4f$ region showing the spectral components for the pristine and treated films.

The $O\ 1s$ spectrum for the treated and untreated WO_3 surfaces (figure 5.7c) two main peaks at 530.5 and 532.6 eV. These peaks have been attributed to oxygen in the WO_3 lattice (O_{lat}) and the surface adsorbed species (O_{ads}) based on literature values [166, 168]. Upon treatment, a third peak (O_{def}) is detected in the deconvolved spectrum, situated at 531.2 eV. This peak may be attributed to oxygen present in the oxygen deficient regions of the WO_3 lattice.

In the plasma treated region shown in Figure 5.8, the main $W^{6+}\ 4f_{7/2}$ peak is shifted from

35.6 to 35.9 eV after 10 passes of the plasma jet. Two additional peaks become discernible at 34.1 and 36.9 eV, assigned to the W^{5+} oxidation state. Similar changes to the surface have also been reported after both Ar^{+} ion bombardment [167] and electrochemical reduction of WO_3 [169]. A new peak (labelled *Con.* in Figure 5.7e) near the Fermi level appears in the XP valence band spectrum of the sample after plasma exposure. Formation of this conduction band has been attributed to occupation of the W $5d$ band in tungsten oxide [170]. As shown in Figure 5.8, W^{5+} is present alongside W^{6+} in the film after plasma reduction, residual $5d$ electrons originating in the W^{5+} centres can therefore appear in the previously empty conduction band of WO_3. After 5 passes of the plasma jet, the relative atomic abundance of these two species are 79 and 21% for W^{6+} and W^{5+} respectively, suggesting a large sub-oxide presence.

5.3.5 ZnO

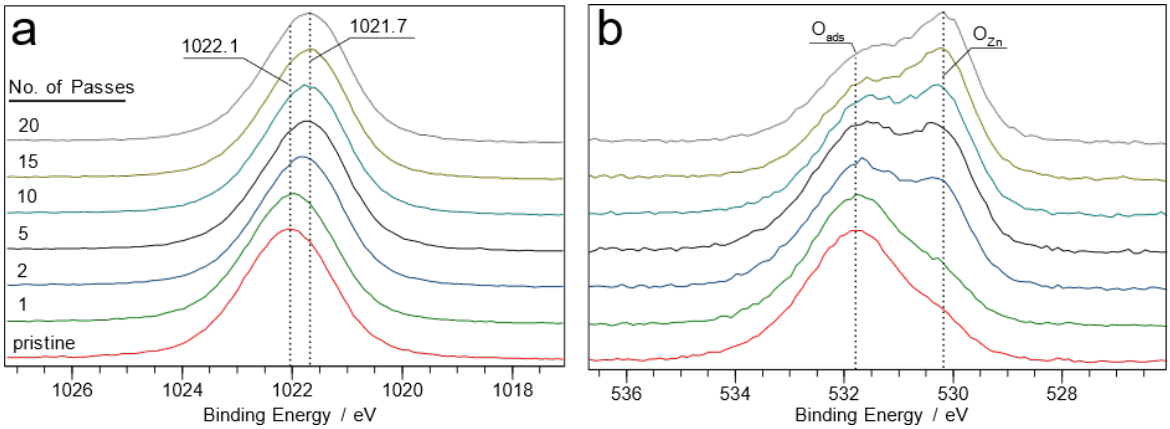

Fig. 5.9 High resolution Zn $2p$ (a) and O $1s$ (b) XP spectra obtained from the films after increasing number of passes of the plasma jet over the surface.

Plasma treated zinc oxide thin films show potential signs of reduction following exposure to H_2 doped plasma, however, in this case the films remain transparent and colourless. High resolution Zn $2p$ XP spectra taken from surfaces exposed to plasma for different durations show a peak shift of approximately 0.4 eV from 1022.0 eV (for pristine ZnO) to 1021.7 eV, as shown in Figure 5.9a. There is also a concurrent decrease of peak FWHM from 1.89 eV to 1.78 eV after 20 passes of the plasma jet over the surface. The O $1s$ spectra (Figure 5.9b) taken from the same points show two major components situated at 530.5 and 531.7 eV attributed to ZnO lattice oxygen (O_{Zn}) and surface bound oxygen (O_{ads})[171]. With increasing number of plasma jet passes over the film, the O_{ads} to O_{Zn} ratio is found to decrease, a change which

was also observed for vacuum annealed ZnO films by Li et al. [172], attributed to emerging oxygen vacancies on the film surface.

A steady decrease in the O/Zn atomic ratio of the film surface is also observed following plasma exposure. This ratio drops from 1.2 in the pristine surface to 0.7 after 20 passes, indicating that plasma treated regions of the film contain sub-stoichiometric amounts of oxygen. Despite the evident oxygen deficiency, the *Zn LMM* Auger electron spectra (Figure 5.10) obtained from the treated surface does not show characteristic peaks arising from metallic zinc, suggesting that the plasma reduction of ZnO does not yield the parent metal (unlike SnO_2 and Cu_2O).

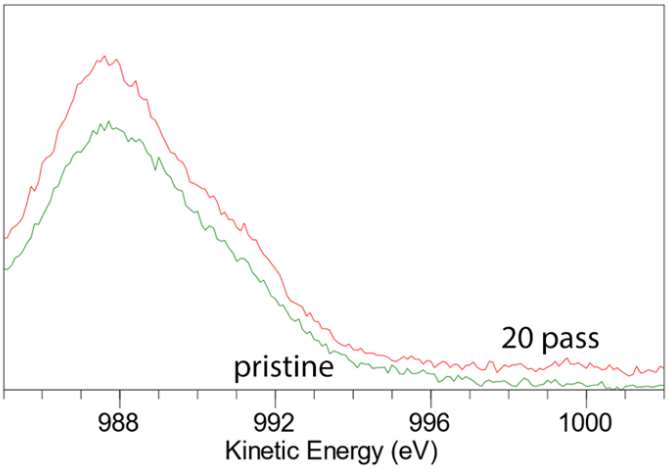

Fig. 5.10 Auger electron spectra obtained from pristine and plasma treated ZnO films.

5.4 Conclusions

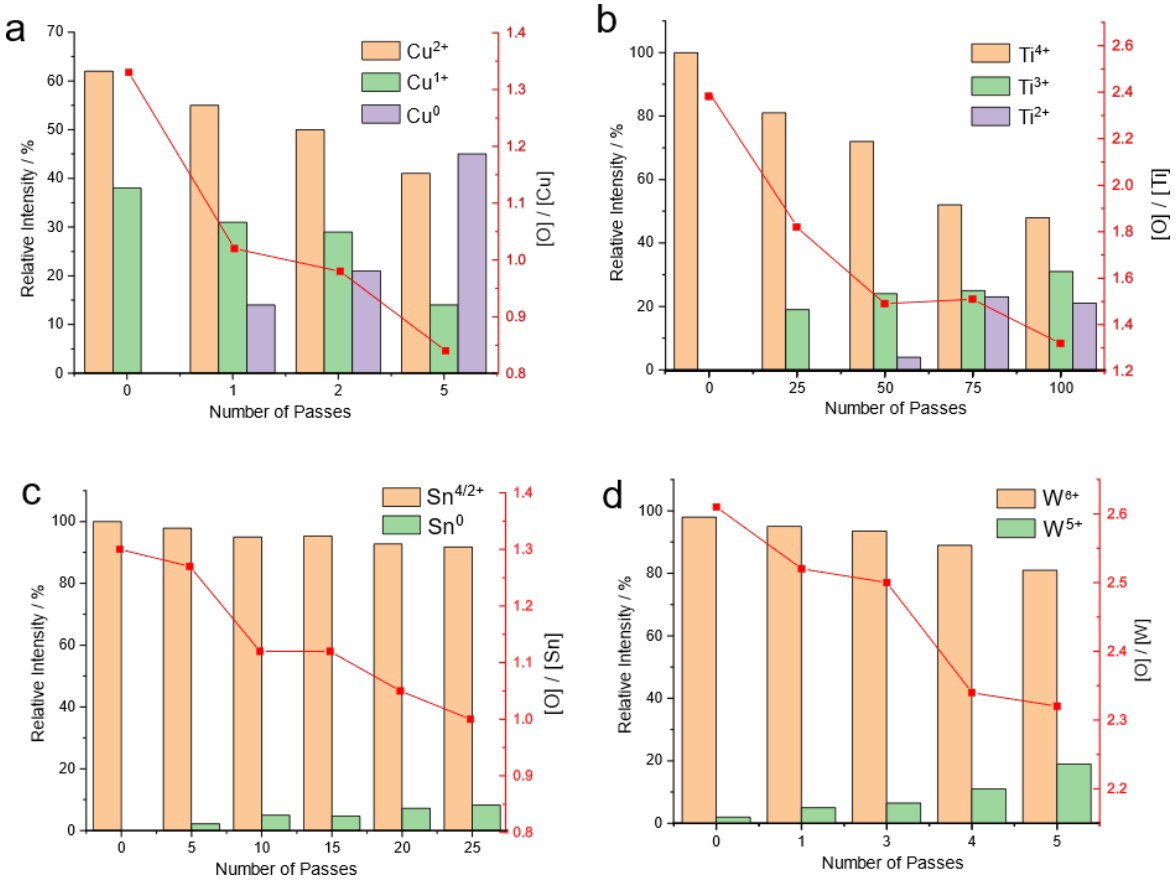

Fig. 5.11 Relative intensities of XP signals associated with different metal oxidation states for *Cu* (a),*Ti* (b), *Sn* (c), *W* (d) before and after different durations of plasma treatment. Relative atomic abundance of oxygen versus parent metal is given in red.

Here, it is shown that hydrogen doped helium atmospheric plasma jet was able to change the redox state of thin films of all of the metal oxides considered. except for *Sn* and *Cu*, reduction of the surface required addition of H_2 into the plasma gas. Figure 5.11 shows a plot of the relative abundances of different redox states as determined by XPS for the oxides considered. Copper (I) oxide was converted to zero valent metal, similar to the findings with the DBD set-up. In fact, after only five passes of the plasma jet over the substrate, amounting to a total of 5 second residence time on any part of the surface, surface composition was found to be composed of 39% $Cu(OH)_2/CuO$, 45% Cu and 16% Cu_2O, as shown in Figure 5.11a. Relative atomic concentrations of oxygen and copper on the surface agreed with these findings, exhibiting a significant drop in $[O]/[Cu]$ atomic ratio from 1.3 to 0.8 after plasma treatment. However, it is likely that the actual percentage of metallic copper is higher, as

the XPS analysis is dominated by the top few atomic layers that are liable to oxidize during handling. A significant portion of the detected oxide is native to the reduced copper surface under ambient air.

XPS studies for titanium dioxide treated with plasma show that the surface contained mixed oxidation states consisting of Ti^{4+}, Ti^{3+} and potentially Ti^{2+} species. For the purposes of analysis, a formal Ti^{2+} state was assumed in this chapter, but based on previous studies of Ti_2O_3 [159] and doped $d1$ titanium oxides[173] the Ti^{2+} peak can also be assigned to final state effects arising from a nominal Ti^{3+} state. Ti^{4+}, Ti^{3+} and Ti^{2+} proportions on the surface is calculated to be 46, 38 and 16%, respectively, after 100 passes of the plasma jet. This corresponds to a total residence time of the plasma jet of 1 min 40 s. This is a high level of redox conversion, especially considering that the plasma source is operated under near-ambient conditions.

Tin and tungsten oxides showed significant change in the oxide due to action of the plasma on the surface, as summarized in Figure 5.11c-d. In the case of tin oxide, metallic tin was detectable after 25 passes, whereas with tungsten, only W^{5+} could be identified via XPS. Similarly, the $[O]/[W]$ ratio on the surface calculated for the pristine and the 5 passes treated surface decreased from 2.6 to 2.3 upon treatment, indicating an oxygen deficient final structure.

The mechanism for this plasma mediated reduction is uncertain at this point and requires further attention. It may be suggested that the reduction pathways for SnO_2 and Cu_2O are distinct from the reduction pathways for WO_3 and TiO_2, this is mainly based on the observation that the reduction of tin and copper oxides do not require hydrogen addition to the plasma stream. For hydrogen reduced samples, atomic hydrogen generated in the plasma plume likely acts as a strong reducing agent, this possibility is discussed further in the following chapter. One potential route suggested is as below:

$$MO_y + e^- \rightarrow [MO_y^-]^* + 2H \rightarrow MO_{y-x} + xH_2O \rightarrow\rightarrow M + yH_2O$$

For pure helium plasma reducible oxides, it is likely that an inelastic electron scattering mediated route is available as discussed previously. Electron beams [174, 175] and high energy synchrotron radiation [164] have both been shown to result in reduction of SnO_2 and Cu_2O under vacuum conditions in the absence of a chemical reducing agent. Exposure to a large dose of electrons originating from atmospheric pressure plasma may result in an analogous process.

In summary, it was unambiguously demonstrated that atmospheric plasma can be used reduce metal oxides for mask-less patterning or surface cleaning/modification applications.

Copper and tin oxides show complete reduction to zero valence metal, titanium, tungsten and zinc oxides form mixed oxides when exposed to the plasma. This technique can be used for introducing oxygen vacancies into numerous catalyst surfaces under ambient conditions, potentially enabling large scale continuous processing of semi-conducting oxides under ambient conditions.

Chapter 6

Plasma Reduced TiO_2 with Improved Catalytic Efficiency

6.1 Introduction

It was shown in Chapter 5 that atmospheric pressure plasma jets can be used to reduce a wide variety of metal oxides including titanium dioxide. In this chapter, the surface composition and catalytic properties of plasma jet reduced porous anatase surfaces are investigated, demonstrating a novel route to catalytically active, reduced TiO_2 formation.

Titanium dioxide is known to be an extremely robust and chemically stable oxide with free energy of formation $\approx -900\ kJ/mol$ [176]. Despite this apparent stability, it can exist in oxygen deficient, disordered forms, commonly known as *black* TiO_2 [177, 178]. Black TiO_2 has found broad applications across diverse fields such as catalysis, fuel cells, supercapacitors [179], microwave absorption [180], dye sensitised solar cells [181], water splitting [182] and environmental pollution removal [183]. This interest is mainly fuelled by black titania's ability to absorb broadband visible light unlike its parent compound, TiO_2 [184].

Visible light absorption of black titania suggests that inherent photocatalytic activity of TiO_2 may be improved under solar illumination by introduction of defects. This indeed is the case; as supported by several reports confirming that "black TiO2" compared to pristine white TiO_2 is a more efficient photocatalyst. However, the utility of this material is currently limited due to the harsh conditions needed to form black TiO_2, in relying on treatment of pre-synthesized TiO_2 with high pressure and/or temperature H_2 gas for durations ranging from 2 hours to 5 days [181, 182]. There is a need to develop more efficient and accessible methods of synthesis, to facilitate the rollout of this extremely promising material to the diverse promised applications.

A variety of methods using different reducing gases or working pressures and temperatures have been described for black TiO_2 synthesis. The initial report on this material first described it as a nanoparticle with a crystalline anatase core and a highly disordered, hydrogen-doped shell. It was produced after hydrogenation of anatase particles under 20-bar H2 atmosphere at 200 $^{\circ}C$ for 5 days [177], resulting in visible light absorption. Origin of broadband absorption in black TiO_2, ranging from UV to NIR, is object of current active research [185, 184].

Peculiar optical properties of black TiO_2 are thought to be stemming from band tail states induced by structural disorder. These states are expected to form a continuum [185], extending to and even overlapping with the conduction band edge [178]. Significant research effort is underway to understand the phenomena governing light absorption and photocatalytic performance of black TiO_2 and other reduced TiO_2 variants containing Ti^{3+} defects [184]. Despite this, it is not entirely clear whether all "black TiO2" reported in literature is the same material, significant differences in characteristics have been reported in literature based on the synthetic route. The role of hydrogen in the mechanism of defect formation is unclear and furthermore, not all reports of hydrogenation result in black TiO_2 [186, 187].

The presence and absence of Ti^{3+} species, oxygen vacancies, $Ti-OH$ and $Ti-H$ groups have all been reported for black titania [186, 187]. For almost all hydrogenation approaches, disordered structural features are observed near the surface of black TiO_2, with a general lattice contraction of the disordered layer, although expansion of the shell has also been reported [178]. The role of the disordered layer is still controversial and it is not clear how it participates in the photocatalytic properties of the material [177]. The structure-property landscape of black TiO_2 remains largely incomplete and it will undoubtedly be subject of further active research throughout this decade.

Considering the extreme conditions required for black titania synthesis, and significant dependence of material characteristics on the chosen synthetic route, a rapid, accessible, and controllable avenue to black titania formation is needed. Plasma processing can be a viable alternative to conventional hydrogenation approaches, dispensing the need for high pressure H_2. Islam et al. [188] have recently demonstrated H_2 plasma reduction of titania at 10 $Torr$ with 400 W H_2 plasma. Similarly, Yan et al.[92] have reported black titania synthesis through 3 kW inductively coupled H_2 plasma at 25 $Torr$ and Mohammedizadeh et al.[189] have demonstrated black TiO_2 synthesis via a hollow-cathode process. In all these reports it was found that the reduced titania showed enhanced photocatalytic activity compared to the parent compounds. It should be noted that a majority of existing studies have relied on powder forms of titania due to the incompatibility of most catalyst support substrates with

the high temperature processing conditions. In addition, vacuum or high-pressure hydrogen apparatus required for existing reduction pathways severely limits the application avenues for black titania.

Despite progress, no route to black titania films at atmospheric pressure and convenient substrate temperatures ($< 200\ ^{\circ}C$) have ever been reported. In this chapter, a rapid, atmospheric pressure plasma method is described for the reduction of titania films into black TiO_2 using a pulsed, hydrogen doped, helium atmospheric pressure plasma jet.

In the previous chapter, reduction capability of atmospheric pressure plasma jets on various metal oxides including mixed rutile-anatase TiO_2 was discussed. Here, a new method of reducing nano-porous catalytic anatase films on fluorine doped tin oxide (FTO) coated glass substrates is demonstrated, allowing large area processing of pre-deposited TiO_2 films at near-ambient conditions. The resulting oxygen deificent films are stable in air under ambient conditions. Owing to the high efficiency of atomic hydrogen generation in atmospheric pressure plasmas [190], a minimal concentration of hydrogen in the working gas is needed, eliminating the hazards associated with high pressure hydrogenation processes. The aim of this chapter is to investigate the effect of plasma treatment on photocatalytic activity of anatase films and relate this change to measured surface chemical and physical transformations due to plasma exposure.

6.2 Experimental

Experiments were conducted in a similar manner to Chapter 5. The plasma jet was used with admixture of hydrogen in the plasma gas to treat the TiO_2 surface. In this work, nano-porous anatase TiO_2 films were deposited onto a conductive FTO glass substrate to evaluate their photoelectrochemical performance. After treatment of a defined area on the electrodes for varying durations, plasma converted black TiO_2 was characterised using XPS, Raman and diffuse reflectance spectroscopy as described in Methods. Optical emission from the plasma was used to determine the jet temperature and understand the plasma gas composition during plasma treatment. Photocatalytic efficiencies of the resulting films were evaluated in a photoelectrochemical cell to establish a relationship between extent of reduction in the TiO_2 substrate and photocatalytic activity.

6.2.1 Sample Preperation

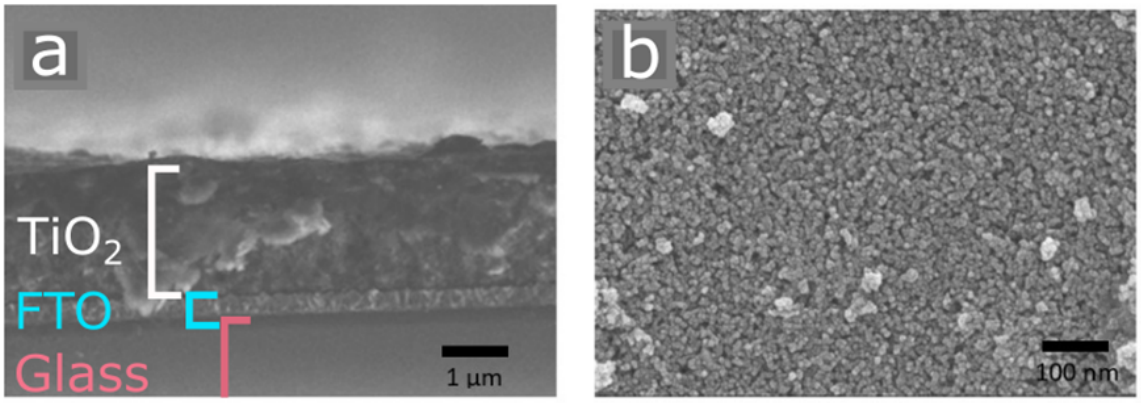

Fig. 6.1 Cross sectional scanning electron micrograph of the nanoporous catalyst supported on glass, conductive FTO layer is visible between the glass and the printed TiO_2 layers (a). Top down micrograph of the as-deposited catalyst.

TiO_2 electrodes used for experiments were screen-printed from nano-titania paste (Solaronix, Switzerland) onto fluorine doped tin oxide (FTO) coated glass substrates (Osilla Ltd., UK) and calcined at 550 $^{\circ}C$ for 1 hour in air. Film thickness of the as-deposited catalyst layers was measured to be $\approx 2.5\ \mu m$ via cross sectional SEM (Figure 6.1a). The particle size for individual TiO_2 grains were $20-30\ nm$ after calcination (Figure 6.1b).

6.2.2 Plasma Treatment

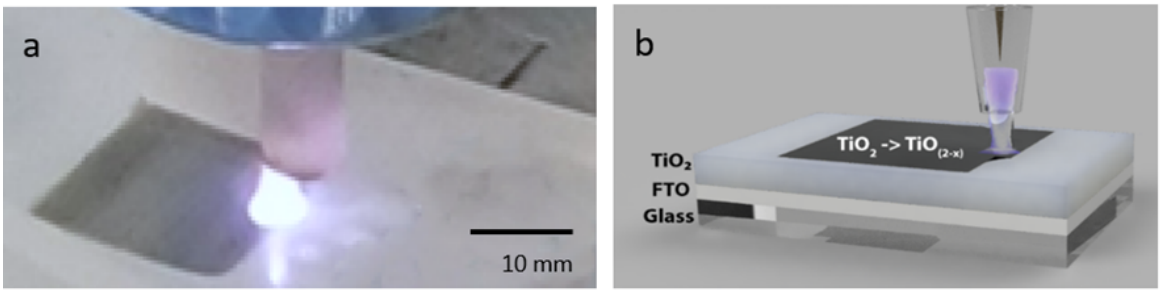

Fig. 6.2 Close-up photograph of the plasma jet impinging on the TiO_2 surface, with reduced TiO_2 appearing black on the white pristine anatase background (a). Computer generated image of the experimental process, showing the electrode layers and the impinging plasma (b).

A pulsed plasma jet (as described in Methods) was used for all experiments (Figure 6.2a-b). Plasma was generated at a tungsten wire electrode inserted coaxially into a capillary nozzle

with 1 *mm* diameter. The electrode is driven by the radio frequency generator operating at 13.56 MHz and 10 *W* forward power, the driving signal was pulse width modulated at 30 *kHz*, 15% duty cycle to minimise sample heating. The driving signal was passed through a matching network tuned to match the high impedance plasma load to the 50 Ω output of the generator.

Working gas mixture of helium and hydrogen (BOC, UK) at a hydrogen admixture of 5 *v.%* was then ignited between the electrode and the TiO_2 surface at a total flow rate of 3.4 *ml* $s-1$. To prepare the black titania photoelectrodes, surfaces of identically prepared titania films were scanned in a serpentine pattern with the plasma jet over a 10 $\times$ 10 *mm* area at constant input power. The rate of travel was fixed at 1 mms^{-1} and 20 traverse passes were required for full coverage of the treatment area.

6.2.3 Functional Characterisation

For photoelectrochemical current measurements, TiO_2 photoanodes were masked to expose a circular area of 28 mm^2 with opaque and inert masking material (3M Corporation, US). All measurements were conducted in a solution of 0.5 *M* Na_2SO_4 electrolyte (Aldritch, UK) with a saturated $Ag/AgCl$ reference electrode (BAS Instruments, USA) and high surface area platinum mesh (Advent, UK) counter electrode. Potentiostatic control was employed via a potentiostat (Autolab, UK) to keep the photoanodes biased at $+0.3$ *V vs.* $Ag/AgCl$ during measurements. For *UV* illumination, a 365 *nm UV* LED was used with power density of 30 *mW* cm^{-2} measured at the target. For illumination in the visible range, a 420 *nm* blue LED light source was used. The impinging light was diffused with a roughly ground quartz window to ensure even illumination across different experiments. All photoelectrodes were front-lit during measurements.

6.2.4 Photocurrent Response Simulation

Computer models present a convenient method of comparing the effects of changes in electron and hole transport rates in photocatalysts. In this work, simulated photocurrents were generated by solving a simplified system of equations based on the work of de Arajuo et al. [191] in Mathematica software [192].

The continuity expressions given below were used (Eqations 6.1 and 6.2) for electron and hole concentrations in a photocatalytic slab:

$$\frac{\partial n_e}{\partial t} = aI_0 + D_e \frac{\partial^2 n_e}{\partial^2 x} - k_{rec} n_e n_h \tag{6.1}$$

$$\frac{\partial n_h}{\partial t} = aI_0 + D_h \frac{\partial^2 n_h}{\partial^2 x} - k_{rec} n_e n_h - k_c n_h \tag{6.2}$$

In these equations, the concentrations of holes and electrons at a given time ($n_h(x,t)$, $n_e(x,t)$) in a one dimensional photocatalyst is given by four terms:

- the creation term aI_0 where I_0 is the incident light intensity and a is the photoconversion efficiency,
- the diffusion term $D_x \frac{\partial^2 n_x}{\partial^2 x}$ where D_x is the diffusion coefficient of x,
- the recombination term $k_{rec} n_e n_h$ where k_{rec} is the recombination rate of holes and electrons,
- and the reaction term $k_c n_h$ where holes are lost as they react with the electrolyte solution with rate constant k_c.

In this model $x = 0$ was taken to be the conductive oxide/titania interface which acts as an ideal electron sink. The thickness of the film (T_{film}) was taken as 2.5 μm, as measured. Only hole transport across the film/electrolyte interface was considered, with 0 electron flux from the electrode to the electrolyte. This gave the boundary conditions $n_e(0,t) = 0$ and similarly $\frac{\partial n_h}{\partial t}|_{x=0} = 0$ and $\frac{\partial n_e}{\partial t}|_{x=T_{film}} = 0$. In the time domain, the chopped illumination was represented as a square wave with a period 120 s and duty cycle of 50%, matching experimental conditions.

For comparing the effects of electron diffusion rates (D_e), the remaining coefficients were fixed at $I_0 = 2 \times 10^2$, $a = 10^5$, $D_h = 10^{-19}$ $m^2 s^{-1}$, $k_{rec} = 10^{-6}$ s^{-1}, $k_c = 0.2$ s^{-1}. These conditions qualitatively represent a system where hole loss to electrochemical reactions is fast compared to electron hole recombination [191]. Under these assumptions, the coupled equations 6.1-6.2 were solved for cases where the electron diffusion coefficient varied from $D_e \cong D_h$ to $D_e \gg D_h$.

6.3 Results and Discussion

Surface-reduced TiO_2 films were prepared by scanning of the plasma jet over the sample surface. The resulting samples are henceforth labelled as $H : TiO_2 - n$, with n indicating the number of passes of the plasma jet over the surface. Each pass corresponds to 2 seconds dwell time of the plasma jet per 1 mm^2.

During the plasma treatment, UV-Vis emission spectrum obtained from the jet plume (Figure 6.3) indicated that atomic hydrogen was being produced in the plasma alongside excited helium and nitrogen species.The major bands identifiable in the emission spectra were due to helium and nitrogen, entrained into the plume as the plasma jet exited the discharge capillary into atmospheric air. Temperature of the plasma gas was monitored by fitting synthetic spectra to the experimentally obtained spectra in the second positive system of N_2 using MassiveOES software [193]. Assuming that the vibrational and rotational states of N_2 are in partial local thermodynamic equilibrium at differing temperatures, the vibrational (T_{vib}) and rotational temperatures (T_{rot}) of N_2 were estimated to be 5500 ± 640 K and 520 ± 60 K respectively.

Due to short lifetimes of rotationally excited states, it is safe to assume that the gas temperature in the plasma plume is well approximated by the rotational temperature $T_{rot} = T_g$. It must also be borne in mind that optically determined T_g is closer to the peak temperature obtained in the plasma plume during the 20 % *on* period of the pulse modulated discharge. As optical spectra collection integrates light emission only while the discharge is active, 520 K represents an upper bound on the plasma jet temperature.

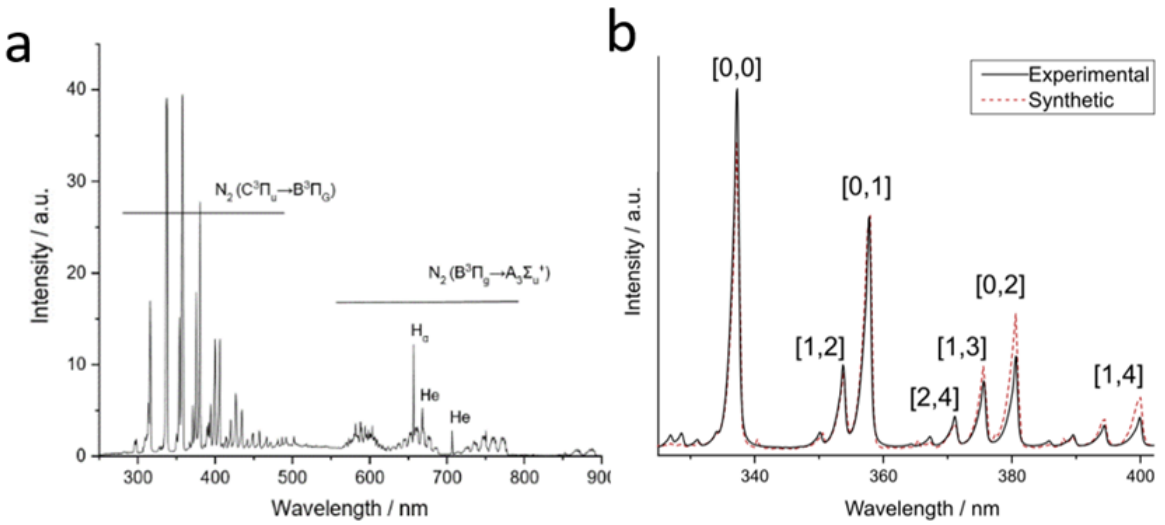

Fig. 6.3 UV-Vis emission spectra obtained from the plasma plume during surface treatment with major emission bands highlighted (a). Comparison of experimental and synthetic spectra for the nitrogen second positive system (b).

After non-thermal plasma treatment, films exposed to hydrogen plasma showed significant darkening, turning from white to deep blue/black (Figure 6.4). The colour change was concomitant with increasing broadband absorption across the visible range upon reduction of the films (Figure 6.4b). Similar to previous experiments with CVD deposited films,

colouration and optical properties of the films were stable for at least 6 months but could be completely reversed upon annealing at 500 $°C$ in air. In the absence of added hydrogen, no colour change was observed, and the films were left unchanged after plasma exposure.

In contrast to the sharp band-gap transition observed in the pristine sample, all plasma-treated samples showed an extended Urbach tail with markedly increased absorption around $400-450\ nm$, close to the bandgap energy. It should be noted that the optical band gap (E_g), estimated from Tauc plot analysis [194] (Figure 6.4c), did not shift significantly ($< 0.05\ eV$) compared to the pristine sample ($E_g = 3.34\ eV$). Therefore, significant optical band gap narrowing was not observed, in contrast to some literature reports on electronic properties of black titania [188, 195, 177]. It should be noted that plasma treatment is most effective on the surface of titania films and thus the effect of the reduction in optical properties is likely underestimated using bulk methods such as UV-Vis spectroscopy. Nevertheless, spectroscopy results showed significant changes in treated films compared to the pristine samples. Bulk resistivity measurements suggested that the impact of the plasma treatment was not insignificant in the bulk, as discussed below.

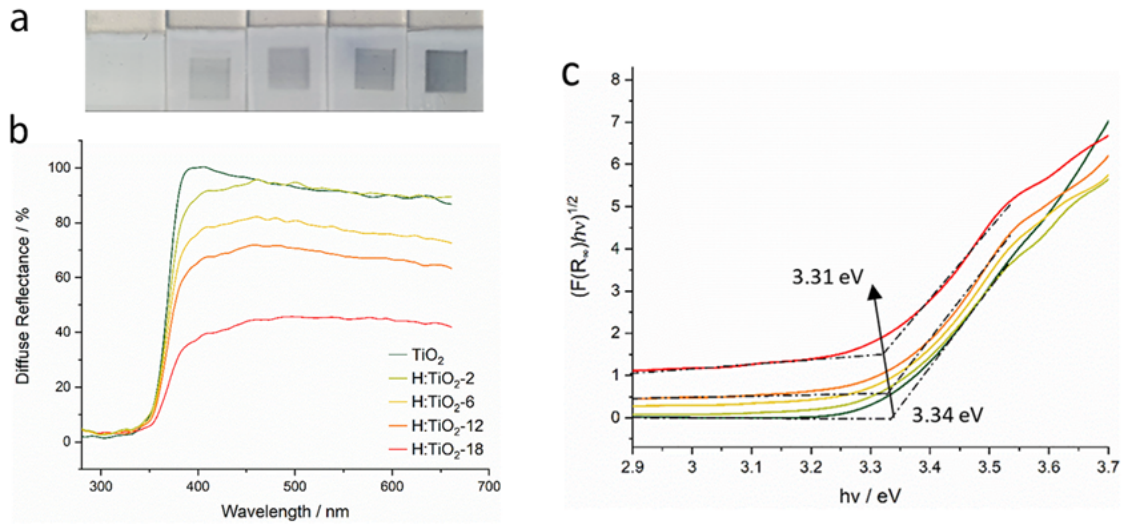

Fig. 6.4 Photographs pristine and treated samples with increasing levels of reduction, selectively reduced black regions are $10 \times 10\ mm$ (a) (from left to right, pristine TiO_2 and $H:TiO_2-n$ with n= 2, 6, 12, 18.). Diffuse reflectance spectrum of pristine (TiO_2) and plasma-treated ($H:TiO_2-n$) films upon increasing number of passes of the plasma jet (b), corresponding Tauc plots of the transformed Kubelka-Munk functions (c).

The surface energy of the reduced titania films was also qualitatively evaluated by measuring the contact angle of water droplets on the film surface. $H:TiO_2$ showed hydrophilic nature with a contact angles as low as $5 \pm 3°$ whereas pristine TiO_2 was more hydrophobic

(contact angle of $50 \pm 1°$). Photographs used for evaluating contact angles are provided in Figure 6.5. This observation is consistent with previous reports of reduced black titania films [188, 189]. Using proton nuclear magnetic resonance evidence, Wang et al. [93] have reported that hydrogenation increases bridging hydroxide group density on the surface TiO_2. Increasing the density of acidic bridging hydroxide groups ($pKa \approx 2.9$) on the titania surface should lead to evolution of a negative charge and increased hydrophilicity when in contact with water. This effect may also have a positive influence on the photocatalytic efficiency of water oxidation by promoting the interaction of water molecules with the catalyst surface.

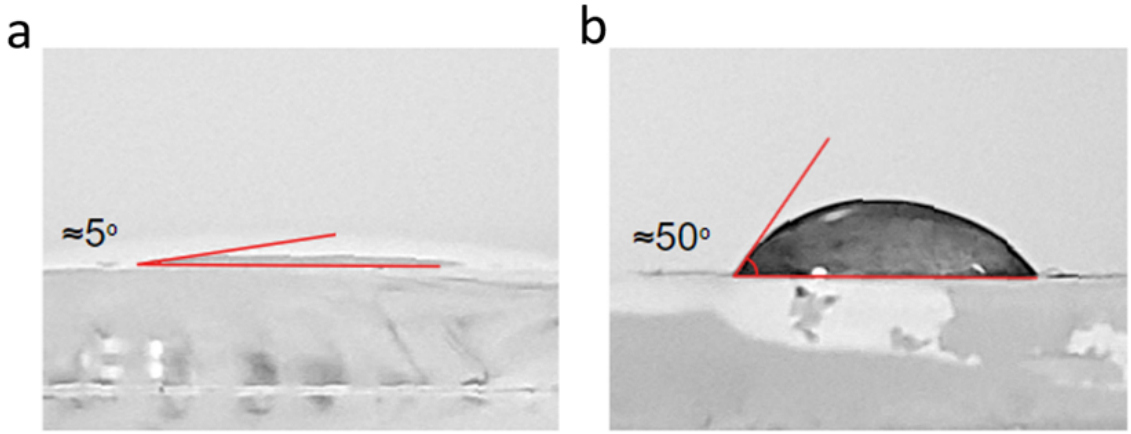

Fig. 6.5 Water drop contact angle for pristine TiO_2(a) and $H : TiO_2 - 12$ (b).

XPS analysis confirmed the gradual reduction of surface Ti_{4+} species upon increasing plasma exposure, as was also demonstrated in the previous chapter. Decomposition of XPS spectra in the Ti $2p$ region of pristine samples showed double peaks (1:2 ratio) due to Ti $2p_{1/2}$ and $2p_{3/2}$ spin orbit split states assigned to Ti^{4+} (Figure 6.6b). Plasma-treated samples showed the evolution of two additional broader peaks and the associated spin orbit split components. Based on previous studies of Ti_2O_3 and doped d*1* titanium oxides [159], the multiple peaks were assigned to a nominal Ti^{3+} state, with the corresponding multiple peak structure arising from final state effects.

Valence band spectra (Figure 6.6d) obtained from the highly reduced $H : TiO_2 - 18$ sample showed differences in band edge position and band tail with respect to pristine TiO_2. Valence band maxima of -2.1 and -2.3 eV were estimated from extrapolation of the linear portion of the corresponding band edges for pristine and black TiO_2 samples, respectively. The defect states in the plasma-treated samples formed an exponential tail extending towards the Fermi level, indicating the presence of additional mid-gap states above the valence band arising from self-doping with Ti^{3+}

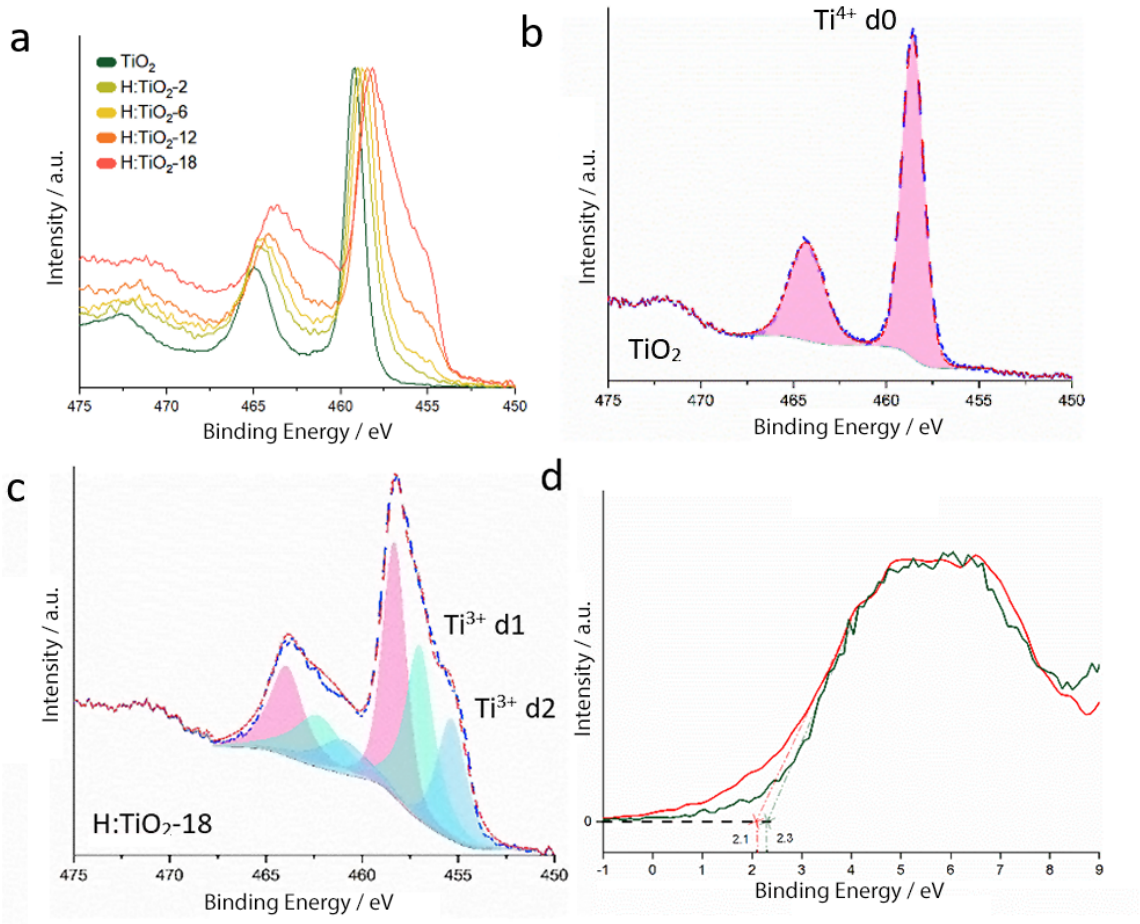

Fig. 6.6 High resolution Ti 2*p* XP spectra from pristine and increasingly plasma-treated reduced samples(a). Peak decomposition analysis of Ti 2*p* XP spectra is highlighted for pristine (b) and $H : TiO_2 - 18$ (c) samples. Corresponding valence bands of pristine (green line) and $H : TiO_2 - 18$ (red line) samples (d).

To further understand the changes induced by plasma exposure, Raman spectroscopy was used to probe the local structure of the treated TiO_2 films (Figure 6.7a). Raman spectra of the samples showed that, up to moderate reduction levels, the only bands visible could be attributed to anatase TiO_2 with Raman active modes at 142, 197, 399, 515 and 630 cm^{-1}. The band assignments based on literature [196] are provided in Figure 6.7b. Reduction led to an overall decrease in band intensity which, together with slight blue shift of the E_g mode at 142 cm^{-1}, suggests an induced short-range disorder upon plasma treatment (Figure 6.7b, inset). This blue shift has been previously attributed to the presence of oxygen vacancies [197, 198, 195]. Prolonged plasma treatment was followed by the appearance of new broad bands at 247 and 341 cm^{-1} in films with XPS determined surface Ti_{3+} content above $\approx 50\ at.\%$ (Figure 6.7b). These additional bands have been attributed to the emergence of a brookite phase and partial amorphization of the highly defective anatase surface with increasing defect density [177]. These observations are consistent with reported analyses of black TiO_2 and show that reduction of anatase leads to disruption of the crystal structure. It is worth noting that despite significant amorphization, at these low reduction temperatures, no anatase to rutile transformation is observed in Raman spectra as this phase change occurs at temperatures above 600 $^{\circ}C$ [199], far higher than the plasma effluent temperature.

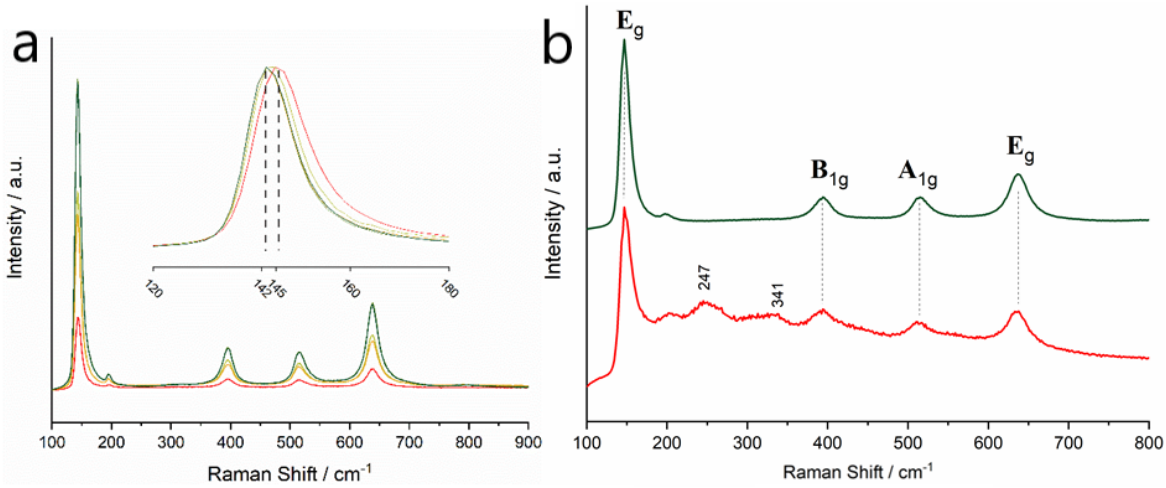

Fig. 6.7 Raman spectra of pristine and reduced TiO_2 samples (a). Inset: normalised E_g band region. Normalised spectra of a highly reduced sample compared to pristine TiO_2 (b).

Photocurrent density was measured under chopped illumination with UV ($\lambda = 365\ nm$) and visible ($\lambda = 420\ nm$) light. Measured photocurrents were higher for all plasma treated samples (Figure 6.8) compared to pristine TiO_2. Absolute photocurrent efficiency of plasma reduced samples increased up to six-fold compared to that of pristine TiO_2 under UV

illumination. Measured photocurrent densities did not follow a linear trend, however, and prolonged plasma treatment (beyond a residence time of 28 $s\ mm^{-2}$ or equivalently, 14 passes of the plasma jet) resulted in a decrease of photocurrent density compared to the maximum current density obtained.

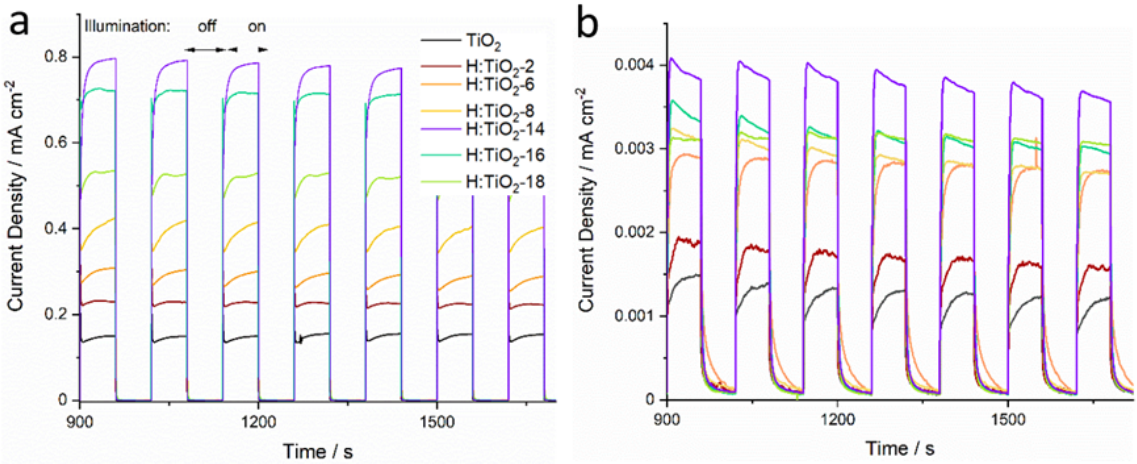

Fig. 6.8 Photocurrent density of prepared TiO_2 photoanodes under chopped illumination with 365 nm (b) and 420nm (b) light.

Surface $[Ti^{4+}]/[Ti^{3+}]$ ratio at maximum photocurrent density enhancement was around 0.45, as determined by XPS. This value likely represents an upper bound on the optimal bulk defect density since the XPS sampling depth is small ($\approx 5\ nm$) compared to the thickness of the film ($\approx 2500\ nm$). For the nano-porous films, it is unlikely that the $[Ti^{4+}]/[Ti^{3+}]$ ratio is homogenous across the bulk and the surface. It is worth noting that highly reduced samples that showed significant disruption of the anatase phase and additional Raman bands appearing (at 247 and 341 cm^{-1}), resulted in lower photocurrent densities compared to the films with optimal defect density. This likely stems from the defects associated with the amorphous phase acting as charge recombination centres. This has been previously shown[191] to result in materials with poor photocatalytic efficiencies.

In contrast to some previous reports [200, 201], only weak enhancement of visible light activity is observed in the atmospheric pressure plasma reduced films (Figure 6.8b). If the band gap energy of anatase had reduced significantly upon reduction, a large relative increase of photocurrent density would be expected under near band-gap illumination. Under 2.95 eV (420 nm) light which is reasonably close to the optically determined band gap energy (3.34 eV), photocurrent enhancement ratios did not differ significantly from values obtained from super-band gap illumination experiments (Figure 6.8a). The reason behind observed

patterns of photocurrent enhancement is therefore likely independent of the changes to band gap energy.

Optical band-gap measurements and valence band XP spectra obtained from samples agree with the assessment that the band edge positions are not shifted to an extent that would cause appreciable visible light activity. Visible light absorption is most likely due to tail states above the valence band maximum (or conduction band minimum) that are formed due self-doping of TiO_2 with Ti^{3+}, yet holes stemming from these tail states do not have a large influence on the overall photocurrent efficiency. A possible explanation for this phenomenon has been brought forward by Wheeler et al. [202] proposing that electron hole pairs stemming from these tail states are liable to rapidly recombine in oxygen vacancy traps that lie beneath the conduction band. Therefore, increasing the number of available trap states results in an observable decrease in photocurrent efficiency for these electron-hole pairs.

The origin of increased catalytic efficiency and its relation to plasma induced Ti^{3+} states is not entirely clear. One stark change observed following plasma reduction is a large increase in conductivity with increasing defect density [203]. This was investigated further by both resistivity measurements and by considering the transient response of photocurrent in chopped light experiments. Using a highly simplified model of a porous photocatalyst, observed transient response profiles of the TiO_2 layers were fit to the calculated response profiles simulating photocurrent transients at increasing electron mobilities. The experimental and model results are provided in Figure 6.9a for comparison.

A significant change in the shape of the transient responses can be observed with increasing reduction of the film surface. This apparent change in response on exposure to light can be qualitatively explained by the two modes of induced photocurrent in the photoanode. The initial transient spike observed in the low mobility case corresponds to the photo-capacitive behaviour of the film as electron hole pairs are generated and electrons close to the FTO/TiO_2 interface rapidly diffuse across this junction, generating a fast current spike. Upon depletion of this narrow zone, the photocapacitive peak subsides. This is followed by a second current transient that corresponds to the catalytic reactions on the electrolyte facing surfaces. These oxidation reactions drive hole depletion in the bulk, and result in concurrent electron diffusion to the electrode.

In the cases where electron mobility is significantly increased, photogenerated electrons can be extracted from deeper within the film. This in-turn leads to a decrease in the overall electron-hole recombination rate and an increase in the overall reaction rate. As the electron extraction is not limited to just a shallow layer, as it is in the case with low electron mobility,

the initial photo-capacitive peak is suppressed and the photocurrent is hole consumption rate limited. Disregarding space-charge effects, photocurrents in the optimally doped samples increase continuously after illumination until they reach a plateau determined by the incident light intensity and the catalytic reaction rate. The observed behaviour closely matches the transient responses provided by the model.

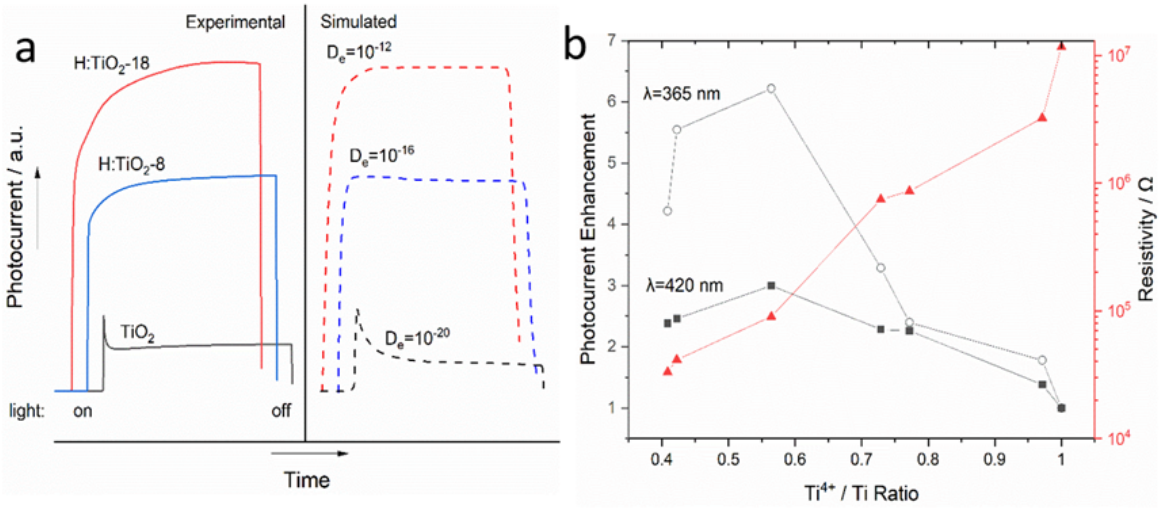

Fig. 6.9 Experimental and simulated photocurrent transients in pristine and selected reduced TiO_2 samples(a). Dependence of photocurrent enhancement ratio and conductivity as a function of defect density, given as the $[Ti^{4+}/Ti]$ ratio (b).

In an n-type semiconductor such as TiO_2, the conductivity of the film is proportional to both electron mobility and charge carrier (electron) density. In reduced films, a drastic drop in bulk resistivity is expected due to both increased carrier donor (Ti^{3+}) density and the predicted effect of increased electron mobility. Resistance measurements, as measured from the film surface to the FTO substrate, show that the resistivity of the highly reduced titania films are 3 orders of magnitude lower than that of pristine TiO_2. Therefore the conductivity of films are correlated with defect density *and* photocatalytic efficiency.

6.4 Conclusions

Atmospheric pressure plasma is shown to rapidly reduce TiO_2, providing a highly accessible approach to synthesis of black titania. The demonstrated reduction route overcomes the need for high pressure and high temperature treatment methods while at the same time avoiding costly vacuum equipment.

Reduced black titania films show superior photocatalytic efficiencies compared to as-deposited films. Measured photocurrent density is found to improve by a factor of up to 6 under both sub and super-bandgap illumination, which is attributed to improved conductivity due to the formation of Ti^{3+} defects. A saturation point is also found, where increasing Ti^{3+} content induces a *decrease* in photocurrent density. This was ascribed to an increase in the number of electron-hole recombination centres, or a transformation of the anatase into a catalytically inactive phase due to amorphization.

Contrary to literature reports of visible light activity and significant band gap narrowing in black TiO_2, it is seen that changes in optical absorption are mainly due to introduced band tail states while the overall band gap narrowing is negligible. As a result, plasma reduced black TiO_2 shows relatively improved, yet on the whole negligible visible light activity, despite intense broadband light absorption as shown by UV-Vis spectroscopy. This is supported by the weak photocurrent response obtained under visible light illumination.

Previous computational studies [204] of titania hydrogenation has shown that generation of Ti^{3+} with atomic hydrogen is thermodynamically favourable at relatively low temperatures both on the surface and subsurface regions. This is contrary to high activation energies predicted for the reaction with molecular H_2. Detection of atomic hydrogen emission in the plasma plume in the experiments, coupled with the fact that no reduction is observed in the absence of hydrogen suggest that plasma generated atomic hydrogen is responsible for the observed process.

The properties of the reduced titania obtained via the plasma jet route demonstrated here are comparable to those based on black titania generated using high temperature and vacuum methods even with conventional deposition techniques and substrates. Furthermore, using a low power plasma jet allows one to selectively pattern the catalytic surface coating and provide controllable levels of defect densities. This is an important step towards the promotion of black titania in a wider range of settings.

Chapter 7

Plasma Jet Direct Printing of Copper

7.1 Introduction

There has been a significant shift in electronics manufacturing techniques the last 20 years. With the explosive growth of electronics industry and the demand for connected electronic devices in many goods, embedded electronic circuits have become ubiquitous. Novel manufacturing techniques have enabled the integration of electronics into fields that range from wearable sensors [205] to embedded, miniature RF identification tags [206].

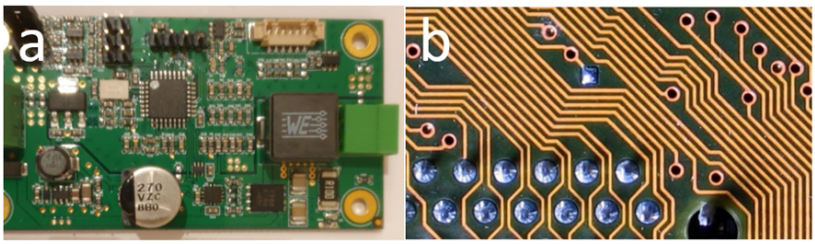

Fig. 7.1 Image of a conventional printed circuit board (PCB) with components soldered in place (a). Close up of copper interconnects that carry electrical signals and power in a PCB (b).

Current electronics manufacturing technology is largely limited to conventional subtractive methods [207]. Majority of electronic products including printed circuit boards, batteries [208] and photovoltaics [209] require conductive interconnects (an example shown in Figure 7.1) that are produced using masked lithographic techniques[210]. These approaches have numerous drawbacks due to both the use of wet-chemistry and the small selection of suitable substrates materials and geometries [207]. Conventional manufacturing methods require an initial lamination of a heat resistant dielectric substrate that primarily consists of

glass-reinforced epoxy, bound by copper foil on both sides. This requires machining and lamination processes. Next, chemical resists with designed circuit patterns are deposited on the copper foil via lithography. Finally, the exposed copper is removed by chemical etching to form the desired circuit traces. This multi-step subtractive manufacturing process outlined in Figure 7.2 is well known as an energy and chemical-intensive method, involving many waste products [211].

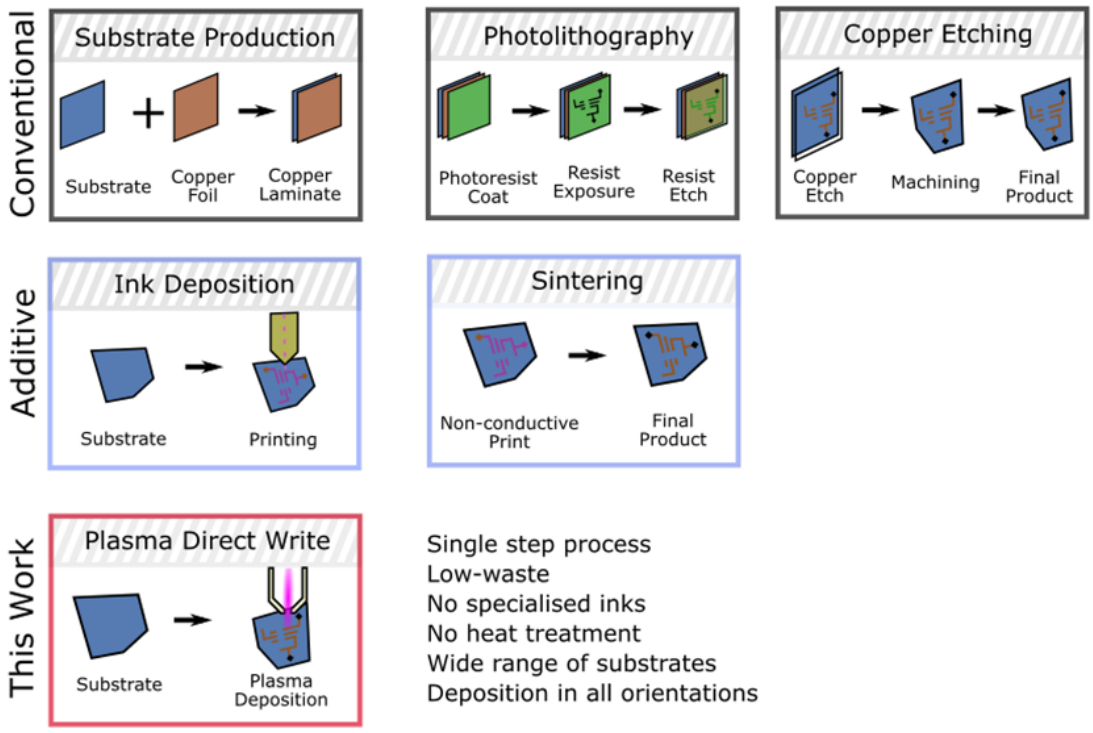

Fig. 7.2 Schematic comparing the key steps in conventional subtractive, additive and the proposed plasma jet assisted manufacturing processes.

Additive manufacturing (AM) methods have more recently come to the fore with significant effort devoted to the development of different forms of printing [212, 213]. These processes promise a significant decrease in the amount of waste generated alongside a wider spectrum of available substrate materials and shapes for housing electronic components. AM works via depositing the desired conductive material onto the substrate in a pre-defined geometry, forgoing inefficiencies in the masking and material removal steps (7.2) associated with subtractive methods.

Significant research effort is dedicated to printing technologies for conductive traces, mainly focused on developing existing methods such as digital printing [214, 215, 215]

followed by sintering [216, 217, 215]. Both laser metal sintering and inkjet printing approaches require the use of highly expensive nanoparticles or organometallic inks and a post-treatment process at elevated temperatures to achieve adhesion and high conductivity [216, 215].Furthermore, a majority of additive manufacturing methods are limited to relatively expensive silver precursors, with copper based alternatives[218, 219] still under development. There is a growing need for new ink formulations or sintering methods that can enable widespread adoption of AM techniques in electronics manufacturing.

So far, atmospheric pressure plasma based additive manufacturing methods have been explored as a viable AM avenue by researchers as discussed in Chapter 1. These methods, although promising, rely either on high temperature, inefficient sputtering phenomena [115, 108, 116] or pre-synthesized nano-particulate inks [109, 112]. These characteristics have so far made plasma-jet printing methods largely unsuitable for manufacturing needs.

This chapter demonstrates a newly developed technique for direct printing of copper traces onto a wide variety of substrates. This proposed method is single-step and does not require post or pre-processing of the print substrate, showing significant advantages over existing methods (Figure 7.2). A micro-plasma jet operated with helium and hydrogen is used to decompose copper ion containing aerosols into mixed copper/copper oxide nanoparticles within the plasma plume. The resulting mixed copper oxide – hydroxide layers are simultaneously reduced and sintered in-situ with the plasma jet, resulting in the generation of conductive copper films on the target surface at low temperatures. The printing technique can be seen as an application of the plasma jet reduction processed previously described in chapters 4 and 5. By varying the print duration, thickness of the film can be controlled, and by translating the plasma jet over the surface, conductive interconnects can be printed.

A number of experiments were conducted to understand the mechanisms behind the newly developed deposition technique. Using SEM imaging and computational fluid dynamics, it was discovered that hollow nanoparticles were generated in the plasma plume from aerosol droplets. The deposition mechanism was also shown to rely on physical impaction of the aerosol. Effects of precursor concentration and plasma gas composition were studied to understand the chemical process behind precursor conversion into metallic copper, showing that plasma jet deposition of copper is a two-stage process beginning with an initial oxide rich deposition phase followed by in-situ reduction to conductive copper.

7.2 Experimental

The plasma jet apparatus as described in Section 2.2.2 was used for deposition of copper onto substrates during experiments. Chemical composition of the resulting films was analysed using Raman and X-ray photoelectron spectroscopy. Scanning electron microscopy and stylus profilometry was used to characterise the morphology of the films after deposition.

Minor modifications were made to the plasma jet apparatus previously described in methods and experimental set-up, the RF generator output ($\approx 15W$) was pulsed at a rate of 20 kHz, with a duty cycle of 20%. Copper containing precursor solutions were introduced in aerosol form and the nozzle assembly of the plasma jet was also modified to optimise the deposition process as discussed in the following sections. Ansys FLUENT [220] computational fluid dynamics (CFD) software suite was used to probe and optimise the multi-phase flow characteristics of the nozzle and compare the results to the experimentally observed behaviour of the plasma deposition apparatus. Details of the CFD approach are presented in Appendix B.

7.2.1 Precursor Introduction

Precursor metal salt solutions were introduced as a fine aerosol into the plasma jet stream. $CuSO_4 \cdot 5H_2O$ (Fluka, US) dissolved in ultrapure water (Milipore, UK) was used as the copper aerosol precursor. All gas flow was controlled via computerised mass flow controllers (Brooks, US) except for aerosol laden gasses which were controlled via manual rotameters (Brooks, US).

Aerosol was generated using coaxial nebulisation with a Type K1 (Meinhardt, US) concentric glass nebuliser. Precursor solution was fed through the nebuliser capillary at a rate of 3 $ml\ min^{-1}$, argon was used as the nebulising gas at a rate of 1 $L\ min^{-1}$. The resulting aerosol laden gas was passed through a large long-necked flask used as a mixing manifold to separate large droplets from the gas flow. Remaining aerosol was then divided into two streams. The aerosol generation set-up is shown diagrammatically in Figure 7.3.

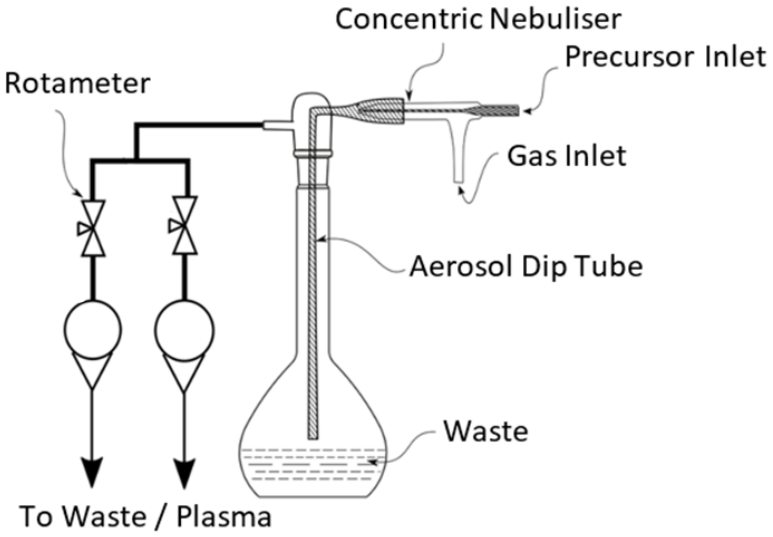

Fig. 7.3 Diagram of the aerosol introduction set-up.

The resulting copper salt laden gas was mixed with dry helium / hydrogen mixture in a manifold attached to the plasma nozzle. For the concentric nebulisation rig, the final volumetric gas composition consisted of 65% aerosol laden argon, 30% helium and 5% hydrogen. The overall volumetric flow rate through the nozzle was 350 $mL\ min^{-1}$.

7.2.2 Jet Nozzle

The plasma jet nozzle is the section of the deposition apparatus where the plasma is ignited, the precursor laden gas is converted into metal containing nanoparticles and transported to the substrate surface. The jet head consisted of a glass tube with a 0.05 *mm* diameter tungsten wire inserted centrally down the axis of the tube (Figure 7.4a-b). The length of tungsten wire inside the plasma head was insulated with glass save for 4 *mm* at the tip where the plasma is generated. The nozzle orifice (Figure 7.4d) was made of a pulled, ground and flame polished borosilicate glass capillary with a 1.9 *mm* diameter and 0.2 *mm* opening, inserted coaxially through a rubber septum over the wire within the glass tube. The electrode tip was placed to sit ≈ 0.1 *mm* above the orifice (Figure 7.4c).

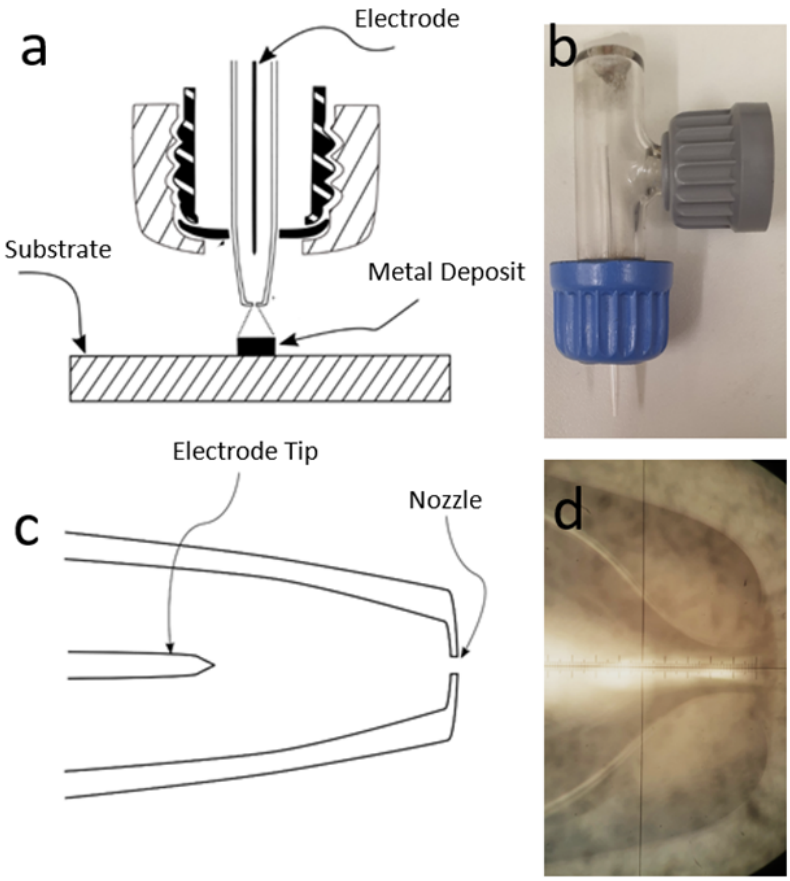

Fig. 7.4 Diagrammatic view (a) and photograph (b) of the plasma deposition nozzle. Diagram (c) and micrograph of the nozzle tip (d), showing the flame polished, rounded orifice.

7.2.3 Schileren Photography

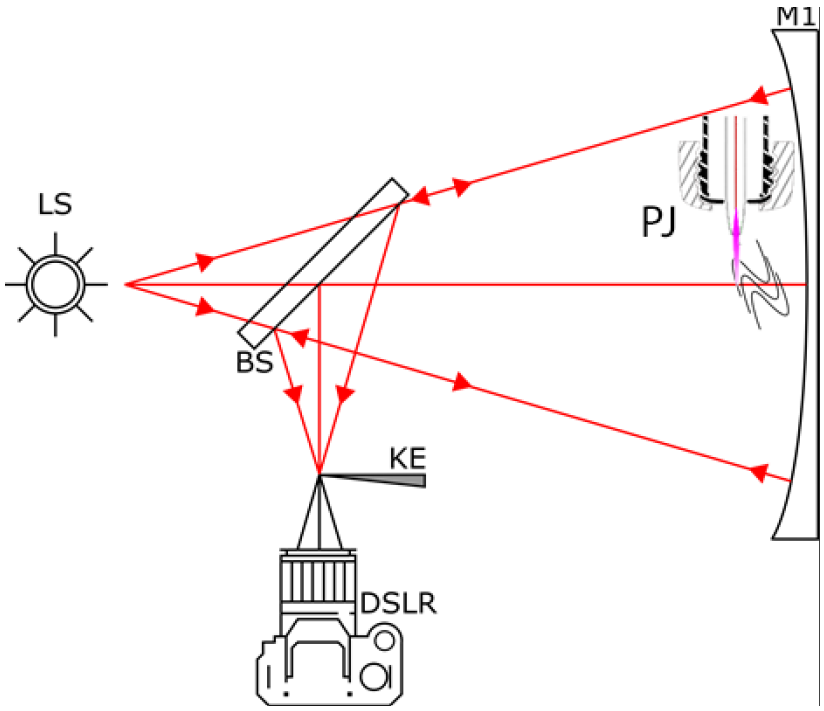

Fig. 7.5 Schematic diagram of the on-axis coincident Schlieren apparatus. LS - Light Source, BS - Beam Splitter, M1 - Mirror, PJ - Plasma Jet, KE - Knife Edge, DSLR – Camera.

Schileren photography is a technique that allows visualisation of small changes in refraction index that occur due to flow or optical medium composition [221]. In this work, a Schileren set-up consisting of a 108 mm parabolic mirror (Edmund Optics, US), LED light source (RS, UK), beam splitter (Thorlabs, Germany) and a condenser lens were used to image the outflow of gas through the plasma-jet during deposition conditions. A schematic diagram of the setup is given in Figure 7.5.

Light was collimated through a condenser lens and passed through an adjustable slit to obtain even illumination of the plasma jet. The beam-splitter was placed in the light path between the plasma nozzle and the slit. The light travelling towards the plasma jet was reflected from the parabolic mirror and the set-up was aligned to focus the reflected light back onto the slit.

A EOS 700D with a 100-400 mm f/4.5-5.6 zoom lens (Canon, Japan) was used to image the plasma jet through the beam-splitter. A knife edge was placed at the focus point of the light between the beam splitter and the camera lens. The knife edge was adjusted prior to imaging to obtain maximum contrast in the Schileren images.

7.2.4 Computational Fluid Dynamics

Computational fluid dynamics (CFD) was used to model the gas flow through the plasma jet nozzle and the flow characteristics of the plasma gas on the substrate surface. The resulting flow fields were used to simulate the injection of solid particles into the stream to better understand the deposition profile and the size selectivity of the plasma printing set-up. The details of the CFD approach are provided in Appendix B.

7.3 Results

On ignition of plasma and introduction of copper containing aerosol, a metallic deposit was rapidly formed over the deposition substrate. By moving the substrate underneath the plasma jet, the metallic deposit could be drawn into a linear and highly adherent, conductive trace. It was found that printing via this method is easily applicable to a wide range of substrates as shown in Figure 7.6. For the following experiments, borosilicate glass microscope slides were used as the deposition substrate. The choice of glass is significant due to its flat, rigid and inert surface which normally makes it difficult if not impossible to print onto using conventional techniques [222].

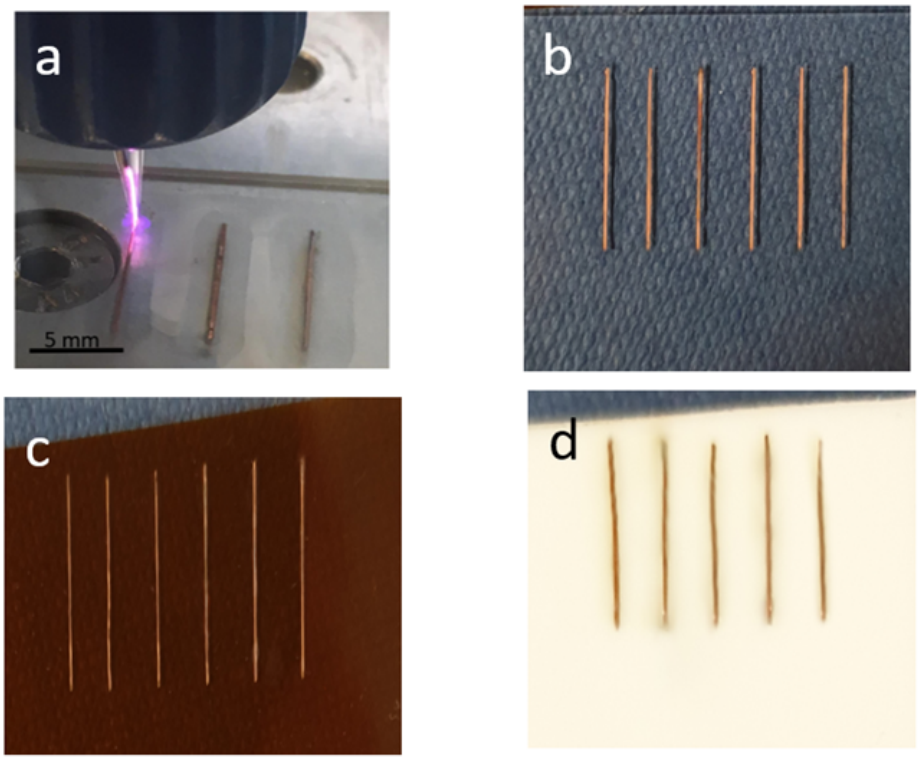

Fig. 7.6 Plasma jet during deposition onto glass substrate (a). Continuous copper traces directly printed onto glass (b), polyimide (c) and PTFE (d). All deposited lines are 10 mm in length and end-to-end conductive.

The conductive printing process requires three key steps to take place:

- transport of the copper containing particles onto the substrate,
- conversion of copper salt precursor into metallic copper via reducing plasma and,
- sintering and densification of the particulate copper layer into a continuous conductive layer.

All these aspects of the process will be discussed in the following sections in order, focusing on the role of plasma in the chemical conversion and sintering processes alongside mass and energy transport phenomena in the plasma plume.

7.3.1 Mass Transport and Deposit Morphology

One of the key questions in this newly developed direct write process is the mode of deposition and mass transfer onto the surface. Previous literature describing copper deposition has indicated that evaporation of copper in the plasma plume is a possibility [116]. Due to the

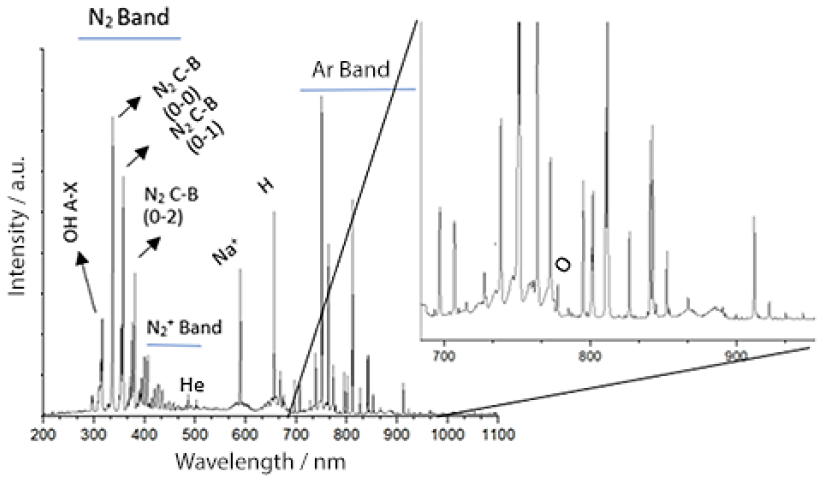

Fig. 7.7 Optical emission spectrum of the atmospheric pressure plasma jet showing the strong contributions originating from N_2 and Ar excited states. Magnified region highlights the line assigned to atomic oxygen at 775 *nm*.

low temperatures previously observed in the plasma plume (Section 6.3), it is highly unlikely that any gas phase copper species are present in the plasma. This is corroborated by optical emission spectroscopy.

The optical emission spectrum is complex reflecting the many contributions from both the working gas mixture and atmospheric species that are entrained into the jet as it exits into air. Above 700 *nm*, the spectrum is dominated by intense emission lines from Ar^+. Atomic oxygen (777 *and* 794 *nm*) and He^+ (728 *nm*) emission lines are also present in this range, as expected. Between 500 and 700 *nm*, hydrogen $H\alpha$ line (656 *nm*) and Na^+ D line (589 nm) are observed along with the nitrogen first negative system. The intense sodium line likely originates from impurities in the aerosol feedstock or emission from *Na* present in the borosilicate plasma nozzle [223]. Below 500 *nm* and into the UV region, the spectra are dominated by the first positive and the second positive systems of N_2. Within the captured range, the strong lines of *Cu I* at 325, 327, and 780 *nm* are not detectable. The emission line at 776 *nm* has been assigned to atomic oxygen rather than the *Cu II* line 780 *nm* [224], based on the total absence of *Cu I* species.

Unlike atmospheric pressure sputtering processes [116, 115] and vapour deposition [225] methods previously reported in literature, volatilisation of copper compounds is not observed under experimental conditions. Therefore the transport of metal mass to the surface occurs in the form of solid particles. One distinguishing feature of this aerosol-jet deposition process, as opposed to a gas phase mode of deposition, is the spatial resolution and selectivity offered by the fine micro-jet nozzle [226]. As the particles entrained in jet flow reach the surface,

copper containing aerosol is *impacted* onto the surface. Impaction involves deposition of particles above a certain aerodynamic radius onto a surface as the fluid streamlines rapidly diverge from perpendicular to parallel to the surface [176]. This process is depicted in Figure 7.8.

In contrast to gas phase transport where diffusion processes are dominant, aerodynamic impaction allows the print geometry to be easily controlled as the copper containing particles follow a near ballistic trajectory. This approach dispenses of the need for masking and vacuum equipment for selective metallisation of substrates.

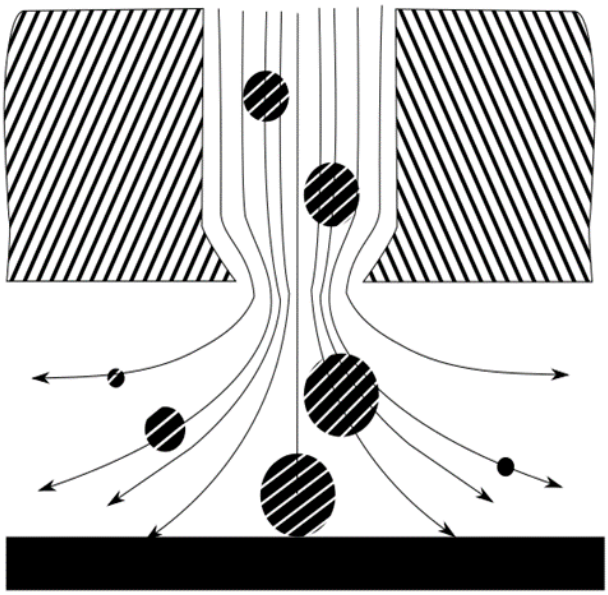

Fig. 7.8 Diagrammatic description of the impaction process from a nozzle (top) where large diameter particles entering from the top are captured on the surface (bottom) and the small particles are lost via the diverging wall jet.

To understand the transport of particles within the plume, computational fluid dynamic models were used to probe flow and particle transport within the jet plume during deposition. With an orifice radius of 0.4 *mm*, and nozzle to substrate distance of 0.5 *mm* (reflecting the experimental set-up), the flow profile in Figure 7.9 shows the clear development of a wide triangular stagnation zone right below the nozzle orifice, extending to the width of the nozzle. At a volumetric flow rate of 0.35 $L\ min^{-1}$ the jet is accelerated from around 3 $m\ s^{-1}$ in the nozzle body to up to 10 m/s in a *wall-jet* parallel to the substrate. A clearly developed 80 μm thick viscous boundary layer is also present in the simulation, between the substrate surface

and the wall-jet.

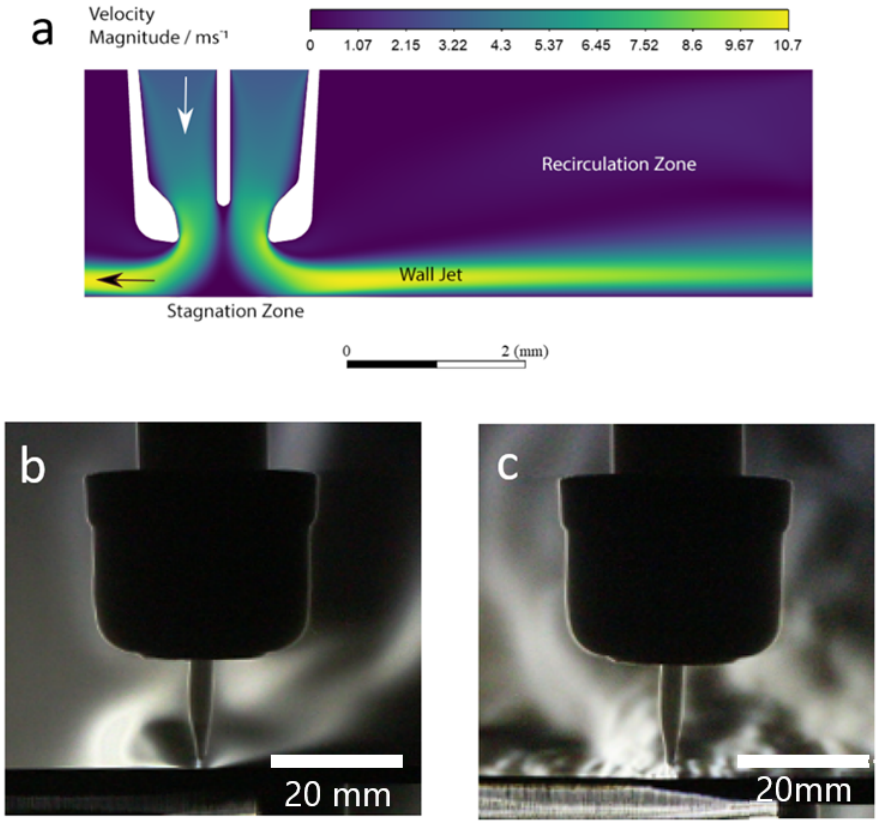

Fig. 7.9 Simulated velocity contours of the plasma jet gas flow, showing the development of a fast-moving laminar wall jet (a). Schileren photographs of the jet with 0.35 (b) and 1.5 (c) $dm^3\ min^{-1}$ volumetric flow through the nozzle, showing the effect of induced turbulence at high flow rates.

The flow profile observed in the CFD simulations are unsurprising as the mass flow rate through the jet is relatively small. The Reynolds number for the flow is 230, given by $R_e = uD_h/v_{arg}$ where u, the mean velocity of the gas is 2.1 $m\ s^{-1}$, flowing down the capillary with hydraulic diameter $D_h = 1.9\ mm$ and the kinematic viscosity of the majority component of the flow, is $v_{arg} = 1.69 \times 10^{-4}\ m^2\ s^{-1}$[227]. Analogously, the wall jet Reynolds number with reference length equal to nozzle height provides a R_e value of approximately 700. At these R_e values where $R_e << 2000$, the flow is predicted to be laminar [228]. The wall jet adheres to the substrate with minimal induced turbulence apart from some weak recirculation above this jet layer.

The laminar flow profile obtained via CFD models is confirmed using Schileren imaging. This imaging technique allows for the visualisation of minute refractive index differences in

the plane of focus of the imaging apparatus[229]. Figure 7.9b shows the thin laminar wall-jet beneath the jet orifice under deposition conditions. To the right of the nozzle, the expanding wall jet and above it, the recirculation zone is visible. Effect of increasing flow rate on the development of turbulence is clearly seen in Figure 7.9.

Impaction of particles relies on sharply diverging fluid streamlines above the substrate surface therefore turbulent flow is detrimental to mass transport from the plasma jet to the substrate. Using Schlieren imaging, it is concluded that the mass flow rate to nozzle diameter ratio must be kept below approximately 0.1 $m^2\ s^{-1}$ to achieve controllable impaction and minimise entrained air within the plasma plume.

Introduction of particles into this laminar jet flow leads to particle impaction onto the surface, as discussed previously. The size of particles that can be collected via this impaction process is predictable and is described by the Stokes number STK given by equation 7.1 [230].

$$\mathrm{STK} = \frac{4Qc\rho d^2}{9\pi\mu W^3} \tag{7.1}$$

Where, Q is volumetric flow rate through the nozzle, c is the Cunningham slip factor [231] for the particle diameter, ρ and d are particle density and diameter respectively, μ is gas viscosity and W is the orifice diameter.

.This shows that STK is proportional to the square of particle diameter (d^2) , and therefore $\sqrt{STK}$ governs the behaviour of the particles that can be collected on the substrate during printing. The value of $\sqrt{STK}$ that results in 50% collection efficiency has been estimated to be around 0.65 for similar nozzle geometries [232, 233]. Calculating the value of $\sqrt{STK}$ as a function of particle size and density illustrates that the range of particles with this experimental geometry is limited to around above 1 μm diameter under ideal conditions.

The cut-off values depend greatly on both the aerosol density and the particle fill factor. If the particles in the plasma plume are composed of fully dense copper, the cut-off diameter (da_{50}) is 700 nm, whereas for a 50% porous $CuSO_4$ particle, this cut-off value lies above 2 μm. A contour plot of calculated cut-off diameter as a function of particle density is shown in Figure 7.10, densities of the experimentally relevant species are provided on the plot to aid comparison.

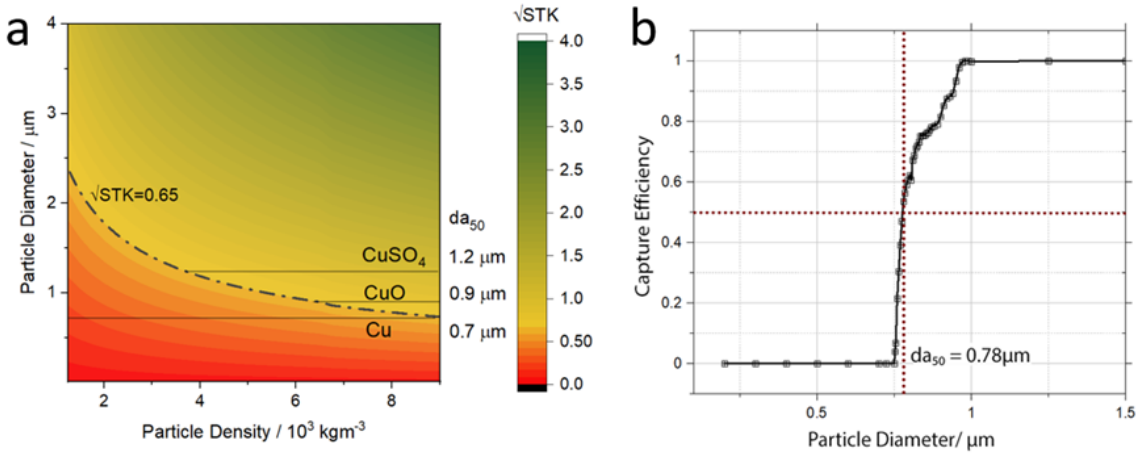

Fig. 7.10 Contour plot of $\sqrt{STK}$ as a function of particle diameter and particle density, highlighting the da_{50} values for experimentally relevant species (a), simulated particle capture efficiency for the plasma jet apparatus obtained via random particle injection into the flow (b).

While Stokes number analysis only provides information on the ideal case, specific geometry and flow characteristics of the experimental set-up are better reflected in the CFD domain. Therefore, particle tracking was done using the solved and converged flow profile by uniformly injecting massive particles into the stream through the nozzle inlet and tracking the movement of the particles till they were all captured or lost in the outlet flow. This process is shown diagrammatically in Figure 7.11a and discussed in further detail in Appendix B.

Fraction of particles deposited from the plume to the surface as a function of particle diameter is given in Figure 7.10b. It is found that Stokes number analysis and the CFD simulation agree quite well in the case of copper particles with resulting da_{50} values of 710 and 780 *nm* respectively.

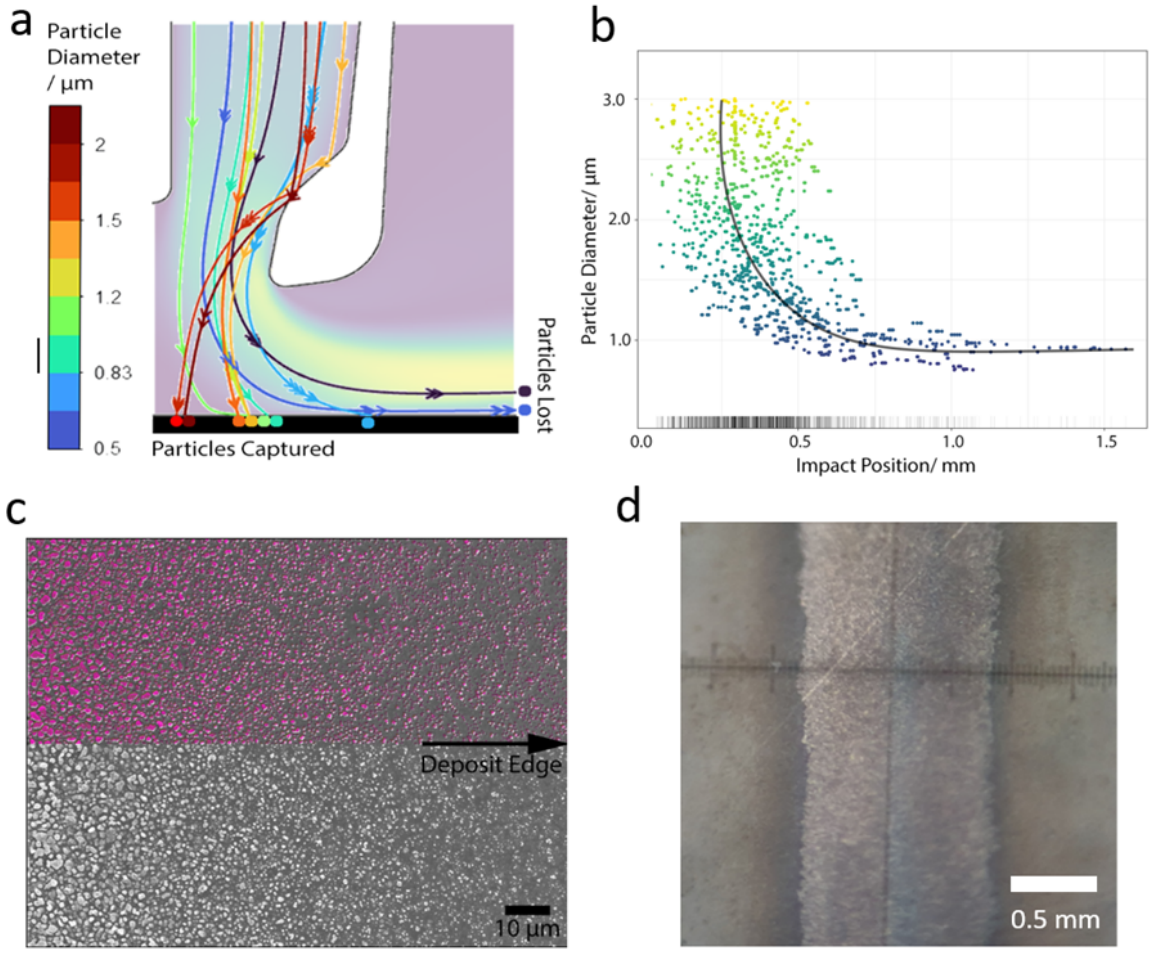

Fig. 7.11 Schematic description of particle tracks for particles with different diameters (a). Impact position vs. particle diameter as obtained from an injection of 1000 particles with uniform diameter distribution between 3 and 0.25 µm, trendline asymptotically approaches the cut-off diameter for the nozzle geometry (b). SEM micrograph of the edge of a deposited trace showing a spatial distribution with smaller particles away from the deposit centre, false colour on top to increase contrast (c). Micrograph of the same trace with visible dark bands around trace edges due to the small particles (d).

In the particle injection model, that larger particles tend to stick to the surface within a radius of around 0.5 *mm* from the jet exit while smaller particles with diameters below 1 μm travel further towards the periphery of the deposited trace or are lost in the wall jet flow (Figure 7.11b). This results in an non-uniform spatial distribution of deposited particles with larger diameters collected below the centre of the plasma jet orifice and smaller, nano-scale particles towards the periphery. Furthermore, virtually no large particles are lost in this process with collection efficiency approaching 100% for particles sizes above 1 μm. These results suggest that plasma jet deposition can be tuned to have near ideal material efficiency

by controlling the size of the aerosol precursor feedstock.

SEM imaging shows that this trend is reflected in the experimental results with a clear distribution of particle sizes at the edge of the deposit where the smaller particles are seen towards the deposit edge (Figure 7.11c). This is also seen in optical micrographs as a thin dark band of discoloration around the edges of the copper trace (Figure 7.11d).

By simulating the behaviour of a swarm of 5000 particles with diameters uniformly distributed between 3 and 0.1 μm, an approximate deposition profile can be generated. The calculated is given in Figure 7.12a, where 0 indicates the axis of symmetry of the system. Under these simulation conditions, the distribution is non-gaussian with two major lobes towards the periphery and a central, smaller spike. This is due to the large stagnation zone that is created above the impact surface and below the coaxial electrode as seen in Figure 7.9a, the stagnation zone deflects or recirculates the particles entering the exact centre of the plasma plume, leading to decreased deposition efficiency in this location.

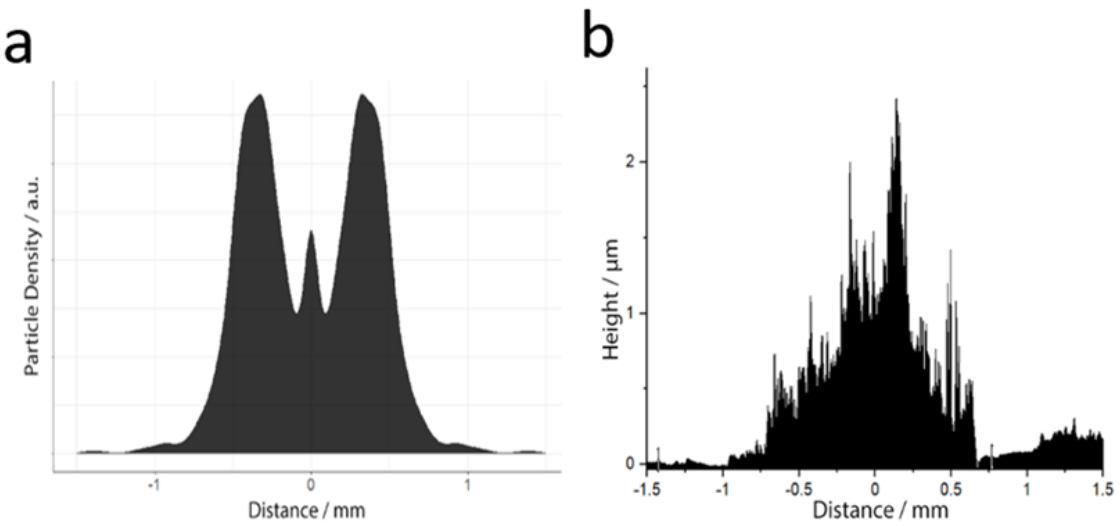

Fig. 7.12 Aggregated impact position density profile (a). Height profile of copper film deposited with 20 s total dwell time and0.31 $M\ CuSO_4$ solution feedstock (b).

The CFD particle injection model is further validated by stylus profilometry results that qualitatively align with the calculated spatial distribution of particle impact positions. Comparing the model output to experimental profilometry data taken from a typical deposit, a similar distribution with a central depression is seen (Figure 7.12). Fortunately, in 2D printing applications, this non-uniformity is averaged out as the substrate is translated beneath the plasma jet.

Despite significant agreement between the computational model and experimental results, one stark difference is apparent upon closer examination. With SEM imaging, the distribution of particles on the surface are found to contain a significant number of smaller sized particles below the calculated cut-off diameter (da_{50}) as shown in Figure 7.13a.

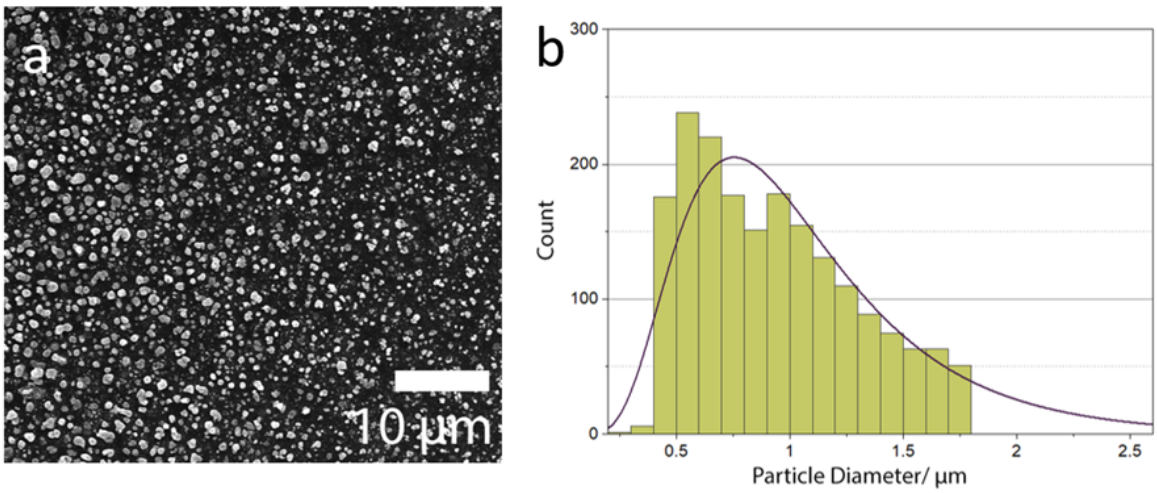

Fig. 7.13 Representative scanning electron micrograph of copper particles on glass (a). The size distribution of the particles obtained from the micrograph with an overlaid log-normal best fit distribution function, showing a higher-than-expected number of sub-micron sized particles on the surface (b).

It is very unlikely that these sub-micron particles shown in Figure 7.13 originate from the jet plume directly. Even under optimal conditions the impaction efficiency for particles smaller than 750 *nm* should be negligible. This suggests that the smaller particles are a result of processes that take place on the surface after impaction and not due to direct deposition. SEM imaging provides additional clues towards their origin, it is seen that individual particles on the surface originate from larger, hollow bodies that fracture on impact with the surface (Figure 7.14b-c). Aerosol particles from loosely bound, hollow, shell-like structures composed of individual nanoparticles with diameters ranging between 5 to 15 *nm*. Depending on their density, these shell-like particles can collapse and fracture on contact with the surface, resulting in localised clusters of copper nanoparticles.

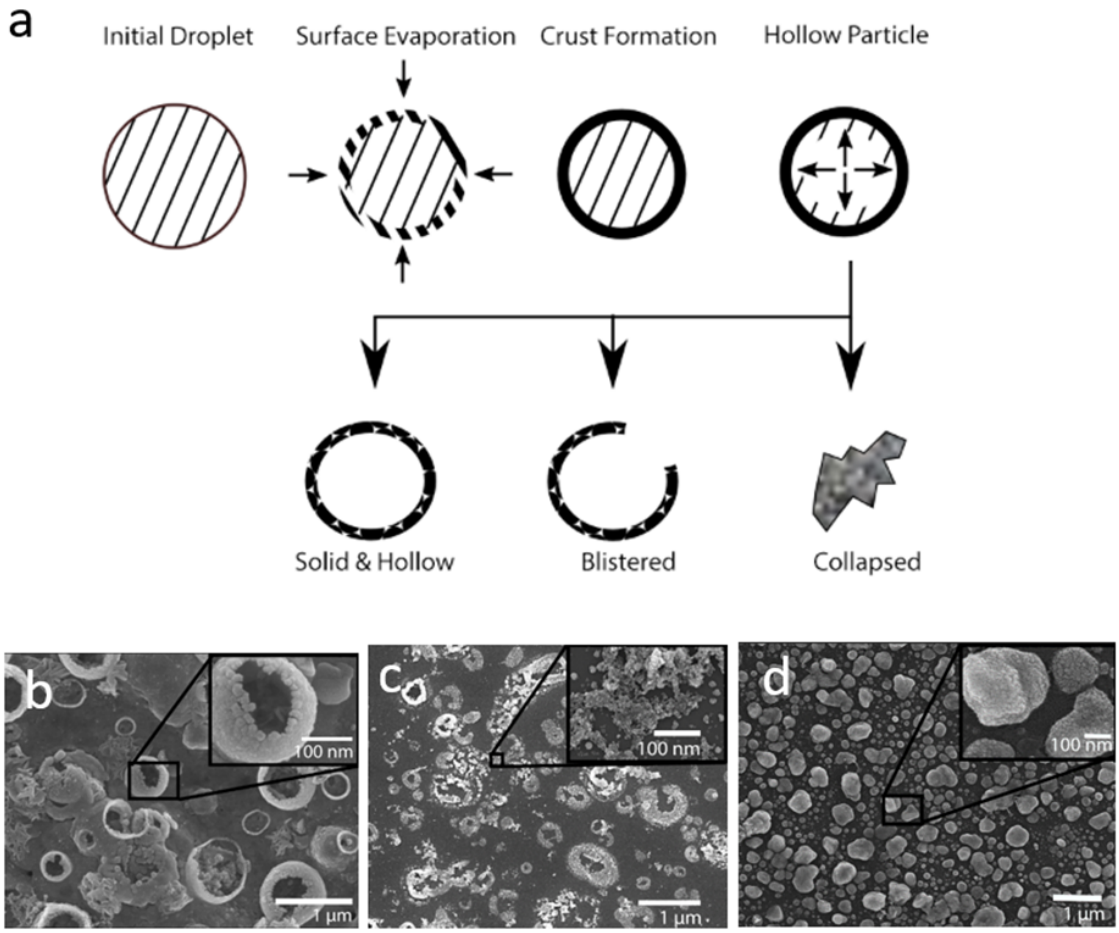

Fig. 7.14 The salt solution aerosol drying process leading to three possible outcomes depending on rate of evaporation and initial concentrations (a). Thick blistered shell particles seen on the deposit surface (b). Thin-hollow shells that disintegrate on contact with surface (b). Solid, fully collapsed nanoparticles (c).

The remnants of these fractured particles range from the 10 *nm* scale to larger aggregates in the $100-500$ *nm* range, explaining the discrepancy between the measured and expected size distributions. The "raspberry" like morphology of these particles likely arise from the rapid drying process that the copper salt laden aerosol undergoes during gas transport and within the plasma plume, combined with the in-situ decomposition and reduction of the crystalline salt into amorphous nanoparticles within the droplets.

This rapid drying process is well known in the field of nanoparticle synthesis [234, 235] and is described schematically in Figure 7.14a. Shortly after generation, the aerosol droplets containing $CuSO_4$ start losing water content to evaporation at the *wet-bulb temperature*, at this point the aerosol travels through the gas manifolds and gets mixed with a large amount

dry gas. Depending on the salt concentration, a permeable shell of copper salts may form around the particles at this stage due to saturation. Upon arrival in the jet nozzle, the aerosol is further heated, resulting in the observed particle morphology.

Under these conditions, the formation of the solid particles from the wet aerosol depend on the ratio of advective to diffusive mass transport within the droplet. If the ratio is much higher than 1, the copper salt precipitates at the outside boundary where the local concentration is above the saturation limit. As more solvent is removed from the droplet, solid phase gets further concentrated within this shell until an internal bubble forms and the particle is transformed into a hollow shell. Partially fractured examples of this hollow shell morphology are visible in scanning electron micrographs (Figure 7.14b) of copper, plasma jet deposited from 1.25 M, saturated $CuSO_4$ solution. Depending on the feedstock salt concentration, the particles can either stay as an intact hollow shell, fracture or not form a shell structure, instead collapse into dense sub-micron particles.

Both blistered, fractured and collapsed particles are found on the deposit surface; with high concentrations of $CuSO_4$ feedstock (1.25 M), the resulting particles display roughly spherical morphology with a 20 nm thick shell (Figure 7.14b), this shell is found to partially fracture on impact with the surface. With decreasing feedstock concentration (0.62 M), these hollow particles are unable to hold together and completely break on impact, leading to circular impressions under electron microscopy with scattered nanoparticles (Figure 7.14c). At even lower concentrations (< 0.31 M), diffusive transport in the aerosol dominates, preventing shell formation and this leads to fully collapsed particles that range from 100 to 500 nm in diameter.

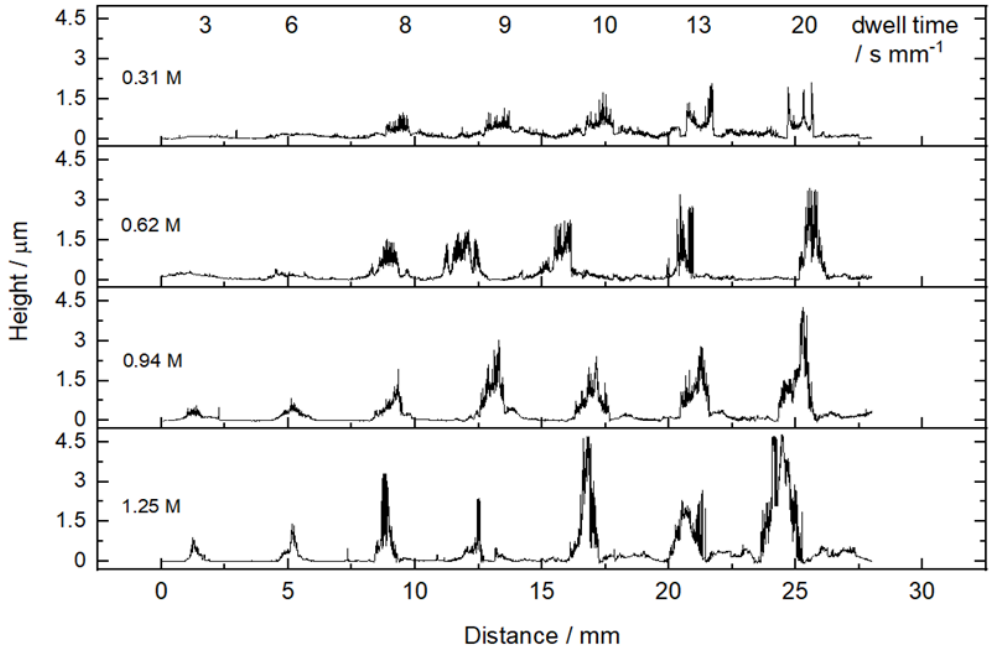

Fig. 7.15 Height profiles of copper traces deposited at different feedstock concentrations at increasing plasma dwell time.

The concentration of feedstock is found to have a significant effect on the thickness of the deposited films. By printing 10 *mm* long traces while repeatedly scanning the plasma jet back and forth over the surface, 28 samples were made with differing thicknesses and differing salt concentrations. The effects of total deposition time and precursor concentration on the resulting traces were probed using stylus profilometry. Resulting height profiles are provided in Figure 7.15.

The profilometry curves shown nearly identical trace widths of around 1.1 *mm* under all conditions. This is in line with CFD predictions (Figure 7.11a). The edges of the deposits appear sharp, providing decent aspect ratio, especially at high precursor concentrations. This is also in agreement with the CFD model and SEM observations where only the smallest particles land on the deposit edge, with a sharp cut-off in spread distance. Visual appearance of the copper lines as seen in the micrographs (Figure 7.11d), also agree with profilometry results, indicating a steep edge around the copper coloured deposits.

By integrating the trace height profiles over their width, it is shown that overall trace cross-section is increased by depositing at increasing precursor concentrations (Figure 7.16). Importantly, not just the rate of deposition but also the efficiency is increased by increasing salt concentrations in the aerosol, for example the 1.25 *M* feedstock, compared to 0.31 *M*,

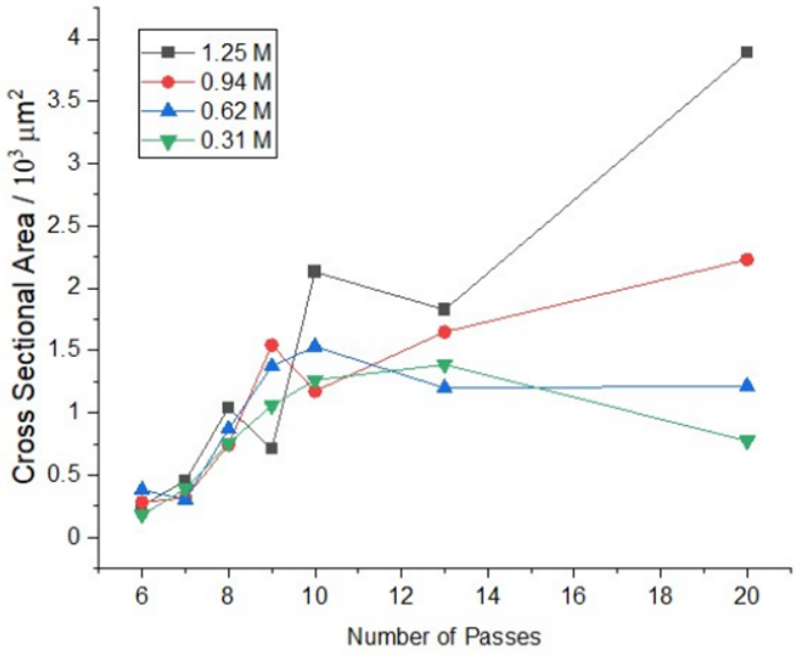

Fig. 7.16 Calculated cross sectional area of deposited copper traces at different $CuSO_4$ feedstock solution concentrations with increasing number of plasma jet passes over the trace.

results in a nearly sixfold increase in deposit cross-section despite only containing four times the copper density. This is due to the larger particles formed with greater aerodynamic diameter when high salt concentrations are used, leading to greater impaction efficiency. This suggests a fundamental trade-off between particle size and deposition speed at a given gas flow rate.

Surprisingly, the trace cross sections do not monotonically increase in cross section with increasing number of jet passes. While the measured samples have significant surface roughness, making it difficult to judge a clear trend, the trace growth appears to display two specific phases marked by different rates of growth as the deposition time is increased. Initially, at all concentrations, the thickness of the deposited layer increases monotonically with each pass of the plasma jet. After 10 to 15 passes of the nozzle, the growth appears to slow down, or even reverse in some cases. This is quite interesting seeing that the total mass transported to the surface must necessarily increase as the plasma jet traverses over the same track multiple times. Simultaneously, a marked decrease in the trace resistivity around this inflection point is noted. Possibly, this is due to densification of the particulate layer, leading to a decrease in measured thickness. Densification leads to improved connectivity between the scattered particles, leading to the onset of end-to-end conductivity.

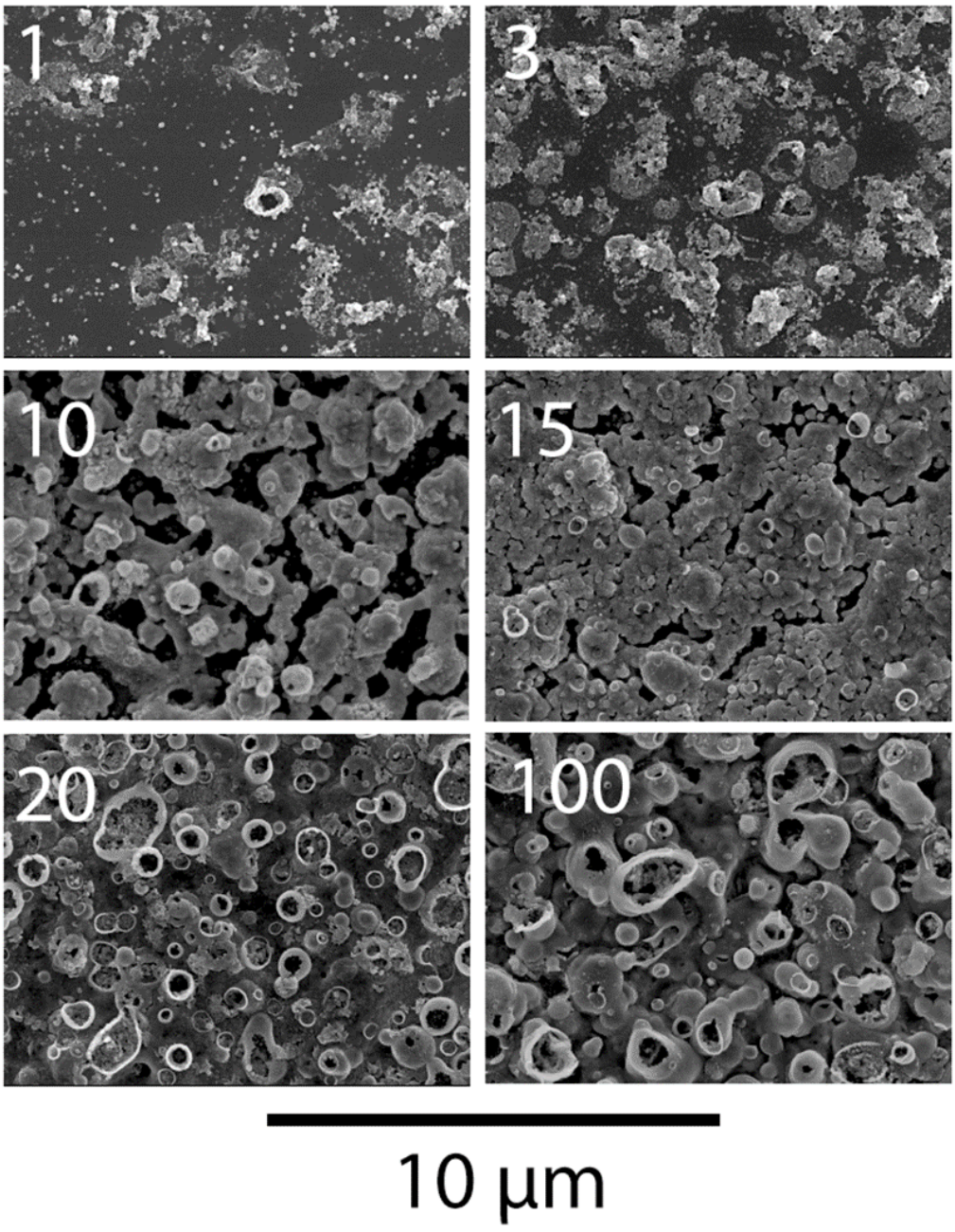

Fig. 7.17 Scanning electron micrographs of trace surfaces obtained at increasing number of deposition passes. The evolution of the scattered particles into a continuous layer is highlighted. The traces are found to become conductive between 10 to 15 passes of the plasma jet over the surface.

The particle collection and sintering process during printing was followed with SEM imaging (Figure 7.17), the surface evolves drastically as it transforms from a collection of sparse particles to partially connected islands to final, fully connected layer decorated with

blistered, hollow shell particles. In this case, the layer is observed to become end-to-end conductive, albeit with high resistivity (12 $k\Omega\ cm^{-1}$) at 10 passes with the plasma jet. Further deposition and densification of the layer leads to continuous decrease in resistivity due to increasing trace cross-section and increased connectivity between the copper grains.

The exact nature of the sintering process is unclear. One possible mode of densification method might rely on Joule heating of nanoparticle contact points due to RF currents passed through the plasma and the thin film, leading to Joule heating at contact points between the particles. There have been previous reports of sintering techniques utilising this type of approach [236], and similar processes, such as spark plasma sintering [237] are well understood.

7.3.2 Chemical Composition of the Deposited Traces

While the physical processes leading to particle deposition have been discussed in detail in the previous section, the chemical transformation leading to deposition of metallic copper from $CuSO_4$ has not yet been considered. This section will describe the chemical composition of the deposited traces alongside potential mechanisms that lead to conversion of copper containing particulates into printed traces.

During the transit of aerosol laden gas through the plasma jet, there are two locations where the $CuSO_4$ precursor can be converted into metallic Cu. First, the transformation may happen in the jet plume during transit of the particles themselves. A second possible location is on the surface, after having impacted the surface, not-yet-metallic particles may then be reduced into elemental copper via a plasma reduction processes discussed in the previous chapters.

To understand this process, the plasma jet was used to inject particles into a volume of anhydrous ethylene glycol, with the hope that the collected particles would provide insight into the chemical species present on the surface right after exiting the jet nozzle. The collected particles were also washed with deionised water and dried for SEM imaging to understand the morphology of the intact particles existing the plasma jet. Unfortunately, the hollow shell particles are found to be unstable in liquids and appeared to fracture into their constituent nanoparticles.

UV-Vis spectra of the particles collected from the plasma jet into ethylene glycol show different absorption peaks depending on whether hydrogen is added to the plasma stream, given in Figure 7.18b. The two absorption maxima at around 295 and 335 nm can be attributed to CuO nanoparticles that are produced in the plasma from decomposition of

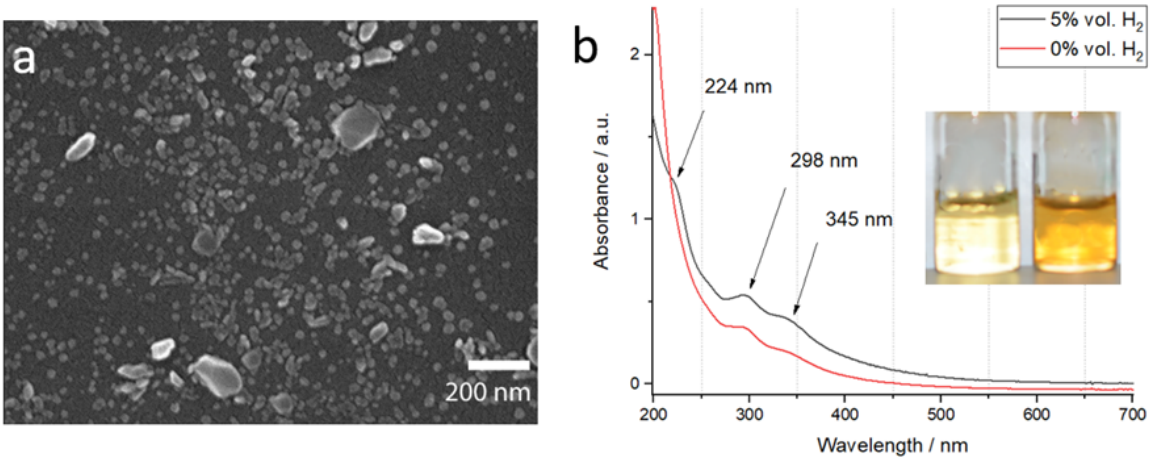

Fig. 7.18 Scanning electron micrograph of nanoparticles collected in ethylene glycol from the plasma plume (a). UV-Vis absorption spectrum of two solutions containing mixed copper oxide nanoparticles, inset showing the colour of the two solutions with the H_2 admixture sample on the right(b).

$CuSO_4$ feedstock [238]. These peaks were present both in the samples collected from both the 5 *v.%* and 0 *v.%* H_2 plasma compositions. The particles produced in the plasma stream with hydrogen admixture showed an additional absorption peak at 285 *nm*, indicating the presence of Cu_2O nanoparticles [239].

It can be assumed that these particles are identical to the particles that make up the *raspberry* hollow structure seen in the film deposition process. Interestingly, no trace of residual $CuSO_4$ could be detected via UV-Vis spectroscopy. This might be attributed to the weak absorption of $CuSO_4$ compared to the phonon absorption of copper oxide nanoparticles, a second possiblity is that atmospheric pressure plasma is able to completely decompose and partially reduce $CuSO_4$ into Cu^+ and Cu^{2+} species.

In the absence a of reducing environment generated via H_2 admixture, the particles are only decomposed into CuO nanoparticles. The addition of H_2 changes the decomposition pathway to yield Cu_2O as well as CuO. This likely plays a key role in the overall deposition process as it was previously demonstrated in Chapters 4 and 5 that Cu^+ species on a surface can be rapidly reduced via helium atmospheric pressure plasma into metallic copper.

It is significant that $CuSO_4$ is completely decomposed within the plasma plume. With a thermocouple, the effluent temperature of the plasma jet is measured to be $\approx 100°C$. Previous spectroscopic measurements suggest a peak temperature of $\approx 220°C$ during plasma pulses. Considering that the thermal decomposition temperature of $CuSO_4$ is above 600 $°C$ [128], it is unlikely that the plasma conversion of $CuSO_4$ to CuO happens via a solely thermal route.

To understand the fate of the particles that have been decomposed and partially reduced once they arrive at the substrate, multiple surface sensitive materials characterisation methods such as Raman, Auger electron and X-ray photoelectron spectroscopy were used to track the spatial and temporal evolution of the printed deposits. The results obtained via Raman spectroscopy from the surface of the deposits agree with the suggestion that the deposited particles contain mixed copper oxides(Figure 7.19). In fact, the surface can be directly coated with a mixture of copper oxides, as seen in Figure 7.19c if hydrogen is not added to the working gas. Under these conditions the deposited traces do not become conductive, as expected .

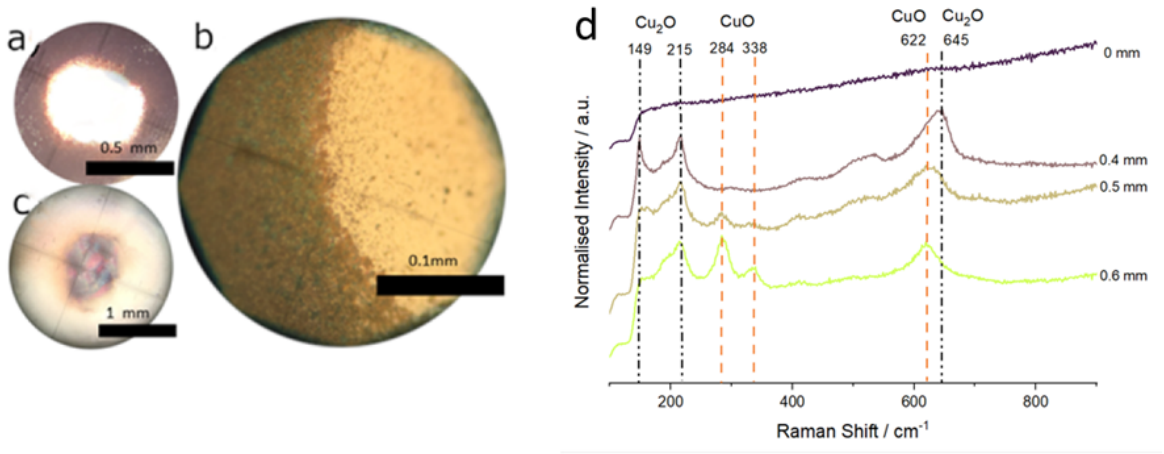

Fig. 7.19 Micrographs of copper deposits. Pure copper spot (a) and edge of the same, showing the boundary between Cu and Cu_2O. CuO spot deposited for 30 s (c). Stacked Raman spectra taken along a line extending outwards from the circular deposit centre, indicating the transition from pure copper (no Raman scattering), to Cu_2O to CuO.

Single spot deposits, pictured in Figure, were produced while the print head was kept static above a glass substrate for 30 s. Raman spectra taken at increasing distances from the center of the deposit show that the centre of the deposit with a metallic coloration shows no Raman scattering. Beyond 0.4 mm from the centre, Cu_2O bands become discernible and beyond 0.5 mm, the spectra consists of contributions from a mixture of Cu_2O and CuO. Relative CuO peak intensities increase with distance from the center. At these locations Cu presence can not be ruled out using Raman spectroscopy alone. CuO peaks seen in this sample were at 284, 338 and 622 cm^{-1}, in good agreement with literature [156].

This spatially non-uniform composition can arise due to two distinct phenomena. One possibility is oxidation via excess entrained atmospheric oxygen at the edge of the plasma plume, this is unlikely in the case of static spot prints due to the shielding effect of the wall

jet produced around the nozzle, as discussed previously. At 5 μm above the substrate, the concentration of O_2 obtained from the CFD model is 1 ppb at a distance of approximately 0.5 mm from the jet center, suggesting that the flow of plasma gas is able to effectively shield the surface from oxidation via entrained air.

A second, more probable reason has to do with the type of particles seen in the periphery of the deposit. These particles are small and dense as they do not form a hollow shell structure (Figure 7.14) and therefore, they are more likely to end up on the periphery of the deposits due to aerodynamic effects. These dense particles do not have as much surface area as the hollow, loosely held *raspberry* structure and the rate of reduction of this type of morphology due to plasma exposure is likely lower.

Raman spectroscopy provides information related to approximately first ≈ 1 μm[240] of the copper surface. Unfortunately this level of sampling depth does not allow us to follow the evolution of the surface as the newly deposited layers are continuously produced and buried under further layers. Furthermore, the chemical composition of deposited particles can not be quantitatively ascertained using Raman spectroscopy alone. To get a better understanding of composition of copper containing deposits, X-ray photoelectron spectroscopy was used to quantify the copper containing compounds that exit the plasma plume.

A representative survey spectrum is provided showing the major contributions to the photoelectron and Auger electron emission from the copper films (Figure 7.20). For all samples produced, the elements present are oxygen, copper, carbon and silicon (from the glass substrate). The major surface contaminant is carbon, likely due to contamination from the atmosphere. Carbon contamination is present on all samples at a level of $5-15$ $at.\%$. Interestingly, no sulphur photoelectron peaks can be detected on the samples even in high resolution scans of the S $2p$ region. This suggests that all the sulphur originating from $CuSO_4$ in the feedstock salt is carried away in the plasma jet plume as a gas, most likely SO_2.

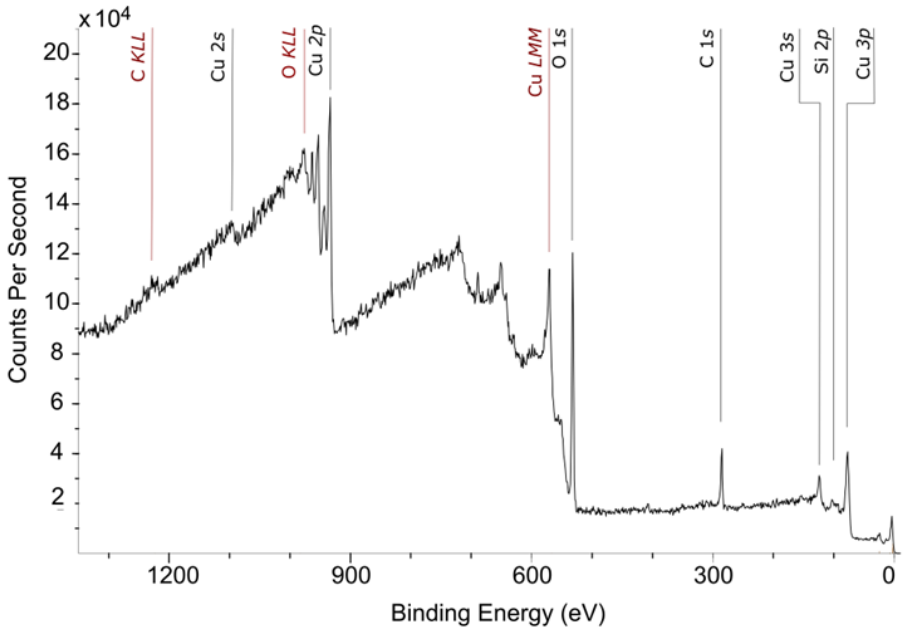

Fig. 7.20 Low resolution survey spectrum from the copper surface with major XP and Auger electron peaks highlighted in black and red, respectively.

High resolution spectra in areas of interest such as Cu $2p$ and O $1s$ show a clear dependence of trace composition on overall deposition time, as shown in Figure. Cu $2p$ high resolution spectra of the deposit surfaces show the characteristic $2p_{1/2}$ - $2p_{3/2}$ spin orbit splitting ($\approx$ 952 and 932 eV) and satellite structures ($\approx$ 942 eV) for all spectra. Satellite structures are more prominent in non-conductive films deposited for a shorter duration, disappearing as deposition time is increased. These satellite features, also known as *shake-up* peaks, occur when the emitted photoelectron leaves the remaining ion at an excited state. As this process results a loss in electron energy, the photoelectron resulting from this process is detected at a correspondingly *higher* binding energy. In copper, the satellite features are associated with the paramagnetic Cu^{2+} oxidation state[149, 241].

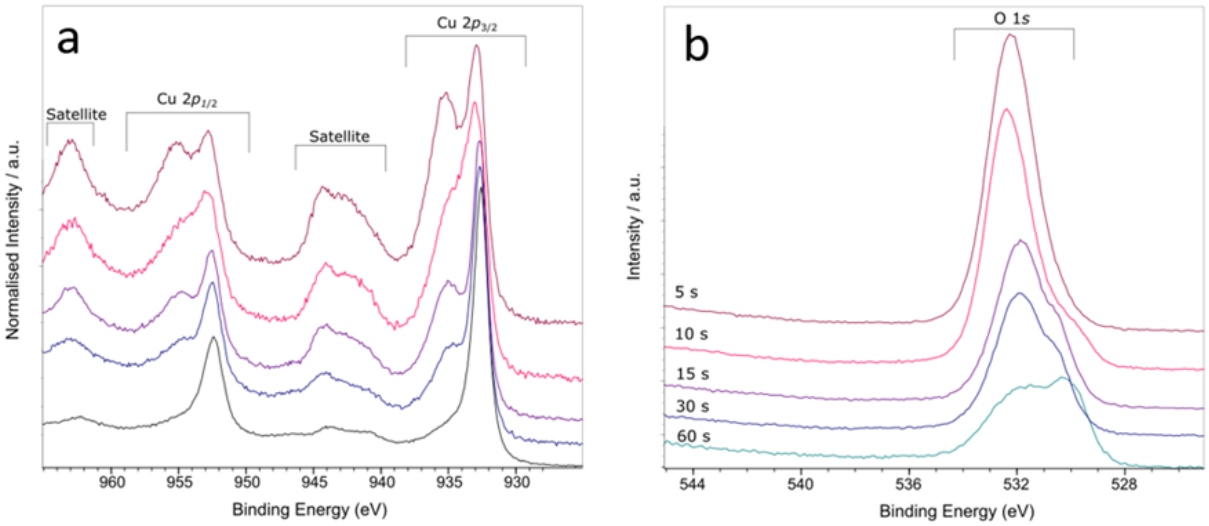

Fig. 7.21 Normalised Cu 2*p* (a) and non-normalised O 1*s* (b) high resolution XP spectra showing the evolution of peak structure at different times during the deposition process.

For deposition times below 10 *s*, *Cu* $2p_{3/2}$ peak is comprised mainly of two components at 934.0 and 932.5 *eV*, corresponding to Cu^{2+} and $Cu^{1+/0}$ oxidation states respectively. Due to the proximity of Cu^{1+} and Cu^{0} peaks, the two components cannot easily be distinguished via XP spectroscopy alone[149]. The peak at 934 *eV* is seen to decrease in intensity as the deposition time increases, suggesting reduction to either metallic copper or Cu_2O.

O 1*s* XP spectra in Figure 7.21b show a major peak at 531.8 *eV*, likely associated with $Cu(OH)_2$ [149] and a second peak at 530.5 *eV* belonging to Cu_2O lattice oxygen. $Cu(OH)_2$ is both a native oxide for copper exposed to ambient atmosphere[242] and a also a decomposition by-product of $CuSO_4$ [243]. At 60 *s* of deposition time compared to 30 *s*, the O 1*s* peak area is found to have reduced to 38% of its initial magnitude, indicating a gradual decrease in surface oxygen concentration. It must be borne in mind the potential interfering species such as $C-O$ and $C=O$ are likely present on the surface, and a similar portion of the oxygen signal for both cases stem from adventitious contamination.

Peak deconvolution of the *Cu* 2*p* spectra in the range of 948 to 928 *eV* was performed to quantify the change in proportions of Cu^{2+} and $Cu^{1+/0}$ contained on the sample, and also to determine other potential species present. Figure shows the deconvolution of two spectra at different times into four major components. Two of the components are associated with Cu^{2+} and $Cu^{1+/0}$ whilst two are assigned to satellite structures.

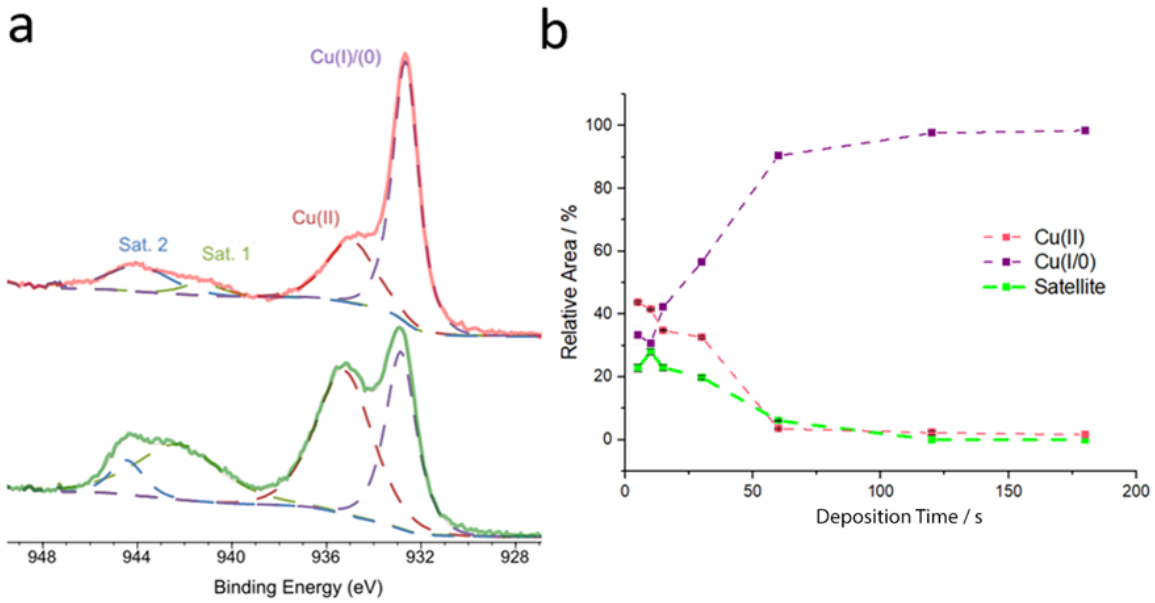

Fig. 7.22 Example decompositions of Cu $2p_{2/3}$ peak region after 30 *s* (top) and 5 *s* (bottom) of plasma deposition (a). Relative photoelectron signal intensity corresponding to deconvolved peak components over time (b).

The evolution of Cu^{2+} and $Cu^{1+/0}$ and satellite signal ratio is plotted over time in Figure 7.22b. Evaluated relative uncertainty obtained for the peak areas were never above 3%, suggesting a good fit to experimental data. Figure 7.22b shows that the ratio of Cu^{2+} main peak to total satellite peak area is mostly constant at 1.75 for samples deposited for less than 60 *s*. This characteristic ratio lies in between the reference values reported for CuO (1.89) and $Cu(OH)_2$ (1.57) [149]. This suggests that the Cu^{2+} species on the surface initially consist of a mixture of $CuSO_4$ decomposition products, mainly CuO and $Cu(OH)_2$. Beyond 60 *s* of deposition time, the sample surface is seen to rapidly reduce to $Cu^{1+/0}$ with minimal Cu^{2+}.

Unfortunately, the Cu^{1+}/Cu^0 ratio can not be approached in a similar manner. The literature positions for metallic Cu and Cu_2O peaks are given at 932.6 and 932.3 eV with FWHM valies of 0.85 and 1.0 eV respectively [149]. The proximity of the two characteristic peaks makes any fitting procedure very susceptible to noise in the XPS data, introducing large uncertainties to the peak area estimates.

Fortunately, Auger electron spectra, while more complex, differs significantly between the 0 and +1 oxidation states of copper. In order to quantify the proportions of metallic Cu and Cu_2O, Auger electron spectroscopy was used with a multicomponent fitting procedure. Reference Auger peak shapes composed of multiple Gaussian / Lorentzian peaks were

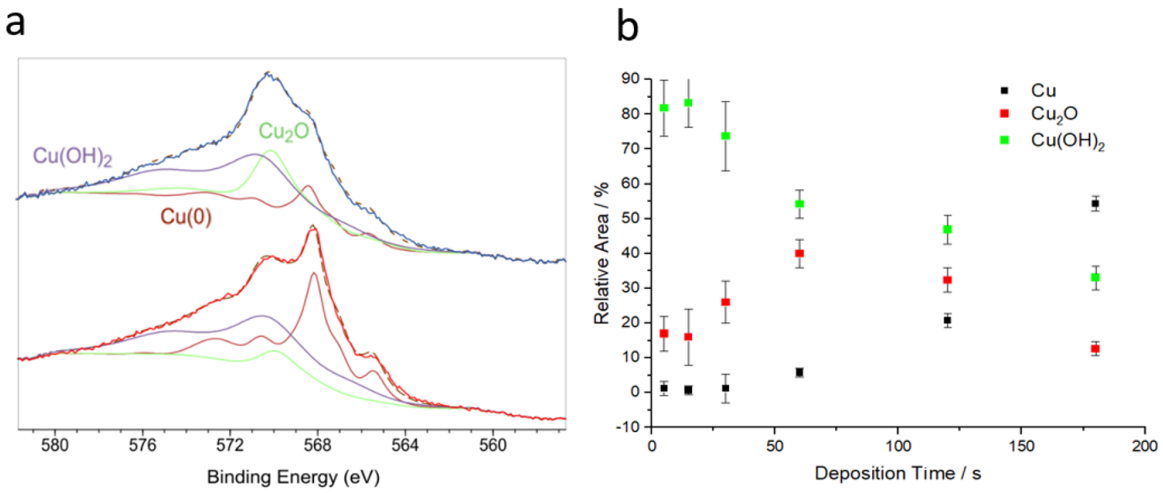

Fig. 7.23 Multi-component decomposition of Auger spectrum obtained from the films after 120 (top) and 175 (bottom) seconds of plasma deposition (a). Relative Auger signal intensity as a function of deposition time.

combined and iteratively fit to the Auger spectra to obtain a decomposition.

Due to the much weaker Auger signal compared to XP spectra, and the inherent uncertainties in fitting multicomponent lineshapes, the composition estimate errors in this procedure were higher, up to 20% for an individual component, as determined via a Monte Carlo procedure [244, 121]. In addition, it was found that joint fitting of Auger signal profiles from both CuO and $Cu(OH)_2$ species was not feasible due to similar reference peak structure [149]. Based on the XPS peak positions, and O 1s data, the Cu^{2+} species on the surface was assumed to consist entirely of $Cu(OH)_2$ for purposes of analysis. Further details of this method and the reference data used can be found in a comprehensive paper by Biesinger [149].

Unsurprisingly, the overall trend of decreasing total oxidation with increasing deposition time is also seen with Auger spectroscopy, complimentary to the XPS data previously discussed. At earlier stages of the process, the composition obtained through Auger spectroscopy and XPS disagree, with Auger fitting overestimating the Cu^{2+} concentration by a factor of two and underestimating the Cu^0 concentration on the surface. At 30 s, XPS spectra show a Cu^{2+}/Cu^{1+} ratio of roughly 1.5 whereas the deconvolution of Auger spectra give a ratio of 3. These discrepancies mainly result from the lack of CuO peak profile inclusion within the Auger emission model.

This discrepancy may also be partially attributed to different escape depths of emitted electrons from Auger and photoemission processes due to having different kinetic energies. On a kinetic energy scale, electrons emitted from Cu 2p have an energy of $\approx 557\ eV$, on the

other hand, Auger electron kinetic energy for Copper *KLL*, independent of illuminating X-ray source (here, $Al\ K-\alpha$), is centred around 920 eV. Based on these values, the calculated inelastic mean free paths of these two electrons are 1 and 1.6 nm (in Cu) respectively [245]. It is therefore likely that XPS and AES collect signals coming from slightly different depths, causing the *AE* spectra to contain signals from species deeper towards the bulk if a depth gradient in species concentration exists.

To see if there is a significant difference in composition beneath the surface, Ar^+ ion bombardment was used to etch the surface of films deposited for 200 s, twice for a duration of 30 minutes at 200 V acceleration. The results, given in Figure 7.24 indicate that beneath a lightly oxidized surface, the bulk of the deposited material is metallic copper with low oxygen inclusion ($< 2\ at.\%$). It must be kept in mind that ion bombardment is known to cause stoichiometric changes in Cu_2O, leading to partial loss of oxygen and potential reduction to Cu^0 [246]. Therefore, conservatively, these results should be considered as indicators of the absence CuO and $Cu(OH)_2$ in the bulk, rather than indicating a total lack of Cu_2O.

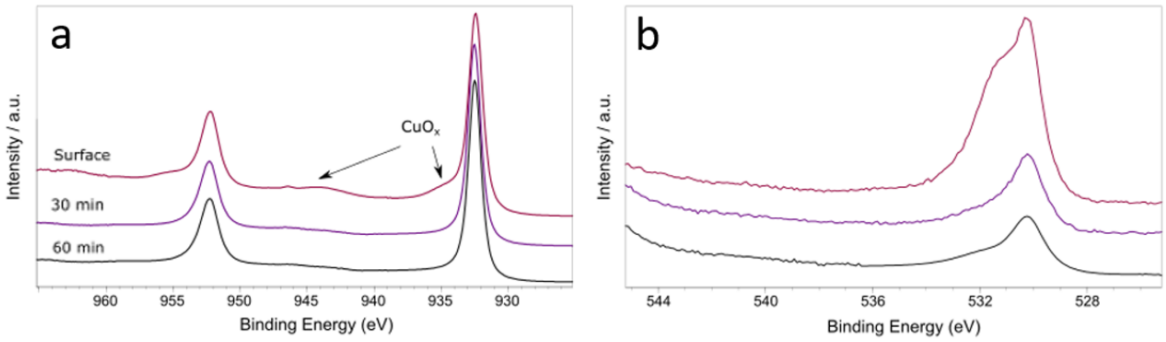

Fig. 7.24 Normalised Cu 2p (a) and non-normalised O 1s (b) XP spectra obtained after argon ion etching, showing the disappearance of copper oxide peaks and a marked decrease in O 1s overall signal intensity.

Results so far indicate that despite continuous deposition of copper containing particles from the plasma plume, the composition of the surface is in flux at the beginning of the deposition process, containing a variety of oxides and hydroxides. Over time, the trend is for the plasma jet to reduce the impacted oxide particles into elemental copper. This gradual reduction speeds up significantly once an appreciable amount of copper has been formed on the surface. After 30 s of deposition with 1.25 M precursor, the surface is conductive and mainly consists of metallic copper.

Under the experimental conditions used, a short *incubation period* exists between oxide and copper deposition. Initially scattered particles on the surface are found to be mainly

composed of mixed oxides, whereas the continuous copper deposits are metallic in nature. It can be deduced that when the deposition takes place on an already metallic substrate, metal is deposited instantaneously. When the surface consists of a semi-conducting or insulating oxide layer, plasma jet reduction is less effective and surface is only gradually converted into metal.

In summary, composition of the existing surface has a significant effect on the further evolution of the deposit. This is an interesting phenomenon that requires further investigation. Likely, the synergistic effect of the newly formed conductive surface with the plasma causes this divergence. It has been shown that the rate of atomic hydrogen generation and electron density in a plasma jet in contact with a surface depends on the conductivity and dielectric constant of the surface. Norberg et al. have suggested significantly increased plasma densities [52] in simulations of plasma jets in contact with metallic targets compared to dielectric surfaces. Similarly, Urabe et al. [247] and Zaplotnik et al. [248] have shown that increasing conductivity of the plasma exposed surfaces leads to increased generation of excited and ionic species above the plasma exposed substrate.

In this work a negative surface bias was demonstrated to halt the reduction of Cu_2O into Cu. Here, it is possible that plasma induced negative surface charge can not be dissipated efficiently by the nanoparticle islands suspended on the insulating glass surface. As the bulk conductivity and total mass of the deposited particles increases, induced surface charge can be dissipated more efficiently, leading to the observed transition from oxide to metal deposition. As reduction rate increases, the conductivity of the surface increases commensurately, leading to a feedback mechanism where the reduction rate increases further until the deposit is oxide-free.

Based on these observations, three major processes can be said to take place near-simultaneously during printing. The deposited layers become conductive, the morphology of the deposits become interconnected rather than sparse and the surface Cu^0 concentration greatly increases.

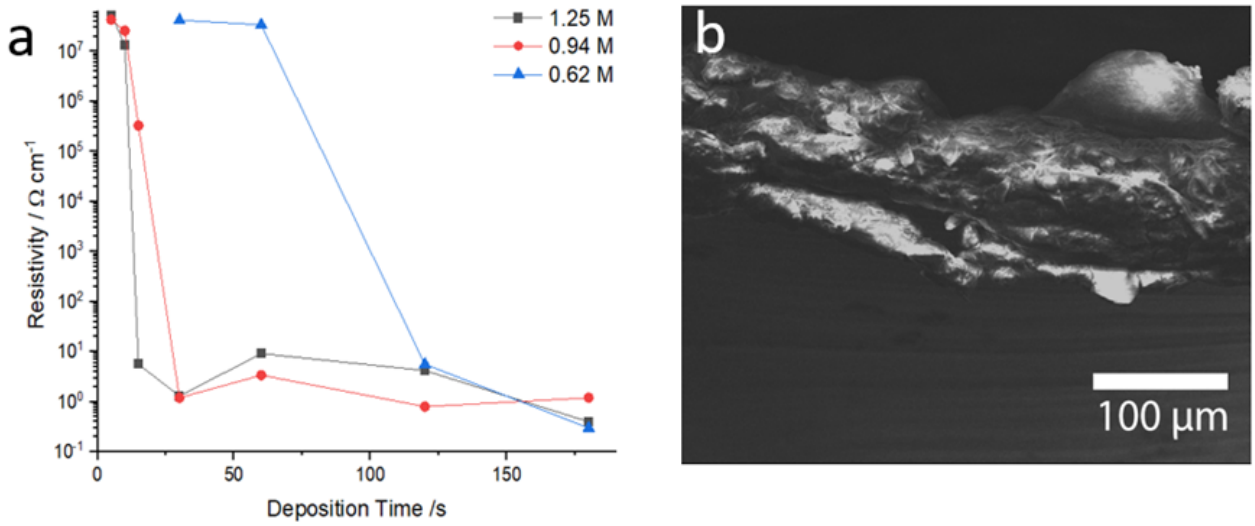

Fig. 7.25 Conductivity of traces deposited at different salt concentrations as a function of total deposition time (a). Cross-sectional scanning electron micrograph of a thick copper trace deposited by repeatedly scanning over the surface with the plasma head (b).

The evolution of bulk resistivity as a function of deposition time is provided below in Figure 7.25a for deposits formed with different concentrations of feedstock. Once deposited and fully reduced, it is found that the measured trace resistances drop precipitously to the order of 0.5 $\Omega\ cm^{-1}$ for 5 μm thick traces. This an order of magnitude higher than bulk copper [128] but comparable to ink-jet printed copper traces that normally require additional sintering [249, 250]. By increasing the trace thickness via repeated passes over the surface or decreasing the jet travel rate, thicker copper build up can be achieved to compensate for the increased resistivity, a micrograph of a 0.1 mm thick trace cross-section demonstrating this approach is provided in Figure 7.25b.

7.4 Conclusions

A novel method capable of deposition of conductive copper traces at atmospheric pressure was demonstrated in this chapter. This method overcomes many of the downsides associated with conventional additive manufacturing methods by combining in-situ nanoparticle generation, decomposition, reduction and densification into a single step. Use of commonly available copper salt feedstock, alongside the meagre power requirements and low temperatures during printing makes this approach especially powerful for use in printed electronics, wearable technologies, and printed sensors. Furthermore, plasma printing, as described, is material

efficient, produces minimal waste and does not rely on pre-synthesized ink formulations that might be cost prohibitive, unstable and prone to oxidation.

The overall mechanism behind the printing process was identified can be summed up by the following steps given in Figure 7.26.

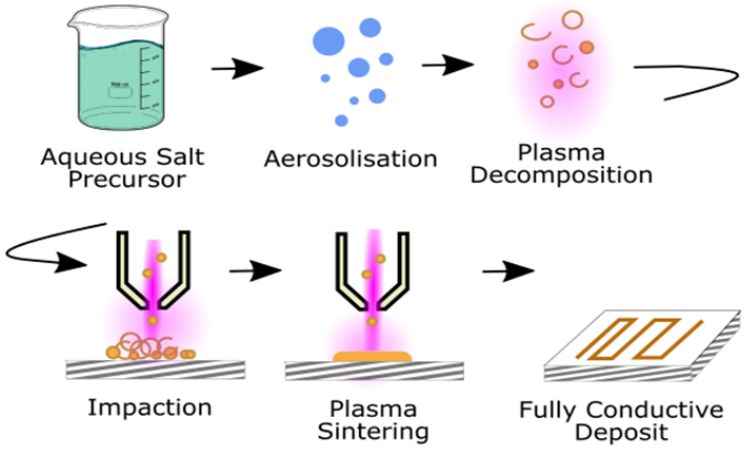

Fig. 7.26 Diagram showing the steps in plasma printing process from precursor to conductive deposits.

Key steps in this process that require further investigation are decomposition, reduction and densification of metal containing particles via atmospheric pressure plasma exposure.In previous chapters, it was shown that plasma reduction of a wider range of metal oxides is possible at atmospheric pressure. Despite this, a clear physical pathway for the fundamental processes taking place is not yet established and would help expand material deposition research. Furthermore, the mechanism behind densification of the metallic prints under plasma jet exposure is not entirely clear and likely relies on both thermal effects due to the plasma plume itself and Joule heating due to the RF currents circulating through the metallic traces.

This work has kept a narrow focus on the deposition of copper from a single precursor with the aim of unveiling the physical and chemical processes taking place during plasma jet printing. At this stage, exploration of alternative *self-reducing* organo-copper precursors[251] such as $Cu(O_2CH)$, and optimisation of parameters such as solvent mixture, aerosol size and plasma gas is critical for further developing this process. Preliminary results (not shown here) have indicate that the use of noble metal precursors such as $HAuCl_4$ and $AgNO_3$ also result in conductive metal deposits, warranting further research into the possibility of printing multiple materials, intermetallic compounds, and alloys in a single-step process.

This technique promises to be a powerful tool in not just electronics manufacture, but in areas such as nanoparticle coatings and even large area, supported catalysis.

Chapter 8

Conclusion

Application of atmospheric pressure plasmas in fields of surface modification and material deposition can open-up new avenues with significant utility in a large number of fields. Research and commercial ventures stand to benefit from adoption of atmospheric plasma processing tools by removing the constraints traditionally imposed by vacuum systems that are not compatible with many environments and substrates of interest. Better understanding of interactions of atmospheric pressure plasmas with surfaces is currently needed to extend the range of potential applications. This work has uncovered the effects of plasma exposure on various metal oxide surfaces via fundamental plasma diagnostics, surface science methods and computer models. Furthermore, a novel application of plasma jets in the field of additive manufacturing was disclosed in the form of plasma jet printing.

This work contributes to the advancement of various fields including atmospheric pressure plasma research, photocatalysis and material deposition. Characterisation and modelling of radio frequency plasma afterglow provides insights into the operation and plasma parameters in atmospheric pressure glow discharges. Plasma fluid modelling and electrostatic probe approaches were employed in at atmospheric pressure, showing considerable agreement between the two methods.

The importance of electron flux to surfaces from plasmas in driving redox reactions on oxide surfaces has been studied and will likely inform future research in this field. Bias dependent modulation of copper oxide reduction in plasma afterglow was demonstrated for the first time, highlighting the importance of plasma electrons in driving oxygen desorption reactions under ambient conditions. The initial work on atmospheric pressure plasma induced reduction was then refined using a plasma *micro-jet*. A method of spatially selective patterning of a large number of metal oxide films was demonstrated, with potential applications in catalysis and electronics for mask-less and vacuum-less surface engineering.

Reducing plasma micro-jet approach was promoted by exploring an immediate application in catalysis. A facile method increasing catalytic efficiency of titania photocatalysts was uncovered. Black titania film production under near ambient conditions was demonstrated, the plasma reduced material was characterised and was found to be similar to existing reports of black titania previously only obtainable through vacuum annealing and high-pressure hydrogen reduction routes.

Existence of Ti^{3+} defects in black titania was confirmed, alongside optimal surface defect densities for photocurrent generation. Increased conductivity due to increased carrier density was proposed as the driver behind observed catalytic enhancement in plasma modified black titania. Atmospheric pressure plasma induced amorphization of anatase under ambient conditions was also reported for the first time. Atmospheric pressure plasma route is likely to help promote wider applications of this improved photocatalyst in commercial and research settings by removing the need for extreme conditions required for conventional synthesis.

By combining the insights obtained in initial work, a novel method of printing using plasma jets was developed. Single-step deposition of conductive copper was shown to be possible using an aerosol assisted approach. The proposed method improves on previously described techniques by forgoing nanoparticulate precursors or vaporisation of metallic targets and instead relies on in-situ reduction of commonly available copper salts.

Significant number of open questions remain. Reasons behind the tendency of certain oxides to spontaneously reduce under noble gas plasma and precise role of electrons in this process is not well understood. The role of atomic vs. molecular hydrogen in the reduction processes of non-spontaneously reducing oxides is also not clear, requiring improved spatially resolved plasma diagnostics and further experiments.

The full capabilities of plasma printing have not yet been explored and the technique as described is still in infancy, requiring significant research effort to understand its range of possible applications *and* limitations. Furthermore, RF plasma jet sintering is itself an interesting avenue that would benefit from further attention. Mechanisms behind the observed sintering process is ambiguous, owing to the large number of chemical species and physical processes taking place at the plasma / solid interface. In addition, there are large gaps in knowledge regarding plasma induced reduction and sintering processes, making it extremely difficult to establish causal links and predict the effects of atmospheric pressure plasma exposure in the context of additive manufacturing. Such an approach would benefit immensely from advanced plasma characterisation and modelling techniques.

8.1 Further Work

Potential of the plasma jet deposition and modification techniques discussed in here is significant, especially in the fields of manufacturing and catalysis. Following the work discussed in this thesis, further development of the plasma jet material deposition technique will continue under a 3.5 year long research project aimed at manufacturing, funded by Engineering and Physical Sciences Research Council, UK. Its aims include the development of multi-material, nanostructured film deposition methods as well as research into generation of intermetallic compounds and alloys. Furthermore, a parallel, 3.5 year long research project based on atmospheric pressure electrocatalyst deposition and modification is planned, funded via Centre for Doctoral Training in Molecular Modelling and Materials Science.

Commercial exploitation of the aerosol assisted atmospheric pressure deposition process is underway, with emerging applications in aerospace and electronics industries. This work is being undertaken under license by Ram Prasad Gandhiraman (NASA Ames Research Center) and Dennis Nordlund (Stanford University).

References

[1] Mott-Smith, H. M. History of "plasmas". *Nature* **233**, 219–219 (1971).

[2] Chen, F. F. *Introduction to plasma physics and controlled fusion*, vol. 1 (Springer, 1984).

[3] Gurnett, D. A. & Bhattacharjee, A. *Introduction to Plasma Physics: With Space and Laboratory Applications* (Cambridge University Press, 2005).

[4] Fauchais, P. & Vardelle, A. Thermal plasmas. *IEEE Trans. Plasma Sci.* **25**, 1258–1280 (1997).

[5] Williams, P. F. *Plasma processing of semiconductors*, vol. 336 (Springer Science & Business Media, 2013).

[6] Townsend, J. S. E. & MacCallum, S. Ionisation by collision in monatomic gases. *Proc. Math. Phys. Eng. Sci.* **124**, 533–545 (1929).

[7] Loeb, L. B. & Meek, J. M. The mechanism of spark discharge in air at atmospheric pressure. *J. Appl. Phys.* **11**, 438–447 (1940).

[8] Raether, H. *Electron avalanches and breakdown in gases* (Butterworths, 1964).

[9] Crompton, R., Elford, M. & Jory, R. The momentum transfer cross section for electrons in helium. *Aust. J. Phys.* **20**, 369–400 (1967).

[10] Paschen, F. Ueber die zum Funkenübergang in Luft, Wasserstoff und Kohlensäure bei verschiedenen Drucken erforderliche Potentialdifferenz. *Ann. Phys.* **273**, 69–96 (1889).

[11] SIGLO Database. www.lxcat.net (Online; retrieved 29 April 2020).

[12] Shi, J. & Kong, M. G. Cathode fall characteristics in a DC atmospheric pressure glow discharge. *J. Appl. Phys.* **94**, 5504–5513 (2003).

[13] Van der Sijde, B. & Van der Mullen, J. Temperature determination in non-LTE plasmas. *J. Quant. Spectrosc. Radiat. Transf.* **44**, 39–46 (1990).

[14] Bruggeman, P. J., Iza, F. & Brandenburg, R. Foundations of atmospheric pressure non-equilibrium plasmas. *Plasma Sources Sci. Technol.* **26** (2017).

[15] Li, H., Heberlein, J. & Pfender, E. Three-dimensional, nonequilibrium effects in a high-intensity blown arc. *IEEE Trans. Plasma Sci.* **33**, 402–403 (2005).

[16] Yabuta, H., Miyahara, H., Watanabe, M., Hotta, E. & Okino, A. Design and evaluation of dual inlet ICP torch for low gas consumption. *J. Anal. At. Spectrom.* **17**, 1090–1095 (2002).

[17] Shi, J. & Kong, M. G. Expansion of the plasma stability range in radio-frequency atmospheric-pressure glow discharges. *Appl. Phys. Lett.* **87** (2005).

[18] Iza, F., Walsh, J. L. & Kong, M. G. From submicrosecond-to nanosecond-pulsed atmospheric-pressure plasmas. *IEEE Trans. Plasma Sci.* **37**, 1289–1296 (2009).

[19] Machala, Z., Marode, E., Laux, C. O. & Kruger, C. H. DC glow discharges in atmospheric pressure air. *J. Adv. Oxid. Technol.* **7**, 133–137 (2004).

[20] Li, B. & Ouyang, J. Comparing investigation of pattern formation in glow and streamer DBD. *Phys. Plasmas* **23** (2016).

[21] Shang, W., Wang, D. & Zhang, Y. Radio frequency atmospheric pressure glow discharge in α and γ modes between two coaxial electrodes. *Phys. Plasmas* **15**, 093503 (2008).

[22] Beauchemin, D. Inductively coupled plasma mass spectrometry. *Anal. Chem.* **80**, 4455–4486 (2008).

[23] Fassel, V. A. & Kniseley, R. N. Inductively coupled plasma - optical emission spectroscopy. *Anal. Chem.* **46**, 1110A–1120a (1974).

[24] Goldman, M., Goldman, A. & Sigmond, R. The corona discharge, its properties and specific uses. *Pure Appl. Chem.* **57**, 1353–1362 (1985).

[25] Reuter, S., Von Woedtke, T. & Weltmann, K.-D. The kINPen—a review on physics and chemistry of the atmospheric pressure plasma jet and its applications. *J. Phys. D: Appl. Phys* **51** (2018).

[26] Gorbanev, Y., Golda, J., Schulz-von der Gathen, V. & Bogaerts, A. Applications of the COST plasma jet: More than a reference standard. *Plasma* **2**, 316–327 (2019).

[27] Golda, J., Held, J., Redeker, B., Konkowski, M., Beijer, P., Sobota, A., Kroesen, G., Braithwaite, N. S. J., Reuter, S., Turner, M., Gans, T., D, O. & Schulz-von der Gathen, V. Concepts and characteristics of the 'COST Reference Microplasma Jet'. *J. Phys. D: Appl. Phys* **49** (2016).

[28] Adamovich, I., Baalrud, S., Bogaerts, A., Bruggeman, P., Cappelli, M., Colombo, V., Czarnetzki, U., Ebert, U., Eden, J., Favia, P. *et al.* The 2017 Plasma Roadmap: Low temperature plasma science and technology. *J. Phys. D: Appl. Phys* **50** (2017).

[29] Samukawa, S., Hori, M., Rauf, S., Tachibana, K., Bruggeman, P., Kroesen, G., Whitehead, J. C., Murphy, A. B., Gutsol, A. F., Starikovskaia, S., Kortshagen, U., Boeuf, J.-P., Sommerer, T. J., Kushner, M. J., Czarnetzki, U. & Mason, N. The 2012 Plasma Roadmap. *J. Phys. D: Appl. Phys* **45** (2012).

[30] Förster, S., Mohr, C. & Viöl, W. Investigations of an atmospheric pressure plasma jet by optical emission spectroscopy. *Surf. Coat. Technol.* **200**, 827–830 (2005).

[31] Xiong, Q., Nikiforov, A. Y., Gonzalez, M. A., Leys, C. & Lu, X. P. Characterization of an atmospheric helium plasma jet by relative and absolute optical emission spectroscopy. *Plasma Sources Sci. Technol.* **22** (2012).

[32] Zhu, X.-M., Pu, Y.-K., Balcon, N. & Boswell, R. Measurement of the electron density in atmospheric-pressure low-temperature argon discharges by line-ratio method of optical emission spectroscopy. *J. Phys. D: Appl. Phys* **42** (2009).

[33] Pei, X., Wu, S., Xian, Y., Lu, X. & Pan, Y. On OH density of an atmospheric pressure plasma jet by laser-induced fluorescence. *IEEE Trans. Plasma Sci.* **42**, 1206–1210 (2014).

[34] Hübner, S., Sousa, J. S., Puech, V., Kroesen, G. & Sadeghi, N. Electron properties in an atmospheric helium plasma jet determined by Thomson scattering. *J. Phys. D: Appl. Phys* **47** (2014).

[35] Jia, F., Sumi, N., Ishikawa, K., Kano, H., Inui, H., Kularatne, J., Takeda, K., Kondo, H., Sekine, M., Kono, A. *et al.* Laser scattering diagnosis of a 60-Hz non-equilibrium atmospheric pressure plasma jet. *Appl. Phys. Express.* **4** (2011).

[36] Langmuir, I. & Jones, H. A. Collisions between electrons and gas molecules. *Phys. Rev.* **31**, 357 (1928).

[37] Shun'ko, E. V. *Langmuir probe in theory and practice* (Universal-Publishers, 2009).

[38] Srivastava, A. K., Garg, M. K., Prasad, K. G., Kumar, V., Chowdhuri, M. B. & Prakash, R. Characterization of atmospheric pressure glow discharge in helium using Langmuir probe, emission spectroscopy, and discharge resistivity. *IEEE Trans. Plasma Sci.* **35**, 1135–1142 (2007).

[39] Prevosto, L., Kelly, H. & Mancinelli, B. Langmuir probe diagnostics of an atmospheric pressure, vortex–stabilized nitrogen plasma jet. *J. Appl. Phys.* **112** (2012).

[40] Xu, K. G. & Doyle, S. J. Measurement of atmospheric pressure microplasma jet with Langmuir probes. *J. Vac. Sci. Technol. A* **34** (2016).

[41] Judée, F., Vaquero, J., Guégan, S., Fouassier, L. & Dufour, T. Atmospheric pressure plasma jets applied to cancerology: correlating electrical configuration with in vivo toxicity and therapeutic efficiency. *J. Phys. D: Appl. Phys* **52** (2019).

[42] Fang, Z., Shao, T., Yang, J. & Zhang, C. Discharge processes and an electrical model of atmospheric pressure plasma jets in argon. *Eur. Phys. J. D* **70**, 1–8 (2016).

[43] Marinov, D. & Braithwaite, N. S. J. Power coupling and electrical characterization of a radio-frequency micro atmospheric pressure plasma jet. *Plasma Sources Sci. Technol.* **23** (2014).

[44] Naudé, N., Cambronne, J., Gherardi, N. & Massines, F. Electrical model and analysis of the transition from an atmospheric pressure townsend discharge to a filamentary discharge. *J. Phys. D: Appl. Phys* **38**, 530 (2005).

[45] Tajima, T. *Computational plasma physics: with applications to fusion and astrophysics* (CRC press, 2018).

[46] Qu, C. *Computational Investigations of Fundamental Plasma Processes in Semiconductor Industrial Applications*. Ph.D. thesis, University of Michigan (2020).

[47] Van Gaens, W. & Bogaerts, A. Kinetic modelling for an atmospheric pressure argon plasma jet in humid air. *J. Phys. D: Appl. Phys* **46** (2013).

[48] Sang, C., Sun, J. & Wang, D. Plasma density enhancement in atmospheric-pressure dielectric-barrier discharges by high-voltage nanosecond pulse in the pulse-on period: a PIC simulation. *J. Phys. D: Appl. Phys* **43** (2010).

[49] Zhang, Y., Wang, H.-y., Jiang, W. & Bogaerts, A. Two-dimensional particle-in cell/monte carlo simulations of a packed-bed dielectric barrier discharge in air at atmospheric pressure. *New J. Phys.* **17** (2015).

[50] Wang, L., Zheng, Y. & Jia, S. Numerical study of the interaction of a helium atmospheric pressure plasma jet with a dielectric material. *Phys. Plasmas* **23** (2016).

[51] Hemke, T., Wollny, A., Gebhardt, M., Brinkmann, R. P. & Mussenbrock, T. Spatially resolved simulation of a radio-frequency driven micro-atmospheric pressure plasma jet and its effluent. *J. Phys. D: Appl. Phys* **44** (2011).

[52] Norberg, S. A., Johnsen, E. & Kushner, M. J. Helium atmospheric pressure plasma jets touching dielectric and metal surfaces. *J. Appl. Phys.* **118** (2015).

[53] Zhu, P., Li, B., Duan, Z. & Ouyang, J. Development from dielectric barrier discharge to atmospheric pressure plasma jet in helium: experiment and fluid modeling. *J. Phys. D: Appl. Phys* **51** (2018).

[54] Jánskỳ, J., Le Delliou, P., Tholin, F., Tardiveau, P., Bourdon, A. & Pasquiers, S. Experimental and numerical study of the propagation of a discharge in a capillary tube in air at atmospheric pressure. *J. Phys. D: Appl. Phys* **44** (2011).

[55] Schutze, A., Jeong, J. Y., Babayan, S. E., Park, J., Selwyn, G. S. & Hicks, R. F. The atmospheric-pressure plasma jet: a review and comparison to other plasma sources. *IEEE Trans. Plasma Sci.* **26**, 1685–1694 (1998).

[56] Grosse, A., Leutner, H. & Stokes, C. Plasma jet chemistry. Tech. Rep., Temple University Philadelphia Research Institute (1961).

[57] Freeman, M. P. A quantitative examination of the LTE condition in the effluent of an atmospheric pressure argon plasma jet. *J. Quant. Spectrosc. Radiat. Transf.* **8**, 435–450 (1968).

[58] Grey, J., Williams, P. M. & Fradkin, D. B. Mixing and heat transfer of an argon arc jet with a coaxial flow of cold helium. *NASA CR-54432* (1964).

[59] Martiniuk, S., Motornenko, O. & Usikov, O. I. Generator of cold plasma. *Akademiia Nauk Ukrains koi RSR Dopovidi Seriia Fiziko Matematichni ta Tekhnichni Nauki* 734–737 (1975).

[60] Martiniuk, S. & Motornenko, O. Some characteristics of a cold-plasma generator. *Akademiia Nauk Ukrains koi RSR Dopovidi Seriia Fiziko Matematichni ta Tekhnichni Nauki* 161–164 (1978).

[61] Koinuma, H., Ohkubo, H., Hashimoto, T., Inomata, K., Shiraishi, T., Miyanaga, A. & Hayashi, S. Development and application of a microbeam plasma generator. *Appl. Phys. Lett.* **60**, 816–817 (1992).

[62] Park, J., Henins, I., Herrmann, H., Selwyn, G., Jeong, J., Hicks, R., Shim, D. & Chang, C. An atmospheric pressure plasma source. *Appl. Phys. Lett.* **76**, 288–290 (2000).

[63] Penkov, O. V., Khadem, M., Lim, W.-S. & Kim, D.-E. A review of recent applications of atmospheric pressure plasma jets for materials processing. *J. Coat. Technol. Res.* **12**, 225–235 (2015).

[64] Fanelli, F. & Fracassi, F. Atmospheric pressure non-equilibrium plasma jet technology: general features, specificities and applications in surface processing of materials. *Surface and Coatings Technology* **322**, 174–201 (2017).

[65] Winter, J., Brandenburg, R. & Weltmann, K. Atmospheric pressure plasma jets: an overview of devices and new directions. *Plasma Sources Sci. Technol.* **24** (2015).

[66] Uhm, H. S., Lim, J. P. & Li, S. Z. Sterilization of bacterial endospores by an atmospheric-pressure argon plasma jet. *Appl. Phys. Lett.* **90** (2007).

[67] Nastuta, A. V., Topala, I., Grigoras, C., Pohoata, V. & Popa, G. Stimulation of wound healing by helium atmospheric pressure plasma treatment. *J. Phys. D: Appl. Phys* **44** (2011).

[68] Ma, S., Lee, M.-H., Kang, S. U., Lee, Y. S., Kim, C.-H. & Kim, K. Development of an atmospheric nonthermal multineedle dielectric barrier discharge jet for large area treatment of skin diseases. *Curr. Appl. Phys.* **24**, 24–31 (2021).

[69] Kim, S. J., Chung, T., Bae, S. & Leem, S. Induction of apoptosis in human breast cancer cells by a pulsed atmospheric pressure plasma jet. *Appl. Phys. Lett.* **97** (2010).

[70] Laroussi, M. Cold plasma in medicine and healthcare: the new frontier in low temperature plasma applications. *Front. Phys.* **8**, 74 (2020).

[71] Graves, D. B. Low temperature plasma biomedicine: A tutorial review. *Phys. Plasmas* **21** (2014).

[72] Sakudo, A., Yagyu, Y. & Onodera, T. Disinfection and sterilization using plasma technology: Fundamentals and future perspectives for biological applications. *Int. J. Mol. Sci.* **20** (2019).

[73] Patelli, A., Verga, E., Nodari, L., Petrillo, S., Delva, A., Ugo, P. & Scopece, P. A customised atmospheric pressure plasma jet for conservation requirements. In *IOP Conference Series: Materials Science and Engineering*, vol. 364, 012079 (IOP Publishing, 2018).

[74] Schalm, O., Patelli, A., Storme, P., Crabbé, A., Voltolina, S., Feyer, V. & Terryn, H. Tarnished silver–copper surfaces reduction using remote helium plasma at atmospheric pressure studied by means of high-resolution synchrotron X-ray photoelectron microscopy. *Corros. Sci.* **178** (2021).

[75] Kusano, Y. Atmospheric pressure plasma processing for polymer adhesion: a review. *J Adhes.* **90**, 755–777 (2014).

[76] Lommatzsch, U., Pasedag, D., Baalmann, A., Ellinghorst, G. & Wagner, H.-E. Atmospheric pressure plasma jet treatment of polyethylene surfaces for adhesion improvement. *Plasma Process Polym.* **4**, S1041–S1045 (2007).

[77] Shaw, D., West, A., Bredin, J. & Wagenaars, E. Mechanisms behind surface modification of polypropylene film using an atmospheric-pressure plasma jet. *Plasma Sources Sci. Technol.* **25** (2016).

[78] Gandhiraman, R. P., Singh, E., Diaz-Cartagena, D. C., Nordlund, D., Koehne, J. & Meyyappan, M. Plasma jet printing for flexible substrates. *Appl. Phys. Lett.* **108** (2016).

[79] Scopece, P., Viaro, A., Sulcis, R., Kulyk, I., Patelli, A. & Guglielmi, M. SiO_x-based gas barrier coatings for polymer substrates by atmospheric pressure plasma jet deposition. *Plasma Process. Polym.* **6**, S705–S710 (2009).

[80] Knake, N., Reuter, S., Niemi, K., Schulz-Von Der Gathen, V. & Winter, J. Absolute atomic oxygen density distributions in the effluent of a microscale atmospheric pressure plasma jet. *J. Phys. D: Appl. Phys* **41** (2008).

[81] Zhang, S., Van Gaens, W., Van Gessel, B., Hofmann, S., Van Veldhuizen, E., Bogaerts, A. & Bruggeman, P. Spatially resolved ozone densities and gas temperatures in a time modulated RF driven atmospheric pressure plasma jet: an analysis of the production and destruction mechanisms. *J. Phys. D: Appl. Phys* **46** (2013).

[82] Thiyagarajan, M., Sarani, A. & Nicula, C. Optical emission spectroscopic diagnostics of a non-thermal atmospheric pressure helium-oxygen plasma jet for biomedical applications. *J. Appl. Phys.* **113** (2013).

[83] Van Gessel, A., Van Grootel, S. & Bruggeman, P. Atomic oxygen TALIF measurements in an atmospheric-pressure microwave plasma jet with in situ xenon calibration. *Plasma Sources Sci. Technol.* **22** (2013).

[84] Norberg, S. A., Johnsen, E. & Kushner, M. J. Formation of reactive oxygen and nitrogen species by repetitive negatively pulsed helium atmospheric pressure plasma jets propagating into humid air. *Plasma Sources Sci. Technol.* **24** (2015).

[85] Lee, S. W., Liang, D., Gao, X. P. & Sankaran, R. M. Direct writing of metal nanoparticles by localized plasma electrochemical reduction of metal cations in polymer films. *Adv. Funct. Mater.* **21**, 2155–2161 (2011).

[86] Lee, S. W., Kumpfer, J. R., Lin, P. A., Li, G., Gao, X. P., Rowan, S. J. & Sankaran, R. M. In situ formation of metal nanoparticle composites via "soft" plasma electrochemical reduction of metallosupramolecular polymer films. *Macromolecules* **45**, 8201–8210 (2012).

[87] Richmonds, C. & Sankaran, R. M. Plasma-liquid electrochemistry: Rapid synthesis of colloidal metal nanoparticles by microplasma reduction of aqueous cations. *Appl. Phys. Lett.* **93** (2008).

[88] Richmonds, C., Witzke, M., Bartling, B., Lee, S. W., Wainright, J., Liu, C.-C. & Sankaran, R. M. Electron-transfer reactions at the plasma–liquid interface. *J. Am. Chem. Soc.* **133**, 17582–17585 (2011).

[89] Hawtof, R., Ghosh, S., Guarr, E., Xu, C., Sankaran, R. M. & Renner, J. N. Catalyst-free, highly selective synthesis of ammonia from nitrogen and water by a plasma electrolytic system. *Sci. Adv.* **5** (2019).

[90] Stuckert, E. P. & Fisher, E. R. Ar/O_2 and H_2O plasma surface modification of sno_2 nanomaterials to increase surface oxidation. *Sens. Actuators B Chem.* **208**, 379–388 (2015).

[91] Schade, H., Smith, Z. E., Thomas III, J. & Catalano, A. Hydrogen plasma interactions with tin oxide surfaces. *Thin Solid Films* **117**, 149–155 (1984).

[92] Yan, Y., Han, M., Konkin, A., Koppe, T., Wang, D., Andreu, T., Chen, G., Vetter, U., Morante, J. R. & Schaaf, P. Slightly hydrogenated TiO_2 with enhanced photocatalytic performance. *J. Mater. Chem. A* **2**, 12708–12716 (2014).

[93] Wang, Z., Yang, C., Lin, T., Yin, H., Chen, P., Wan, D., Xu, F., Huang, F., Lin, J., Xie, X. & Jiang, M. H-doped black titania with very high solar absorption and excellent photocatalysis enhanced by localized surface plasmon resonance. *Adv. Funct. Mater.* **23**, 5444–5450 (2013).

[94] Sawada, Y., Tamaru, H., Kogoma, M., Kawase, M. & Hashimoto, K. The reduction of copper oxide thin films with hydrogen plasma generated by an atmospheric-pressure glow discharge. *J. Phys. D: Appl. Phys* **29**, 2539 (1996).

[95] Sabat, K., Rajput, P., Paramguru, R., Bhoi, B. & Mishra, B. Reduction of oxide minerals by hydrogen plasma: an overview. *Plasma Chem. Plasma Process.* **34**, 1–23 (2014).

[96] Sui, Y., Zorman, C. A. & Sankaran, R. M. Plasmas for additive manufacturing. *Plasma Process, Polym.* **17** (2020).

[97] Hsu, Y.-w., Li, H.-C., Yang, Y.-J. & Hsu, C.-c. Deposition of zinc oxide thin films by an atmospheric pressure plasma jet. *Thin Solid Films* **519**, 3095–3099 (2011).

[98] Chang, K.-M., Huang, S.-H., Wu, C.-J., Lin, W.-L., Chen, W.-C., Chi, C.-W., Lin, J.-W. & Chang, C.-C. Transparent conductive indium-doped zinc oxide films prepared by atmospheric pressure plasma jet. *Thin Solid Films* **519**, 5114–5117 (2011).

[99] Babayan, S., Jeong, J., Schütze, A., Tu, V., Moravej, M., Selwyn, G. & Hicks, R. Deposition of silicon dioxide films with a non-equilibrium atmospheric-pressure plasma jet. *Plasma Sources Sci. Technol.* **10**, 573 (2001).

[100] Fakhouri, H., Salem, D. B., Carton, O., Pulpytel, J. & Arefi-Khonsari, F. Highly efficient photocatalytic TiO_2 coatings deposited by open air atmospheric pressure plasma jet with aerosolized TTIP precursor. *J. Phys. D: Appl. Phys* **47** (2014).

[101] Chen, Q., Liu, Q., Hubert, J., Huang, W., Baert, K., Wallaert, G., Terryn, H., Delplancke-Ogletree, M.-P. & Reniers, F. Deposition of photocatalytic anatase titanium dioxide films by atmospheric dielectric barrier discharge. *Surf. Coat. Technol.* **310**, 173–179 (2017).

[102] Bornholdt, S., Wolter, M. & Kersten, H. Characterization of an atmospheric pressure plasma jet for surface modification and thin film deposition. *Eur. Phys. J. D* **60**, 653–660 (2010).

[103] Carton, O., Ben Salem, D., Bhatt, S., Pulpytel, J. & Arefi-Khonsari, F. Plasma polymerization of acrylic acid by atmospheric pressure nitrogen plasma jet for biomedical applications. *Plasma Process and Polym.* **9**, 984–993 (2012).

[104] Lommatzsch, U. & Ihde, J. Plasma polymerization of HMDSO with an atmospheric pressure plasma jet for corrosion protection of aluminum and low-adhesion surfaces. *Plasma Process and Polym.* **6**, 642–648 (2009).

[105] Malinowski, S., Herbert, P. A. F., Rogalski, J. & Jaroszyńska-Wolińska, J. Laccase enzyme polymerization by soft plasma jet for durable bioactive coatings. *Polymers* **10**, 532 (2018).

[106] Brooks, A., Woollard, S., Hennighan, G. & von Werne, T. Plasma polymerization: A versatile and attractive process for conformal coating. In *SMTA International Conference* (Surface Mount Technology Association, Orlando, FL, 2012).

[107] Beier, O., Pfuch, A., Horn, K., Weisser, J., Schnabelrauch, M. & Schimanski, A. Low temperature deposition of antibacterially active silicon oxide layers containing silver nanoparticles, prepared by atmospheric pressure plasma chemical vapor deposition. *Plasma Process Polym.* **10**, 77–87 (2013).

[108] Zhao, P., Zheng, W., Meng, Y. & Nagatsu, M. Characteristics of high-purity Cu thin films deposited on polyimide by radio-frequency Ar/H_2 atmospheric-pressure plasma jet. *J. Appl. Phys.* **113** (2013).

[109] Gandhiraman, R. P., Jayan, V., Han, J.-W., Chen, B., Koehne, J. E. & Meyyappan, M. Plasma jet printing of electronic materials on flexible and nonconformal objects. *ACS applied materials & interfaces* **6**, 20860–20867 (2014).

[110] Lazea-Stoyanova, A., Vlad, A., Vlaicu, A. M., Teodorescu, V. S. & Dinescu, G. Synthesis of copper particles by non-thermal atmospheric pressure plasma jet. *Plasma Process Polym.* **12**, 705–709 (2015).

[111] Kredl, J., Kolb, J. F., Schnabel, U., Polak, M., Weltmann, K.-D. & Fricke, K. Deposition of antimicrobial copper-rich coatings on polymers by atmospheric pressure jet plasmas. *Materials* **9**, 274 (2016).

[112] Dey, A., Lopez, A., Filipič, G., Jayan, A., Nordlund, D., Koehne, J., Krishnamurthy, S., Gandhiraman, R. P. & Meyyappan, M. Plasma jet based in situ reduction of copper oxide in direct write printing. *J. Vac. Sci. Technol. B* **37** (2019).

[113] Hong, J., Yick, S., Chow, E., Murdock, A., Fang, J., Seo, D. H., Wolff, A., Han, Z., Van Der Laan, T., Bendavid, A. *et al.* Direct plasma printing of nano-gold from an inorganic precursor. *J. Mater. Chem. C.* **7**, 6369–6374 (2019).

[114] Kornbluth, Y., Mathews, R., Parameswaran, L., Racz, L. M. & Velásquez-García, L. F. Nano-additively manufactured gold thin films with high adhesion and near-bulk electrical resistivity via jet-assisted, nanoparticle-dominated, room-temperature microsputtering. *Addit. Manuf.* **36** (2020).

[115] Nakahiro, H., Zhao, P., Ogino, A., Zheng, W., Meng, Y. & Nagatsu, M. Effect of hydrogen reduction on characteristics of Cu thin-films deposited by RF-driven Ar/H_2 atmospheric pressure plasma jet. *Appl. Phys. Express.* **5**, 056201 (2012).

[116] Zhao, P., Zheng, W., Watanabe, J., Meng, Y. D. & Nagatsu, M. Highly conductive Cu thin film deposition on polyimide by RF-driven atmospheric pressure plasma jets under nitrogen atmosphere. *Plasma Process Polym.* **12**, 431–438 (2015).

[117] Connor, N. O., Gandhiraman, R. P., Doyle, C., James, B., Williams, D. E. & Daniels, S. Room temperature deposition of tunable plasmonic nanostructures by atmospheric pressure jet plasma. *J. Mater. Chem.* **22**, 9485–9489 (2012).

[118] Saito, S., Razzak, M., Takamura, S. & Talukder, M. Development of asymmetric double probe formula and its application for collisional plasmas. *J. Appl. Phys.* **107** (2010).

[119] Phelps Database. private communication. www.lxcat.net (Online; retrieved 29 April 2020).

[120] Rumble Jr, J., Bickham, D. & Powell, C. The NIST X-ray photoelectron spectroscopy database. *Surf. Interface Anal.* **19**, 241–246 (1992).

[121] Walton, J., Wincott, P., Fairley, N. & Carrick, A. *Peak fitting with CasaXPS: a casa pocket book* (Accolyte Science, 2010).

[122] Shi, J., Liu, D. & Kong, M. G. Mitigating plasma constriction using dielectric barriers in radio-frequency atmospheric pressure glow discharges. *Appl. Phys. Lett.* **90** (2007).

[123] Massines, F., Messaoudi, R. & Mayoux, C. Comparison between air filamentary and helium glow dielectric barrier discharges for the polypropylene surface treatment. *Plasmas Polym.* **3**, 43–59 (1998).

[124] Pagliarani, A., Kenyon, A., Thornhill, N., Sirisena, E., Lee, K. & Law, V. Process harmonic pulling in RIE plasma-tool. *Electron. Lett.* **42**, 120–121 (2006).

[125] Law, V. & Anghel, S. Compact atmospheric pressure plasma self-resonant drive circuits. *J. Phys. D: Appl. Phys* **45** (2012).

[126] Chase, M., Jr. NIST-JANAF Themochemical Tables, Fourth Edition. *J. Phys. Chem. Ref. Data* (1998).

[127] Lienhard, I. & John, H. *A heat transfer textbook* (Phlogiston Press, 2005).

[128] Lide, D. R. *CRC handbook of chemistry and physics*, vol. 85 (CRC press, 2004).

[129] Chang, Z., Jiang, N., Zhang, G. & Cao, Z. Influence of Penning effect on the plasma features in a non-equilibrium atmospheric pressure plasma jet. *J. Appl. Phys.* **115** (2014).

[130] Marques, L., Jolly, J. & Alves, L. Capacitively coupled radio-frequency hydrogen discharges: The role of kinetics. *J. Appl. Phys.* **102** (2007).

[131] Lebedev, Y. A. & Shakhatov, V. Diagnostics of a nonequilibrium nitrogen plasma from the emission spectra of the second positive system of N_2. *Plasma Phys. Rep.* **32**, 56–71 (2006).

[132] Pellerin, S., Cormier, J., Richard, F., Musiol, K. & Chapelle, J. A spectroscopic diagnostic method using UV OH band spectrum. *J. Phys. D: Appl. Phys* **29**, 726 (1996).

[133] Pipa, A., Reuter, S., Foest, R. & Weltmann, K. Controlling the NO production of an atmospheric pressure plasma jet. *J. Phys. D: Appl. Phys* **45** (2012).

[134] Linstrom, P. J. & Mallard, W. G. The NIST Chemistry WebBook: a chemical data resource on the internet. *J. Chem. Eng. Data* **46**, 1059–1063 (2001).

[135] Golubovskii, Y. B., Maiorov, V., Behnke, J. & Behnke, J. Modelling of the homogeneous barrier discharge in helium at atmospheric pressure. *J. Phys. D: Appl. Phys* **36**, 39 (2002).

[136] Lazarou, C., Koukounis, D., Chiper, A., Costin, C., Topala, I. & Georghiou, G. E. Numerical modeling of the effect of the level of nitrogen impurities in a helium parallel plate dielectric barrier discharge. *Plasma Sources Sci. Technol.* **24** (2015).

[137] Yao, C.-W., Chang, Z.-S., Ma, H., Xu, G., Mu, H. & Zhang, G.-J. Experimental research on mode transitions of atmospheric pressure helium dielectric barrier discharge. *IEEE Trans. Plasma Sci.* **44**, 2576–2588 (2016).

[138] Massines, F., Gherardi, N., Naudé, N. & Ségur, P. Recent advances in the understanding of homogeneous dielectric barrier discharges. *EPJ Appl. Phys.* **47**, 22805 (2009).

[139] Jiang, N. Electron beam damage in oxides: a review. *Rep. Prog. Phys.* **79** (2015).

[140] Dulub, O., Batzilln, M., Solovev, S., Loginova, E., Alchagirov, A., Madey, T. E. & Diebold, U. Electron-induced oxygen desorption from the TiO_2 (011)-2$\times$ 1 surface leads to self-organized vacancies. *Science* **317**, 1052–1056 (2007).

[141] Liu, Y., Liu, Y., Mu, R., Yang, H., Shao, C., Zhang, J., Lu, Y., Shen, D. & Fan, X. The structural and optical properties of Cu_2O films electrodeposited on different substrates. *Semicond. Sci. Technol.* **20**, 44 (2004).

[142] Balkanski, M., Nusimovici, M. A. & Reydellet, J. First order Raman spectrum of Cu_2O. *Solid State Commun.* **7**, 815–818 (1969).

[143] Ellis, H., McDaniel, E., Albritton, D., Viehland, L., Lin, S. & Mason, E. Transport properties of gaseous ions over a wide energy range. part ii. *At. Data Nucl. Data Tables* **22**, 179–217 (1978).

[144] Nadesalingam, M., Mukherjee, S., Somasundaram, S., Chenthamarakshan, C., de Tacconi, N. R., Rajeshwar, K. & Weiss, A. Effect of vacuum annealing on the surface chemistry of electrodeposited copper (I) oxide layers as probed by positron annihilation induced Auger electron spectroscopy. *Langmuir* **23**, 1830–1834 (2007).

[145] Poulston, S., Parlett, P. M., Stone, P. & Bowker, M. Surface oxidation and reduction of CuO and Cu_2O studied using XPS and XAES. *Surf. Interface Anal.* **24**, 811–820 (1996).

[146] Fleisch, T. & Mains, G. Reduction of copper oxides by UV radiation and atomic hydrogen studied by XPS. *Appl. Surf. Sci.* **10**, 51–62 (1982).

[147] Godyak, V. A. Measuring EEDF in gas discharge plasmas. In *Plasma-Surface Interactions and Processing of Materials*, 95–134 (Springer, 1990).

[148] Knotek, M. Stimulated desorption. *Rep. Prog. Phys.* **47**, 1499 (1984).

[149] Biesinger, M. C. Advanced analysis of copper X-ray photoelectron spectra. *Surf. Interface Anal.* **49**, 1325–1334 (2017).

[150] Kohl, H. & Reimer, L. *Transmission electron microscopy: physics of image formation* (Springer, 2008).

[151] Menzel, D. Electron stimulated desorption: Principles and recent developments. *Surf. Sci.* **47**, 370–383 (1975).

[152] Smith, D. J., McCartney, M. & Bursill, L. The electron-beam-induced reduction of transition metal oxide surfaces to metallic lower oxides. *Ultramicroscopy* **23**, 299–303 (1987).

[153] Govardhan, K. & Grace, A. N. Metal/metal oxide doped semiconductor based metal oxide gas sensors—a review. *Sens. Lett.* **14**, 741–750 (2016).

[154] Poulston, S., Price, N. J., Weeks, C., Allen, M. D., Parlett, P., Steinberg, M. & Bowker, M. Surface redox characteristics of mixed oxide catalysts used for selective oxidation. *J. Catal.* **178**, 658–667 (1998).

[155] Xu, J.-C., Shi, Y.-L., Huang, J.-E., Wang, B. & Li, H.-L. Doping metal ions only onto the catalyst surface. *J. Mol. Catal. A Chem.* **219**, 351–355 (2004).

[156] Debbichi, L., Marco de Lucas, M., Pierson, J. & Kruger, P. Vibrational properties of CuO and Cu_4O_3 from first-principles calculations, and Raman and infrared spectroscopy. *J. Phys. Chem. C* **116**, 10232–10237 (2012).

[157] Diebold, U. & Madey, T. TiO_2 by xps. *Surf. Sci. Spectra* **4**, 227–231 (1996).

[158] Gonbeau, D., Guimon, C., Pfister-Guillouzo, G., Levasseur, A., Meunier, G. & Dormoy, R. XPS study of thin films of titanium oxysulfides. *Surf. Sci.* **254**, 81–89 (1991).

[159] Kurtz, R. L. & Henrich, V. Comparison of Ti 2 p core-level peaks from TiO_2, Ti_2O_3, and Ti metal, by XPS. *Surf. Sci. Spectra* **5**, 179–181 (1998).

[160] Chen, S., Xiao, Y., Wang, Y., Hu, Z., Zhao, H. & Xie, W. A facile approach to prepare black TiO_2 with oxygen vacancy for enhancing photocatalytic activity. *Nanomaterials* **8**, 245 (2018).

[161] Sener, M. E., Sathasivam, S., Palgrave, R., Cabrera, R. Q. & Caruana, D. J. Patterning of metal oxide thin films using a H_2/He atmospheric pressure plasma jet. *Green Chem.* **22**, 1406–1413 (2020).

[162] Sasaki, M., Sasaki, M., Tsutsumi, T., Ishikawa, K. & Hori, M. Formation of spherical Sn particles by reducing SnO_2 film in floating wire-assisted H_2/Ar plasma at atmospheric pressure. *Sci. Rep* **10**, 1–12 (2020).

[163] Stranick, M. A. & Moskwa, A. SnO_2 by XPS. *Surf. Sci. Spectra* **2**, 50–54 (1993).

[164] Giefers, H., Porsch, F. & Wortmann, G. Kinetics of the disproportionation of SnO. *Solid State Ion.* **176**, 199–207 (2005).

[165] Szilágyi, I. M., Fórizs, B., Rosseler, O., Szegedi, Á., Németh, P., Király, P., Tárkányi, G., Vajna, B., Varga-Josepovits, K., László, K. *et al.* WO_3 photocatalysts: Influence of structure and composition. *J. Catal.* **294**, 119–127 (2012).

[166] Fleisch, T. H. & Mains, G. J. An XPS study of the UV reduction and photochromism of MoO_3 and WO_3. *J. Chem. Phys.* **76**, 780–786 (1982).

[167] Xie, F., Gong, L., Liu, X., Tao, Y. T., Zhang, W. H., Chen, S. H., Meng, H. & Chen, J. XPS studies on surface reduction of tungsten oxide nanowire film by Ar^+ bombardment. *J Electron. Spectrosc.* **185**, 112–118 (2012).

[168] Leftheriotis, G., Papaefthimiou, S., Yianoulis, P. & Siokou, A. Effect of the tungsten oxidation states in the thermal coloration and bleaching of amorphous WO_3 films. *Thin Solid Films* **384**, 298–306 (2001).

[169] Xu, N., Sun, M., Cao, Y., Yao, J. & Wang, E. Influence of pH on structure and photochromic behavior of nanocrystalline WO_3 films. *Appl. Surf. Sci.* **157**, 81–84 (2000).

[170] De Angelis, B. & Schiavello, M. X-ray photoelectron spectroscopy study of nonstoichiometric tungsten oxides. *J. Solid State Chem.* **21**, 67–72 (1977).

[171] Chang, F.-M., Brahma, S., Huang, J.-H., Wu, Z.-Z. & Lo, K.-Y. Strong correlation between optical properties and mechanism in deficiency of normalized self-assembly ZnO nanorods. *Sci. Rep.* **9**, 1–9 (2019).

[172] Li, X., Wang, Y., Liu, W., Jiang, G. & Zhu, C. Study of oxygen vacancies influence on the lattice parameter in ZnO thin film. *Mater. Lett.* **85**, 25–28 (2012).

[173] Kurtz, R. L. & Henrich, V. UHV cleaved single crystal Ti_2O_3 (1012) by UPS and XPS. *Surf. Sci. Spectra* **5**, 182–185 (1998).

[174] Losev, A., Rostov, K. & Tyuliev, G. Electron beam induced reduction of CuO in the presence of a surface carbonaceous layer: an XPS/HREELS study. *Surf. Sci.* **213**, 564–579 (1989).

[175] Lin, T.-Y., Lee, S.-K., Huang, G.-M., Huang, C.-W., Tai, K.-L., Huang, C.-Y., Lo, Y.-C. & Wu, W.-W. Electron beam irradiation-induced deoxidation and atomic flattening on the copper surface. *ACS Appl. Mater. Interfaces* **11**, 40909–40915 (2019).

[176] Garvin, D., Parker, V. B. & White Jr, H. J. *CODATA thermodynamic tables* (Springer-Verlag New York Inc., New York, NY, 1987).

[177] Chen, X., Liu, L., Peter, Y. Y. & Mao, S. S. Increasing solar absorption for photocatalysis with black hydrogenated titanium dioxide nanocrystals. *Science* **331**, 746–750 (2011).

[178] Chen, X., Liu, L. & Huang, F. Black titanium dioxide (TiO_2) nanomaterials. *Chem. Soc. Rev.* **44**, 1861–1885 (2015).

[179] El-Gendy, D. M., Ghany, N. A. A. & Allam, N. K. Black titania nanotubes/spongy graphene nanocomposites for high-performance supercapacitors. *RSC Adv.* **9**, 12555–12566 (2019).

[180] Xu, J., Qi, X., Luo, C., Qiao, J., Xie, R., Sun, Y., Zhong, W., Fu, Q. & Pan, C. Synthesis and enhanced microwave absorption properties: a strongly hydrogenated TiO_2 nanomaterial. *Nanotechnology* **28** (2017).

[181] Ullattil, S. G., Thelappurath, A. V., Tadka, S. N., Kavil, J., Vijayan, B. K. & Periyat, P. A sol-solvothermal processed "Black TiO_2" as photoanode material in dye sensitized solar cells. *Sol. Energy* **155**, 490–495 (2017).

[182] Wang, G., Wang, H., Ling, Y., Tang, Y., Yang, X., Fitzmorris, R. C., Wang, C., Zhang, J. Z. & Li, Y. Hydrogen-treated TiO_2 nanowire arrays for photoelectrochemical water splitting. *Nano Lett.* **11**, 3026–3033 (2011).

[183] Bi, Q., Huang, X., Dong, Y. & Huang, F. Conductive black titania nanomaterials for efficient photocatalytic degradation of organic pollutants. *Catal. Letters* **150**, 1346–1354 (2020).

[184] Rahimi, N., Pax, R. & Gray, E. M. Review of functional titanium oxides. ii: Hydrogen-modified TiO_2. *Prog. Solid State. Ch.* **55**, 1–19 (2019).

[185] Zhang, K. & Park, J. H. Surface localization of defects in black TiO_2: enhancing photoactivity or reactivity. *J. Phys. Chem. Lett.* **8**, 199–207 (2017).

[186] Rajaraman, T., Parikh, S. P. & Gandhi, V. G. Black TiO_2: A review of its properties and conflicting trends. *Chem. Eng. J.* **389** (2020).

[187] Ullattil, S. G., Narendranath, S. B., Pillai, S. C. & Periyat, P. Black TiO_2 nanomaterials: a review of recent advances. *Chem. Eng. J.* **343**, 708–736 (2018).

[188] Islam, S. Z., Reed, A., Nagpure, S., Wanninayake, N., Browning, J. F., Strzalka, J., Kim, D. Y. & Rankin, S. E. Hydrogen incorporation by plasma treatment gives mesoporous black TiO_2 thin films with visible photoelectrochemical water oxidation activity. *Micropor. and Mesopor. Mat.* **261**, 35–43 (2018).

[189] Mohammadizadeh, M., Bagheri, M., Aghabagheri, S. & Abdi, Y. Photocatalytic activity of TiO_2 thin films by hydrogen DC plasma. *Appl. Surf. Sci.* **350**, 43–49 (2015).

[190] Yue, Y., Kondeti, V. & Bruggeman, P. Absolute atomic hydrogen density measurements in an atmospheric pressure plasma jet: generation, transport and recombination from the active discharge region to the effluent. *Plasma Sources Sci. Technol.* **29** (2020).

[191] de Araujo, M. A., Gromboni, M. F., Marken, F., Parker, S. C., Peter, L. M., Turner, J., Aspinall, H. C., Black, K. & Mascaro, L. H. Contrasting transient photocurrent characteristics for thin films of vacuum-doped "grey" TiO_2 and "grey" NbO_5. *Appl. Catal. B* **237**, 339–352 (2018).

[192] Inc., W. R. Mathematica, Version 12.2. URL https://www.wolfram.com/mathematica. Champaign, IL, 2020.

[193] Voráč, J., Synek, P. *et al.* MassiveOES: Open source software–bringing big data processing to spectroscopy. In *International conference on Data-driven Plasma Science* (2018).

[194] Makuła, P., Pacia, M. & Macyk, W. How to correctly determine the band gap energy of modified semiconductor photocatalysts based on UV–Vis spectra. *J. Phys. Chem. Lett.* **9**, 6814–6817 (2018).

[195] Naldoni, A., Allieta, M., Santangelo, S., Marelli, M., Fabbri, F., Cappelli, S., Bianchi, C. L., Psaro, R. & Dal Santo, V. Effect of nature and location of defects on bandgap narrowing in black TiO_2 nanoparticles. *J. Am. Chem. Soc.* **134**, 7600–7603 (2012).

[196] Ohsaka, T., Izumi, F. & Fujiki, Y. Raman spectrum of anatase, TiO_2. *J. Raman Spectrosc.* **7**, 321–324 (1978).

[197] Zimbone, M., Cacciato, G., Sanz, R., Carles, R., Gulino, A., Privitera, V. & Grimaldi, M. G. Black TiO_x photocatalyst obtained by laser irradiation in water. *Catal. Commun.* **84**, 11–15 (2016).

[198] Leshuk, T., Parviz, R., Everett, P., Krishnakumar, H., Varin, R. A. & Gu, F. Photocatalytic activity of hydrogenated TiO_2. *ACS Appl. Mater. Interfaces* **5**, 1892–1895 (2013).

[199] Hanaor, D. A. & Sorrell, C. C. Review of the anatase to rutile phase transformation. *J. Mater. Sci.* **46**, 855–874 (2011).

[200] Pei, Z., Ding, L., Lin, H., Weng, S., Zheng, Z., Hou, Y. & Liu, P. Facile synthesis of defect-mediated TiO_{2-x} with enhanced visible light photocatalytic activity. *J. Mater. Chem.* **1**, 10099–10102 (2013).

[201] Zou, X., Liu, J., Su, J., Zuo, F., Chen, J. & Feng, P. Facile synthesis of thermal-and photostable titania with paramagnetic oxygen vacancies for visible-light photocatalysis. *Chem. Eur. J.* **19**, 2866–2873 (2013).

[202] Wheeler, D. A., Ling, Y., Dillon, R. J., Fitzmorris, R. C., Dudzik, C. G., Zavodivker, L., Rajh, T., Dimitrijevic, N. M., Millhauser, G., Bardeen, C. *et al.* Probing the nature of bandgap states in hydrogen-treated TiO_2 nanowires. *J. Phys. Chem. C* **117**, 26821–26830 (2013).

[203] Choi, H., Moon, S.-I., Song, T. & Kim, S. Hydrogen-free defects in hydrogenated black TiO_2. *Phys. Chem. Chem. Phys.* **20**, 19871–19876 (2018).

[204] Andreev, A. S., Kuznetsov, V. N. & Chizhov, Y. V. Atomic hydrogen activated TiO_2 nanocluster: DFT calculations. *J. Phys. Chem. C.* **116**, 18139–18145 (2012).

[205] Bonato, P. Wearable sensors and systems. *IEEE Eng. Med. Biol. Mag.* **29**, 25–36 (2010).

[206] Subramanian, V., Chang, P. C., Huang, D., Lee, J. B., Molesa, S. E., Redinger, D. R. & Volkman, S. K. All-printed RFID tags: materials, devices, and circuit implications. In *19th International Conference on VLSI Design held jointly with 5th International Conference on Embedded Systems Design*, 6 (IEEE, 2006).

[207] Petherbridge, K., Evans, P. & Harrison, D. The origins and evolution of the PCB: a review. *Circuit World* (2005).

[208] Gaikwad, A. M., Arias, A. C. & Steingart, D. A. Recent progress on printed flexible batteries: mechanical challenges, printing technologies, and future prospects. *Energy Technol.* **3**, 305–328 (2015).

[209] Fields, J., Pach, G., Horowitz, K., Stockert, T., Woodhouse, M. & van Hest, M. F. Printed interconnects for photovoltaic modules. *Sol. Energy Mater. Sol. Cells* **159**, 536–545 (2017).

[210] LaDou, J. Printed circuit board industry. *Int. J. Hyg. Environ. Health* **209**, 211–219 (2006).

[211] Dong, Y., Bao, C. & Kim, W. S. Sustainable additive manufacturing of printed circuit boards. *Joule* **2**, 579–582 (2018).

[212] Saengchairat, N., Tran, T. & Chua, C.-K. A review: Additive manufacturing for active electronic components. *Virtual Phys. Prototyp.* **12**, 31–46 (2017).

[213] Agrawal, R. & Vinodh, S. State of art review on sustainable additive manufacturing. *Rapid Prototyp. J.* (2019).

[214] Calvert, P. Inkjet printing for materials and devices. *Chem. Mater.* **13**, 3299–3305 (2001).

[215] Cummins, G. & Desmulliez, M. P. Inkjet printing of conductive materials: a review. *Circuit World* (2012).

[216] Jang, Y.-R., Joo, S.-J., Chu, J.-H., Uhm, H.-J., Park, J.-W., Ryu, C.-H., Yu, M.-H. & Kim, H.-S. A review on intense pulsed light sintering technologies for conductive electrodes in printed electronics. *Int. J. Precis. Eng. Manuf.* 1–37 (2020).

[217] Almquist, G. *Evaluation of emerging additive technologies for circuit board manufacturing*. Master's thesis, Chalmers University of Technology (2019).

[218] Li, W., Sun, Q., Li, L., Jiu, J., Liu, X.-Y., Kanehara, M., Minari, T. & Suganuma, K. The rise of conductive copper inks: challenges and perspectives. *Appl. Mater. Today* **18** (2020).

[219] Karthik, P., Singh, S. P. *et al.* Copper conductive inks: synthesis and utilization in flexible electronics. *RSC Adv.* **5**, 63985–64030 (2015).

[220] Matsson, J. *An Introduction to ANSYS Fluent 2020* (SDC Publications, 2020).

[221] Davies, T. Schlieren photography—short bibliography and review. *Opt. Laser Technol.* **13**, 37–42 (1981).

[222] Hrehorova, E., Rebros, M., Pekarovicova, A., Bazuin, B., Ranganathan, A., Garner, S., Merz, G., Tosch, J. & Boudreau, R. Gravure printing of conductive inks on glass substrates for applications in printed electronics. *J. Disp. Technol.* **7**, 318–324 (2011).

[223] Hasanuzzaman, M., Rafferty, A., Sajjia, M. & Olabi, A. Properties of glass materials. In Hashmi, S. (ed.) *Reference Module in Materials Science and Materials Engineering* (Elsevier, Amsterdam, 2016).

[224] Sugar, J. & Musgrove, A. Energy levels of copper, Cu I through Cu XXIX. *J. Phys. Chem. Ref. Data* **19**, 527–616 (1990).

[225] Awaya, N. & Arita, Y. Plasma-enhanced chemical vapor deposition of copper. *Jpn. J. Appl. Phys* **30**, 1813 (1991).

[226] Secor, E. B. Principles of aerosol jet printing. *Flex. Print. Electron.* **3** (2018).

[227] Lemmon, E. W., Huber, M. L. & McLinden, M. O. NIST reference fluid thermodynamic and transport properties - REFPROP. *NIST Standard Reference Database* **23**, v7 (2002).

[228] Shashi Menon, E. Chapter five - fluid flow in pipes. In Shashi Menon, E. (ed.) *Transmission Pipeline Calculations and Simulations Manual*, 149–234 (Gulf Professional Publishing, Boston, 2015). URL https://www.sciencedirect.com/science/article/pii/B9781856178303000055.

[229] Zheng, Y., Wang, L., Ning, W. & Jia, S. Schlieren imaging investigation of the hydrodynamics of atmospheric helium plasma jets. *J. Appl. Phys.* **119** (2016).

[230] Marple, V. A. & Willeke, K. Impactor design. *Atmos. Environ.* **10**, 891–896 (1976).

[231] Allen, M. D. & Raabe, O. G. Slip correction measurements of spherical solid aerosol particles in an improved Millikan apparatus. *Aerosol Sci. Tech.* **4**, 269–286 (1985).

[232] Loo, B. W., Adachi, R. S., Cork, C. P., Goulding, F. S., Jaklevic, J. M., Landis, D. A. & L., S. W. A second generation dichotomous sampler for large-scale monitoring of airborne particulate matter. In *Annual Meeting of the American Institute of Chemical Engineers* (American Institute of Chemical Engineers, Houston, TX, 1979).

[233] Marple, V. A. & Chien, C. M. Virtual impactors: a theoretical study. *Environ. Sci. Technol.* **14**, 976–985 (1980).

[234] Okuyama, K. & Lenggoro, I. W. Preparation of nanoparticles via spray route. *Chem. Eng. Sci.* **58**, 537–547 (2003).

[235] Eslamian, M. & Shekarriz, M. Recent advances in nanoparticle preparation by spray and microemulsion methods. *Recent Pat. Nanotechnol.* **3**, 99–115 (2009).

[236] Allen, M. L. *Nanoparticle sintering methods and applications for printed electronics*. Ph.D. thesis, Aalto University (2011).

[237] Mamedov, V. Spark plasma sintering as advanced *pm* sintering method. *Powder Metall.* **45**, 322–328 (2002).

[238] Shahmiri, M., Ibrahim, N. A., Shayesteh, F., Asim, N. & Motallebi, N. Preparation of PVP-coated copper oxide nanosheets as antibacterial and antifungal agents. *J. Mater. Res.* **28**, 3109 (2013).

[239] Dutta, B., Kar, E., Bose, N. & Mukherjee, S. Significant enhancement of the electroactive β-phase of PVDF by incorporating hydrothermally synthesized copper oxide nanoparticles. *RSC Adv.* **5**, 105422–105434 (2015).

[240] Opilik, L., Schmid, T. & Zenobi, R. Modern Raman imaging: vibrational spectroscopy on the micrometer and nanometer scales. *Annu. Rev. Anal. Chem.* **6**, 379–398 (2013).

[241] Yin, L., Adler, I., Tsang, T., Matienzo, L. & Grim, S. Paramagnetism and shake-up satellites in X-ray photoelectron spectra. *Chem. Phys. Lett.* **24**, 81–84 (1974).

[242] Mencer, D., Hossain, M., Schennach, R., Grady, T., McWhinney, H., Gomes, J., Kesmez, M., Parga, J., Barr, T. & Cocke, D. On the surface analysis of copper oxides: the difficulty in detecting cu3o2. *Vacuum* **77**, 27–35 (2004).

[243] Darezereshki, E. & Bakhtiari, F. A novel technique to synthesis of tenorite (cuo) nanoparticles from low concentration cuso4 solution. *J. Min. Metall. B* **47**, 73–78 (2011).

[244] Singh, B., Hesse, R. & Linford, M. R. Good practices for XPS (and other types of) peak fitting. *Vac. Technol. Coat* **12**, 25–31 (2015).

[245] Powell, C. J. & Jablonski, A. The NIST electron effective-attenuation-length database. *J. Surf. Anal.* **9**, 322–325 (2002).

[246] Panzner, G., Egert, B. & Schmidt, H. P. The stability of CuO and Cu_2O surfaces during argon sputtering studied by XPS and AES. *Surf. Sci.* **151**, 400–408 (1985).

[247] Urabe, K., Morita, T., Tachibana, K. & Ganguly, B. N. Investigation of discharge mechanisms in helium plasma jet at atmospheric pressure by laser spectroscopic measurements. *J. Phys. D: Appl. Phys* **43** (2010).

[248] Zaplotnik, R., Bišćan, M., Popović, D., Mozetič, M. & Milošević, S. Metastable helium atom density in a single electrode atmospheric plasma jet during sample treatment. *Plasma Sources Sci. Technol.* **25** (2016).

[249] Li, D., Sutton, D., Burgess, A., Graham, D. & Calvert, P. D. Conductive copper and nickel lines via reactive inkjet printing. *J. Mater. Chem.* **19**, 3719–3724 (2009).

[250] Deng, D., Qi, T., Cheng, Y., Jin, Y. & Xiao, F. Copper carboxylate with different carbon chain lengths as metal–organic decomposition ink. *J. Mater. Sci.: Mater. Electron.* **25**, 390–397 (2014).

[251] Farraj, Y., Grouchko, M. & Magdassi, S. Self-reduction of a copper complex mod ink for inkjet printing conductive patterns on plastics. *Chem. Commun.* **51**, 1587–1590 (2015).

[252] COMSOL Multiphysics, Burlington, MA, US. *Introduction to COMSOL multiphysics version 5.5* (2019).

[253] Alappat, C., Basermann, A., Bishop, A. R., Fehske, H., Hager, G., Schenk, O., Thies, J. & Wellein, G. A recursive algebraic coloring technique for hardware-efficient symmetric sparse matrix-vector multiplication. *ACM Trans. Parallel Comput.* **7**, 1–37 (2020).

[254] Hagelaar, G. & Pitchford, L. Solving the boltzmann equation to obtain electron transport coefficients and rate coefficients for fluid models. *Plasma Sources Sci. Technol.* **14**, 722 (2005).

[255] Godyak, V. & Demidov, V. Probe measurements of electron-energy distributions in plasmas: what can we measure and how can we achieve reliable results? *J. Phys. D: Appl. Phys* **44** (2011).

[256] Ellis, H., Pai, R., McDaniel, E., Mason, E. & Viehland, L. Transport properties of gaseous ions over a wide energy range. *At. Data Nucl. Data Tables* **17**, 177–210 (1976).

[257] Breden, D., Miki, K. & Raja, L. Self-consistent two-dimensional modeling of cold atmospheric-pressure plasma jets/bullets. *Plasma Sources Sci. Technol.* **21** (2012).

[258] Wendt, J. F. *Computational fluid dynamics: an introduction* (Springer Science & Business Media, 2008).

[259] Date, A. W. *Introduction to computational fluid dynamics* (Cambridge University Press, 2005).

[260] Menter, F. R., Matyushenko, A. & Lechner, R. Development of a generalized k-ω two-equation turbulence model. In *Symposium der Deutsche Gesellschaft für Luft-und Raumfahrt*, 101–109 (Springer, 2018).

[261] Hu, S., Seshadri, S. & McFarland, A. R. Cfd study on compound impaction in a jet-in-well impactor. *Aerosol Sci. Tech.* **41**, 1102–1109 (2007).

[262] Hu, S. *Application of computational fluid dynamics to aerosol sampling and concentration*. Ph.D. thesis, Texas A & M University (2010). Texas A & M University.

Appendix A

Computational Modelling of Atmospheric Pressure Plasma

This appendix discusses the computational approach used in modelling atmospheric pressure plasmas in Chapters 3 and 4. A fluid model is used, as described below. Fluid model approach reduces computational complexity of large-scale plasma modelling to a more tractable size by considering the plasma behaviour as a continuous fluid rather than as discrete particles. In this thesis, a simplified discharge model is established and solved using finite element methods. COMSOL Multiphysics software [252] suite was used for generating and solving the models using the PARDISO [253] solver. Computational geometry used in the models were taken from the experimental configurations described in Chapters 2 and 3.

Computational Plasma Modelling

Computational models of plasmas aim to capture key parameters such as electron density and energy, reaction rates and particle fluxes in a plasma. To do so, highly coupled physical phenomena such as particle transport and chemical reaction rates must be simultaneously solved for in the entire domain. This section provides a brief outline into fluid plasma models and finite element methods used in this thesis.

Boltzmann Equation

Electron transport in any plasma can be described kinetically by solving the Boltzmann equation. The Boltzmann equation describes the evolution of particle number distribution $f(r,v,t)$ in terms of position (r), velocity (v) and time (t).

$$\frac{\partial f}{\partial t} + v \bullet \nabla_r \, f(r,v,t) + a \bullet \nabla_v \, f(r,v,t) = C\left(\frac{\partial f}{\partial t}\right) \tag{A.1}$$

This equation sets up a continuity relationship, where the flux of particles through fixed volume d^3r is governed by drift $(v \bullet \nabla_r \, f)$ and and acceleration $(a \bullet \nabla_r \, f)$ due to applied forces. In addition to transport phenomena, in plasmas particles are also generated and lost via collisional processes, the collision operator $C\left(\frac{\partial f}{\partial t}\right)$ is used to account for creation and removal of particles.

As an example, for electrons in an applied electric field the third term in Equation A.1 can be written as,

$$\frac{e}{m_e}(E \bullet \nabla_V f) \tag{A.2}$$

Where e is the fundamental charge, m_e is the mass of an electron and E is the applied electric field accelerating the electrons.

Computing a solution for this equation in the 3+3 dimensions of space and velocity is incredibly computationally intensive and can only be solved for simple models for a few particles or for reduced models as 0-dimensional cases by assuming spatial uniformity in velocity fields. As an example, in this work, Bolsig+ software [254] was been used in Chapter 3 to estimate electron energy distribution functions (EEDFs) in 0-dimensional helium plasma. In real cases, where spatial uniformity approximation breaks down, alternative approaches are used to evaluate plasma parameters.

Fluid Models

To overcome the computational difficulty of treating each particle as numerically distinct entities, fluid simulations reformulate the problem in terms of macroscopic quantities and fluxes. This reformulation, called the drift-diffusion model, describes the plasma using pre-determined electron energy distributions, calculated transport coefficients and a source term.

Electron Transport

At a fixed point, under this approximation, the change in electron density over time is given by the equation:

$$\frac{\partial}{\partial t}(n_e) + \nabla \bullet \Gamma_e = R_e \tag{A.3}$$

Where Γ_e is the electron flux and R_e is the source term describing the generation and loss of electrons due to inelastic collisions. The flux term contains both diffusive and migrative components and is expressed as:

$$\Gamma_e = -(\mu_e \bullet E) n_e - \nabla (D_e n_e) \tag{A.4}$$

Where mu_e is the electron mobility coefficient, and D_e is the electron diffusion coefficient. In the fluid case, both electron transport coefficients, μ_e and D_e, are parameters that can be pre-calculated for the 0 dimensional case as a function of mean electron energy using reference cross-sectional data. This abstraction avoids the forces on individual particles and instead considers the plasma as a continuum.

To obtain the migrative flux term, the electric field due to charged particles is solved via Poisson's equation $\nabla^2 V = -\frac{\rho}{\varepsilon}$ for potential V, as a function of space charge density ρ.

The source term can be calculated by considering the inelastic cross sections for the species in the plasma and expressing the reactions in terms of calculated rate coefficients (k_i) for reactions i. The rate coefficient is then solely dependent on electron energy, reaction cross section and an appropriately chosen electron energy distribution function (EEDF). The rate coefficient for reaction i is then expressed as:

$$k_i = \sqrt{\frac{2e}{m}} \int \varepsilon \bullet \sigma_k(\varepsilon) \bullet f(\varepsilon)\ d\varepsilon \tag{A.5}$$

Where ε is electron energy, $\sigma_k(\varepsilon)$ is the cross-section function of the target species and $f(\varepsilon)$ is the EEDF. Once rate coefficients for all reactions are known, the source term can then be calculated by summing over all the relevant reactions:

$$R_e = \sum_{i=1}^{M} k_i n_i n_e \tag{A.6}$$

Where n_i is the number density of the species taking part in the electron impact reaction. Taken together, equations A.4 and A.6 comprise the drift-diffusion model for plasmas.

Electron Energy Transport

While the drift-diffusion model as presented so far has provided for electron number density and flux, electron energy has not been discussed. Analogous to electron density flux, Electron energy flux in the system can be calculated by considering the rate of change of electron energy density:

$$\frac{\partial}{\partial t}(n_\varepsilon) + \nabla \cdot \Gamma_\varepsilon + E \cdot \Gamma_e = Q_\varepsilon \tag{A.7}$$

Where Γ_ε is the electron energy flux, expressed in the same form as Equation A.4 where electron energy mobility and energy diffusivity coefficients replace the electron transport parameters. Q_ε is the total loss or gain of energy due to collision processes, which is calculated using:

$$Q_\varepsilon = \sum_{i=1}^{M} k_i n_i n_e \Delta\varepsilon_i \tag{A.8}$$

Where $\Delta\varepsilon_i$ is change in electron energy due to collision process i.

Discretisation

Space and time dependent partial differential equations (PDEs) discussed above cannot be solved analytically. Instead, finite element methods are used to discretize the function domain and substitute numerical model equations to approximate the PDEs. Finite element methods rely on approximating the target function by a weighted set of basis functions. As an example, function $g(x)$ can be discretised in domain x using linear combinations of basis functions ψ_i:

$$g = \sum_i u_i \psi_i \tag{A.9}$$

Where u_i is the coefficient for basis function ψ_i. This requires the domain x to be discretised into an arbitrary number of intervals. Graphically, this process is shown using linear basis functions in Figure.

One significant benefit of this approach is that the discretisation interval can be chosen arbitrarily. As Figure A.1 shows, in intervals where the gradient of g is large, the error in the numerical model equation is also large. By increasing the density of intervals in a subset of the domain, the accuracy of the method can also be increased, approaching the analytical solution. In this thesis, discretisation of the spatial domain is done via *meshing* the 2D axisymmetrical model into rectangular and triangular elements.

Models Used in This Work

Two related models were built for plasma fluid simulation, reflecting the experimental geometry of the dielectric barrier discharge source. A time dependent solution was used due

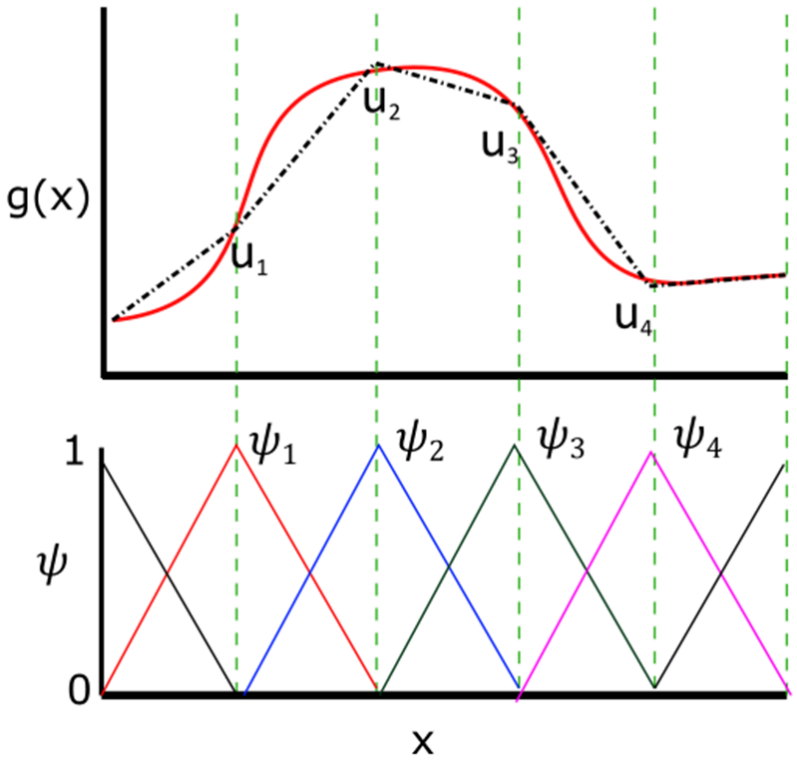

Fig. A.1 Graphical representation of discretisation of function $g(x)$ using basis functions.

to the constantly changing electrode potentials in the RF powered discharge. In the following sections, the parameters relevant to the simulations will be described for the two models.

Geometry Description

The first model, henceforth called "DBD" contains only the discharge volume within the dielectric tube, dielectric barrier and the driven electrodes. The DBD model was set-up to mirror the experimental conditions seen in Chapter 3. A second model was also produced, called "DBD-EL" replicating the experiments with Cu_2O in Chapter 4. The two models are identical apart from the presence a coaxial electrode pair inserted within the discharge tube in the DBD-EL model.

DBD Model

Figure A.2 shows the discharge geometry of the DBD discharge tube, the central region shaded in blue indicates the area where the fluid plasma model was solved. The area of interest for this model was the discharge volume between the electrodes and the afterglow region extending away from the central discharge. The model dimensions were the same as described in Chapter 2.

DBD-EL Model

Figure A.3 shows the geometry of the DBD-EL model, with the inserted coaxial electrode highlighted. This model was identical to the DBD model with the addition of the auxillary electrode assembly, modelled in full, to probe the effect of an external field within the plasma afterglow. Dimensions of the auxillary electrode were taken from the experimental set-up described in Chapter 4.

The internal volume of the discharges, shown in blue in Figures A.3 and A.2, was set up as the plasma finite element simulation domain. All elements of the geometry in contact with the plasma were assigned boundary conditions reflecting the experimental setup, these boundary conditions are also labelled in Figures A.3 and A.2. The electrodes were modelled as electrical terminals with the top electrode serving as the plasma ground and the bottom electrode serving as the powered terminal. Two ends of the tube were designated as insulators where all plasma species can freely escape. The simulation domain was restricted to the internal volume of the quartz tube with no consideration of the gas inlet or the outlet. A list of all boundary conditions for both models are given in Table A.1 below.

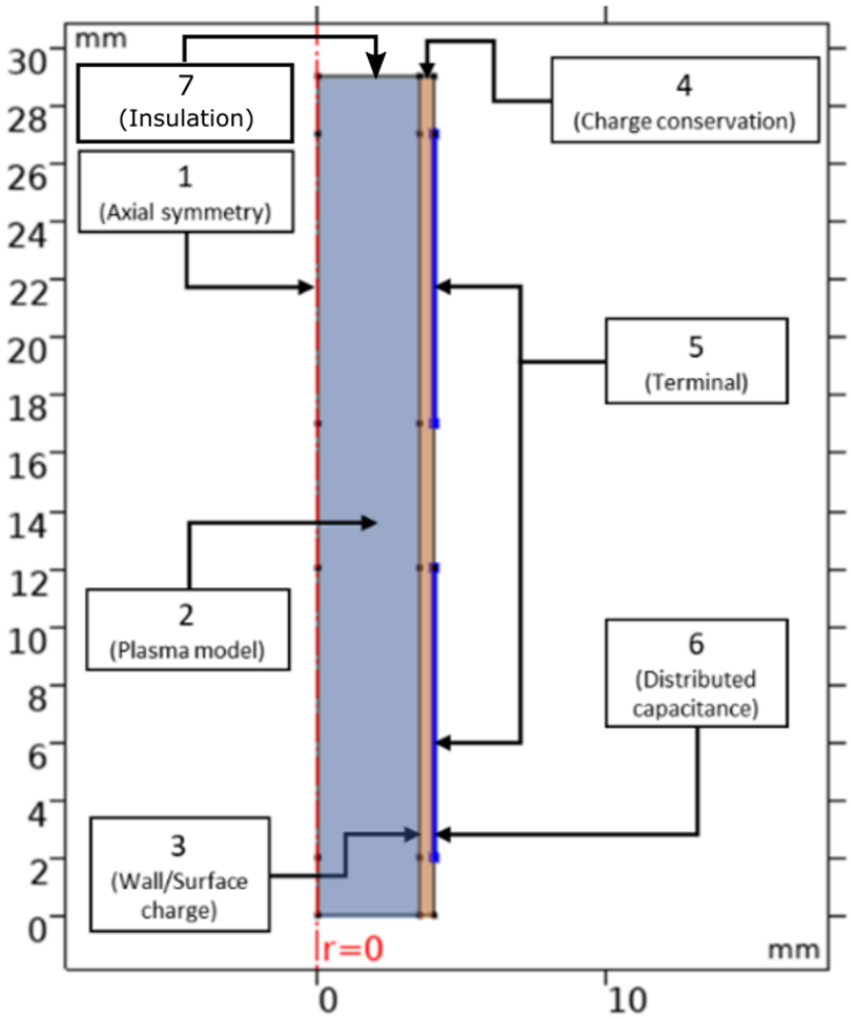

Fig. A.2 Discharge geometry of the DBD model with boundary conditions and the plasma simulation domains labeled. Red line at r=0 indicates the axis of symmetry.

Meshing

The geometries were discretized into mesh elements using a mixed rectangular and triangular mesh approach. For the DBD model, the discretization consisted entirely of rectangular mesh elements (Figure A.4), with a total of 4128 rectangular elements, providing 19502 degrees of freedom. The boundary elements used to define the rectangular mesh were distributed according to a geometric sequence as to have a higher mesh density between the electrodes, where the electric field is the strongest, and near the walls of the geometry. Additional boundary layers were added on the internal wall boundary in contact with the plasma to further decrease the minimum mesh size down to 500*nm* adjacent to the wall boundaries.

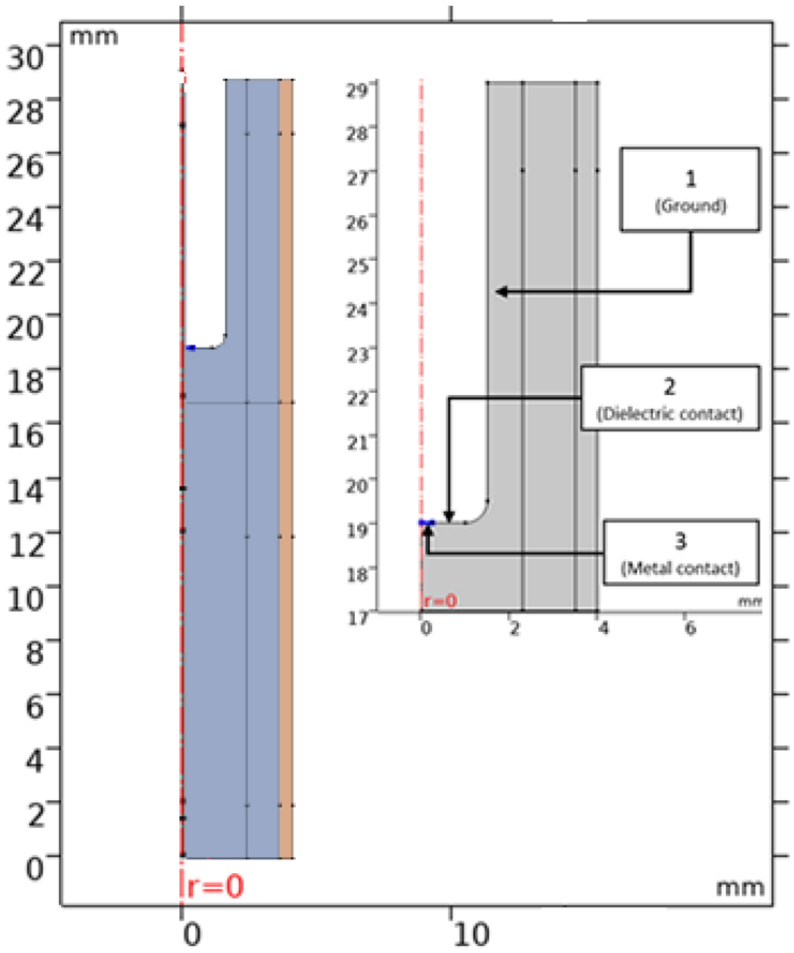

Fig. A.3 Discharge geometry of the DBD-EL model with inset showing the electrode boundary conditions.

The DBD-EL model was discretized using a combination of regular rectangular and triangular mesh elements (Figure A.5). The mapped rectangular mesh from the DV model was used in all areas apart from the region around the central electrode where the mesh density was increased by an order of magnitude. The tip of the electrode was discretized with a uniform distribution of boundary elements, with a minimum element size of 350 nm, and 20 boundary layers were added to its surface, with a minimum thickness of 100 nm. This yielded a total number of 34104 mesh elements, providing 122593 degrees of freedom. The discrepancy in the size of the two models were due to this additional mesh density. The increased mesh density was required as significant electric field gradients were generated upon the introduction of the auxiliary electrode assembly, requiring increased mesh quality for convergence.

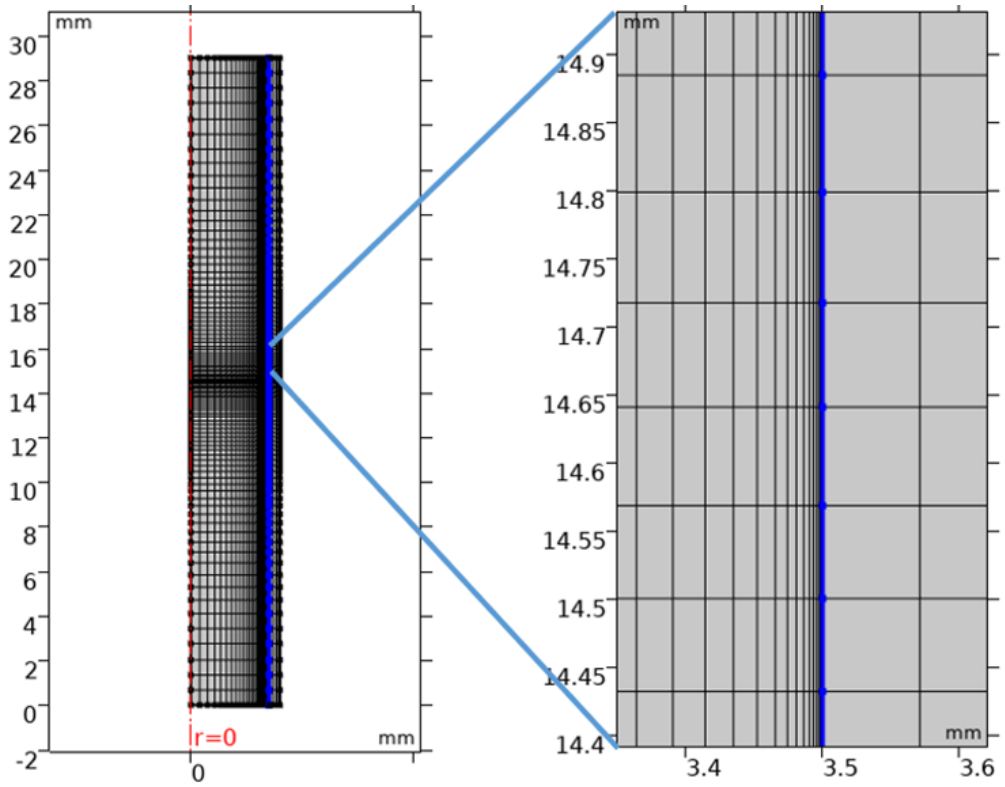

Fig. A.4 Rectangular mesh elements of the DBD model (right), showing the increased mesh density in the area between the driven electrodes. Magnified region (right) shows the high refinement of the mesh along the plasma - dielectric boundary.

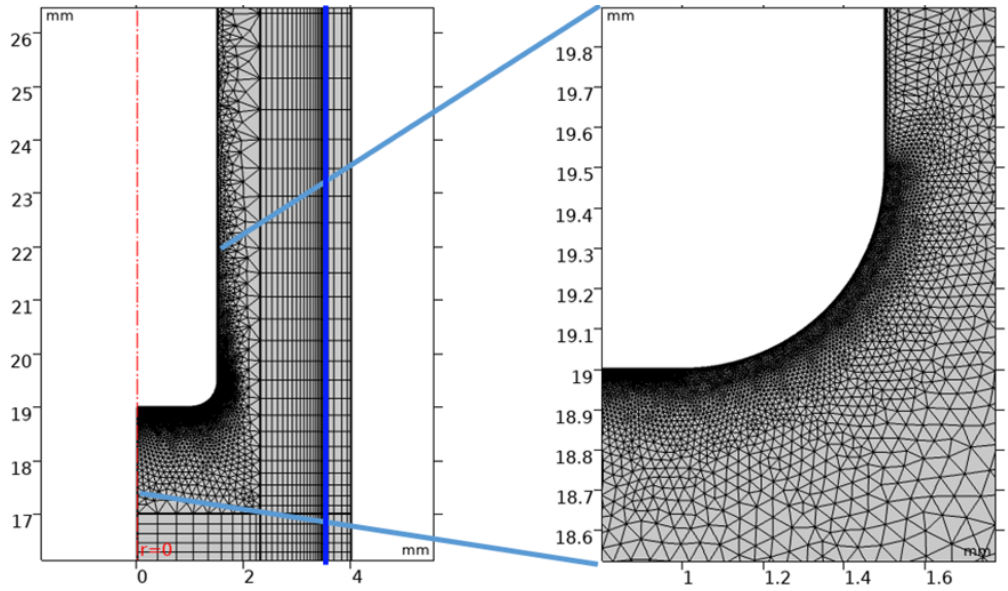

Fig. A.5 High density mesh elements around the auxillary electrode geometry in the DBD-EL model (left), magnified view of the electrode surface facing the plasma discharge showing a high density of mesh elements near the boundaries.

A.1 Plasma Chemistry

A highly simplified reaction and species model was used in the discharge to restrict the model size by limiting the degrees of freedom. No contaminant gases were modelled, as the expected levels of impurities in the gas were low. It is known that even small amounts of molecular gas impurities can have a significant effect on the discharge characteristics, unfortunately this model did not capture these effects due to omission of potential impurities in the plasma gas.

The four species considered, their transport parameters and secondary electron emission coefficients (γ) are presented in Table A.2 . Electron energy distribution function was chosen to be in the form of a Druyvesteyn distribution [255] rather than Maxwellian. This was done as a Druyveystein distribution was found to be a better match to the EEDFs calculated via a 0-dimensional model.. Diffusion coefficients were computed using the general Einstein relation (GER) directly, while mobility coefficients of the charged species were taken from Ellis et al. [256] The model temperature and pressure was kept uniform and stable at 360 K and 1 atm respectively.

Table A.2 Chemical species and transport coefficients considered in the fluid models.

Species	Mobility	Diffusivity	γ
e	$3 \times 10^{24}\ V^{-1}m^{-1}s^{-1}$	From GER	-
He	-	From GER	-
He*	-	From GER	0
He+	f(E/N)	From GER	0.1

Eight gas phase and two surface reactions were considered in the plasma discharge model. Cross-sectional data was used where available for the electron impact reactions. Further reactions were added via the use of Arrhenius parameters. For excited species and ion impact onto the dielectric walls the sticking coefficients (S_c) were set to unity. Table provides the relevant parameters for the reaction set used in this work.

Table A.3 Reaction rate expressions and sticking coefficients considered in the fluid models.

Reaction	Type	Rate constant / S_c	$\delta\varepsilon$	Reference
e + He → e + He	Elastic	$f(n_e, T_e)$	-	[11]
e + He^+ → He^*	Recombination	$7.13 \times 10^{-17} T_e^{-0.5}$ $m^3 s/mol$	-	[257]
2e + He^+→ He^* +e	Recombination	$1.04 \times 10^{-20} T_e^{-4.5}$ $m^6 s/mol$	-	[257]
e + He → e + He^*	Excitation	$f(n_e, T_e)$	-19.8 eV	[11]
e + He^* → e + He	De-excitation	$1.10 \times 10^{-17} T_e^{0.31}$ $m^3 s/mol$	19.8 eV	[257]
e + He → 2e + He^+	Ionisation	$f(n_e, T_e)$	-24.6 eV	[11]
e + He^* → 2e + He^+	Ionisation	$f(n_e, T_e)$	-4.78 eV	[11]
He^+ → He	Surface	$S_c = 1$	-	
He^* → He	Surface	$S_c = 1$	-	

A.1.1 Model Initialisation

The DBD model was initialised by providing the initial electron density and temperature as a gaussian profile centred between the electrodes, with peak values of 1×10^8 cm^{-3} and $3eV$ respectively, decaying to near 0 around the plasma boundaries. Helium ion density was initialized identically to the electron density to satisfy the electroneutrality constraint. Neutral species were initialized using a mass constraint at 1 atm, excited species density was set to a minimal molar fraction of 1×10^{-15}. For the DBD-EL model, the converged quantities taken from the DV model solution were used for initialisation in order to speed up the solution.

A.1.2 Solution and Convergence

Both models were solved using the PARDISO solver. The models were solved in a time dependent manner, periodic solutions were not possible due to the sizes of the resulting models. Time steps taken by the solver were in the picosecond range, a fraction of the excitation period of 74 ns. Convergence was assumed when the relative change in electron density in the centre of the discharge was below 50 ppm between two cycles of the driving RF waveform, this is shown graphically in FigureA.6. Convergence was reached after 350 RF cycles, after this point the model was run for a further 100 cycles to ensure a steady state solution. The total run time for both models was approximately 33 μs. The total solve time for the DBD and DBD-EL models were 52 and 109 hours, respectively.

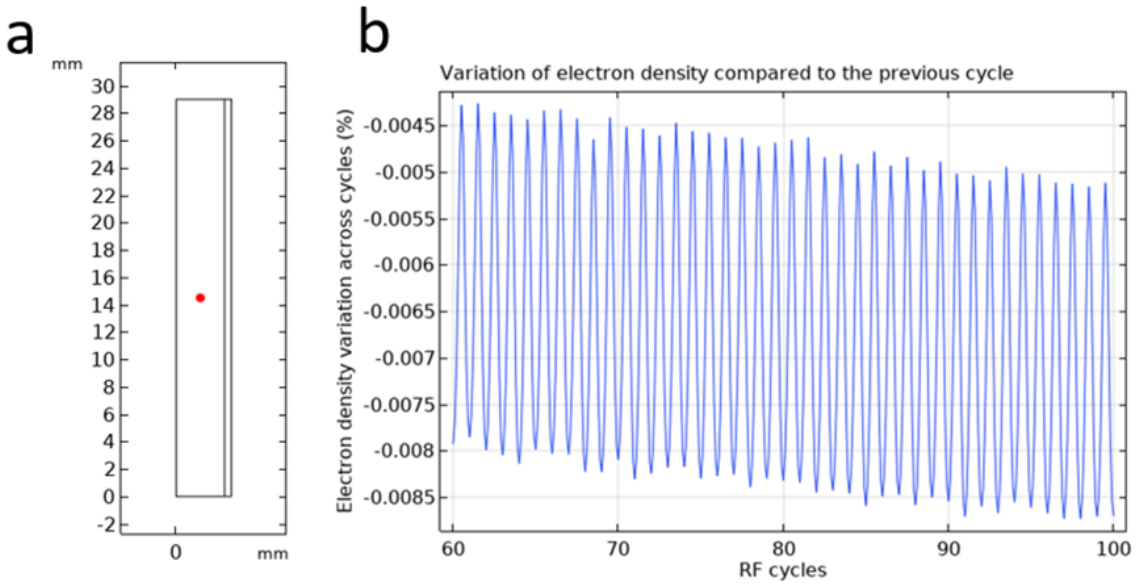

Fig. A.6 Point in model geometry where the electron density was measured for determination of convergence (a). The variation in electron density across simulated RF cycles (b).

Table A.1 Boundary conditions and their descriptions as used in the computational plasma models

Boundary Condition	Boundary Condition Expression	Description	Boundary	
			DBD	DBD-EL
Metal contact	$\int_{\partial\Omega}(\mathrm{n}\cdot\mathrm{J_e}+\mathrm{n}\cdot\mathrm{J_i})\mathrm{dS} = \mathrm{I_{circuit}}$	Sum of ion $(n\mathrm{J_i})$ and electron $(n\mathrm{J}_e)$ flux into the surface is equal to plasma circuit current $(\mathrm{I_{circuit}})$.		3 ,1
Insulation	$-n\cdot\Gamma_e = 0$ $-\mathrm{n}\cdot\Gamma_i = 0$ $-\mathrm{n}\cdot\Gamma_\epsilon = 0$	No net flux of electrons (Γ_e) ions $(\Gamma)_i$and electron energy (Γ_ϵ) across the boundary.	7	
Dielectric contact	$\frac{\partial\sigma_s}{\partial \mathrm{t}} = \mathbf{n}\cdot\mathbf{J_e}+\mathbf{n}\cdot\mathbf{J_i}$	The surface charge density (σ_s) is the sum of collected ion and electron flux to the surface.	3	2
Distributed capacitance	$n\cdot D = \sigma_s + C_s$	Surface potential (D) is determined by charge density and distributed capacitance of the surface.	6	

Appendix B

Computational Fluid Dynamics in Plasma Jet Deposition

An understanding of gas-solid interaction and aerosol particle deposition is required to fully understand the experimental results obtained during plasma jet deposition. Using computational fluid dynamics (CFD), flow characteristics of gas plumes can be simulated with reasonable accuracy and this approach can be further expanded to probe aerosol deposition through a jet of gas. Fluent 2020 [220] (Ansys, USA) software suite was used in this work to implement CFD models paralleling experimental conditions. $k-\omega$ model was used to model and optimise flow characteristics of the plasma deposition nozzle and multiphase flow simulations were used to understand the behaviour of aerosol particles in the plasma jet. This Appendix will provide a short introduction to CFD methods and describe the simulation techniques used in plasma jet deposition. Further detail can be found in a number of books that treat the subject in an in-depth manner [258, 259].

B.1 CFD Procedure

CFD analysis of the plasma jet requires three distinct steps. First, a mesh is generated, transferring the experimental geometry into the computational domain and then subdividing the volume of interest into mesh units that can be used to numerically solve the model. Secondly, the CFD software is used with the relevant parameters to arrive at a converged solution for gas flow in the simulation domain. Third, virtual particles are injected into the simulation to track their behaviour. The velocity field, taken from the CFD solution, is used to calculate the resulting forces on these aerosol particles in a Lagrangian reference frame

where each particle is considered separately. The following sections will cover all three processes in order.

B.1.1 Meshing

The reference geometry for the plasma jet nozzle was obtained from optical micrographs of the experimental set-up and converted into an axisymmetric model in Fluent. The distance to the deposition surface was kept also identical to what used in the experiments. Experimental details are provided in Section 7.2. The resulting geometry and mesh are shown in Figure B.1

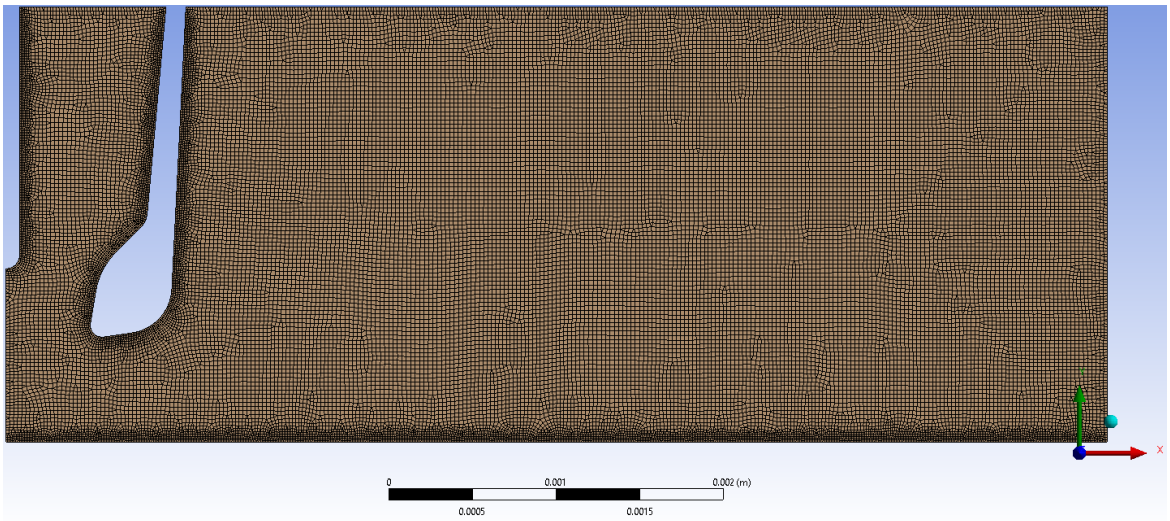

Fig. B.1 The model geometry and the resulting mesh for CFD calculations, scale bar is 2 *mm* in length.

The overall geometry was constrained in a 7×2.5 *mm* box. Only the nozzle and the electrode were modelled, with the rest of the nozzle assembly simply reduced to a solid wall, at the top of the domain. The bottom bounding wall was the substrate surface. Final mesh consisted of 35595 elements, with minimum edge length of 1 μm. The electrode centre was considered the axis of symmetry of the entire system and the rest of the models were solved accordingly.

B.1.2 Fluid Flow Solution

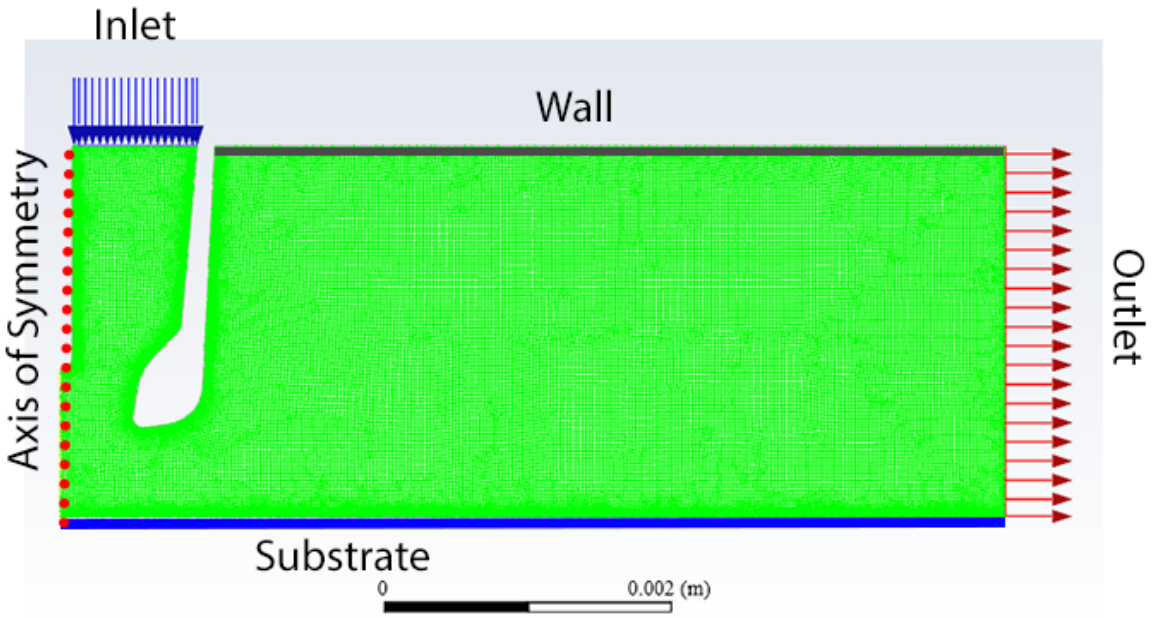

Fig. B.2 The boundary conditions used in the CFD simulation domain.

Fluent software was used for solving the velocity and species concentrations in the plasma plume. The 2 equation $k-\omega$ GEKO model was used for the viscous flow simulations [260] as implemented in Fluent. The choice of $k-\omega$ model was based on previous demonstrations of efficacy in CFD studies of aerosol sampling impactors [261, 262]. Overall, the effect of turbulent dispersion in experiments and simulations were minimal at the flow rates considered, making the specific choice of viscous flow model have a minimal impact on the results.

Initial Conditions

The jet inlet was specified as a mass flow inlet, mirroring the experimental conditions. The final volumetric gas composition was approximated as consisting of 70 *v.%* argon and 30 *v.%* helium, disregarding the hydrogen and water vapour content in the gas flow. Overall volumetric flow rate through this inlet was 350 $mL\ min^{-1}$. The temperature of gas inlet was kept fixed at 100 $^{\circ}C$ in line with experimental measurements.

For initialisation, the entirety of the simulation domain was considered to be made up of synthetic air consisting of 70 *v.%* nitrogen and 30 *v.%* oxygen. The outlet surrounding the jet was designated as a pressure outlet at 1 *atm*. The turbulent intensity at both the inlet and outlet was set to 0, assuming fully laminar flow.

All walls were considered to be no-slip, assuming zero fluid velocity in contact with the wall.

CFD Solution

The CFD solver was run in a time dependent manner till convergence was reached. Convergence criteria required scaled residuals to decrease to 10^{-4} as implemented in FLUENT.

B.2 Particle Path Analysis

For tracking aerosol behaviour in the plasma plume during deposition, a discrete phase model was used. In this scheme, the trajectory of a particle is calculated by the integration of the forces acting on the particle. The resulting force is then used to calculate the position of the particle within the simulation cell and the next position of the particle given a certain time-step.

Drag force and gravity were the external forces considered in calculating the particle trajectories. No collisions or two-way coupling effects between the fluid and particle flow were considered.

B.2.1 Particle Injection

For tracking particle paths, particles were injected in to the simulation domain with a uniform spatial distribution at the inlet. The aerodynamic sizes of the particles were randomly distributed between 0.2 and 3 μm due to lack of information on the experimental distribution. The particle density was chosen to be $8.9 g\ cm^{-3}$, assuming fully dense copper particles.

The substrate surface was considered to have a capture efficiency of 100% meaning that particles were considered *on-wall* if they collided with the substrate wall, otherwise they were considered *lost*. Inner surfaces of the deposition nozzle were set to have 0 capture efficiency, meaning that all particles colliding with either the electrode or the nozzle surface would be reflected back into the gas stream.